THE HENRYK NIEWODNICZAŃSKI
INSTITUTE OF NUCLEAR PHYSICS
POLISH ACADEMY OF SCIENCES

Search for ultra-high energy photons through preshower effect with gamma-ray telescopes

Kévin Almeida Cheminant

Supervisor
Dr. hab. Dariusz Góra

A thesis submitted in fulfillment of the requirements for the degree of

Doctor of Philosophy

in the

Henryk Niewodniczański Institute of Nuclear Physics
Polish Academy of Sciences

Krakow, 2020

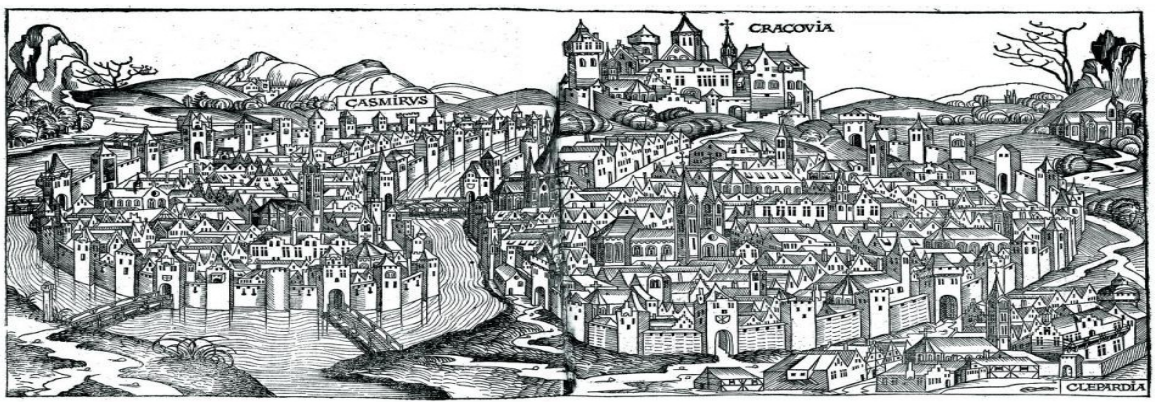

"M. Le Verrier a aperçu le nouvel astre sans avoir besoin de jeter un seul regard vers le ciel; il l'a vu au bout de sa plume."

François Arago, 1846

Abstract

As ultra-high energy photons (EeV and beyond) propagate from their sources of production to Earth, radiation-matter interactions can occur, leading to an effective screening of the incident flux. In this energy domain, photons can undergo e^+/e^- pair production when interacting with the surrounding geomagnetic field, which in turn can produce a cascade of electromagnetic particles called *preshower*. Such a cascade can initiate air showers in the Earth's atmosphere. Gamma-ray telescopes, such as the next-generation gamma-ray observatory Cherenkov Telescope Array, can detect these showers thanks to the Cherenkov radiation they emit. The feasibility of detecting such phenomena using Monte-Carlo simulations of nearly-horizontal air showers is studied, considering the example of the La Palma site of the Cherenkov Telescope Array. The efficiency of a multivariate analysis in correctly identifying preshower events initiated by 40 EeV photons and cosmic-ray dominated background simulated in the energy range 10 TeV – 10 EeV, is investigated. The effective areas for such events are also calculated and event rate predictions related to different ultra-high energy photons production models are presented. The expected number of preshowers from diffuse emission of ultra-high energy photon for 30 hours of observation is estimated around 3.3×10^{-5}, based on the upper limits put by the Pierre Auger Observatory, and is at the level of 2.7×10^{-4} (5.7×10^{-5}) when considering the upper limits of the Pierre Auger Observatory (Telescope Array) on ultra-high energy photon point sources. However, ultra-high energy photon emission may undergo possible "boosting" due to gamma-ray burst, increasing the expected number of preshower events up to 0.17, and yielding a minimum required flux of ~ 0.2 km^{-2}yr^{-1} to obtain one preshower event, which is about a factor 10 higher than upper limits put by the Pierre Auger Observatory and Telescope Array (0.034 and 0.019 km^{-2}yr^{-1}, respectively).

Acknowledgements

Working on the most important part of my studies, for four years, in a foreign country, could never have been done without the people that have guided and supported me. First of all, I would like to thank my supervisor, Dariusz Góra, whose expertise and dedication have made this work absolutely captivating and full of surprises. His little pushes when I felt stuck, and sometimes lost, are truly appreciated. I am also grateful to Piotr Homola who gave me the opportunity to start my PhD thesis within the CREDO collaboration. His enthusiasm and his curiosity have kept mine sharper than ever, encouraging me to explore all possible solutions to a given problem. I would like to thank all the people at IFJ that have contributed to making this journey, a fantastic one: Konrad for his assistance and his friendship from the very beginning; Niraj for our long talks outside the institute and his help with my programming issues that were quite frequent; Alex for enduring with me the difficulties of being a foreign PhD student; Beata and Monika for being the two most helpful secretaries I have ever met, making administrative paperwork much easier to handle; and Jan Pękala for his comments, significantly improving the quality of this dissertation. I am also thankful to Konrad Bernlöhr for his very detailed answers to my issues regarding the *sim_telarray* package and to the staff of ACC Cyfronet AGH-UST for their always helpful supercomputing support.

This dissertation is the result of many great encounters that have forged my interest for the field of astroparticle physics over the years. I am eternally grateful to Mr. Cenac, my midschool physics teacher, who gave me a taste for physics early on and managed to stimulate the scientific curiosity of a carefree teenager. My first steps in the world of astroparticle physics were made possible thanks to Dr. Bob and Jodi Christiansen, from the Cal Poly San Luis Obispo university. I cannot thank them enough for the opportunities they gave me. I also want to thank Stefano Gabici from APC, who supervised my master's thesis and introduced me to the difficult world of theoretical gamma-ray astronomy. Our discussions over sushis are always something I look forward to.

Without the support of my family and my friends, I would not have reached this very important milestone of my life. I dedicate this thesis to my

mom and my sister, for their constant love, care and attention. No words are strong enough to express my gratitude. I also thank my father and my friends, whether in France, Poland or the US, who have been a driving force: Martichou, the nicest person I have ever met; Alexandre, for the countless endless nights that have made this PhD thesis much longer than it should have been; Alexander, a great friend that needs to finally accept that France was always been on the winning side; Róża, for being by my side throughout the writing of this thesis and for having to endure my very changing mood; Caroline, who always finds a way to make me smile; Natalia, for helping me keeping my head up and constantly supporting me; James, for his chill and friendship despite the distance; Magda, for her bright mind and all the crazy moments we have shared; Lukiki, for her everlasting frienship; and all my other friends, who have made my life better and who I could not mentioned in these already too long acknowledgements.

Last but not least, I also want to dedicate this thesis to Erin. Not everything worked out as we had planned but I am eternally grateful to you. Your strength, intelligence and perseverance have shaped the person I am and I would not have reached half of my objectives without your love.

Contents

INTRODUCTION

In astroparticle physics, several theoretical models predict the production of ultra-high energy (UHE) photons (EeV and beyond), that would constitute a fraction of the ultra-high energy cosmic-ray (UHECR) flux seen on Earth. Whether they emerge as the result of the interaction of UHE protons or nuclei with the cosmic microwave background (CMB), or from the decay of super-massive particles, the direction of propagation of UHE photons is unaffected by electromagnetic fields, which makes them valuable messengers in the identification of sources of UHECRs. Nevertheless, the highest energy events observed by the leading collaborations, the Pierre Auger Observatory and Telescope Array, are not considered photon candidates, if the present state-of-the-art air-shower reconstruction procedures are applied.

The most straightforward explanation for the absence of UHE photon observations could simply be related to the absence of physical mechanisms responsible for their production, therefore refuting predictions made by both classical bottom-up and exotic top-down scenarios of UHECR production. Although rather simplistic and quite effortless, such an explanation remains fully conceiveable, as recent experimental limits from the Pierre Auger Observatory and Telescope Array on the UHE photon flux strongly disfavor the exotic models. Alternatively, as predicted by Lorentz invariance violation models, UHE photons may decay after a very short period of time (of the order of 1 second). In this case, their decay occurs nearly immediately after their production and gives them no chance to reach the Earth, making direct observations of such photons almost impossible. One can also speculate that UHE photons do not reach the Earth because of some yet unknown, or not well-understood, processes occurring before entering the Earth's atmosphere. As these photons travel through space, they may interact with electromagnetic fields of different origin and produce cascades of secondary particles of lower energy. Such screening effect leads to the production of air showers, whose properties may differ from the ones of unconverted photons. Consequently, the lack of conclusive observations of UHE photons could also be related with the fact that existing air-shower reconstruction techniques are not capable of distinguishing

hadronic showers and showers induced by UHE photons which would have first generated an electromagnetic shower before entering the atmosphere.

Since such a process may occur at very large distances from Earth, the transverse size of the mentioned cascades can be comparable with the Earth's diameter. A good candidate for such a mechanism is an electromagnetic shower induced by an UHE photon interacting with the solar magnetic field. The particles within this shower could be spread on a global scale and may be observed through the analysis of the spatial and time correlation between the multiple subsequent air showers produced. Such endeavor has been undertaken by the Cosmic-Ray Extremely Distributed Observatory collaboration, which provided the framework within which this work was carried out.

In this dissertation, particular attention was given to the case where such photons interact with the geomagnetic field up to several thousands kilometers above the Earth's atmosphere, and produce electron-positron pairs which, in turn, radiate bremsstrahlung photons. This ensemble of electromagnetic particles rushing towards the atmosphere is called preshower. This preshower channel of observation has not yet been studied by the existing cosmic-ray and gamma-ray observatories, and therefore, investigating it constitutes a pioneer research focus of astroparticle physics.

The observation of gamma rays from the ground can be performed with Imaging Atmospheric Cherenkov Telescopes (IACT) which record the Cherenkov light emitted by the charged particles of the air showers produced by these gamma rays. Three major observatories are presently collecting data in both hemispheres, allowing a full-sky survey of the Universe at the highest energies. In the northern hemisphere, the Major Atmospheric Gamma-ray Imaging Cherenkov (MAGIC) telescopes and the Very Energetic Radiation Imaging Telescope Array (VERITAS) have been operating since 2005 and 2007, respectively, while the High Energy Stereoscopic System (H.E.S.S.) has produced results in the southern hemisphere since 2003. So far, the highest energies of detected gamma rays reach a few hundred of TeVs.

However, due to the low expected flux of particles in the UHE domain and to the energy threshold of IACTs, the standard vertical mode of observation of gamma-ray telescopes is no longer efficient. In this energy range, the detection of air showers is usually performed by arrays of particle detectors on the ground, such as the Pierre Auger Observatory and Telescope Array, which extend over several hundred or thousand of square kilometers. Nevertheless, in this dissertation, the use gamma-ray telescopes in a non-standard approach, i.e. in the nearly-horizontal direction (high zenith angles), is considered. Nearly-horizontal air showers have their hadronic and electromagnetic components absorbed in the atmosphere, leaving muons as the dominating component in the later development stages. This muonic component signif-

icantly varies from one primary to another and can be used to assess the differences in the characteristics of extensive air showers produced by different primaries, such as unconverted photons, protons and iron nuclei, in order to identify how distinctive preshower-induced showers may be. Consequently, looking at nearly-horizontal air showers makes possible the isolation of the muonic component, as well as the study of the separation power between the cosmic-ray dominated background and the preshower effect one could obtained using gamma-ray telescopes. Furthermore, looking for air showers at high zenith angles offers a greater collection area, about 10-100 times larger, compared to the typical aperture of gamma-ray experiments in the standard mode of observation. However, due to the geometry of the cascade development, the Cherenkov light detected by the IACT cameras is produced further away from the telescopes. In the TeV domain, such a characteristic leads to the formation of very small images in the cameras, often within a single pixel, and therefore results in a poor photon/hadron separation. Nevertheless, in the EeV domain, the dominating muonic component can produce brighter and larger images such that a good separation can be recovered.

In this work, the study of the properties of preshowers was carried out by investigating different energies for the primary photons, as well as different arrival directions, with a particular attention given to the case where photons are headed towards La Palma – the selected northern hemisphere site for the future Cherenkov Telescope Array (CTA-North) and present MAGIC location – in a nearly-horizontal direction. To do so, the PRESHOWER algorithm was used.

When these preshowers fall into the atmosphere, they may in turn initiate extensive air showers. The properties of these showers, such as their composition, their longitudinal development, their ground distribution, and the origin of the Cherenkov light they emit, can be examined via the CORSIKA simulation software.

As previously mentioned, the Cherenkov light emitted by extensive air showers can be recorded by the cameras of IACTs in the form of images generated by triggered pixels. The main focus is set on simulating the cameras properties and the geographical location of CTA-North with the *sim_telarray* package. The images formed by the cosmic-ray background and preshower-induced air showers are analyzed and compared, through a set of geometrical parameters – called Hillas parameters – that characterize these images. With a multivariate analysis using Boosted Decision Trees (BDT), the cosmic-ray background/converted UHE photon separation power obtained assuming properties of the CTA-North design, and for different preshower scenarios (point/diffuse source of UHE photons), was investigated.

From the results of the multivariate analysis, the aperture of CTA-North,

as well as the number of events that should be detected based on the flux of UHE photons predicted by different models (Greisen–Zatsepin–Kuzmin effect, super-heavy dark matter, etc.), were calculated.

This dissertation is organized as follows: in Chapter 1, the fundamental physics of extensive air showers, as well as the latest measurements of UHECRs performed by leading experiments, are reviewed. In Chapter 2, UHE photons are discussed: how they might be produced, the results of searches performed by cosmic-ray experiments and the properties of magnetic cascades they may generate when interacting with different electromagnetic fields. Chapter 3 briefly discusses the underlying principles of gamma-ray astronomy, addressing the characterisitcs of nearly-horizontal air showers. The Cherenkov Telescope Array is also introduced. In Chapter 4, the properties of preshowers at CTA-North are analyzed and the features of the extensive air showers produced by different primaries at high-zenith angles, including the characteristics of the images they form in the telescopes cameras, are examined. Chapter 5 investigates the cosmic-ray background/converted UHE photon separation obtained with the help of BDT. Finally, in Chapter 6, the aperture and the event rate of preshowers are calculated, taking into account different production models and upper limits set by the Pierre Auger Observatory and Telescope Array. The influence of different simulation parameters on the camera images is also discussed and futher research perspectives are provided.

1. Ultra-High Energy Cosmic Rays

The discovery of cosmic rays by Victor Hess in 1912 opened a new window on the Universe [1], providing a new channel of observation on some of the most energetic events occuring in the cosmos. In the twentieth century, many experiments dedicated to the detection of cosmic rays saw the day, seeking to reveal their origin and their nature. Above 10^{14} eV, cosmic rays interact with the atmosphere and produce atmospheric cascades of secondary particles that can be detected on the ground. Since the first evidence of cosmic rays with energy above 10^{17} eV [2], also referred to as ultra-high energy cosmic ray (UHECR), remarkable progresses have been made in the quest for understanding the properties of the most energetic particles ever observed. Yet, UHECRs are still shrouded in mystery and unanswered questions. Are they of Galactic or extragalactic origin? Are the observed anisotropies providing any clue about the nature of their sources? What physical mechanisms may allow to accelerate particles to such extreme energies? How do they interact with magnetic fields and background radiation as they travel through space? How does their composition evolve as a function of the energy? Most recent results obtained by leading collaborations such as the Pierre Auger Observatory (Auger) and Telescope Array (TA) have provided a better understanding of the properties of UHECRs by reducing both systematics and statistical uncertainties, essentially thanks to hybrid modes of observation and larger exposure. Figure 1.1 shows the most up-to-date cosmic-ray spectrum measured by multiple ground-based experiments, covering 7 orders of magnitude in energy. Nevertheless, the characteristics of UHECR remain poorly understood for the most part, and much effort is still being devoted to strengthening our knowledge of these elusive particles. In this chapter, a concise review of the physical processes responsible for particle cascades initiated by the interaction of UHECRs with the atmosphere, is given. Detection techniques of such cascades are also discussed and the latest results obtained by leading UHECR experiments are presented, before reviewing some of the propagation effects affecting UHECRs. Their possible sources of production are also addressed in the last section.

1.1 Extensive Air Showers

When ultra-high energy particles (protons, nuclei, photons or neutrinos) interact with the oxygen and the nitrogen molecules composing the atmosphere, they initiate cascades of secondary particles which characteristics are a function of the properties of the atmospheric layer they propagate through and of the type of physical interactions occuring at different stages of the cascade development. In the initial phase of the cascading process, the number of particles increases while the energy per particle drops and distinct components

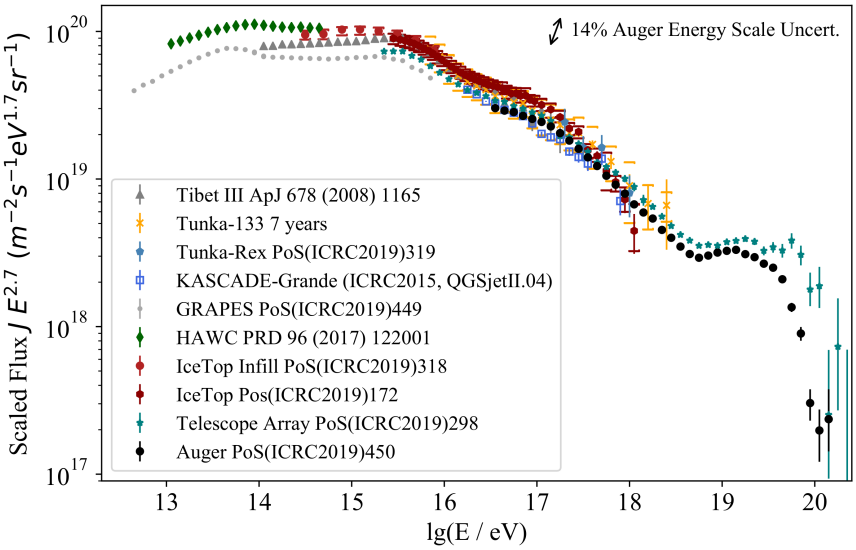

Figure 1.1: Energy spectrum of cosmic rays observed by several ground-based experiments. Figure taken from [3].

emerge, namely the hadronic, electromagnetic and muonic components (see Figure 1.2). Such growth carries on until a maximum is reached, as particles below a certain energy threshold are no longer capable of producing additional particles and as atmospheric absorption processes, such as ionization, take over. As many as $10^6 - 10^9$ secondary particles may reach the ground over a surface that can extend up to several square kilometers – such phenomenon is often referred to as *Extensive Air Shower* (EAS). In this section, a definition of the *atmospheric depth*, the quantity used to investigate the behavior of EAS's at different stages of their development, is given. Then, some of the toy models that have been developed in order to describe electromagnetic and hadronic shower properties, are described. The most important particle interactions are summarized and an outline of the transport equations that govern the particle content of both hadronic and electromagnetic showers, is given. Finally, the relation between the muon content and the nature of the UHECR primary is discussed, and the different EAS characteristics, that play an essential role in the photon/hadron separation, are highlighted.

1.1.1 Atmospheric depth

As secondary particles produced in EAS's traverse several kilometers of atmospheric layers, absorption processes, mainly ionization of the medium, may occur along the path of propagation. In order to characterize how the number

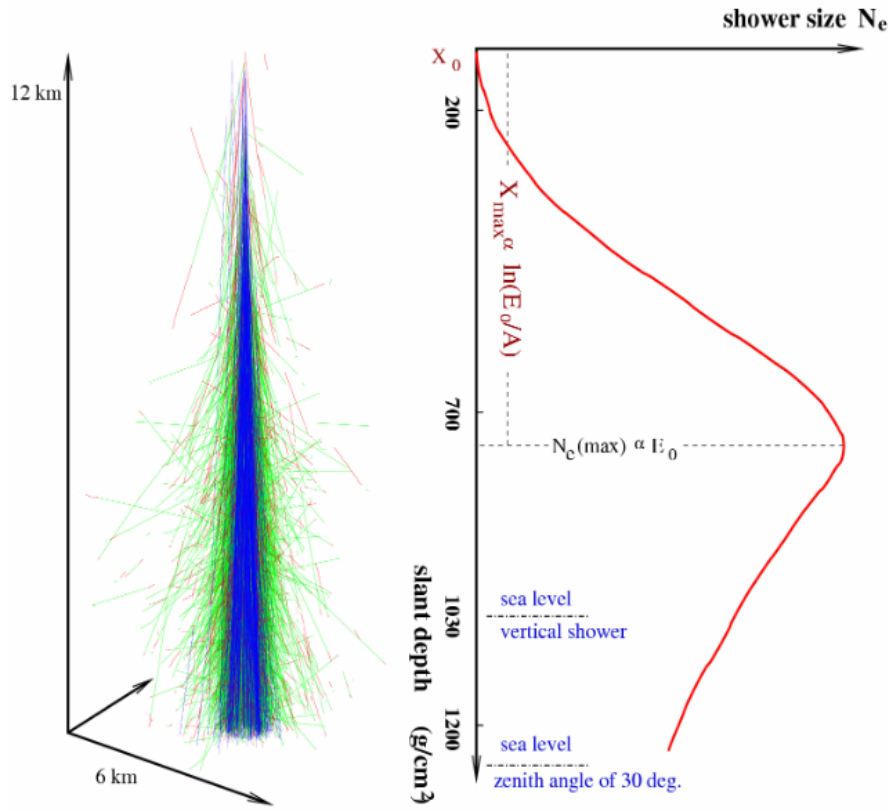

Figure 1.2: Characterization of EAS development as a function of the slant depth (electrons, hadrons and muons are represented in blue, green and red, respectively), produced by a 10^{20} eV proton. The depth of maximum development $X_{\max}$ as well as the number of electrons N_e as a function of the depth are shown (see Heitler's and Heitler-Matthews' models in Sections 1.1.2 & 1.1.3 for more details on these quantities).

of such interactions varies with the amount of atmosphere travelled through, one can rely on the *vertical atmospheric depth* X (in $\mathrm{g\,cm^{-2}}$), also called *column density*, which represents the amount of atmospheric mass thickness an EAS has already penetrated when observing it at an altitude z_{obs} (see Figure 1.2). It is expressed as a function of the atmospheric mass density ρ_{atm}, which in turn is a function of the altitude z:

$$X(z_{\mathrm{obs}}) = \int_{z_{\mathrm{obs}}}^{\infty} \rho_{\mathrm{atm}}(z)\mathrm{d}z. \tag{1.1}$$

The atmospheric pressure P_{atm} is defined by the amount of mass m weighting on a cross-sectional area A at an altitude z such that:

$$P_{\text{atm}}(z_{\text{obs}}) = \frac{1}{A}\int g\mathrm{d}m = g\int_{z_{\text{obs}}}^{\infty}\rho_{\text{atm}}(z)\mathrm{d}z, \tag{1.2}$$

where $g = 9.8\ \mathrm{m\,s^{-2}}$ is the gravitational acceleration and is considered constant. One can notice from Equations 1.1 and 1.2 that the vertical atmospheric depth is simply proportional to the pressure.

Consequently, the atmospheric pressure drops by an amount $\mathrm{d}P_{\text{atm}}$ when the observation level is increased by a quantity $\mathrm{d}z_{\text{obs}}$ such that:

$$\mathrm{d}P_{\text{atm}} = -g\,\rho_{\text{atm}}\,\mathrm{d}z_{\text{obs}}. \tag{1.3}$$

Additionally, assuming that the air behaves as an ideal gas in hydrostatic equilibrium, one can write that $P_{\text{atm}} = \rho_{\text{atm}} r\,T$ where r is a constant that depends on the nature of the gas and is equal to $287\ \mathrm{J\,kg^{-1}\,K^{-1}}$ for the air, and T is the air temperature, assumed to be independent of the altitude. This state equation allows us to write:

$$\frac{\mathrm{d}P_{\text{atm}}}{P_{\text{atm}}} = \frac{-g}{r\,T}\mathrm{d}z_{\text{obs}}. \tag{1.4}$$

The solution of Equation 1.4 can be written as:

$$P_{\text{atm}}(z_{\text{obs}}) = P_0\exp\left(\frac{-g}{r\,T_0}z_{\text{obs}}\right), \tag{1.5}$$

where $P_0 = 1.01\times10^5$ Pa and $T_0 = 15°\mathrm{C}$ are the pressure and the temperature at ground level, respectively. Plugging Equation 1.5 into Equation 1.2 and integrating results in:

$$X(z_{\text{obs}}) = \int_{z_{\text{obs}}}^{\infty}\rho_{\text{atm}}(z)\mathrm{d}z = X_0\exp\left(\frac{-g}{r\,T_0}z_{\text{obs}}\right), \tag{1.6}$$

where $X_0 = P_0/g = 1033.9\ \mathrm{g\,cm^{-2}}$ is the atmospheric vertical depth at ground level. By definition, $X = 0\ \mathrm{g\,cm^{-2}}$ at the top of the atmosphere.

The definition of the atmospheric depth given by Equation 1.6 holds true for secondary particles coming in the vertical direction. However, when considering UHECR primaries entering the atmosphere at high zenith angle, these secondary particles must travel through a larger layer of atmosphere and it becomes more convenient to express the vertical depth along the path

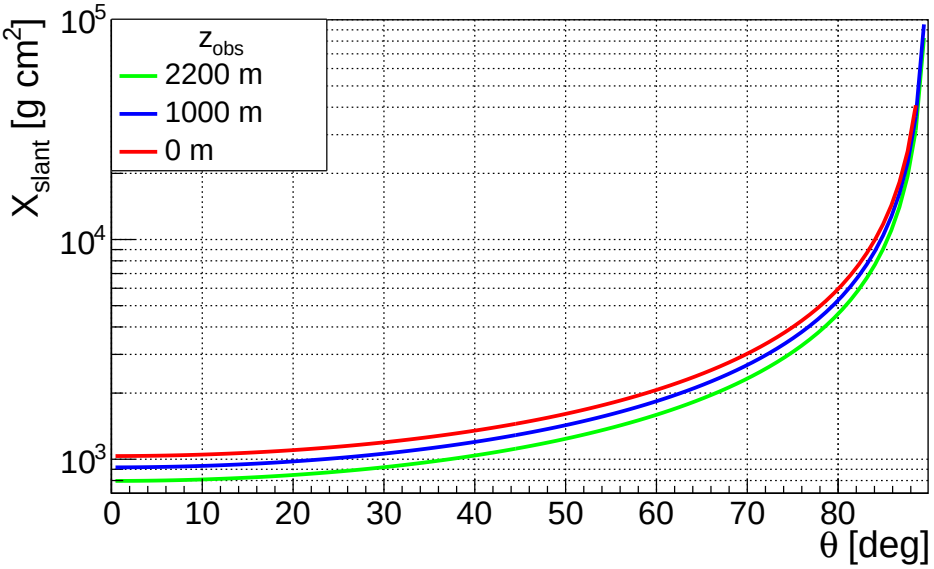

Figure 1.3: Slant depth as a function of the zenith angle of the incoming UHECR primary obtained using Equation 1.7. The observation levels are taken at sea level (red), 1000 m (blue) and 2200 m (green), which are equivalent to vertical ($\theta = 0°$) atmospheric depths of 1033.9 g cm^{-2}, 918.4 g cm^{-2} and 796.6 g cm^{-2}, respectively.

of propagation of particles, i.e. along the EAS core axis. Such quantity is referred to as *slant depth* and can be expressed as a funtion of the zenith angle θ:

$$X_{\mathrm{s}}(z_{\mathrm{obs}}, \theta) = \frac{X(z_{\mathrm{obs}})}{\cos(\theta)}. \tag{1.7}$$

Figure 1.3 shows the evolution of X_{s} as a function of the zenith angle of the incoming UHECR primary and for different observation levels, using Equation 1.7. However, this equation holds true for zenith angles up to $\sim 60°$ for which the flat atmosphere approximation remains valid. For larger zenith angles, the curvature of the Earth must be taken into account, as atmospheric depths are overestimated in a planar geometry. The corrected slant depth $X_{\mathrm{s,curv.}}$ can be expressed analytically after introducing the *Chapman function*[1] [4], such that:

$$Ch(z_{\mathrm{obs}}, \theta) = \frac{X_{\mathrm{s,curv.}}(\theta, z_{\mathrm{obs}})}{X(z_{\mathrm{obs}})} \tag{1.8}$$

$$= x \sin(\theta) \int_0^{\theta} \frac{\exp(x - x \sin(\theta)/\sin(\phi))}{\sin^2(\phi)} \mathrm{d}\phi, \tag{1.9}$$

[1]For low zenith angles, Equation 1.9 approximates to $1/\cos(\theta)$ and for $\theta = 0°$, $X_{\mathrm{s,curv.}}(\theta, z_{\mathrm{obs}}) = X(z_{\mathrm{obs}})$.

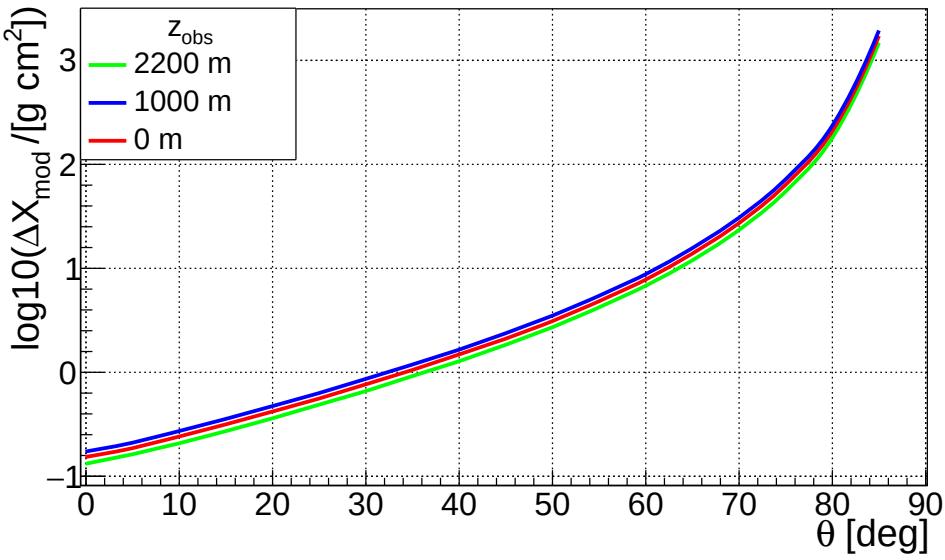

Figure 1.4: Difference in atmospheric depth between the flat atmosphere approximation and the curved atmosphere model as a function of the zenith angle and of the observation altitude. **Note**: The fact that 0 is not exactly reached for $\theta = 0°$ is due to the use of the approximation of the Chapman function written in Equation 1.10 to plot this figure. At low-zenith angle, the Chapman function approximates to $1/\cos(\theta)$ and ΔX_{mod} is therefore equal to 0 at $\theta = 0°$.

where $X(z_{\text{obs}})$ is the vertical depth at observation level z_{obs} calculated using Equation 1.6 and $x = (R_E + z_{\text{obs}})/z_0$ with $R_E = 6371$ km, the radius of the Earth and z_0, the local scale height such that $z_0 \equiv k_B T_0/Mg$, where k_B is the Boltzmann constant and M is the mean molecular mass. This function corresponds to the ratio of the slant depth – taking into account the curvature of the Earth – of an incoming particle with a zenith angle θ over the vertical depth ($\theta = 0°$), both observed at a z_{obs} altitude. Although several approximations have been developed to describe Equation 1.9 [5], the one worked out by Swider is particularly accurate in the range $\theta = [0°; 85°]$ [6] and can be written as[2]:

$$Ch(z_{\text{obs}}, \theta) = -x\cos(\theta)\sqrt{1 + 2\,x - W}\left[\sqrt{W} + \frac{1}{2\sqrt{W}}\left(1 - \frac{1}{2\,W} + \frac{3}{4\,W^2} - \frac{15}{8\,W^3}\right)\right], \tag{1.10}$$

where $W = x(1 - \sin(\theta))$. In order to characterize the variations obtained when taking into account the curvature of the Earth, the difference $\Delta X_{\text{mod}} = X_{\text{s}} - X_{\text{s,curv.}}$ as a function of the zenith angle is plotted (see Figure 1.4), for the same observation levels as in Figure 1.3. Although the changes are not

[2]For $\theta = 0°$, Equation 1.10 is a few thousandths below 1 for any value of x, which explains the small divergence from 0 seen in Figure 1.4 at $\theta = 0°$.

substancial for zenith angles below 75°, one should notice that above this value, the atmospheric depths are significantly affected by the change of geometry, losing up to more than 1000 $\mathrm{g\,cm^{-2}}$.

Although numerical integrations with layer-dependent atmospheric models are beyond the scope of this work, the values obtained for $X_{\mathrm{s,curv.}}$ are in good agreement with the results from the work found in [7], in which numerical integration is performed for 5 layers of atmosphere along the path length of the particle trajectory and which is used in the simulation package of EAS's used in this dissertation.

The longitudinal profile of EAS's is often characterized by the evolution of the energy deposited in the atmosphere and of the particle content as a function of the slant depth (see Figure 1.2). The atmospheric depth at which an EAS reaches its point of maximum development is written X_{max}. Unless specified otherwise, the slant depth values shown in further sections all refer to the slant depth which takes into account the curvature of the Earth and will be simply noted X for more clarity.

1.1.2 Electromagnetic Showers

Electromagnetic cascades can either be produced by gamma-ray primaries or through the decay of neutral pions in EAS's produced by hadrons. The continuous feed of photons through the latter channel leads to different characteristics in both modes of production. However, the interactions at stake remain the same and are described below. Before giving a concise description of what these interactions are and of the analytical approach that allows to describe how electromagnetic showers form, the toy model developed by Heitler in [8] is discussed. Despite restrictive approximations, this model is capable of predicting some of the features of electromagnetic showers with high accuracy.

A. Heitler's Model

Monte-Carlo simulations derived from the analytical study of electromagnetic showers can constitute a great tool to obtain a detailed description of the evolution of particle cascades. However, a simpler approach through toy models, as the one introduced by Walter Heitler in [8], is also capable of providing an accurate prediction of some of the quantities that characterize electromagnetic showers without the need for high-performance computing. In his model, Heitler first establishes some simple approximations:

- The energy E_0 of the primary photon is assumed to be significantly greater than the critical energy E_c^{em} for which collisional energy losses of electrons become predominant.

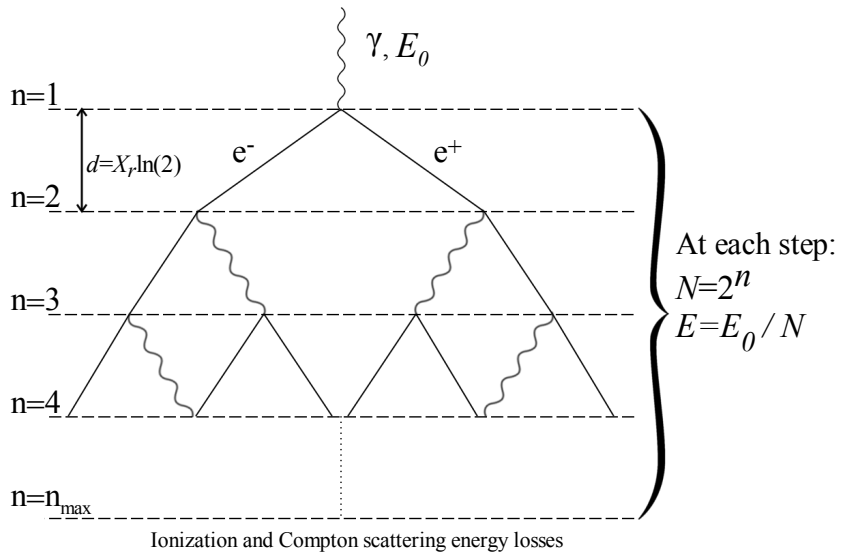

Figure 1.5: Heitler's toy model: a primary photon with energy E_0 produces a pair of electron and positron. After traveling a splitting length d, which depends on the the radiation length X_r, each member of the pair radiates one bremsstrahlung photon and a new generation of electromagnetic particles goes through the same process. At each stage, the *daughter* particles equally share the energy of the *parent* particle and after n splitting lengths, the total amount of particles in the cascade equals to 2^n. The multiplication stops after n_{max} splitting lengths, as collisional losses outweigh the radiative ones below a critical energy $E_c^{\rm em} = E_0/2^{n_{max}}$.

- ➢ Collisional energy losses and Compton scattering are ignored for particles with energy greater than $E_c^{\rm em}$ and annihilation of positrons with free electrons is disregarded.
- ➢ After traveling one radiation length d, electrons and positrons each produce only one bremsstrahlung photon. The cross section for bremsstrahlung emission is assumed to be independent of the electrons and positrons energy.
- ➢ The energy of the *parent* particle (photon, electron or positron) is assumed to be equally divided between the two outgoing particles.

With these assumptions in mind, Heitler's model can be described as such: a primary photon with energy E_0 produces a pair of electron and positron, each with energy $E_0/2$. After traveling a *splitting* length $d = X_r\ln(2)$, where $X_r = 37.1\ \mathrm{g\,cm^{-2}}$ is the average radiation length in the air, both electron and positron radiates one bremsstrahlung photon, each carrying half of the energy of the incoming particle. This new generation of electrons, positrons and photons undergoes the same interaction processes until the electrons and

positrons reach a critical energy $E_c^{\rm em}$ below which radiative energy losses are overpowered by ionization and Compton scattering energy losses. In the air, this critical energy is approximately equal to 85 MeV. A schematic view of Heitler's model is shown in Figure 1.5. The number of particles N in the shower after n splitting length, such that the penetration depth is $X = nX_r\ln(2)$, is equal to 2^n and each particle in the shower carries an energy $E = E_0/N$. Consequently, the critical energy is reached for $n = n_{\rm max}$ where the energy per particle is therefore $E_c^{\rm em}$ and the maximum number of particles $N_{\rm max}^H$ is:

$$N_{\rm max}^H = \frac{E_0}{E_c^{\rm em}} = 2^{n_{\rm max}}. \tag{1.11}$$

From Equation 1.11, the expression of $n_{\rm max}$ can be derived, such that:

$$n_{\rm max} = \frac{\ln(E_0/E_c^{\rm em})}{\ln(2)}. \tag{1.12}$$

As discussed in Section 1.1.1, the depth at which a shower reaches its maximum is characterized by the quantity $X_{\rm max}$. Using the expression of the penetration depth X given above, $X_{\rm max}$ can be written:

$$X_{\rm max} = n_{\rm max}X_r\ln(2) = X_r\ln(E_0/E_c^{\rm em}). \tag{1.13}$$

As seen from Equation 1.13, primaries with higher energy initiate showers that reach their maximum development deeper in the atmosphere, i.e. have larger expected $X_{\rm max}$. In order to characterize how $X_{\rm max}$ varies with the energy E_0 of the primary, the so-called *elongation rate* D^γ is introduced. It represents the change in $X_{\rm max}$ per decade of primary energy:

$$D^\gamma = \frac{{\rm d}X_{\rm max}}{{\rm dlog}_{10}(E_0)} = 2.3X_r. \tag{1.14}$$

In the air, the elongation rate is approximatel equal to 85 $\mathrm{g\,cm^{-2}}$ per energy decade. Despite the strong assumptions made by Heitler, some essential features of air showers are accurately described:

- The maximum number of particles is proportional to the primary energy E_0.
- The depth at which this maximum is reached is proportional to the logarithm of the the primary energy $\ln(E_0)$.

A full understanding of Heitler's model requires to highlight some its limitations. First of all, because collisional losses are ignored and particles are assumed to remain within the shower, the maximum number of particles is

overestimated. Secondly, for the same reasons and under the hypothesis that each electron and positron only radiates one bremsstrahlung photon, the ratio of the number of electrons and positrons over the number of photons is also overestimated. According to Heitler's model, the total number of electrons and positrons $N^H_{e,\max}$ is approximately equal to $(2/3)N^H_{\max}$. In fact, many photons are radiated per splitting length and electromagnetic showers actually contain far more photons than electrons when $X_{\max}$ is reached.

B. Electromagnetic Interactions and Transport Equations

In order to understand how EAS's are formed and how their content and longitudinal profiles may vary with the nature and the energy of the primaries that initiate them, the different types of particle interactions occurring in the atmosphere must be described. In this section, the various physical processes that are responsible for electromagnetic showers at the highest energies, are reviewed. The so-called *transport equations* (or *cascade equations*), as studied in [9], that describe the evolution of the particle content as a function of the slant depth, are discussed, taking into account the particle interactions at stake.

At high energy, whether initiated by a gamma ray primary or fed by the neutral pion decay channel of hadronic interactions, the development of electromagnetic showers is lead by the production of e^-/e^+ pair and the emission of bremsstrahlung photons in the vicinity of atomic nuclei. Below a certain critical energy, ionization losses of electrons and Compton scattering of photons are responsible for the slow-down of the EAS development and the shower eventually dies out.

Pair production

Photons propagating in the atmosphere may interact with nuclei of nitrogen and oxygen, and produce pairs of electrons and positrons. The presence of nuclei insures the conservation of momentum as the photon's momentum must be absorbed, causing a recoil of the nuclei. Although the threshold energy $E^{\rm pp}_{\rm th}$ for such process to occur is defined by the fact that the photon must have an energy that is at least twice as large as the electron's rest mass $m_e c^2$, it also depends directly on the mass m_A of the target nuclei with mass number A:

$$E^{\rm pp}_{\rm th} = 2m_e c^2 \left(1 + \frac{m_e}{m_A}\right). \tag{1.15}$$

From Equation 1.15, one can observe that the heavier the target nucleus, the smaller the threshold energy. For nitrogen with a rest mass of ~ 13 GeV,

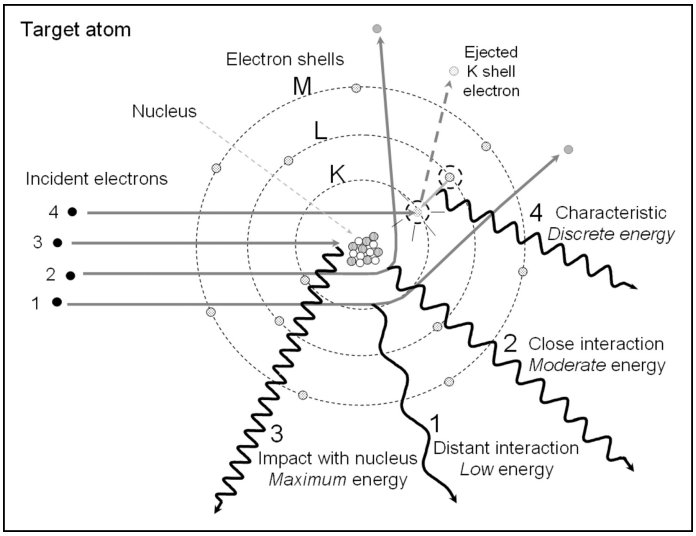

Figure 1.6: Photon production of incident electrons as they interact with the electromagnetic field of the nuclei and emit bremsstrahlung photons (1,2,3) or kick an electron from one of the atomic shells before an electron located on a higher level fills the vacancy and emits a photon (4). Figure taken from [11].

$E_{\rm th}^{\rm pp} \simeq 1.06$ GeV is obtained. The cross section for pair production is a function of the atomic number Z of the element composing the medium [10]:

$$\sigma_{\rm pp}(Z) = 4Z^2\alpha_s r_e^2 \left[\frac{\ln(191\, Z^{-1/3})}{9} - \frac{1}{54}\right], \tag{1.16}$$

where Z is the atomic number of the medium; $\alpha_s \simeq 1/137$ is the fine structure constant; and r_e is the electron classical radius. The $1/54$ factor accounts for the possible pair production in the field of the atomic electrons. As one can notice, this expression does not show any dependence on the energy of the photon that initiated the pair production. Moreover, target nuclei with higher atomic number have larger cross sections for pair production and therefore, pair production is more likely to occur. For nitrogen ($Z = 7$), this leads to a cross section of approximately $\sim 5.61 \times 10^{-30}$ m$^2 \simeq 56$ mb.
The energy of the photon undergoing pair production is equally splitted between the electron and the positron. Photons of higher energy produce pairs that are more collimated. However, while the positron is likely to annihilate when encountering another free electron, the electron produced via pair production may carry on and lose energy via bremsstrahlung radiation.

Bremsstrahlung radiation

Electrons traveling in the vicinity of atomic nuclei may interact with the

nuclei electromagnetic field and get deflected and decelerated by the existing Coulomb force. As momentum is lost, the incident electrons emit so-called *bremsstrahlung* photons. The energy of these photons depends on the nature of the material the electrons are passing through and on the distance between the electrons and the target nuclei, as shown by tracks 1 and 2 in Figure 1.6. Two important properties can be highlighted: electrons interacting with the electromagnetic field at smaller distances emit photons of higher energy (larger electron deflections) and the fraction of the energy of the incident electrons emitted in the form of bremsstrahlung photons increases with the energy of the electons and the atomic number of the target nuclei. These features are well illustrated by the energy loss per unit of column depth dX function derived in [10]:

$$\left(\frac{dE_e}{dX}\right)_{\text{brem}} = -\frac{N}{A}\int_0^{E_e - m_e c^2} \sigma_{\text{br}}(E_e, E_\gamma) E_\gamma dE_\gamma, \tag{1.17}$$

where E_e and E_γ are the energy of the incident electrons and of the emitted photons, respectively; N is the number density of the target material; and m_e and c are the mass of the electron and the speed of light, respectively. The bremsstrahlung cross-section σ_{br}, as introduced by Bethe and Heitler [12], can be written as:

$$\sigma_{\text{br}}(E_e, E_\gamma) = \frac{4Z^2 \alpha r_e^2}{E_\gamma} F(E_e, E_\gamma). \tag{1.18}$$

The function $F(E_e, E_\gamma)$ characterizes the screening of the nuclear electromagnetic field by the atomic electrons. In the high energy range, Equation 1.17 takes the following form:

$$\left(\frac{dE_e}{dX}\right)_{\text{brem}} = \frac{4NZ}{A} \alpha r_e^2 E_e \left[\ln\left(\frac{191}{Z^{1/3}}\right) + \frac{1}{18}\right], \tag{1.19}$$

where the $1/18$ factor accounts for the possible interactions with the electromagnetic field of the atomic electrons.

In relation to the previous section about atmospheric depth, the radiation length in $\mathrm{g\,cm^{-2}}$ can be introduced to define the bremsstralhung energy loss as a function of the average amount of atmosphere an electron has traveled through to emit a photon [12]:

$$\left(\frac{dE_e}{dX}\right)_{\text{brem}} \simeq -\frac{E_e}{X_r}. \tag{1.20}$$

For an atmosphere composed of 75% nitrogen and 25% oxygen, the average radiation length X_r is around $37.1\ \mathrm{g\,cm^{-2}}$. For a vertical EAS observed at the sea level ($X_0 \simeq 1033.9\ \mathrm{g\,cm^{-2}}$), its atmospheric depth corresponds to around

28 radiation lengths. However, below the critical energy E_c^{em} (this energy decreases with the atomic number Z of the medium), ionization losses become more dominant and bremsstrahlung emission ceases.

Ionization

For energies below E_c^{em}, electrons mostly lose their energy through the ionization of atoms, which leads to the slow decline of the EAS development. For electrons with energies $> m_e c^2$, the energy loss due to ionization per column depth can be expressed as [12]:

$$\left(\frac{dE_e}{dX}\right)_{\mathrm{ion}} = -2\pi r_e m_e c^2 Z N \ln\left(\frac{E_e^3}{2m_e c^2 I}\right), \tag{1.21}$$

where I is the ionization potential of the medium and is proportional to the atomic number Z of the medium. As expected, energy losses due to ionization are more substancial for denser media composed of heavier nuclei. The critical energy E_c^{em} for which ionization becomes dominant can be obtained when Equations 1.19 and 1.21 are equal:

$$\left(\frac{dE_e}{dX}\right)_{\mathrm{ion}} = \left(\frac{dE_e}{dX}\right)_{\mathrm{brem}}. \tag{1.22}$$

For the atmosphere, E_c^{em} is approximately equal to 85 MeV. The electrons that are stripped away from their nuclei are of small energy and ionization is therefore considered as a process of dissipation rather than of multiplication.

Compton scattering

Another low energy interaction lies in the scattering of photons on an atomic electron, resulting in a transfer of energy to the latter and of the emission of a photon of lesser energy. Such interaction is referred to as Compton scattering. For photons with energies $\ll m_e c^2$, the Compton scattering cross section is approximately equal to the Thomson cross section $\sigma_{\mathrm{Th}} = 665$ mb. For higher energies, the cross section can be written as:

$$\sigma_C(E_\gamma) = \sigma_{\mathrm{Th}} \frac{3m_e c^2}{8E_\gamma}\left[\ln\left(\frac{2\mathrm{E}_\gamma}{\mathrm{m_e c^2}}\right) + \frac{1}{2}\right], \tag{1.23}$$

where E_γ is the energy of the incident photon. The opposite process through which an electron loses energy when interacting with a photon is called inverse Compton scattering and is responsible for the production of very high energy gamma rays in the Universe when electrons scatter with the CMB.

Transport equations

Although Heitler's model provides a clear and simple tool to investigate some of the features of electromagntic showers, a more detailed picture can be obtained via the cascade equations that govern the development of such showers and that take into account particle decay and interactions. Such endeavor was undertaken and presented by Rossi & Greisen [9], developing elegant solutions of these equations for electromagnetic showers under different approximations. The so-called *Approximation A* describes the development of these showers for energies above the critical energy E_c^{em}, defined in the discussion about Heitler's toy model, ignoring collision energy losses and Compton scattering. However, in this dissertation, a particular attention is given to EAS's with high zenith angles, meaning that their electromagnetic component travels through a thickness of atmosphere that is large enough for collisional energy losses to eventually dominate. Such component is therefore most likely absorbed before reaching the ground. For that reason, a short review of *Approximation B*, for which ionization of the medium is taken into account and id considered to be constant with respect to energy (Compton scattering is still neglected), is given. In fact, the transport equations between both approximations only differ in an additional term accounting for ionization losses in the equation of the evolution of the electron content. Following Rossi & Greisen notation, the equation that governs the change in content of electrons with energy between E and $E + dE$ as a function of the atmospheric depth X can be expressed such that:

$$\frac{\partial_{\pi(E,X)}}{\partial X} = \underbrace{2\int_0^1 \gamma\left(\frac{E}{u}, X\right)\psi_0(u)\frac{du}{u}}_{T_1} - \underbrace{\int_0^1 \left[\pi(E,X) - \frac{1}{1-v}\pi\left(\frac{E}{1-v}\right)\right]\phi_0(v)dv}_{T_2} + \underbrace{\epsilon\frac{d\pi(E,X)}{dE}}_{T_3}, \tag{1.24}$$

where $\pi(E, X)$ is the differential electron spectrum as a function of the electron energy E and the atmospheric depth X. The different terms in Equation 1.24 describe the interaction processes affecting electrons that were previously discussed:

- T_1 - **Pair production**: taking $u = E/W$, photons with energy W greater than E produce electrons and positrons in the energy range (E,dE). $\gamma(W, X)$ is the differential photon spectrum and $\psi_0(u)$ is the differential probability for pair production per radiation length. The latter is taken in the case of complete screening, i.e. the electric field of atomic electrons completely screens the one of the nuclei (valid for large impact distances and high energies).

- T_2 - **Bremsstrahlung radiation**: this type of interaction leaves electrons "alive" with lower energies. Therefore, electrons of energy E' both leave (1^{st} term in the brackets) and enter (2^{nd} term in the brackets) the interval (E,dE) by radiating a photon of energy $W = vE'$. $\phi_0(v)$ is the differential probability of bremsstrahlung radiation per radiation length and is also taken for complete screening.

- T_3 - **Ionization**: electrons traveling through an atmospheric thickness dX lose an amount of energy ϵ due to collisions with atomic electrons.

Equation 1.24 is coupled to the transport equation of photons which describe the evolution of the content of photons with energy between W and $W + dW$ as a function of the atmospheric depth X:

$$\frac{\partial\gamma(W,X)}{\partial X} = \underbrace{\int_0^1 \pi\left(\frac{W}{v},X\right)\phi_0(v)\frac{dv}{v}}_{T_1'} - \underbrace{\sigma_0\gamma(W,X)}_{T_2'}, \tag{1.25}$$

where the quantities appearing are the same as the one described in the case of electrons. The terms in Equation 1.25 refer to different processes affecting the photon content:

- T_1' - **Bremsstrahlung radiation**: taking $v = W/E$, electrons of energy E greater than W emit photons in the energy range (W,dW).

- T_2' - **Pair production**: photons with energy in the interval (w,dW) produce pairs of electrons and positrons. σ_0 is the total probability for pair production and is a function of the atomic number Z of the medium.

C. Properties of Electromagnetic Showers

Although solving Equations 1.24 and 1.25 is well beyond the scope of this dissertation, I present the solutions obtained by Greisen [13] in the case of showers initiated by photons of energy W_0, and discuss some of the shower features that are derived, such as the longitudinal profile, the lateral spread and the shower-to-shower fluctuations. The results are also compared to Monte-Carlo simulations in order to assess the accuracy of these solutions.

The number of electrons contained in a shower initiated by a photon of energy W_0 as a function of the scaled atmospheric depth t can be written:

$$N_e^G(W_0,t) = \frac{0.31}{\sqrt{\beta_0}}\exp\left[t\left(1-\frac{3}{2}\ln(s)\right)\right], \tag{1.26}$$

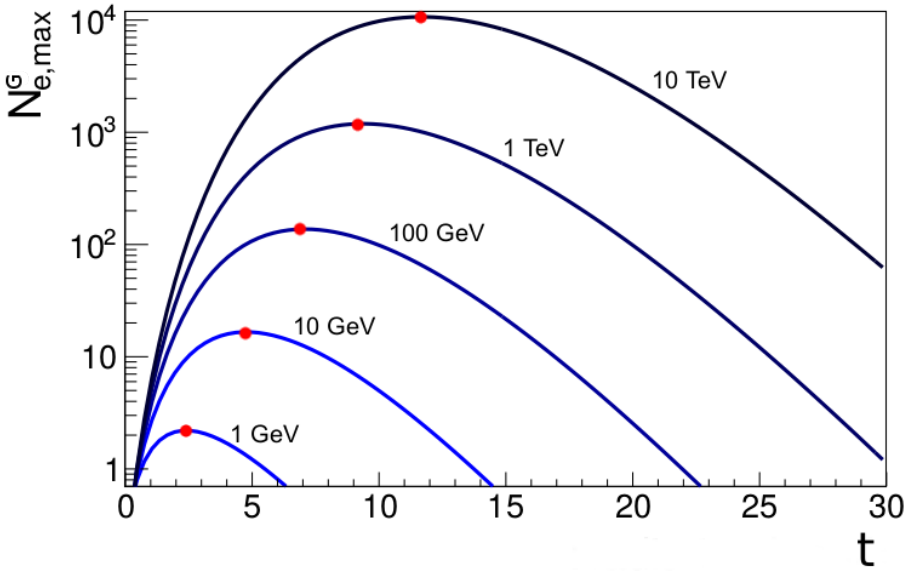

Figure 1.7: Longitudinal profiles: number of electrons as a function of the number the reduced length for several photon primary energies. The $t_{\max}$ at which the showers reach their maximum is shown by the red dots. These profiles are obtained for $E_c^{\text{em}} = 85$ MeV (in the air) using Equation 1.28.

where $\beta_0 = \ln(W_0/E_c^{\text{em}})$; $t = X/X_r$ is the number of radiation lengths (reduced length); and s is the *shower age* that characterizes the stage of development of the shower such that:

$$s = \frac{3t}{t + 2\beta_0}. \tag{1.27}$$

The shower starts at $s = 0$, then the number of particles increases with atmospheric depth until it reaches its maximum at $s = 1$ before starting to decrease for $s > 1$.

Longitudinal profile

The longitudinal profile of electrons contained in electromagnetic showers can be obtained by plotting Equation 1.27 as a function of the number of radiation lengths. In Figure 1.7, profiles of showers initiated in the air by primary photons of different energies are shown. By setting $s = 1$ in Equation 1.26, the maximum number of electrons is obtained:

$$N^G_{e,\max}(W_0) = \frac{0.31}{\sqrt{\beta_0}} \frac{W_0}{E_c^{\text{em}}}. \tag{1.28}$$

Values of $N^G_{e,\max}$ are plotted on Figure 1.7 with red dots for each one of the longitudinal profiles. The estimated depth at which these showers reach their maximum as well as the maximum number of electrons according to Greisen's analytical solution and Heitler's toy model are given in Table 1.1.

Comparing Heitler's estimation of the maximum number of electrons to Greisen's, one can notice a significant discrepancy between the given numbers. While Heitler's value is obtained by assuming that 2/3 of the maximum number of particles are electrons, Greisen finds a value almost 7 orders of magnitude lower, mostly due to the fact that ionization is taken into account in Greisen's Approximation B. Connecting the maximum number of particles $N^H_{\max}$ given by Heitler's model to the maximum number of electrons found by Greisen $N^G_{e,\max}$, a factor $g = 10$ can be introduced such that $N^G_{e,\max} \simeq N^H_{\max}/g$ [14].

Monte-Carlo simulations were performed by Stanev [10] in order to assess the accuracy of Rossi & Greisen analytical solutions in [9] and Greisen's approximated solution given by Equation 1.26. The Monte-Carlo algorithm is described in [15] and allows to include some physical features that are not taken into account in the analytical approach, such as Compton scattering or the energy dependence of the cross section for the particle interactions. Figure 1.8 shows the number of electrons and photons for a photon primary with energy $W_0 = 1$ TeV and a threshold energy set at 10 MeV. The number of electrons in the analytical approach is higher than the one obtained through Monte-Carlo simulations. Such difference can be explained by the fact that the former describes the total number of electrons while the latter does not take into account electrons below the energy threshold. On the other hand, simulations allow to give a more detailed description of bremsstrahlung radiation and consequently, the number of photons is significantly higher once the shower maximum is reached. The agreement between Rossi & Greisen's solution and Equation 1.26 is excellent through the entire shower development.

W_0 (GeV)	$X^\gamma_{\max}$ (g cm^{-2})	$N^G_{e,\max}$	$N^H_{e,\max}$
1	89	2	8
10	176	17	78
100	262	137	784
1000	347	1191	7842
10000	432	10673	78423

Table 1.1: Summary of quantities used to describe longitudinal profiles of electromagnetic showers for different primary photon energies. The maximum number of electrons is obtained from Equation 1.27 in the third column and from Heitler's estimation ($N^H_{e,\max} = (2/3)N^H_{\max}$ with $N^H_{\max}$ taken from Equation 1.11) in the fourth one. Taken from [10]

.

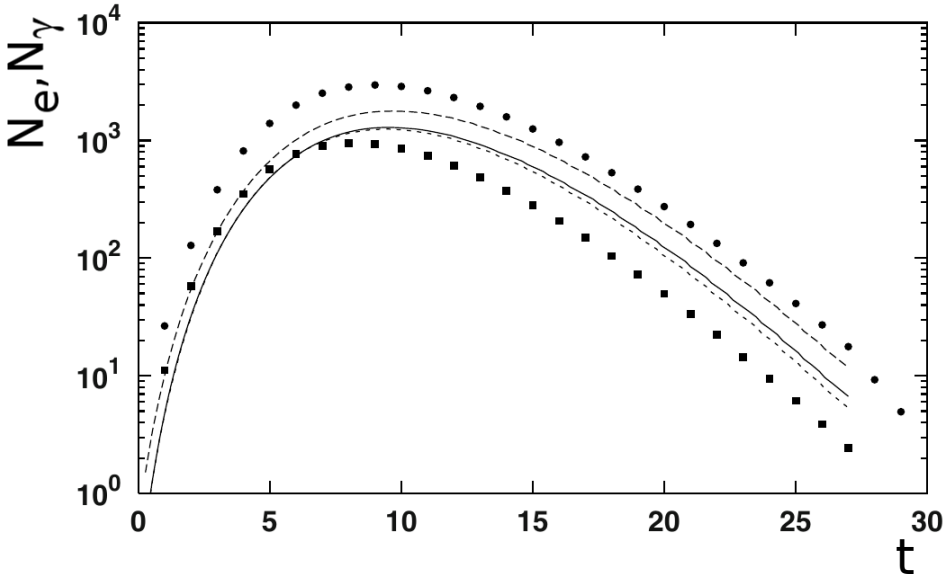

Figure 1.8: Longitudinal profiles of electron and photon contents, for a shower generated by a 1 TeV photon. The solid line and the long-dashed line represent the number of electrons and photons in the case of Rossi & Greisen's Approximation B solution, respectively. The short-dashed line is the number of electron given by Equation 1.26. The dots and the square are the number of photons and electrons givent by Monte-Carlo simulations, respectively. Taken from [10].

Shower-to-shower fluctuations

One significant disadvantage of the analytical approach is that it describes the average behavior of showers and does not account for the fluctuations that may affect their development. Indeed, for a given primary energy, the depth at which showers reach their maximum as well as the number of particles at a given depth may vary significantly shower-to-shower. These fluctuations may find their origins in the altitude at which the first interaction (pair production in the case of a primary photon) occurs and depend on the overall characteristics of the interactions at stake. The number of particles at a given depth vary such as [13]:

$$\langle \delta \ln(N) \rangle = 0.7[s - 1 - 3\ln(s)]. \tag{1.29}$$

Fluctuations of the number of particles are at their lowest around the maximum of the shower, as shown by Equation 1.29 for $s = 1$ and by Monte-Carlo simulations performed by Stanev [10]. In first approximation, one can assume that $X_{\max}$ is a function of the altitude of first interaction: a primary photon splitting into a pair of electron and positron deeper in the atmosphere pro-

duces a shower that will reach its maximum closer to the surface.

Lateral distribution

Secondary particles produced by bremsstrahlung and pair production are emitted with a scattering angle that depends on the nature of the interaction and of the particles at stake, and on the energy. Moreover, multiple Coulomb scattering are also responsible for the spread of electrons in the shower. Consequently, investigating the lateral spread of the shower as a function of the depth can reveal informations about the nature of the primary and its energy. The shower front can be approximated by the shape of a disk with the density of particle being higher at the center (shower core). Currently, most descriptions of the evolution of the density of particles as a function of the distance to the shower core, as found in [16] and [17], are based on the Nishimura-Kamata-Greisen (NKG) function [18, 19]:

$$\rho_e(R, X) = C\frac{N_e(X)}{R_0^2}\left(\frac{R}{R_0}\right)^{s-1}\left(1+\frac{R}{R_0}\right)^{s-4.5}, \tag{1.30}$$

where $\rho_e(R, X)$ is the electron density at a given depth X and distance to the shower core R; C is a normalization constant; and R_0 is the Molière radius which characterizes the lateral spread of low-energy electrons and is equal to 78 m in the air, at sea level, and increases with altitude. As Coulomb scattering is the main source of lateral spread, low-energy electrons, which are subject to larger deflection angles, are found in larger abundance further away from the shower core, where electrons of higher energy remain concentrated. Moreover, electromagnetic showers initiated at shallower depth tend to have wider lateral distributions.

As shown by simulations performed by Stanev [10], Equation 1.30 tends to overestimate the maximum lateral spread of electrons. Furthermore, because the radiation length for pair production is larger than the one for ionization, electrons suffer greater deflections than photons and the number of photons at larger distances from the core is greater than the number of electrons. Such characteristic leads to a flatter distribution of photons while the electron lateral spread has a sharper peak closer to the shower core.

D. Muon content in Electromagnetic Cascades

The muon content of EAS's constitutes an important quantity that can help assessing the type of primary that initiated it and its primary energy. While more extensive details regarding this remark are given in Section 1.1.4, here, the possibility for EAS's produced by photon primaries to develop a

muonic component is discussed. So far, such feature has been ignored by Greisen and Heitler's model on the basis that pair production is the dominant interaction process for particle multiplication. Nevertheless, electromagnetic showers may also develop a muonic counterpart through the interaction of photons with atomic nucleons resulting in the production of charged pions[3]. Such physical process, referred to as *photopion production*, consists of the two following channels:

$$\gamma + p \rightarrow n + \pi^+$$
$$\gamma + n \rightarrow p + \pi^-$$

The subsequent decay of charged pions leads to the production of muons, which mean free path is significantly larger than electrons and photons, and to the creation of a hadronic component that can be quite substancial if the first pions are produced soon after the first interaction of the primary with the medium. Because the cross section for photopion production is relatively low, electromagnetic showers are poor in muons. For that reason, and as I will discuss in the next sections, the muon content can be used to discriminate EAS's produced by photons from EAS's produced by hadrons.

1.1.3 Hadronic Showers

Hadronic showers are initiated when a proton or a heavy nucleus interacts with nuclei of a target medium and a cascade of secondary particle is generated. After the first primary interaction, charged and neutral pions are produced through the decay of kaons, with a ratio of charged to neutral pions of 2 to 1. Neutral pions, having a mean lifetime of $\sim 8.4\times10^{-17}$ s, decay immediately into two photons (with a branching ratio of 0.98), which initiate the electromagnetic counterpart. On the other hand, charged pions mean lifetime is longer by 10 orders of magnitude compared to neutral pions (decay via the weak rather than the electromagnetic force) and they are more likely to re-interact with the target nuclei and generate the second generation of charged and neutral mesons. As their energy decreases, their decay length becomes shorter than the interaction length and further multiplication is limited by the decay to muons and neutrinos (with a branching ratio of 0.99). While hadrons travel deeper due to their interaction length being larger than the typical radiation length of the electromagnetic component, they also lose energy at a faster rate due to the large multiplicity at each interaction point.

Analogously to the previous section, I discuss the toy model developed by Matthews [14] which provides an accurate estimation of these features.

[3]Neutral pions may also be produced, which decay to photons.

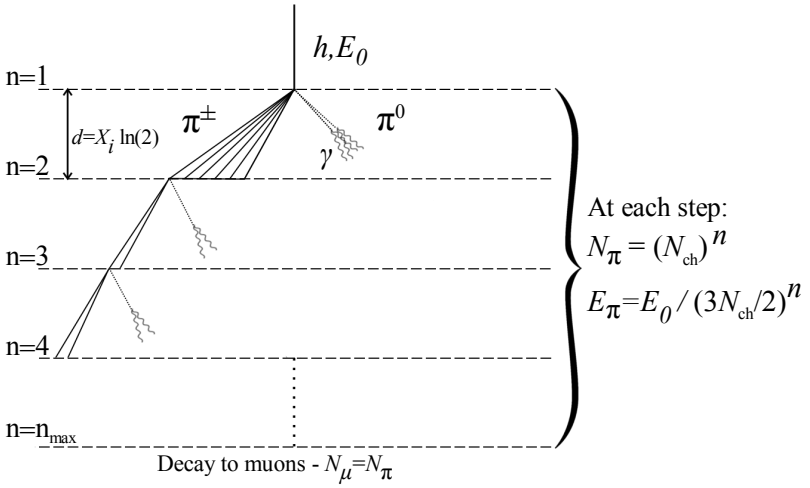

Figure 1.9: Heitler-Matthews' toy model: a primary hadron with energy E_0 produces N_π charged pions and $N_{\rm tot} - N_\pi$ neutral pions in a ratio of 2:1. While neutral pions rapidly decay to photons and initiate the electromagnetic counterpart, charged pions produce a new generation of pions after traveling a splitting length d that depends on the interaction length X_i. The multiplication stops after n_{max} splitting lengths, as charged pions are more likely to decay to muons.

Thereupon, I review the transport equations that describe the evolution of the flux of hadrons and mesons before examining hadronic shower properties. Finally, I give a short summary of some of the hadronic interaction models that have been developed at low and high energy, and that are used in Monte-Carlo simulations of EAS's.

A. Heitler-Matthew's Model

Following up on the toy model for electromagnetic showers developed by Heitler, Matthews worked out a similar approach by generalizing such model to showers initiated by hadrons and nuclei [14]: a primary hadron interacts with the medium and produces $N_{ch} = 10$ charged particles and $N_{ch}/2$ neutral pions. The neutral pions rapidly decay to photons while charged pions travel through a splitting length $d = X_i \ln(2)$, where X_i is the interaction length of charged pions ($X_i \simeq 120\ \mathrm{g\,cm^{-2}}$ in the air for pions), and interact again to produce a new generation of charged and neutral pions. At each step, one third of the energy of the new generation is transferred to the electromagnetic component through the neutral pion decay. Such process carries on until the energy per pion is smaller than the critical energy E_c^h (~ 20 GeV in the air) for which the decay length becomes smaller than X_i. This critical energy decreases with increasing primary energy. At this point, charged pions decay to muons such that the number of muons N_μ^p is equal to the total number of charged

pions at the last splitting length. The energy carried by each charged pion after passing through n layers can be written as:

$$E_\pi = \frac{E_0}{\left(\frac{2}{3}N_{\rm ch}\right)^n}, \tag{1.31}$$

while the total energy carried by the pions, in amount of $(N_{\rm ch})^n$, can be estimated to be around $(2/3)^n E_0$ and the remaining energy is carried by the electromagnetic component.

One interesting consequence of Matthews model is that the energy of the primary can be estimated by simply knowing the electron and muon content of the shower. This energy is a function of the critical energies $E_c^{\rm em}$ and E_c^h for electromagnetic and pion multiplication respectively, and of the number of electrons and muons at the shower maximum (assuming $N_\mu^p = N_\pi$). Condsidering the case of atmospheric showers and taking into account the reduction factor $g = 10$ previously used to obtain the real number of electrons, the primary energy can be expressed as:

$$E_0 \approx 0.85(N_e + 24N_\mu^p), \tag{1.32}$$

where the number of muons N_μ^p and electrons N_e grow as a function of the primary energy:

$$N_\mu^p \approx 10^4 \left(\frac{E_0}{1\,\text{PeV}}\right)^{0.85} \;;\; N_e \approx 10^6 \left(\frac{E_0}{1\,\text{PeV}}\right)^{1.03}. \tag{1.33}$$

When the inelasticity – the process by which the initial hadron does not completely vanish and carries a large fraction of the primary energy after the first interaction – is taken into account, the muon size increases at a faster rate since a smaller fraction of the energy is transferred to neutral pions. Moreover, the depth at which the hadronic shower reaches its maximum is directly estimated from the first generation of electromagnetic showers:

$$X_{\rm max}^p = \left[470 + 58\log_{10}\left(\frac{E_0}{1\,\text{PeV}}\right)\right]. \tag{1.34}$$

Because only the first generation of electromagnetic shower is taken into account, the values of $X_{\rm max}^p$ are underestimated by approximately 100 $\text{g}\,\text{cm}^{-2}$. On the other hand, the elongation rate is not affected by this approximation and is estimated around 58 $\text{g}\,\text{cm}^{-2}$ per decade of energy in the air, a value significantly lower than in the case of purely electromagnetic showers which can be explained by the larger multiplicity and the growing hadron-air interaction cross section.

In order to characterize hadronic showers produced by nuclei with atomic mass $A > 1$, the superposition model developed in [14] assumes that a shower initiated by a nucleus with energy E_0 is the sum of showers generated by independent nucleons with energy E_0/A. As in the case of single proton showers, the primary energy can be recovered by assessing the electron and muon content of the shower:

$$E_0 \approx 0.85(N_e + 25N_\mu^A). \tag{1.35}$$

where the muon content is obtained by calculating the muon content of a shower initiated by a proton of energy E_0/A (solving Equation 1.33) and can be written such as:

$$N_\mu^A = N_\mu^p A^{0.15}. \tag{1.36}$$

The dependence on the atomic mass A highlights the fact that heavier nuclei produce showers with larger muon content. One of the reason lies in the fact that lower energy nucleons transfer less energy into the electromagnetic component and more muons can be therefore produced. Such feature strenghtens the idea that muons constitute an effective discrimination factor to identify primaries. Analogously, the depth of maximum development $X_{\max}^A$ can also be expressed as a function of $X_{\max}^p$:

$$X_{\max}^A = X_{\max}^p - X_r \ln(A). \tag{1.37}$$

Since $\ln(A)$ is always greater or equal to 0, showers initiated by heavier nuclei reach their maximum at shallower depth than in the case of protons and similarly to the muon content, this aspect can also be used to discriminate showers.

B. Transport Equation of Hadronic Showers

In a similar approach to Greisen's derivation of the coupled transport equations for electromagnetic showers, Gaisser formulated a transport equation for hadronic showers taking into account the evolution of nucleons and mesons fluxes [20]. In this analytical model, ionization losses are ignored and the development of showers is governed by competing interactions and decays of particles. In a medium with mean mass A, a particle of type i traversing an atmospheric depth dX has a probability dX/X_i to interact and dX/d_i to decay, where X_i and d_i are the interaction and decay lengths, respectively:

$$X_i = \frac{A m_p}{\sigma_i^{\text{air}}} \; ; \; d_i = \rho \, \gamma \, c \, \tau_i, \tag{1.38}$$

where m_p is the proton mass; σ_i^{air} is the cross section depending on the type and energy of the particle, and on the nature of the medium of density ρ; γ is the Lorentz factor of the particle; and τ_i is its mean lifetime. Therefore, the number of particles of type i at depth X with energy E_i, $N_i(E_i, X)$, varies as a function of the depth such as:

$$\frac{dN_i(E_i,X)}{dX} = \underbrace{-\frac{N_i(E_i,X)}{X_i}}_{T_1} \underbrace{-\frac{N_i(E_i,X)}{d_i}}_{T_2} + \underbrace{\sum_{j=i}\left[\int_E^\infty \frac{F_{ji}(E_i,E_j)}{E_i}\frac{N_j(E_j,X)}{X_j}dE_j\right]}_{T_3}, \tag{1.39}$$

where the different terms are described as follows:

- ➢ T_1: absorption term accounting for particles of type i lost to interactions.
- ➢ T_2: absorption term accounting for particles of type i lost to decays.
- ➢ T_3: source term accounting for the production of particles of type i with energy E_i by particles of type j with energy E_j. The F_{ji} characterizes the inclusive cross section of the production of particles of type i through the interaction of particles of type j with the target nuclei.

C. Muon Production via Meson Decay

Muons in hadronic showers can be produced via the decay of charged pions and kaons, which also produces muon (anti)-neutrinos:

$$\pi^\pm \to \mu^\pm + \nu_\mu(\overline{\nu}_\mu)$$
$$K^\pm \to \mu^\pm + \nu_\mu(\overline{\nu}_\mu)$$

Assuming that one pion produces one muon, the number of muons with energy greater than 1 GeV in a shower initiated by a nucleon carrying an energy E_0 can be written:

$$N_\mu(E_\mu > 1\,\text{GeV}) \approx 10\left(\frac{E_0}{\epsilon_\pi}\right)^{0.78}, \tag{1.40}$$

where $\epsilon_\pi = 115$ GeV is the critical energy for which the probability of interacting equals the one of decaying. Although the spectral index differs from Equation 1.33, the dependence of the number of muons on the primary energy remains one of the main feature of the muon content.

In order to get a better understanding of how the muon content may vary with the zenith angle, the case of showers produced in the atmosphere by

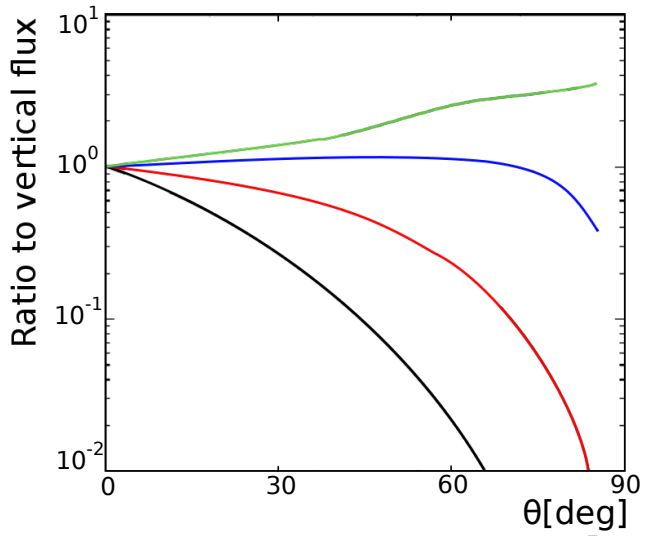

Figure 1.10: Variation of the muon flux as a function of the zenith angle θ, as a ratio to the vertical flux and for different muon energies in GeV/c: 1 (black), 10 (red), 100 (blue) and 1000 (green). Figure taken from [10].

cosmic rays is investigated and the results that are presented in [10, 20] are highlighted. For stable hadrons and under the assumption that the interaction length is independent of the energy, Equation 1.39 can be simplified (without the term accounting for decay) and a solution for the number of nucleons as a function of the energy and the atmospheric depth can be obtained for the measured cosmic-ray spectrum:

$$N_N(E, X) = g(0)\exp\left(\frac{-X}{\Lambda_N}\right) E^{-(\Gamma+1)}, \tag{1.41}$$

and which satisfies the boundary condition $N_N(E, 0) = 1.7E^{-2.7}\text{nuc.}/\text{cm}^2\text{sr s (GeV/A)}$ from the measurement of the cosmic-ray spectrum at the top of the atmosphere, such that $\Gamma = 1.7$. $g(0)$ is a constant obtained from the derivation of the given solution and Λ_N is the attenuation length and which highlights the fact that the nucleon flux decreases exponentially as the shower develops deeper into the atmosphere. The ratio of neutrons to protons increases from 0.11 at the top at the atmosphere to a value close to 1 when large amount of atmosphere is traveled through.

To investigate how the muon flux behaves as a function of the energy and the atmospheric depth, one must first assess how the flux of pions produced via hadronic interactions vary. In [20], Gaisser derives the vertical flux for low-energy pions ($E \ll \epsilon_\pi$) and high-energy muons ($E \gg \epsilon_\pi$). In the latter case, pion decay is ignored (valid approximation for vertical showers) while in

the former the pion content varies as:

$$N_\pi(E,X) = N_N(E,0)\frac{Z_{N\pi}}{X_N}\exp\left(\frac{-X}{\Lambda_N}\right)\frac{X\,E}{\epsilon_\pi}, \tag{1.42}$$

where $Z_{N\pi}$ is the spectrum-weighted moment of the inclusive cross section $N + air \to \pi$.

Ignoring muon decays and energy losses, the muon spectrum in the atmosphere can be written as a function of the zenith angle such that:

$$\frac{dN_\mu(E)}{dE} \simeq 0.14E^{-2.7}\left[\frac{1}{1+\frac{1.1E\cos(\theta)}{115\,\mathrm{GeV}}} + \frac{0.054}{1+\frac{1.1E\cos(\theta)}{850\,\mathrm{GeV}}}\right], \tag{1.43}$$

where the first term accounts for pion decay and the second one for kaon decay (850 GeV is the critical energy analogous to ϵ_π for kaons). From Equation 1.43, several characteristics can be emphasized. First of all, in the case of vertical showers, mostly low energy muons are produced since only low-energy pions have short enough decay lengths. On the other hand, showers with high zenith angles are more likely to see a raise in the high-energy muon flux due to the fact that high-energy pions travel through large amount of atmosphere and are therefore more likely to decay. However, since this equation is derived under the approximation that energy losses and muon decays are ignored, the muon flux at low energy tend to be overestimated for energies below ϵ_π.

Figure 1.10, obtained from Monte-Carlo simulations, shows how the muon flux changes with the zenith angle and at different energies. The flux at low energies drops rapidly with the zenith angle as muons are subjected to greater energy losses and are more likely to decay to electrons and neutrinos. As higher energies are probed, the flux becomes more significant at large zenith angles than in the case of vertical showers since high-energy pions travel larger distances and may decay as a consequence.

D. Gaisser-Hillas Parametrization and Fluctuations

The longitudinal profile of hadronic showers was parametrized by Gaisser & Hillas in [21] and was shown to be a function of the first interaction depth X_1 and of the number of particles $N_{\max}$ at maximum development:

$$N(X) = N_{\max}\left(\frac{X-X_1}{X_{\max}-X_1}\right)^{(X_{\max}-X_1)/\lambda}\exp\left[-\frac{X-X_{\max}}{\lambda}\right], \tag{1.44}$$

where λ is the mean free path. $N_{\max}$ being a function of the primary energy, Equation 1.44 can be used to fit air shower data and infer on the energy carried by the primary. In such case, the measurement of both electron and muon

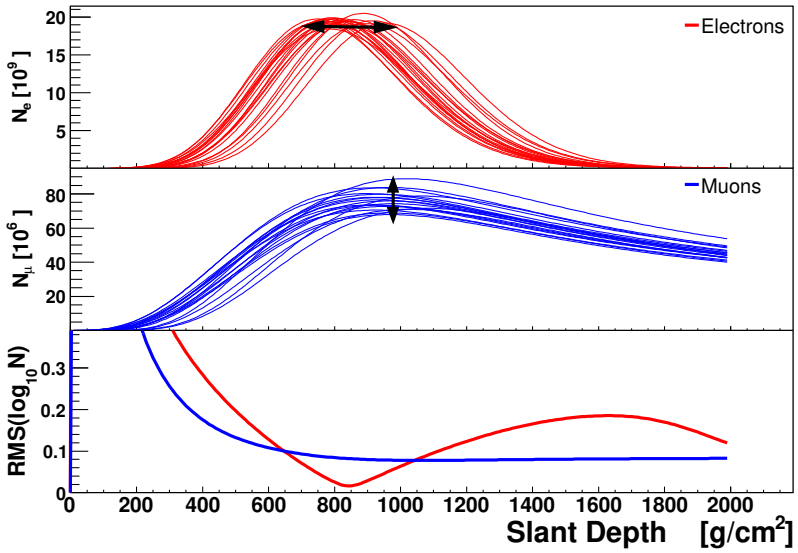

Figure 1.11: Longitudinal profiles of electron (top) and muon (center) content of 20 proton EAS's with energy $10^{19.5}$ eV. The root mean square of the number of particles as a function of the slant depth is shown in the bottom panel. Figure taken from [22].

content at $X_{\max}$ can provide an accurate estimation of such energy. However, fluctuations inherent to hadronic showers may involve large uncertainties on the actual energy reconstruction.

Figure 1.11 shows the electron and muon profiles of EAS's produced by $10^{19.5}$ eV protons. Fluctuations in both $X_{e,\max}$ and $N_{\mu,\max}$ are clearly visible. Their origins may be found in the depth at which the first interaction occurs and in the intrinsic fluctuations of hadronic interactions: fraction of energy transfered to the electromagnetic component, multiplicity after each interaction, energy losses and decay processes, etc. The bottom panel of Figure 1.11 shows that fluctuations in the number of electrons are at minimum around $X_{e,\max}$ while the number of muons suffers larger variations at the beginning of the shower development. In the ultra-high energy domain, estimating the values $X_{\max}$ and $N_{e,\max}$ of an air shower from a set of measurements can be subject to large uncertainties which stem from the hadronic models and their extrapolation to energies beyond the reach of laboratory experiments. Such uncertainties lead to fluctuations of the reconstructed primary type and energy of observed EAS's.

E. Hadronic Interaction Models

The interpretation of EAS measurements heavily rely on the results obtained from Monte-Carlo simulations and consequently, on the features of the

hadronic models that are used to characterize particle interactions in simulation algorithms that describe the cascades development, such as CORSIKA (COsmic Ray SImulations for KAscade) [23]. In fact, different hadronic models may lead to important differences in expectations regarding some of the EAS characteristics such as the number of muons or the depth of maximum development. Such discrepancy, most significant in the ultra-high energy domain, mostly stems from the inaccessibility of certain phase space regions to accelerator experiments and to the typical energies of EAS's. One important consequence lies in the systematic uncertainties that cosmic-ray experiments suffer from when assessing the mass composition of UHECRs as well as the reconstructing the EAS energy.

Some of the hadronic model features that may affect Monte-Carlo simulations include the multiplicity, i.e. the number of secondary particles produced at each hadronic interaction; the inelastic cross section, i.e the probability for an hadronic interaction to occur; or the inelasticity, i.e. the fraction of energy carried by the parent particle after an interaction. Although these parameters tend to increase with the energy in p-air collisions, their absolute values differ from one model to another as highlighted in [24] and shown in Figure 1.12. The observed discrepancy between models at the highest energies is essentially due to the lack of data in that energy range. In Figure 1.12, three models are taken into consideration: QGSJETII-04 [25, 26], EPOS-LHC [27] and SIBYLL 2.3C [28]. While the structure as well as the details of these models are beyond the scope of this dissertation, differences regarding the evolution of hadronic interaction parameters from one model to another may be discussed.

First of all, one noticeable feature is the fact the extrapolation of the cross section at the highest energies in p-air collisions are consistent between models while it diverges in the case of π-air collisions. On the other hand, large variations are observed in the multiplicity for both types of interactions. Similar behavior is seen in the evolution of the inelasticity. The divergence of these three parameters has serious consequences for the simulations performed to reconstruct the features of observed EAS's. The impact of the inelastic cross section on the development of EAS's is important as it affects both the depth of first interaction X_1 and the number of particles (electrons and muons) at the surface, as well as their shower-to-shower fluctuations. Lower estimations may significantly reduce the number of interactions occuring and therefore, raise $X_{\max}$ (deeper cascades). Similarly, higher multiplicity increases the number of particles produced at each interaction and the number of particles at ground level, and also has an influence on the $X_{\max}$. The effect of the extrapolation of these parameters to the highest energies on some of the EAS observables such as the mean $X_{\max}$, the number of electrons and muons, as well as their fluctuations, is well described in [22]. Investigating the case of $10^{19.5}$ eV proton

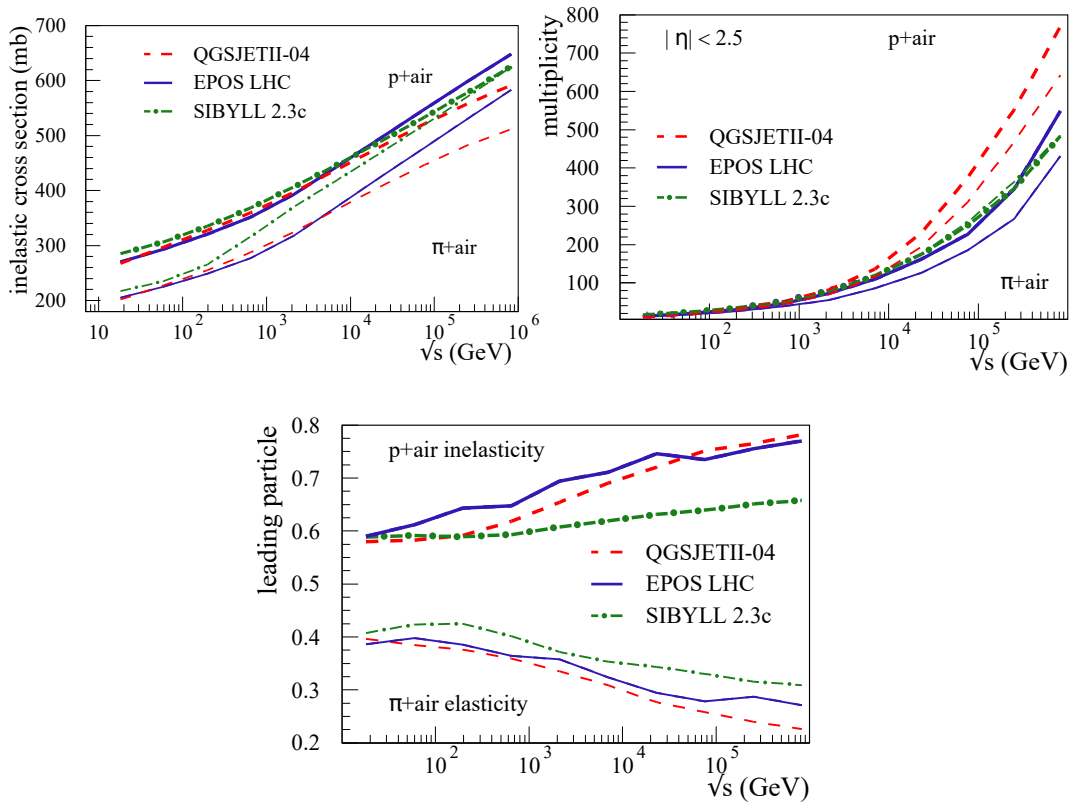

Figure 1.12: Inelastic cross section (top-left), multiplicity (top-right) and inelasticity (bottom) of p-air (thick lines) and π-air (thin lines) collisions as a function of the center of mass energy, for different hadronic models. Figures taken from [24].

and iron primaries, several results are highlighted:

- For both primaries, the mean $X_{\max}$ as well as its fluctuations mainly depend on the cross-section.

- While the number of muons is positiviley correlated with the multiplicity (higher multiplicity results in more muons), this correlation is negative in the case of the number of electrons, and the fluctuations of the number of electrons (muons) is mostly driven by the multiplicity (elasticity) parameter.

Figure 1.13 shows the expectations set by the aforementioned hadronic models (DPMJET III.17-1 [29]) is also included) on the mean $X_{\max}$ and on the number of muons at the surface (for 40° zenith angle) as a function of the primary energy (iron or proton). One important feature is the identical elongation rate of the mean $X_{\max}$ for all hadronic models and for both types of primaries. As highlighted in [22], the behavior of the $X_{\max}$ fluctuations is

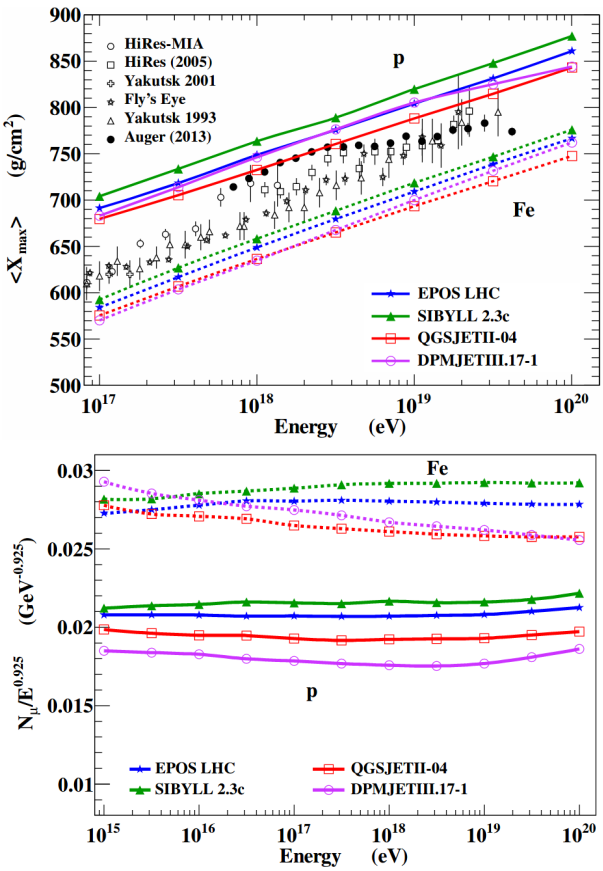

Figure 1.13: *Top*: Mean $X_{\max}$ for EAS produced by iron (dashed line) and proton (solid lines) primaries expected from different hadronic models, as a function of their energy. Data from various experiments are also displayed. *Bottom*: Number of muons expected at ground level scaled by a $E^{0.925}$ factor for the same primaries and for various hadronic models. EAS's with a zenith angle of 40° are considered. Figures taken from [24].

mostly governed by the cross section parameter. The top-left panel of Figure 1.12 shows that this parameter is fairly consistent between hadronic models in the case of p-air collisions. Consequently, $X_{\max}$ fluctuations vary very little with the considered models and mass composition analyses can be strengthen by comparing the RMS and the mean $X_{\max}$ values for a given primary. On the other hand, the number of expected muons at ground level depends on the hadronic model used. Indeed, as muons are largely produced by the decay of pions, the number of pions contained in the EAS has a significant impact on the number of muons found at different stages of the shower. In turn, the number of pions is a function of the multiplicity which, as shown in the top-right panel of Figure 1.12, diverge between models at the highest energies.

While the expected mean $X_{\max}$ suffers from uncertainties that are pre-

dominantly due to the nature of the first interaction, observables related to muons, such as Muon Production Depth (MPD) and the number of muons at ground level, are directly linked to the description of pion interactions in the EAS. Measurements of these observables could effectively constrain the parameters governing these interactions and improve the accuracy of hadronic models [30].

Muon Deficit

The uncertainties previously highlighted have a significant impact on the interpretation of the measurements performed by cosmic-ray experiments on the mass composition as a muon excess is observed in the data by Auger [31] and TA [32] (both introduced later on) compared to hadronic model expectations. Also expressed as a muon deficit in Monte-Carlo simulations, such discrepancies were quantified by Auger, using various hadronic models to compare with data obtained in the energy range 6-16 EeV with zenith angles lower than 60° [33]. Introducing a rescaling factor for R_E and R_{had} for the measured electromagnetic and hadronic signals, respectively, the signals from Monte-Carlo simulations were matched to the recorded ones. Figure 1.14 shows the phase space of these rescaling factors for different hadronic models and different compositions (pure proton or mixed). While the electromagnetic signal does not need any rescaling for any scenario, the hadronic signal must be rescaled by a factor 1.3-1.6 depending on the models considered. Such results are consistent with the muon excess found in [31].

A similar conclusion was reached in [34], where agreements between simulations and data regarding the electromagnetic and muonic components in several experiments were studied. After cross-calibration of the energy scales, the observed muon densities were scaled and compared to expectations from different hadronic models. While such densities were found to be consistent with simulations up to 10^{16} eV, at higher energy, the muon deficit increases in several experiments.

1.1.4 Discrimination of Extensive Air Showers

The description of the properties of EAS's produced by different types of primaries given in the previous sections allows us to summarize the main observables that can be used to discriminate EAS's initiated by gamma rays from the ones produced by protons and nuclei. To illustrate their differences, Figure 1.15, which shows Monte-Carlo simulations of 300 GeV gamma and proton-induced air showers, is used as a reference.

➢ First of all, the lateral spread of hadronic showers, which can reach up

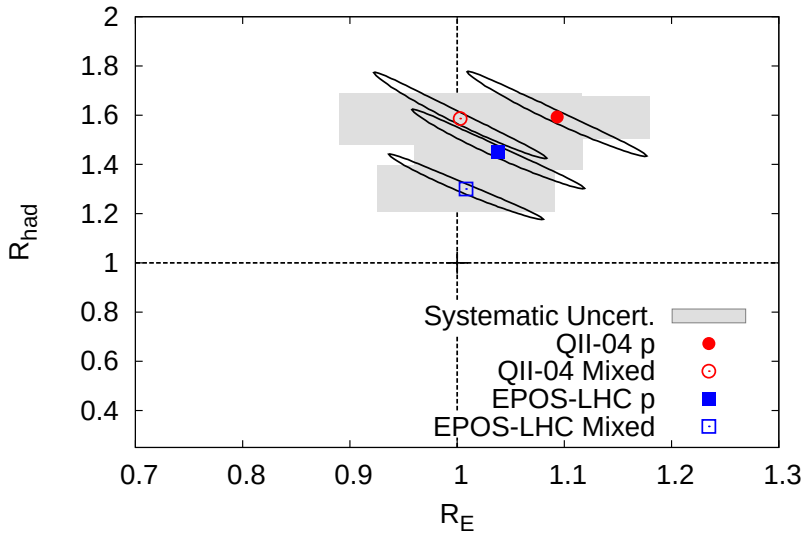

Figure 1.14: Phase space of the electromagnetic and hadronic scaling factors for different hadronic models and compositions. The 1σ statistical and systematical uncertainties are represented by the ellipses and grey boxes, respectively. Figure taken from [31].

to several kilometers, is mostly caused by the characteristic large transverse momentum of mesons within the shower. On the other hand, electromagnetic showers lateral spread is the result of Coulomb scattering which spreads out particles within a diameter of 200 m at maximum development. On the ground and for energies above 10 TeV, this discrepancy can be observed by installing detectors with large spacing between one another, allowing to find correlations between triggered stations on distances up to several kilometers. Another way of expressing that statement is to note that electromagnetic showers would trigger smaller clusters of detectors compared to hadronic EAS's.

➢ As previously mentioned, hadronic and electromagnetic cascades have significantly different muon contents. Although Figure 1.15 shows no muons in the latter case, it was shown that the muon content of electromagnetic showers is in fact non-zero, although several orders of magnitude lower than hadronic showers [36]. Directly measuring the muon content at ground level or looking for particular muon light emission such as rings of Cherenkov light (see Chapter 3) constitute a powerful tool to indentify the nature of the primary.

➢ Overall, the first interaction point of electromagnetic showers tends to occur at higher altitudes. They also develop and die out faster than hadronic showers and their longitudinal profiles are more uniform. In other words, hadronic showers are initiated deeper in the atmosphere,

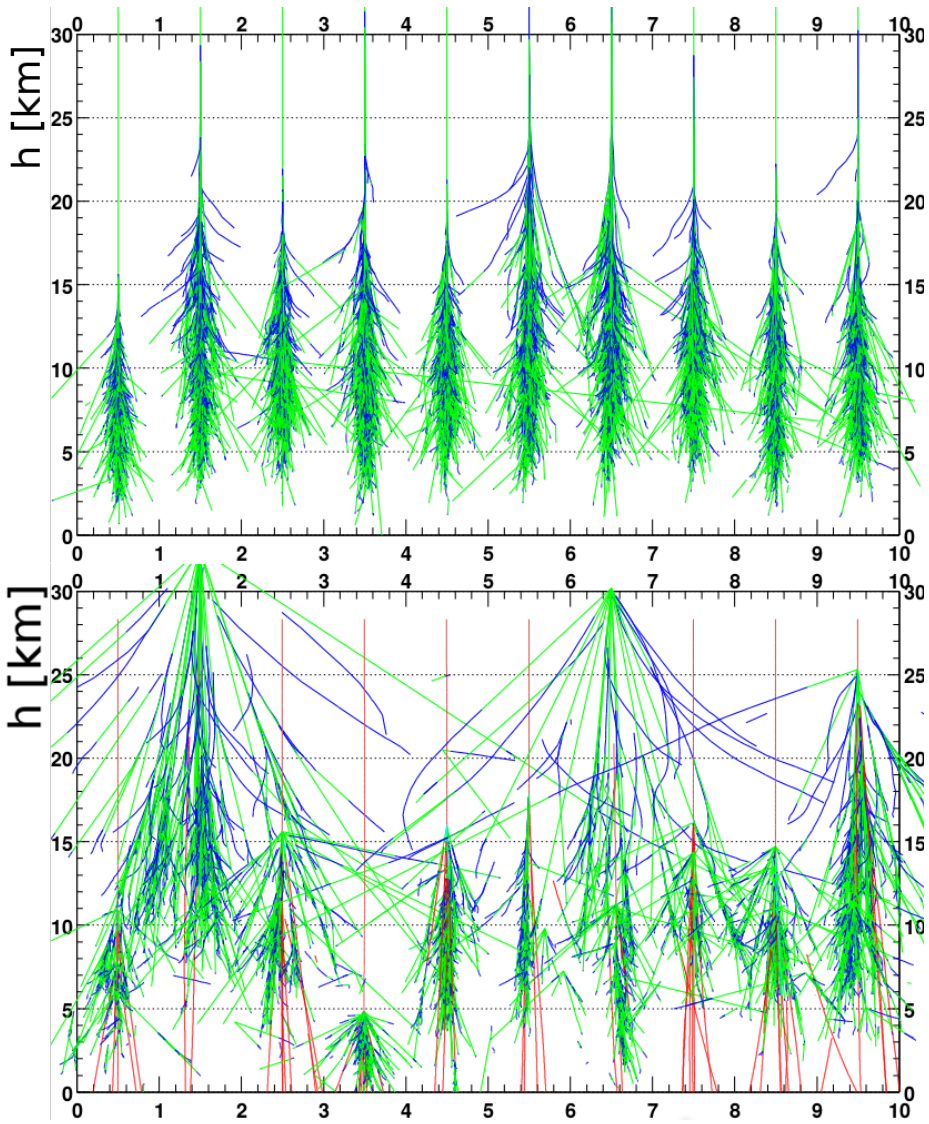

Figure 1.15: Schematic view of 10 showers produced by 300 GeV gamma rays (top) and protons (bottom). Photons, electrons and muons are represented by green, blue and red tracks, respectively. Figures taken from [35].

reach their maximum development closer to the surface, and show larger shower-to-shower fluctuations. Measurements of the longitudinal profiles can be perfomed via the detection of fluorescence light emission from nitrogen molecules in the air or of Cherenkov radiation, which can provide an excellent discrimination tool when compared with Monte-Carlo simulations.

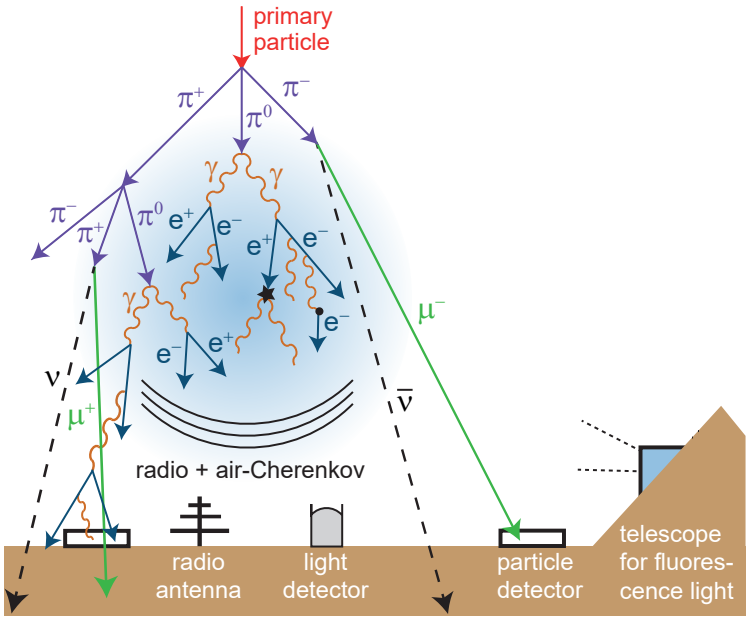

Figure 1.16: Air showers can be detected through various channels of observation. Although particle detectors and fluorescence telescopes are the most prevalent techniques in the ultra-high energy domain, EAS's can also be observed via the Cherenkov light they emit (see Chapter 3) or via the radio emission due to interactions of charged particles with the geomagnetic field [37] or to the Askaryan effect [38]. Figure taken from [39].

1.2 Ground Detection of Ultra-High Energy Cosmic Rays

Due to the large energy range covered by the cosmic-ray spectrum and to the variety of interactions governing the development of EAS's in the amosphere, multiple detection techniques are employed conjointly with Monte-Carlo simulations in order to estimate the energy of the primaries as well as their arrival direction. Figure 1.16 shows a panel of different types of detectors used to detect EAS's from the surface. In the ultra-high energy domain, surface detectors (such as scintillators or water-Cherenkov detectors) measuring the amount of charged particles passing through together with fluorescence light detections are most commonly used. Such techniques focus on the reconstruction of the longitudinal profiles of EAS's along with their lateral distributions. Presently, state-of-the-art UHECR experiments such as Auger and TA are both using an hybrid observation mode by combining fluorescence detectors (FDs) and particle detectors. Before discussing the various results regarding UHECRs, the basic principles of these detection techniques are briefly reviewed and these two experiments are introduced.

1.2.1 Particle Detectors

The capacity to detect an EAS at ground level depends on two factors: the energy of the primary that initiated the air shower, and the altitude at which the particle detectors are placed. As seen in the previous section, the number of particles contained in the EAS grows with the energy of the primary, while higher altitude means a shorter distance to the shower $X_{\max}$, i.e. closer to the height at which the maximum number of particles is reached. In the ultra-high energy domain, the energies at stake are sufficiently high so that a large number of particles can be expected at relatively low altitudes ($\sim 1000 - 2000$ km a.s.l.). Charged particles contained in air showers that reach the surface may be detected via different types of detectors. In UHECR experiments, the most popular ones are scintillators and water-Cherenkov. The physical principle of the former relies on the excitation of a medium displaying scintillation properties (plastic or organic), a process through which photons are reemitted by the medium after being excited by ionizing radiation passing through. On the other hand, water-Cherenkov detectors are based on the Cherenkov photon emission by particles traveling faster than the phase velocity in water. Scintillators and water-Cherenkov detectors are both coupled to electronic light sensors such as photomultiplier tubes (PMTs), which convert the lower energy photons to electrons via a photocathode as a result of the photo-electric effect. The number of electrons is then multiplied as they reach several dynodes, and an electronic signal that can be read and analyzed, even for low incident fluxes, is formed.

In order to observe EAS's, particles detectors are usually laid out in a grid pattern with a spacing distance d_{sp} between them. The array triggers when multiple neigbor detectors are hit within a time interval Δt, which depends on both the data acquisition system and on the zenith angle up to which the experiment wants to observe. If the trigger requirements are met, each detector records the time of arrival of the signal as well as the particle density or the deposited energy. The latter two are often converted into a signal in units of Vertical Equivalent Muons (VEM), which corresponds to the signal released by a muon passing through the detector in the vertical direction. While the direction of arrival of the EAS is obtained by analizing the time delays between the triggered detectors, the core position is calculated by fitting the signal of all detectors with a lateral distribution function (LDF). By doing so, one can obtain the signal strength as a function of the distance to the core. Because of the uncertainties of the recorded signals, several LDFs with different free parameters may be used. However, the obtained LDFs may intersect at a certain distance r_{opt} from the core of the shower, therefore allowing analyses to avoid large fluctuations in the signal [17, 40]. Such feature has one important advantage: the signal at this distance is independent of the fitting and can

be used as an energy estimator $S(r_{\rm opt})$ of the EAS when compared to calorimetric measurements from FDs or to Monte-Carlo simulations. To account for the atmospheric attenuation of the EAS as a function of the zenith angle, $S(r_{\rm opt})$ is often normalized to $S(\theta)$ – the signal $S(r_{\rm opt})$ the same EAS would have produced if coming at a θ° zenith angle – by using the Constant Intensity Cut (CIC) to obtain the attenuation curve from the data [41]. In order to indentify the mass of the primary that initiated the air shower, it is often recommended to have separate detectors for electrons and muons. As discussed in the previous section, hadronic showers contain more muons than electromagnetic showers and the amount of electrons reaching the surface increases with $X_{\rm max}$, which is related to the nature of the primary.

1.2.2 Fluorescence Detectors

While ground arrays can provide a good estimation of the lateral distribution of air showers particle density, FDs are capable of reconstructing their longitudinal profiles via the isotropic light emitted in the UV range by nitrogen molecules as they re-emit the energy they initially absorded from incoming charged particles. The intensity of such light is positively correlated with the number of particles in the shower [42]. FDs are usually made up of optical telescopes with cameras composed of PMTs which trigger one after the other as the EAS develop in the atmosphere. Consequently, the track formed on the detectors by the triggered PMTs as well as the difference between their trigger timestamps allow the reconstruction of both the impact distance and the angular direction of the showers. In stereo observation mode, the intersection of the planes defined by the detectors position and the tracks facilitates the geometrical reconstruction and angular resolutions lower than 1° can be obtained.

The longitudinal profile of the air showers can be described by Equation 1.44 and important quantities such as the depth of the showers maxima as well as the maximum number of particles can be retrieved. On the other hand, the calorimetric measurement of the energy deposited in the atmosphere by the showers and provided by the fluorescence detectors, offers the possibility to give a reliable estimation of the primary energy. However, the isotropic nature of the fluorescence light makes such technique efficient only at the highest energies, and necessary observation conditions include moonless nights and atmospheric properties leading to low absorption, thus reducing the duty cycle of fluorescence detectors down to approximately 10-15%. The altitude and temperature dependency of the fluorescence light yield, as studied by the Fly's Eye experiment [43], can be explained by the important role played by the atmospheric pressure: excitation becomes more probable when pressure is higher

(more molecules to interact with for a given pathlength) while fluorescence yield drops due to higher chance of emitted light to interact with neighboring molecules.

Additionally, not all particles in the showers generate fluorescence light. Muons, neutrinos and hadrons may carry away large fractions of the primary energy as they do not interact. This fraction, sometimes referred to as *missing* or *invisible* energy, decreases as the primary energy increases, and can reach values above 10% for primaries with energy $E \sim 10^{18}$ eV. The observed anti-correlation between the missing and the primary energy is mostly due to the fact that particles of higher energy are more likely to interact than to decay. Furthermore, for a given energy, heavier nuclei tend to show more significant fractions of missing energy, as the energy per nucleon tends to be lower and mesons produced subsequently have lower energies and are more likely to decay. These features highlight the fact that properly estimating the missing energy is an essential procedure when investigating the mass composition of cosmic rays. FDs coupled to ground arrays may use the information obtained from the latter, such as the muon content [44], to assess this energy (this coupling also offers better geometrical reconstruction as the lateral distribution on ground provides the impact position of the EAS) or Monte-Carlo simulations can be performed in the same endeavor, making the missing energy estimation dependent on the hadronic interaction models used.

1.2.3 Telescope Array

Located in the desert of Utah, USA, Telescope Array (TA) is the largest hybrid cosmic-ray experiment in the northern hemisphere [45], with an energy sensitivity range from 10^{16} to 10^{20} eV. Covering an area of around 700 km^2, the 507 surface detectors (SDs) consist of two superimposed plastic scintillators of 3 m^2 each. SDs are distanced from one another with a spacing $d_{\mathrm{sp}} = 1.2$ km (see Figure 1.17). Solar panels and communication systems complete the detectors set-up. The energy estimator $S(r_{\mathrm{opt}})$ of the SDs is obtained by taking the density of shower particles at a distance of $r_{\mathrm{opt}} = 800$ m from the core position via a fit of the lateral distribution. The energy of the primary is recovered by using look-up tables obtained from Monte-Carlo simulations in order to find the correspondence between the primary energy and the S(800m)-zenith angle parameters. In fact, TA also performed estimations of the primary energy using the CIC method described in Section 1.2.1. It was shown in [46] that the two reconstruction methods agreed at $\sim 3\%$ level.

TA also includes a total of 36 FDs distributed on three different sites (see thick blue squares in Figure 1.17), each telescope being composed of 256 PMTs. The telescopes pointing direction can span over up to 120° in azimuth

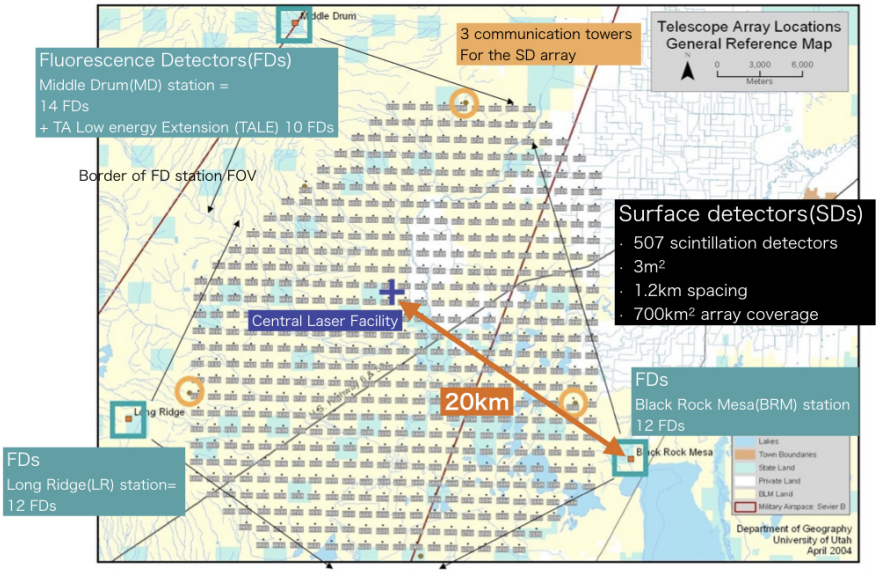

Figure 1.17: Map of TA site, where grey boxes represent the surface detectors and the thick blue squares reprensent the fluorescence telescopes locations. The Central Laser Facility helps to assess the aerosol content in the atmosphere. Figure taken from [45].

angle (with a 16° field-of-view(FOV)) and up to 33° in zenith angle (with a 14° FOV). The shower geometry is determined using the reconstruction methods for monocular and stereo observations described in Section 1.2.2. The missing energy is evaluated based on iron and proton simulations at UHE performed in [47], using Linsley's parametrization [48]. $X_{\max}$ is obtained by analyzing the signal in each of the triggered PMTs while the energy of the primary is found after integrating the shower profile.

The energy scale of the SDs is calibrated using an energy-independent calibration factor of 1/1.27 [49]. In order to insure precision in the range of 100% SD efficiency, only events from FDs with $E_{\mathrm{FD}} > 6.3 \times 10^{18}$ eV and with zenith angle $\theta < 55°$ are selected for energy spectrum analysis purposes. One should however note that the TA SDs can reach 1.6×10^{18} eV with an efficiency of 10%. The systemic uncertainties derived for the energy scale at TA is about 21%.

The Telescope Array Low-Energy Extension (TALE), located north of the array, consists of 10 FDs that are sensitive to Cherenkov radiation emitted by the charged particles of the EAS, and of 80 scintillation counters with smaller spacing (400 m and 600 m), thus lowering the energy threshold down to $10^{16.5}$ eV. Cosmic rays with energies below 0.1 EeV can be detected using such

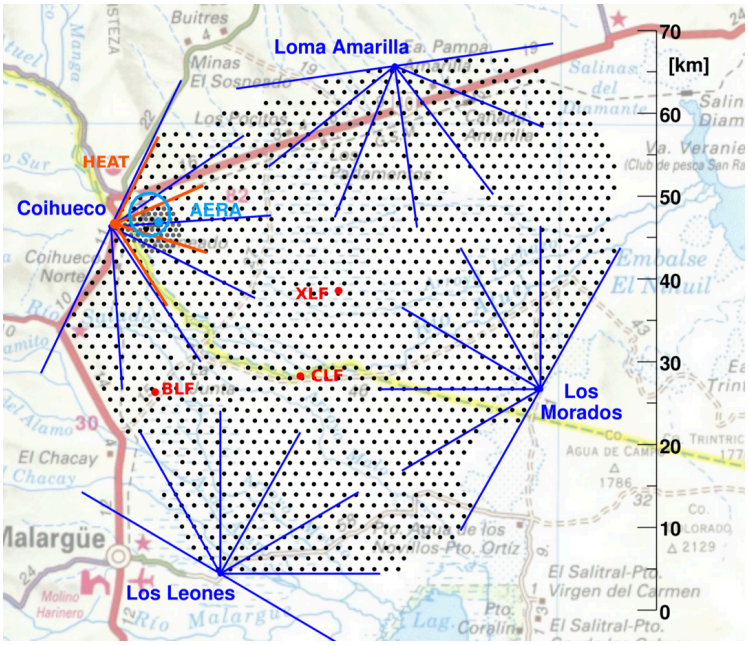

Figure 1.18: Schematic view of the Pierre Auger Observatory. The black dots represent the water-Cherenkov SD tanks while the blue lines represent the FOV of each of the 24 telescopes making up the 4 FDs stations. HEAT and AERA (see description in the text) are shown in red and light blue, respectively. The laser facilities XLF and CLF are also displayed. Figure taken from [51].

method, therefore significantly decreasing the energy threshold to $\sim 2 \times 10^{15}$ eV [50].

Finally, in order to obtain higher statistics, the TA×4 project is currently underway. Its purpose is to extend the existing array by increasing the covered aread up to 3000 km^2 by distributing 500 SDs, spaced by 2.08 km, over two sites, northeast and southeast of the current experiment. Additionally, both sites will be overlooked by one FD station composed of twelve telescopes.

1.2.4 The Pierre Auger Observatory

The Pierre Auger Observatory (Auger) is an UHECR experiment located in the southern hemisphere, near Malargüe, Argentina [52, 51] that has been operating for more than 15 years and has accumulated an exposure of about 100 000 km^2 sr yr. 1660 Cherenkov-water detectors, filled with 12 tons of purified water and spaced from one another by a distance $d_{\mathrm{sp}} = 1.5$ km, cover an area of 3000 km^2 (see Figure 1.18). The Cherenkov radiation emitted by the electrons and muons passing through the tanks is detected by 3 PMTs, which send the recorded data to the Central Data Acquisition System in Malargüe. The area is overlooked by 4 FDs stations each composed of 6 telescopes with

cameras of 440 pixels (440 PMTs). The combined field of view of each station is 180° in azimuth and 28.6° in elevation.

When an EAS triggers the SDs, the energy estimator is taken at $r_{\text{opt}} = 1000$ m. Normalized to $S(38°)$ using the CIC method, the energy of SD events is obtained by looking at the correlation between $S(38°)$ and the energy E_{FD} measured by the FDs. Such relationship can be described by a simple power law $E_{\text{FD}} = AS(38°)^B$, where A and B are obtained by fitting the data. Energy reconstruction of hybrid events (seen by both SDs and FDs) is performed for events with $E_{\text{FD}} > 3 \times 10^{18}$ eV and with zenith angle $\theta < 60°$. Overall, thanks to the calibration measurements offered by the hybrid detection approach, the absolute energy scale of both experiments shows minimal dependence on hadronic interaction models and systematic uncertainties on the energy scale are estimated around 14%.

A denser array of 61 SDs, with spacing $d_{\text{sp}} = 750$ m, uses a similar energy reconstruction procedure as the main array and reduces the energy threshold down to 10^{17} eV. Finally, the three high-elevation fluorescence telescope (HEAT) are also sensitive to Cherenkov radiation emitted by the charged particles of the EAS, allowing measurements down to $\sim 3.2 \times 10^{16}$ eV [53]. Furthermore, 150 radio antennas from the Auger Engineering Radio Array (AERA) also measure low-energy showers by recording their radio pulses in the frequency range of 30 to 80 MHz [54].

Auger is currently undergoing upgrades, including the implemention of plastic scintillators on top of each SD station, and the addition of a fourth PMT in each tank to increase their dynamic range [55]. The 3.8 m^2 scintillator detectors layers should allow a better discrimination between electrons and muons triggering the stations and therefore, a better identification of the mass of UHECRs and a better understanding of the physical processes at stake at the highest energies.

1.3 Measurements of Ultra-High Energy Cosmic Rays

In this section, some of the most important up-to-date results in UHECR astronomy performed by Auger and TA are presented, and the paradigm shifts these measurements bring forward are discussed.

1.3.1 Energy Spectrum

Accurate measurements of the UHECR energy spectrum are fundamental in our understanding of physical processes capable of producing these parti-

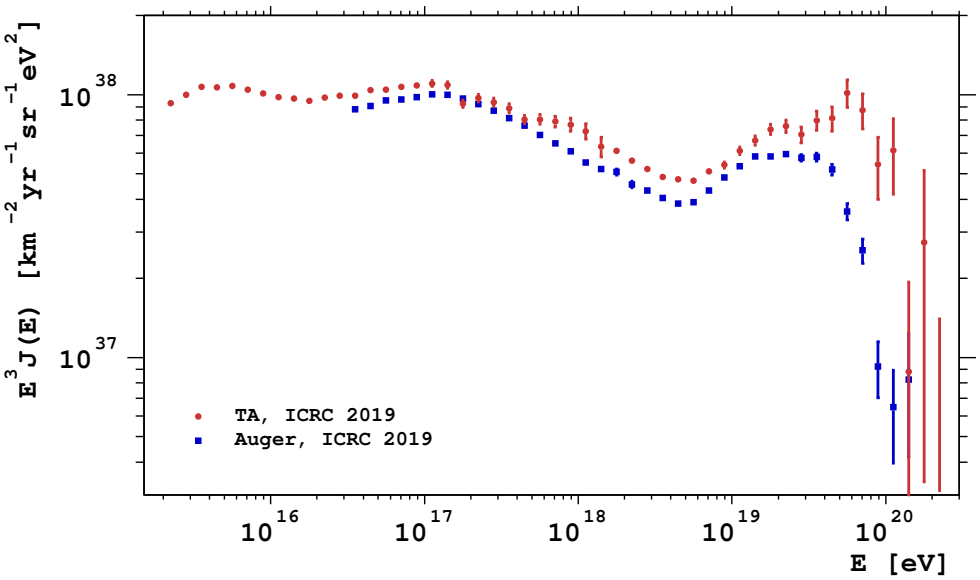

Figure 1.19: Energy spectra as measured by TA (red) and Auger (blue) scaled by E^3. The *second knee* at $\sim 0.15 \times 10^{18}$ eV, the *ankle* at $\sim 5 \times 10^{18}$ eV as well as the cut-off at $\sim 5 \times 10^{19}$ ev are easily identifiable. Plot taken from [56] and data obtained from [57] and [45].

cles, and of altering their propagation properties. However, several issues arise when trying to perform such measurements. First of all, the low flux above 10^{17} eV prevents any sort of direct detection for multiple reasons: as of today, no space-based detectors has been designed large enough to account for such low statistics, and secondly, UHECRs reaching the Earth interact with the atmosphere and produce extensive air showers of secondary particles (see Section 1.1). Therefore, cosmic-ray experiments probing this energy range must rely on ground detection of these EAS's. Such aspect has a strong impact on the quality of the energy reconstruction as it directly relies on hadronic interaction models which accuracy in the UHE domain depends on the energies reached in terrestrial accelerators. These systematic uncertainties must therefore be taken into account when investigating the UHECR energy spectrum at the highest energies.

Such technical difficulty is in fact well illustrated by the measurements performed by AGASA and HiRes collaborations at the beginning of the 21^{st} century. A flux suppression – the so-called Greisen–Zatsepin–Kuzmin (GZK) cut-off [58, 59] – around $10^{19.6}$ eV is in fact expected due to the interaction of UHECRs with the CMB and the photo-pion production associated to it (see Section 1.4.2 for more details). While AGASA was reporting the absence of such a cut-off [60, 61], HiRes claimed to observe a strong flux suppression at the energy predicted by the GZK effect [62, 63]. In addition to the large

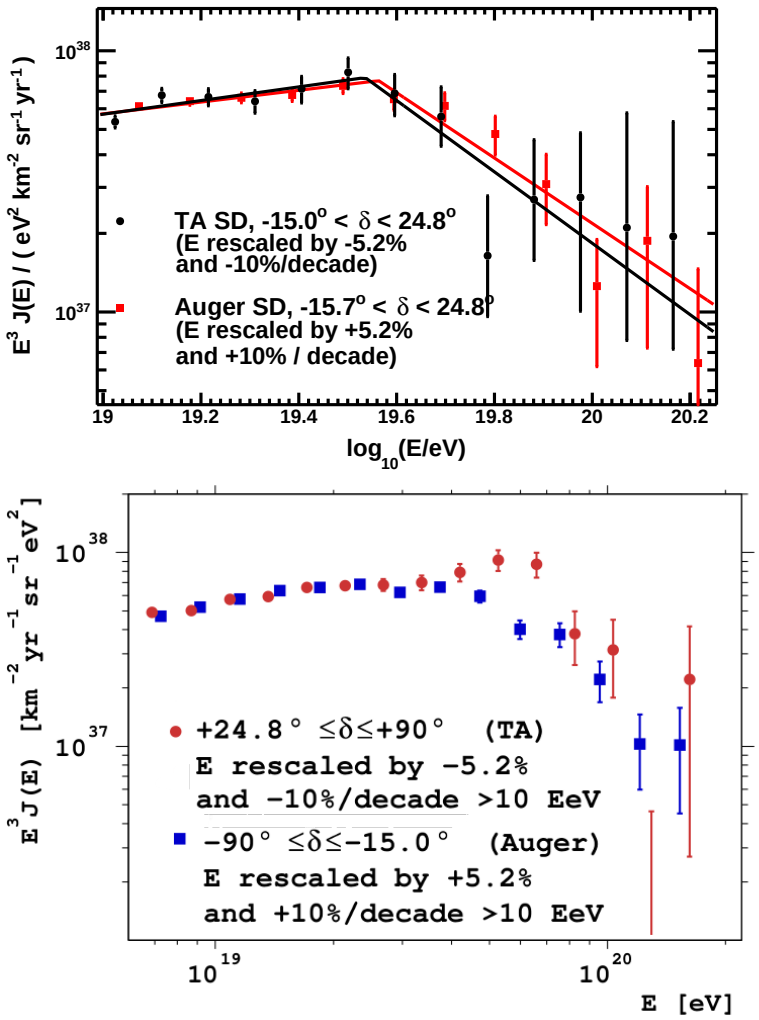

Figure 1.20: *Top*: Auger and TA energy spectra above 10^{19} eV in the common declination band after rescaling. *Bottom*: Same as on the upper panel but in the opposite declination band (southernmost for Auger and northernmost for the TA). Figures taken from [56].

statistical errors due to a very low number of detected events in the trans-GZK energy domain, this discrepancy could also be due to the significant differences in observation techniques between the two collaborations (ground detection for AGASA versus fluorescence detection for HiRes), as the sources of systematic uncertainties were different. Both experiments presented errors in the energy reconstruction above 25% for energies greater than 3×10^{19} eV.

Figure 1.19 shows the most up-to-date UHECR energy spectrum measurements performed by TA [46] and by Auger [57], combining all different types of observation techniques described in Sections 1.2.1 and 1.2.2. Focusing

on energies above 10^{17} eV, one can notice that both spectra show similar spectral features up to the flux suppression around 4×10^{19} eV. The *second-knee* region, found at $(0.15 \pm 0.02) \times 10^{18}$ eV by Auger [64] and at $(0.11 \pm 0.01) \times 10^{18}$ eV for TA [65], shows a softening of the energy spectrum over an energy range of 100 PeV which could be signature of a decrease of Galactic iron nuclei [66]. The so-called *ankle* reflects the transition from Galactic to extragalactic cosmic rays and is characterized by a hardening of the spectrum around $(6.2 \pm 0.9) \times 10^{18}$ eV for Auger and $(4.9 \pm 0.1) \times 10^{18}$ eV for TA. The region between the *ankle* and the cut-off found at $(50 \pm 7) \times 10^{18}$ eV for Auger and $(71 \pm 4) \times 10^{18}$ eV for TA can be described by a double broken power-law. It is in this region that significant discrepancies between the two observatories can be noted and that cannot be explained by the systematic uncertainties on the energy scale alone.

In [56], a special attention is given to the differences observed between Auger and TA energy spectra. The offset shown in Figure 1.19 between the two energy spectra can be attributed to a mismatch of the order of 10% in the energy scale due to different fluorescence yields. However, after renormalization ($+5.2\%$ for Auger and -5.2% for TA), these differences persist at higher energies. In order to investigate such discrepancies, only the declination band common to both observatories is considered. An additional energy-dependent rescaling of $+10\%$ for Auger and of -10% for TA is required in order to match both energy spectra, but is yet to be explained. The results of these procedures are shown on the top panel of Figure 1.20. On the other hand, when the same rescaling is performed on mutually exclusive declination band (southernmost for Auger and northernmost for TA), an excess around 60×10^{18} eV in TA energy spectrum is observed (see bottom panel of Figure 1.20).

Understanding the origin of the relative systematic uncertainties between Auger and the TA is of first importance in order to explain the observed discrepancies in the energy spectra. Moreover, the origin of the flux suppression above the GZK energy is yet to be identified, as it may be explained either by the GZK effect or by the maximum energy of particle acceleration processes at the source. In the former case, a light composition would be favored for sources located within 50-100 Mpc. On the other hand, a cut-off caused by a maximum effficiency of acceleration processes at the sources would favor a much heavier composition, as heavier nuclei can be accelerated to greater energies [68]. In [67], the energy spectrum was fitted assuming different composition mixtures that could correspond to these scenarios. As shown in Figure 1.21, the energy spectrum measured around the cut-off energy can be described by compositions dominated by light (top panel) or heavy (bottom panel) nuclei. Both mixtures seem to describe the measured energy spectrum and therefore, precise measurements of the UHECR masses at the highest energy would allow

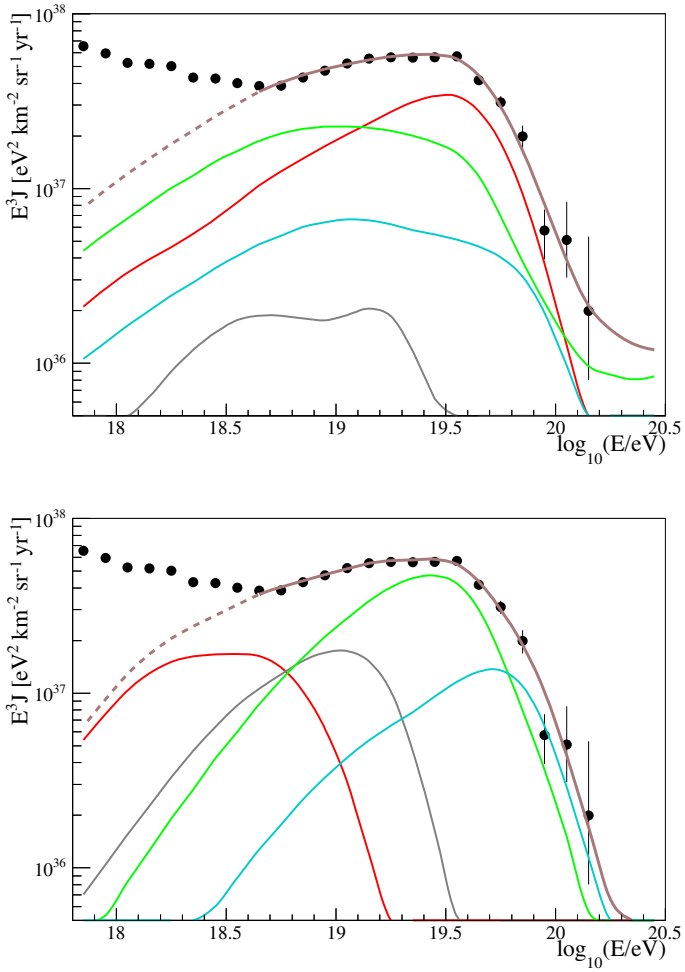

Figure 1.21: Energy spectrum measured by Auger and fitted assuming different compositions. Different colors represent different element spectra: proton (red), helium (grey), nitrogen (green) and iron (blue). The combined spectra are shown in purple. Figures taken from [67].

to discriminate between the two possible origins of the cut-off.

1.3.2 Mass Composition

In order to achieve a better comprehension of the features that characterize the energy spectrum, a thorough analysis of the composition should be carried out. At the highest energies, the mass composition of cosmic rays can be investigated via the measurement of the atmospheric column depth $X_{\max}$ at which EAS reach their maximum development. However, because of the large shower-to-shower fluctuations, that may affect the longitudinal development

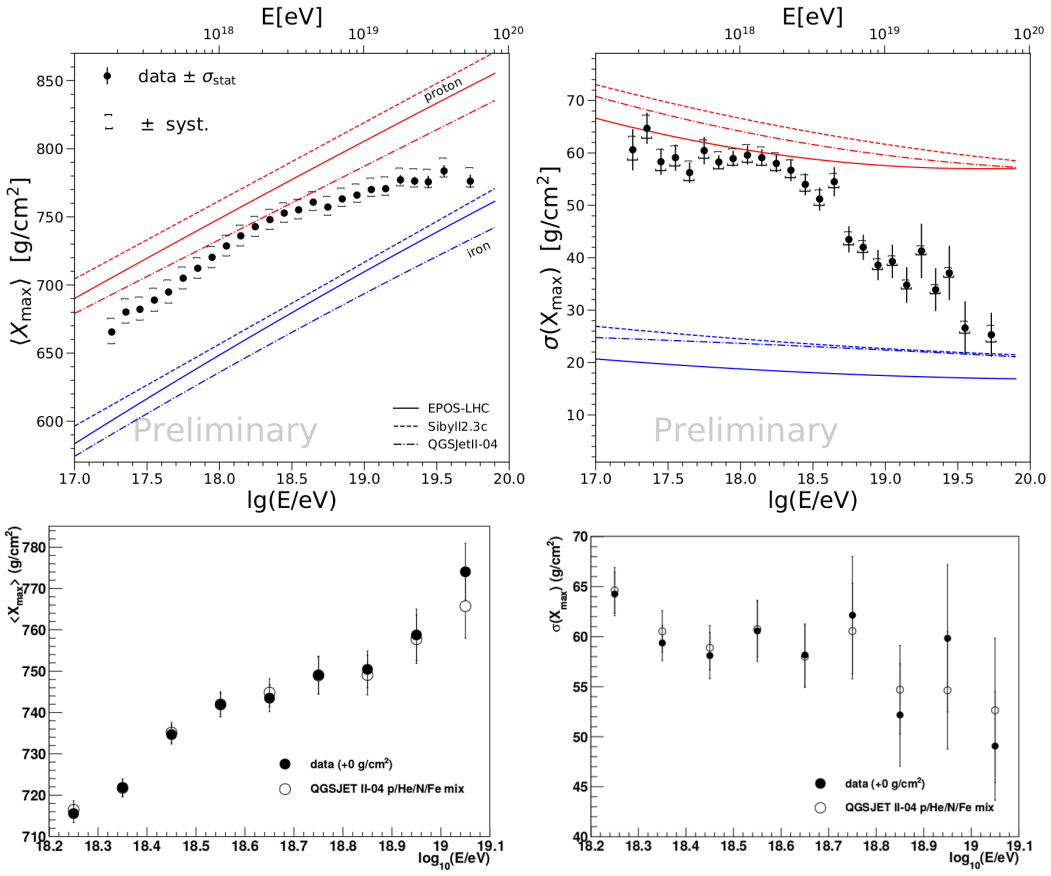

Figure 1.22: *Top*: Mean $\langle X_{\max} \rangle$ (left) and standard deviation $\sigma(X_{\max})$ (right) measured by Auger. Predictions obtained from Monte-Carlo simulations using two different hadronic interaction models (QGSJetII-04 and EPOS-LHC) and for proton and iron primaries are also shown. Figures taken from [69]. *Bottom*: Mean $\langle X_{\max} \rangle$ (left) and standard deviation $\sigma(X_{\max})$ (right) measured by TA. Data is compared to Monte-Carlo simulations for a mix of $57\%, 18\%, 17\%, 8\%$ of proton, helium, nitrogen, and iron, respectively. Figures taken from [70].

of EAS's, identifying the primary that initiated such EAS's may prove to be a rather difficult task on an event-by-event basis. Instead, a statistical approach is adopted and variables describing samples of showers are considered. The mean $\langle X_{\max} \rangle$ of the $X_{\max}$ distribution at a given energy is directly related to the mass of the primaries, while the variance $\sigma(X_{\max})$ gives informations about the relative proportion of the chemical elements, i.e. the spread of the mass, and about the shower-to-shower fluctuations (iron showers fluctuates less than proton ones, on average). As mentioned in Section 1.1, EAS's produced by protons reach their maximum development deeper in the atmosphere (larger $\langle X_{\max} \rangle$) and tend to have greater $X_{\max}$ variations (larger $\sigma(X_{\max})$) than EAS's

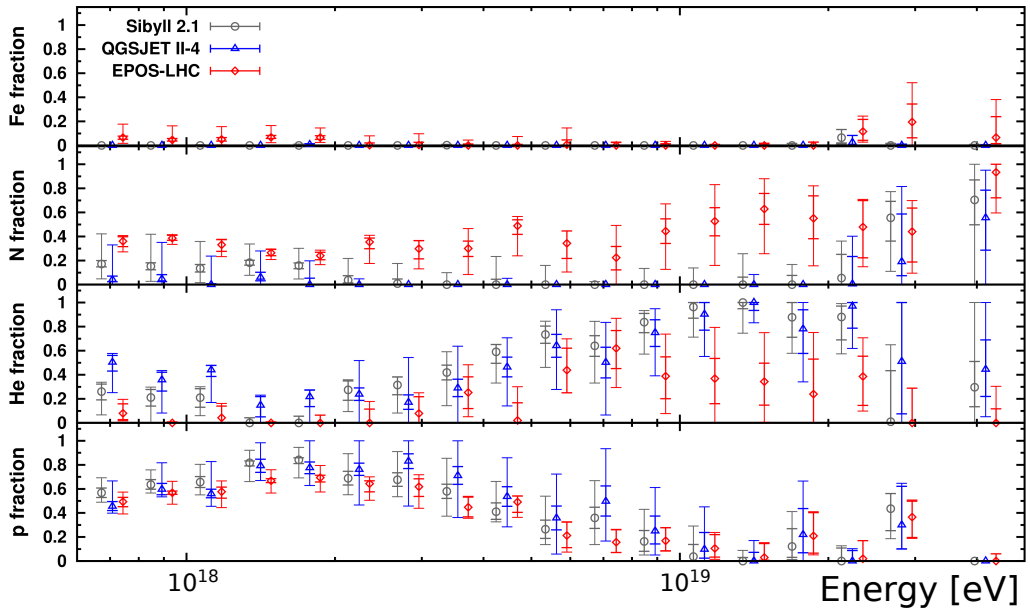

Figure 1.23: Fraction of different elements in UHECR composition as a function of the energy, obtained by fitting the $X_{\max}$ measurements using different hadronic models. Figure taken from [71].

generated by iron primaries. Additionally, the variation in muon content can be measured on the ground and used in combination with $X_{\max}$ measurements to investigate the UHECR composition as a function of the energy.

Using the hybrid mode of observation of EAS's, both Auger and TA have reported on the analysis of the $X_{\max}$ distributions [69, 70]. Results are shown in Figure 1.22. Auger measurements of $\langle X_{\max} \rangle$ point towards a chemical composition getting lighter up to 2×10^{18} eV with an elongation rate around 77 g cm^{-2} per energy decade below this energy and around 26 g cm^{-2} per energy decade above, hinting to a heavier composition in UHECRs of the highest energies. Moreover, up to the ankle energy, the $X_{\max}$ fluctuations reach a maximum, indicating a possible mixed composition of light elements, while they become less important as the energy increases above the ankle, revealing a less mixed composition and reinforcing the predominance of heavy nuclei expected from the $\langle X_{\max} \rangle$ measurements. On the other hand, measurements performed by TA seem to be best fitted by a mixed composition of $57\%, 18\%, 17\%, 8\%$ of proton, helium, nitrogen, and iron, respectively, between 1.6×10^{18} and 1.2×10^{19} eV. While the uncertainties on the $X_{\max}$ measurements allow the possibility of a break in the elongation rate, a constant elongation rate in this energy range cannot be excluded.

Because the two experiments analyze the $X_{\max}$ measurement with dif-

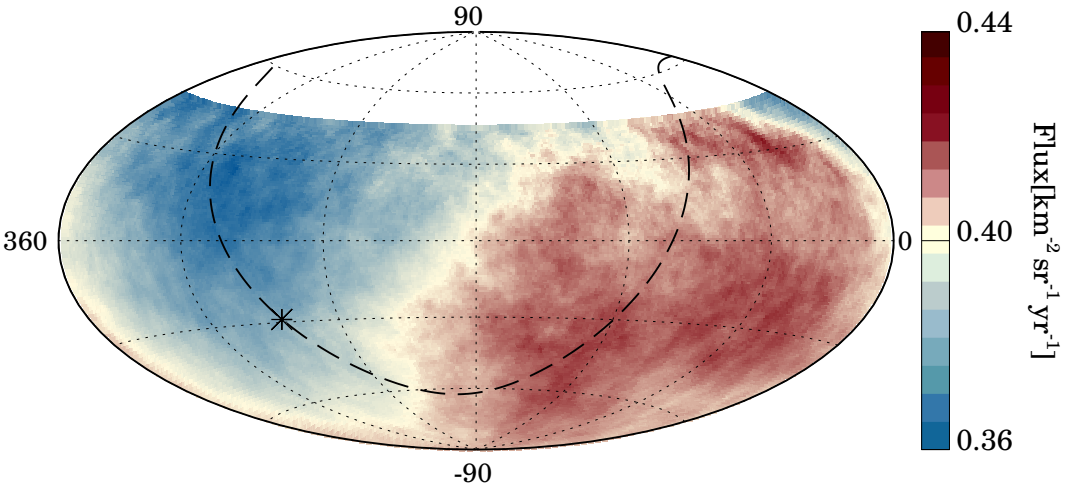

Figure 1.24: UHECR flux observed by Auger above 8 EeV. The Galactic plane is represented by the thick dashed line, and the Galactic center by the star. Figure taken from [51].

ferent methods, a direct comparison of the results is not possible. In order to overcome this issue, a joint group was formed by Auger and TA [72]. Using the different mass composition fits used by Auger to describe their $X_{\max}$ measurements, Monte-Carlo simulations based on these fits were performed and used as an input for the TA detectors response simulation. The group concluded on the compatibility of the results of the two experiments in the common energy band and within the systematic uncertainties.

Detailed studies of the composition measured by Auger were presented in [71, 73]. The main results, shown in Figure 1.23, can be interpreted as a composition mixture than tends to get heavier as the energy increases, helium and nitrogen being more predominant while the fraction of protons decrease past the ankle. None of the hadronic models considered seem to predict large fractions of iron in UHECR primaries. However, a significant number of data points have p-values below 0.1, which shows that the none of the combinations were able to fully reproduce the $X_{\max}$ distributions. The ongoing upgrades, allowing precise muon measurements and larger exposure, of Auger and TA described in Section 1.2 should shed more light on the composition of UHECRs and provide a better understanding of their sources.

1.3.3 Anisotropies

The existence of distinct features in the UHECR spectrum, such as the ankle or the cut-off, inevitably raises the question of their origin. However, the presence of strong magnetic fields in the path of propagation of UHECRs makes tracing back their exact source of emission non-trivial and the sources

of UHECRs are still enshrouded in mystery. Although very little deviation from isotropy has been observed around the ankle by Auger [74] and TA [75], evidences for anisotropies at higher energies and on different scales have been accumulating.

Searches for large-scale anisotropies have been performed by both experiments. In the case of Auger, a dipolar modulation with an amplitude of $\sim 6.6\%$ including events with energy above 8 EeV and zenith angle up to 80° was observed $\sim 125°$ away from the Galactic center (see Figure 1.24), hinting at an extragalactic origin [74, 76, 77]. Such result was confirmed by a joint group of Auger and TA collaborations in a full-sky search [78]. On the other hand, TA has reported on correlation between data with energy above 57 EeV and the Large Scale Structure (LSS) of the Universe, rejecting the isotropic distribution at a 3 sigma confidence level for smearing angles up to 30° [75, 79].

On intermediate scales, Auger has also looked for overdensities over the whole field of view [80]. An excess, in an angular window of 27° centered in the direction of the closest radio-galaxy, Centaurus A, was found at energies above 37 EeV, with a one-sided post-trial significance of 3.9σ. Additionally, searches for correlation between UHECR arrival directions and various catalogs of extragalactic objects, such as 2MRS [81], Swift-BATS AGNs [82] and the 3FHL of $\gamma-$AGNs [83], were performed [80, 84]. The maximum likelihood was found for starbust galaxies, at energies above 38 EeV, with a post-trial significance of 4.5σ. In the northern hemisphere, using 11 years of data acquisition, TA has observed a hot spot in a circle of 20° radius when considering events with energies above 57 EeV, with a significance of 2.9σ in an isotropic sky [85].

1.4 Propagation Effects

UHECRs traveling in the Galactic and intergalactic medium are affected by various physical interactions that may change their composition, their energy and their direction of propagation. While the surrounding magnetic fields are mostly responsible for the latter, UHECR interactions with photons have a stronger impact on the mass and the energy. In this section, the influence of these interactions on the UHECR nature and propagation is discussed.

1.4.1 Magnetic Deflection

One of the reason why it seems difficult to associate observed anisotropies with the position of known sources of various nature is tighly connected to the presence of magnetic fields along the path of propagation of UHECRs, resulting in a deflection of their direction and a delay of their time of arrival to Earth. As UHECRs may travel through environments of different nature

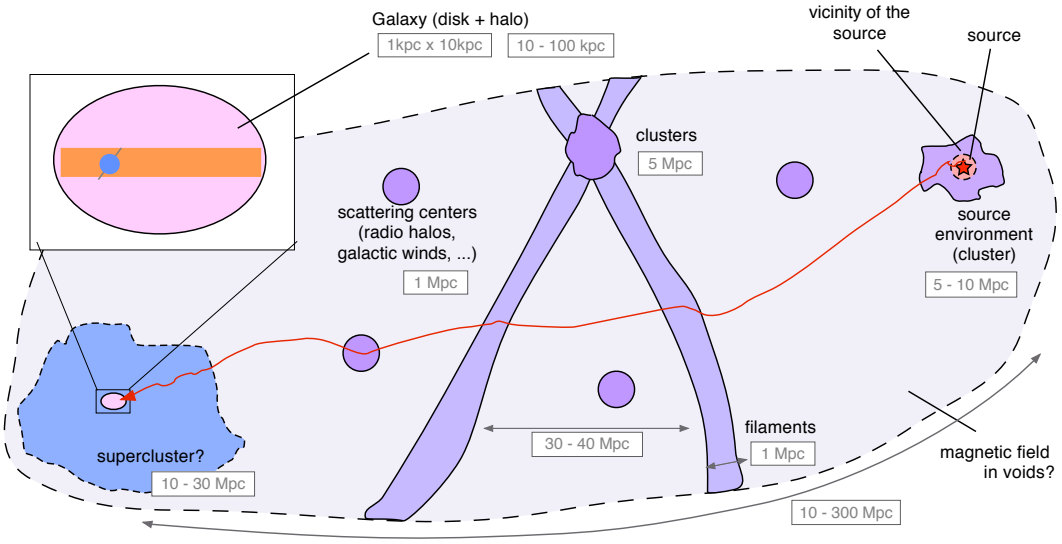

Figure 1.25: Schematic view of some of the sources of magnetic fields UHECRs may encounter on their way from their sources of emission to Earth. The characteristic size of these sources are given. Figure taken from [89].

(around the source, or in the intergalactic, Galactic and interstellar medium), the characteristics of the local magnetic fields may show great variations and major difficulties arise when trying to account for their effects on the UHECR measurements. The main argument in favor of the extragalactic origin of UHECRs comes from the typical value of their gyroradii, which is too high for them to be contained within our Galaxy. In general, particles with higher energy and smaller charge, i.e. larger rigidity, are less affected by magnetic fields. The Galactic magnetic field (GMF) is not uniform, therefore different directions of propagation induce different angular deflections [86]. While protons of several tens of EeV can be deflected by less than 10° while propagating in the GMF [87], 10^{18} eV protons tend to follow the GMF line [88]. Nevertheless, the influence of the GMF on the UHECR propagation remains weak, acting more like a smearing agent of the initial source and scattering particles at angles directly dependent of the particles rigidity.

The influence of the extragalactic magnetic field (EGMF) on UHECR propagation is more difficult to determine as the intergalactic medium is composed of clusters of galaxies, filaments and regions of void (see Figure 1.25). While its origin is still being debated – relic of the primordial Universe or astrophysical sources such as radio-jets or galactic winds [90, 91] – measurements of the Faraday rotation and of secondary emission from blazars have provided estimations of its strenght, ranging from 10^{-15} to 10^{-9} G with local peaks at few μG [92, 93]. The time of arrival, as well as the energy spectrum and the arrival direction of UHECRs are all affected by the EGMF [88, 94]. Indeed, the

increased pathlength can cause a delay of several thousands of years, making the search for correlations between gamma-ray/neutrino sources and UHECR detection particularly challenging. On the other hand, the reconstruction of UHECR arrival direction is directly linked to the inhomogeneity of the EGMF. While UHECRs propagating in weak fields ($< 10^{-12}$ G) are deflected by $\sim 1°$ [89], the angular deflection tends to increase when traveling through regions of stronger magnetic fields or considering the lower end of the UHECR energy spectrum. In a turbulent EGMF, the deflection angle θ experienced by an UHECR of energy E propagating over a distance D can be expressed as a function of the typical coherence length λ and magnetic field strength B of the EGMF [95, 96]:

$$\theta \simeq 0.025° \left(\frac{D}{\lambda}\right)^{1/2} \left(\frac{\lambda}{10\,\mathrm{Mpc}}\right) \left(\frac{B}{10^{-11}\,\mathrm{G}}\right) \left(\frac{E}{10^{20}\,\mathrm{eV}}\right)^{-2}. \tag{1.45}$$

Overall, the numerous magnetic fields encountered by UHECR strongly affect the measurements performed on Earth and the search for UHECR sources must take them into account. In this context, the multi-messenger approach searching for nearby gamma-ray and neutrino emissions constitutes a possible solution to the issues arising from the effects of these magnetic fields.

1.4.2 Greisen-Zatsepin-Kuzmin Effect and Photo-Nuclear Disintegration

UHECR path of propagation is steeped in a photon background of various components, such as the CMB and the infrared-ultraviolet background. While the former is the relic light of the recombination epoch (when first atoms were formed and the Universe became transparent to radiation), the latter is the signature of various physical processes occurring in stars, quasars and other astrophysical objects. As such, these components affect the energy loss of UHECRs as they propagate in the intergalactic medium. Protons interacting with the photon fields may produce pions or e^-/e^+ pairs (Bethe-Heitler process). The top panel of Figure 1.26 shows the energy loss length of protons at different energies from the described physical processes (see references in [89] for the photon background and associated energy losses functions). Above 50 EeV, the energy loss of protons is dominated by their interaction with the CMB, producing the GZK cut-off, resulting in the shortening of the propagation length of protons in the extragalactic medium. At the highest energies, protons reaching the Earth must therefore have been produced within a distance that is mostly defined by the GZK energy loss function (as shown in Figure 1.26, other processes contribute to the total energy loss of protons as well), i.e. in the local Universe.

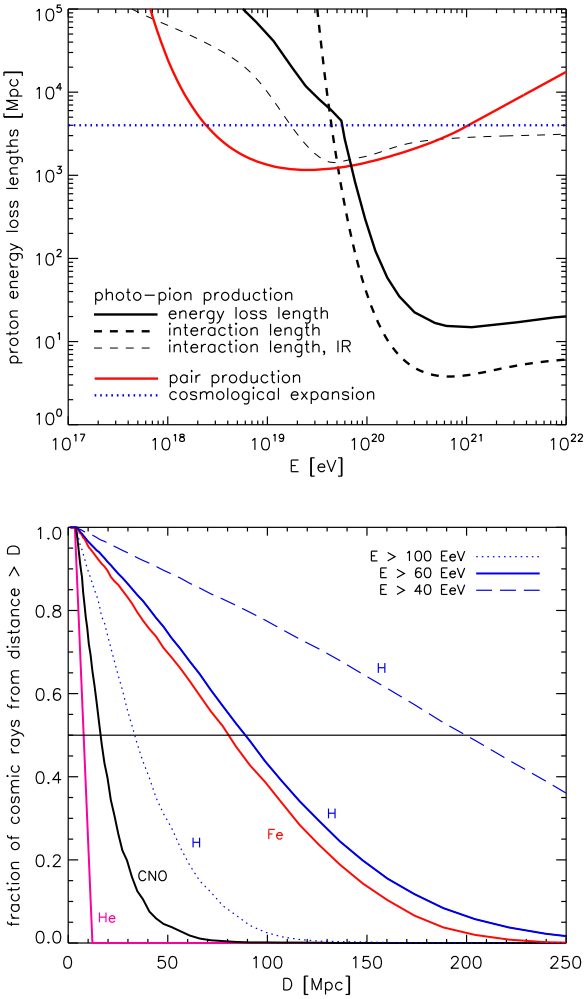

Figure 1.26: *Top*: Energy loss distance of protons as a function of the energy. Photo-pion production losses are shown for interactions with the CMB (thick-dashed line) and the IR photon background (thin-dashed line). Pair production is shown in red and horizon due to the Universe expansion is represented by the blue-dotted line. The total energy loss length is shown by the solid black line. *Bottom*: Fraction of various chemical elements that can propagate over a distance D. Protons are shown for energies above 40, 60 and 100 EeV while other elements are only shown for energies above 60 EeV. Figures taken from [89].

While UHE nuclei lose energy in the same interactions as protons, they may also undergo photodisintegration. In this scenario, a nucleus of mass A interacts with background photons to produce a nucleus of mass $< A$ and nucleons. Such effect is most significant for nuclei of intermediate masses. As the bottom panel of Figure 1.26 shows, iron nuclei may propagate on larger distances without being affected by photodisintegration [97, 98]. In other words,

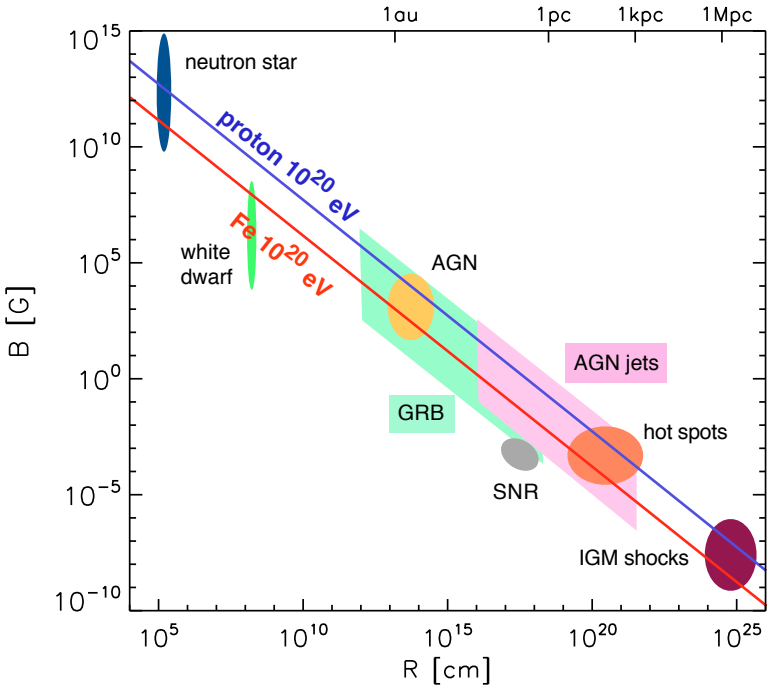

Figure 1.27: Hillas diagram: Characteristic magnetic field/size phase-space of potential sources of UHECRs. Sources above the blue (red) line can confine iron nuclei (protons) up to 10^{20} eV. Figure taken from [89].

nuclei of lower A tend to disintegrate at lower energies. Such feature can lead to an excess of iron nuclei in UHECR composition measurements.

1.5 Sources of Ultra-High Energy Cosmic Rays

As previously mentioned, the study of anisotropies in the arrival direction of UHECRs inevitably raises the question of the nature of their source of production. In this section, a short overview of the possible sources of UHECRs is presented, as well as the necessary conditions that must be met for UHECR production. The so-called *top-down* models, which predict the production of UHECRs from the decay of supermassive particles, are also discussed.

1.5.1 Astrophysical Objects

In order for astrophysical sources to be capable of accelerating cosmic rays to the highest energies, several conditions must be met. These conditions allow to select the list of potential candidate sources and provide a research focus

for correlations of source postions with anisotropies:

➢ The search for extragalactic sources of UHECRs is mostly motivated by the fact that the Larmor radius of UHECRs (several hundreds of kpc) is significantly larger than the characteristic size of our Galaxy (few kpc), preventing charged particles to be efficiently confined in order for them to be accelerated to the required energies. This condition can be summarized by the equation describing the maximal acceleration energy an astrophysical object can provide to a particle of charge Z, given its size R and its typical magnetic field strength B, and introduced in [68]:

$$E_{\max} \simeq 10^{15}\,\mathrm{eV} \times Z \left(\frac{B}{1\,\mu\mathrm{G}}\right)\left(\frac{R}{1\,\mathrm{pc}}\right). \tag{1.46}$$

Figure 1.27 shows the so-called Hillas diagram, a representation of the $B - R$ phase space in which various astrophysical objects are placed. Objects above the red line can accelerate iron nuclei up to 10^{20} eV, while the ones above the blue one, such as neutron stars, gamma-ray bursts (GRBs), active galactic nuclei (AGN) and intergalactic medium (IGM) shocks, meet the criterion to accelerate protons up to the same energy.

➢ Another key factor of the acceleration mechanism is the characteristic time t_{acc} it requires to accelerate particles to the energies of detected UHECRs. For obvious reasons, this time must be smaller than the age of the emitting source. It is also required that this time be shorter than the characteristic time of energy losses, mostly caused by interactions with the photon background, synchrotron emission and hadronic interactions. Finally, t_{acc} must be small enough for the accelerating particles to remain confined within the region of acceleration. As performed in [99], t_{acc} is compared to the dynamical time of the source in order to obtain the minimum magnetic luminosity required for acceleration of 100 EeV protons:

$$L_B > 10^{45} Z^{-2} \mathrm{erg/s}. \tag{1.47}$$

Such lower bound prevents Seyfert galaxies as well as TeV blazars from producing such energetic protons [100].

➢ One more requirement lies in the fact that the sources must have enough energy to be able to produce the UHECR flux observed on Earth, which is estimated around $5 \times 10^{43}\,\mathrm{erg\,Mpc^{-3}\,yr^{-1}}$. This criterion is met by most astrophysical objects, and especially transient sources such as GRBs [101] and AGN flares [102, 103].

1.5.2 Top-Down Models

The observation of UHECRs beyond the GZK cut-off, at energies sometimes above 10^{20} eV, presents a serious challenge to the paradigm that such particles gain their energy via acceleration mechanisms. As discussed in the previous section, the requirements on the properties of potential sources of UHECRs are quite stringent: most considered candidates for UHECR production can hardly reach the energies observed on Earth. When taking into account energy losses occurring in the source neighborhood and along the path of propagation, the likelihood that these sources may be responsible for these UHECRs drops even more. Several solutions to this issue can be compiled in the so called *top-down* models, which group all the scenarios where UHECRs are produced through the decay or the annihilation of a supermassive particle X. The details of these models are well beyond the scope of this thesis – extensive reviews can be found in [104, 105, 106] – and only the basic principles of some of these models are intoduced. Nevertheless, all these models must satisfy several conditions in order to be able to explain UHECR measurements.

- ➢ The lifetime of the X particles must allow them to decay at recent cosmological time.
- ➢ In order for the subsequent UHECRs to be able to reach Earth without suffering from significant energy losses, the X particles must be decaying in the local Universe.
- ➢ The X particles must be massive enough to produce UHECRs at the highest observed energies.
- ➢ The decay rate and the density of X particles must fit the observed flux of UHECRs.

One of the most discussed top-down model involving supermassive metastable particles is the Super-Heavy Dark Matter (SHDM) model [107, 108, 109]. Produced in the Early Universe in the inflationary epoch[4], these particles would compose a small fraction of the cold dark matter present in the galactic halo, with masses larger than 10^{12} GeV. Their long lifetime, allowing them to decay at present time, is expected to be due to discrete gauge symmetries and other possible physical effects [107, 108]. Nevertheless, the result of SHDM particle decay is a combination of UHE photons and protons, the former being the dominant component. The fact that SHDM particles are predicted to exist with the galactic halo, overdensities of UHECRs should be observed in the

[4]Several theories regarding the production of SHDM parrticles exist, involving vacuum fluctuations during the inflation [110] or cryptons from string models [111].

direction of the galactic center, in contradiction with the anisotropies searches performed by Auger and TA.

Among the existing top-down models, one can mention topological defects (TD), such as magnetic monopoles [112, 104] or cosmic strings [113]. Supposedly formed in the early Universe, their stability would allow them to survive until our cosmological epoch. However, collapses of these TDs, like monopole-antimonopole annihilation [114] or string collapse [113], may produce GUT-scale mass particles, which in turn may decay to leptons and quarks. Through a process referred as *fragmentation*, the quarks form jets of hadrons in the UHE domain, and leptons decay to photons and neutrinos [115].

Another top-down model that includes the production of UHECRs is the *Z-bust* model [116, 117]. In this scenario, UHE neutrinos produced in distant sources annihilate against the relic background neutrinos pervading the galactic and supergalactic halos, producing Z bosons. As these bosons decay, secondary protons, photons and neutrinos are generated. One may argue that such model does not solve the problem of the origin of UHECRs as UHE neutrinos are most likely produced through the interaction of UHECRs with the CMB. Nevertheless, such scenario does however solve the horizon problem that arises for very distant sources, as UHE neutrinos can travel freely through space before interacting with relic neutrinos, allowing UHECRs to reach the Earth without suffering significant energy losses in the process.

2. Ultra-High Energy Photons and Magnetic Cascades

Over the last two decades, UHECR measurements seem to have raised many more questions, especially at the highest energies, where the nature of UHECR sources remains an open problem. The cut-off observed by Auger and TA at $\sim 5 \times 10^{19}$ eV may originate either from the GZK effect or from maximum energy reached at acceleration sites. The deflection of UHECRs by magnetic fields in the extragalactic medium makes tracing them back to their original sources a difficult task. In the context of multimessenger astronomy, other particles carrying information about physical processes affecting UHECRs, such as UHE photons, may help identify these sources for two main reasons. First of all, their direction of propagation is unaffected by magnetic fields and therefore one can retrace their source of production with greater precision. As seen in the previous chapter, UHE photon emission is also associated with various physical processes related to UHECRs, from production (top-down models) to propagation (GZK effect). Moreover, detection of UHE photons would allow to test Lorentz invariance violation (LIV) models by searching for time delays between photons of different energies [118, 119], as illustrated by the recent lower limits on the LIV energy scale set by the MAGIC collaboration and resulting from the observation of TeV gamma rays from GRB190114C [120, 121].

Independently of the source of production, UHE photons propagating through magnetic fields can produce pairs of e^-/e^+ which subsequently radiate synchrotron radiation. The probability of such phenomenon to occur raises with the energy of the primary. It is therefore possible to consider that electromagnetic cascades may reach the Earth instead of single UHE photons. The characteristics of such cascades depends on the distance at which they were produced and on the energy of the UHE photon primary. The probability for pair creation also depends on the direction of propagation, as the transverse component of the considered magnetic fields plays a major role in both pair creation and synchrotron emission. In this chapter, the general properties of UHE photons, and the characteristics of the EAS's they produce, are reviewed. Then, the latest results of searches for diffuse and point sources of UHE photons by Auger and TA are discussed. In the second part, the underlying mechanisms of electromagnetic showers produced in magnetic fields are highlighted and two examples found in the literature are examined: in the geomagnetic (also called **preshower effect**) and solar magnetic fields.

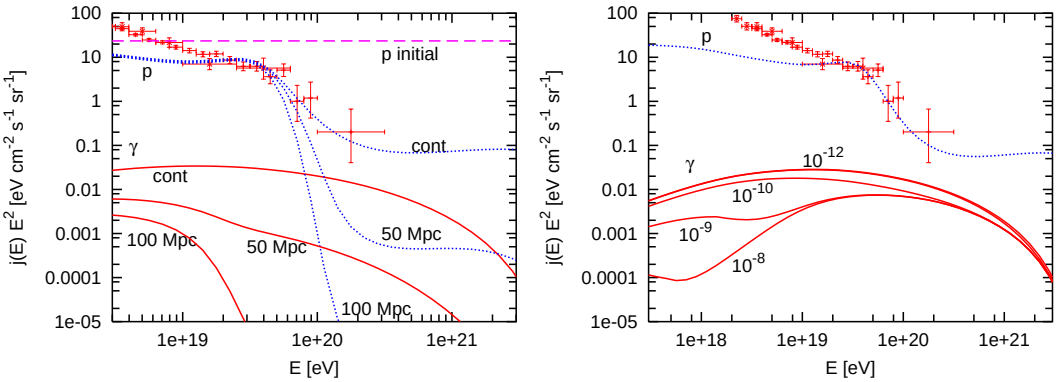

Figure 2.1: *Left*: Flux of UHE photons (red lines) as a function of the energy and the minimal distances to the sources. The UHECR proton flux (blue dotted lines) is normalized to HiRes data (red crosses) [124] at 4×10^{19} eV and described by a spectral law $\propto E^{-2}$. The dashed pink line represents the initial proton flux. *Right*: Flux of UHE photons (red lines) as a function of the energy and of the strength of the EGMF in Gauss. Figures taken from [106].

2.1 Ultra-High Energy Photon Flux

Observing UHE photons and assessing their fraction in UHECRs would be a step forward in our understanding of the Universe in the UHE domain and could act as a discriminating factor regarding the origin of UHECRs. Such endeavor was undertaken in [106], where the fluxes of UHE photons expected from the GZK effect and from various top-down models were compared. In the former case, a dependence was observed on the UHECR spectrum, as the UHE photon flux increases with the maximum energy at the source and for smaller spectral indices; on the minimal distance to the sources, as most UHE photons are expected to be emitted within 100 Mpc (see left panel of Figure 2.1); on the radio background, as higher background increases energy losses of UHE photons through pair creation; and on the EGMF, as larger values of the EGMF induces lower fluxes of UHE photons (see right panel of Figure 2.1). On the other hand, all the top-down models considered in that study (TDs, Z-burst and SHDM) produce UHE photon fluxes that are significantly larger or comparable to the flux generated by the GZK effect. Using data from Auger [122], AGASA and Yakutsk arrays [123], upper limits on the UHE photon flux already severely constrain top-down models as the source of UHE photons and by extension, of UHECRs.

Measuring the UHE photon flux would also allow to investigate the mass composition of UHECRs as different fractions are expected for different primary mixes [125, 126]. In the presence of a photon background, UHE protons produce neutral and charged pions whose decay generates a flux of UHE pho-

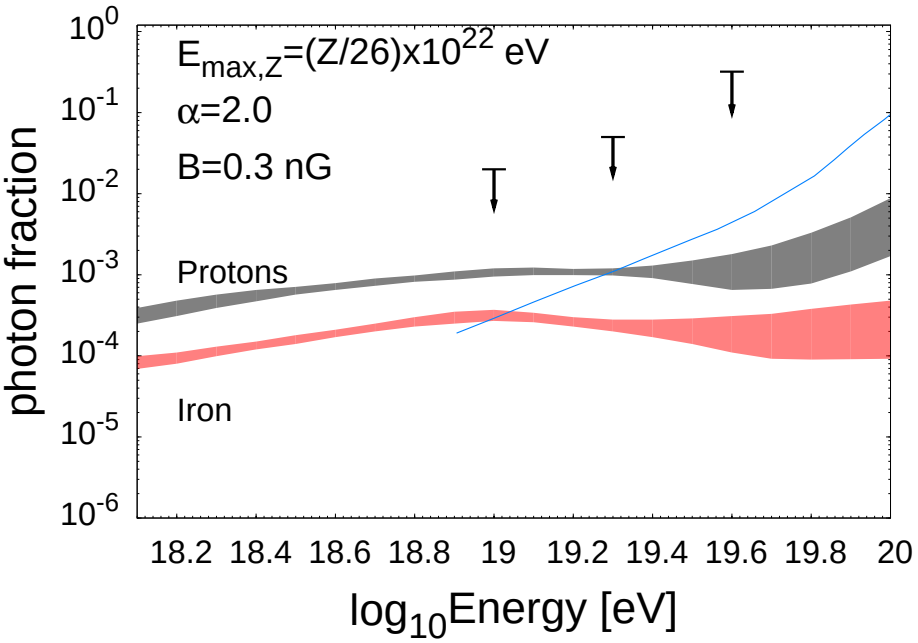

Figure 2.2: Expected photon fraction for pure proton (grey) and iron (red) compositions. The injection spectrum of UHECRs is taken such as the spectral index is $\alpha = 2$ and the maximun energy is such that $E_{\mathrm{max,Z}} = (Z/26) \times 10^{22}$ eV, where Z is the atomic number. 2009 upper limits from Auger are also displayed [127], and its ultimate reach is shown by the thin blue line. Figure taken from [125].

tons, while heavy nuclei such as iron, mainly disintegrate to lighter nuclei and nucleons of smaller energy. Consequently, a smaller flux of UHE photons is expected if UHECRs are mostly composed of heavier nuclei (about one order of magnitude lower than if UHECRs are protons - see Figure 2.2). In [125], it was also noted that the presence of sub nano-Gauss EGMFs resulted in a smaller expected flux of UHE photons, in agreement with [106].

Accurate modelisation of the production and the propagation of UHE photons is a key factor in the estimation of the flux observed on Earth. Codes such as CRPropa [128] allow to include multiple production channels and propagation effects that seem to increase the photon horizon for sub nano-Gauss EGMFs. However, one important factor limiting our understanding of the UHE photon flux lies in the inaccuracy of the mapping of EGMFs and photon backgrounds, making the reduction of the uncertainties on the UHE photon fraction and flux a challenging tast. Such a mapping would in fact greatly benefit from UHE photon observation and could significantly constrain parameters of the extragalactic background and to some extent, their origin.

2.2 Extensive Air Showers produced by Ultra-High Energy Photons

The development of air showers initiated by UHE photons is governed by three main physical effects [129]. The Landau-Pomeranchuk-Migdal (LPM) effect [130, 131, 132] is the reduction of the Bethe-Heitler cross-section for pair production and bremsstrahlung emission due to destructive interferences between multiple scattering sites. The major consequences of such an effect are the slow-down of the cascade development, as fewer interactions occur, and a higher mean $X_{\max}$. Secondly, photo-nuclear interactions, although largely dominated by electromagnetic processes, are responsible for the production of muons, as previously discussed in Section 1.1.2 of Chapter 1. Nevertheless, it is important to note that $X_{\max}$ and muon content values depend on the extrapolation of photo-nuclear interactions to the highest energies [133], leading to large uncertainties for both observables, and consequently to the proper identification of primaries. The third important effect is the preshower effect, which describes the conversion of an UHE photon to a pair of e^-/e^+ after interacting with the geomagnetic field [134]. The pair radiates synchrotron photons, and a collection of lower energy electromagnetic particles reaches the top of the atmosphere. Each one of these particles produce its own air shower but due to the resolution of UHECR experiments, they are indistinguishable from each other. Another consequence of such effect is that $X_{\max}$ tend to reach smaller values, making the air shower more similar to the ones initiated by nuclei. On the other hand, EAS's that are produced by UHE photons and that have converted in the geomagnetic field, do not display a significantly different muon content from the ones produced by unconverted photons [135]. More details about this particular effect are given in Section 2.4.2.

The impact of the LPM and the preshower effects is well illustrated by the fitting of the longitudinal profile of the 3.2×10^{20} eV event observed by the Fly's Eye experiment [136], including or not these effects [137], and shown in Figure 2.3. When only the LPM effect is accounted for, the cascades reach their maximum closer to the ground. On the other hand, when both effects are taken into account, the shapes as well as the peaks of the longitudinal profiles are much more similar to the data of the Fly's Eye event. Therefore, when searching for UHE photons in existing data using Monte-Carlo simulations, both LPM and preshower effects must be included in order to prevent a misidentification of the primary if the muon content of the shower is not available.

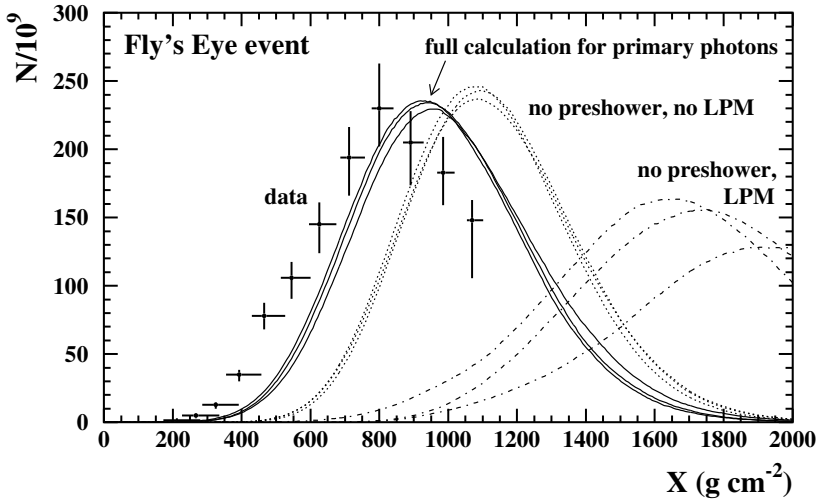

Figure 2.3: Longitudinal profiles obtained for the Fly's Eye event reported in [136], taking into account the LPM and the preshower effects (solid lines), only the LPM effect (dashed line) and none of the effects (dotted line). Figure taken from [137].

2.3 Searches for Ultra-High Energy Photons with Cosmic-Ray Experiments

Searches for UHE photons have been performed by multiple experiments and are the subject of constant updates, as more data is collected and finer analyses are performed. In this section, the latest results published by Auger and TA regarding the diffuse emission of UHE photons, as well as their search for point sources, are highlighted.

2.3.1 Diffuse sources

Thanks to the large exposure accumulated by both Auger and TA, a statistical approach to the search of UHE photons in the collected data can be carried out. Using almost 15 years of data, Auger has been able to put stringent upper limits on the integral diffuse UHE photon flux above 10 eV [138]. In their analysis, events recorded by the SDs with zenith angle $30° < \theta < 60°$ are considered. In order to prevent uncertainties due to hadronic models, only EAS's produced by photons are simulated. The background sample is obtained by using a subset of 2% of the data, that is then discarded. The observables used to discriminate between UHE photons and UHE nuclei are the LDF (see Section 1.2.1 of the previous chapter) and the risetime of the signal in all trig-

gered stations. In general, EAS's produced by UHE photons are expected to have a steeper LDF, i.e. weaker signal at larger distances from the shower core, and slower risetime, due to dominating electromagnetic component compared to muons. After applying a selection cut such that 50% of the simulated UHE photons passes the cut, 11 events in the data are found above the threshold. Upper limits at 95% C. L. are derived and show a significant improvement at the highest energies due to the large exposure. These limits are plotted in Figure 2.4, along with the ones at lower energies (< 10 EeV), where $X_{\max}$ measured with the FDs are used as an discrimination parameter.

In a similar analysis, TA performed a search for the evidence of a diffuse UHE photon flux in 9 years of data [139]. Monte-Carlo simulations for both photons and protons above 10^{18} eV were run, with the photon spectrum being the same as the one from Auger previously described ($\propto E^{-2}$) and the zenith angle range extending from 0° to 60°. 16 parameters, including the ones used in Auger analysis, as well as the number of triggered stations and the shower front curvature, were used as discriminating variables in a multivariate analysis aimed at obtaining the best photon/proton separation. The distributions of the resulting estimator for the simulated photon and proton samples are then compared to the data. No photon candidates are found at energies above $10^{18.5}$, 10^{19} and $10^{19.5}$ eV while one candidate is found above 10^{18} eV and 10^{20} eV, which is compatible with background expectations (having a photon-like shower in Monte-Carlo simulations of protons). Consequently, upper limits at 95% C.L. are derived for these energies and plotted in Figure 2.4.

The results shown in Figure 2.4 are compared to the prediction from various UHE photon production models that were previously described. As one can notice, top-down models are severaly constrained by the limits set by Auger and TA, while the observation of cosmogenic photons from the GZK effect seems to be finally within range for both experiments.

2.3.2 Point Sources

The horizon of UHE photons is limited to a few Mpc due to energy loss processes on photon backgrounds. Therefore, if UHE photons are the results of the interaction of UHECRs with their surrounding environment (intergalactic/interstellar medium or photon background) in the vicinity of their source of production, searches for point sources of UHE photons can be performed by cross-correlating observed UHECR directions with catalogs of astrophysical objects suspected to be sufficiently energetic to produce these UHECRs. Such strategy was adopted by Auger using 8 years of data recorded in hybrid mode of observation, and with energy between $10^{17.3}$ eV and $10^{18.5}$ eV [142]. The arrival directions of the events contained in the data is compared to the cat-

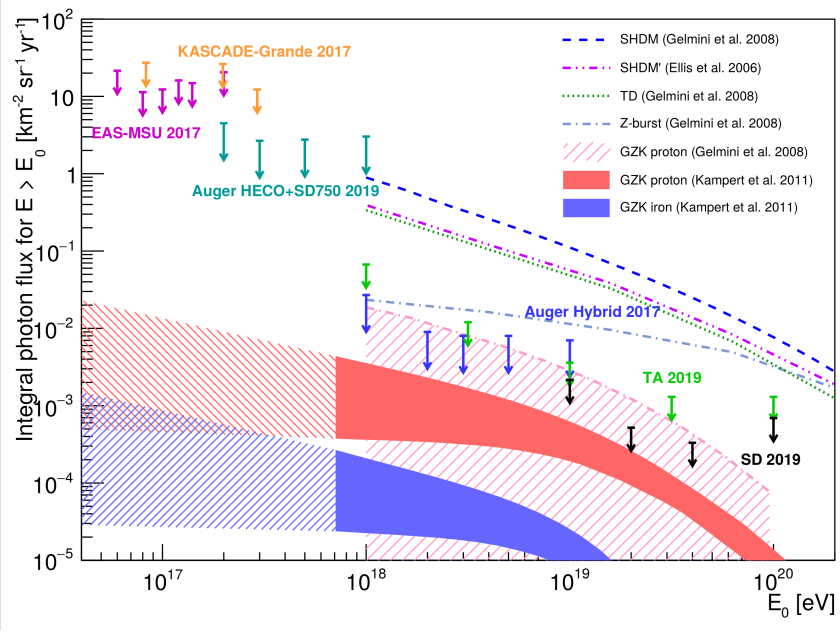

Figure 2.4: Upper limits on the diffuse UHE photon flux at 95% C.L. put by TA [139] (green) and Auger [138] (black and blue), and at 90% C.L. by EAS–MSU [140] (purple) and KASCADE-Grande [141] (orange) at lower energies.Predictions on the UHE photon flux from the GZK effect involving protons and iron nuclei [106, 126] as well as from top-down models such as SHDM, TD and Z-burst [106, 111] are also displayed. The values for the SHDM model, the GZK emission and Auger limits at 40 EeV, expressed in $\mathrm{km}^{-2}\mathrm{yr}^{-1}\mathrm{sr}^{-1}$, are 2.7×10^{-2}, 4.1×10^{-4} and 3.4×10^{-4}, respectively. Figure taken from [138].

alogs of 12 classes of Galactic and extragalactic objects such as low-mass and high-mass X-ray binaries, pulsar wind nebulae, the Large Magellanic Cloud, the Galactic center and the core region of Centaurus A. In total, more than 360 potential sources of UHE photons are included in the analysis. No significant excess is found for any of the considered sources, and upper limits are set on each of the analyzed classes of objects. The study concludes that one possible interpretation of the results is that UHE photons could in fact be produced by transient sources such as flares of GRBs or AGN, that are not included in this work. Nevertheless, it is also possible that EeV photons are in fact produced by more distant sources and that the subsequent UHE photon flux is supressed through energy loss processes.

Using the same data set and the same Monte-Carlo simulations as in their search for a diffuse flux of UHE photons, TA performed a blind search for point sources of UHE photons for energies greater than 10^{18}, $10^{18.5}$, 10^{19}, $10^{19.5}$ and 10^{20} eV [143]. No evidence for photon signal was found and photon-flux upper limits are set at all considered energies. These limits are conservative, due to the fact that pure proton composition is assumed in the Monte-Carlo

simulations, and to the possible overestimation of the energy attibuted to recorded events. Although the limit set above 10^{18} eV is about three times higher than Auger [142], the larger energy range studied allows to put UHE point-source photon-flux upper limits above $10^{18.5}$ eV for the first time.

2.4 Photons Cascading in Local Magnetic Fields

Photons propagating through space may, under certain conditions, produce electromagnetic showers without the need of matter to interact with. As described in [144], photons have a non-zero probability to convert to pairs of e^-/e^+ if traveling with sufficient energy ($h\nu \gtrsim 2m_e c^2$, where h is the Planck constant, ν is the frequency of the photons, m_e is the mass of the electron and c is the speed of light in vacuum) in intense magnetic fields. Such probability is an increasing function of the parameter

$$\chi \equiv \frac{1}{2}\left(\frac{h\nu}{m_e c^2}\right)\left(\frac{B_{\rm tr}}{B_q}\right), \tag{2.1}$$

where $B_{\rm tr}$ is the strength of the magnetic field component transverse to the direction of the photons and $B_q \equiv m_e^2 c^3/e\hbar$, with e the charge of the electron and $\hbar$ the reduced Planck constant, is the natural quantum mechanical measure of the magnetic field strength. It can be expressed as a function of the photon attenuation coefficient

$$\alpha_\gamma(\chi) = \frac{1}{2}\left(\frac{\alpha_s}{\lambda_e}\right)\left(\frac{B_{\rm tr}}{B_q}\right)T(\chi), \tag{2.2}$$

where α_s is the fine structure constant, $\lambda_e = (h/m_e c)$ is the Compton wavelength of the electron and $T(\chi) \simeq 0.16\chi^{-1}\kappa^2_{2/3}(2/3\chi)$ is a dimensionless function of the modified Bessel function $\kappa_{2/3}$. It is interesting to note that for a given primary photon energy, this coefficient increases with the strength of the local magnetic field, but that for a given field strength, $\alpha_\gamma(\chi)$ peaks at a maximum photon energy defined as $h\nu_{{\rm max},\gamma} = 12(B_q/B_{\rm tr})m_e c^2$. Finally, over a distance of propagation R, the conversion probability can be written as

$$P_{\rm conv}(R) = 1 - \exp[-\int_0^R \alpha_\gamma(\chi) dl]. \tag{2.3}$$

Because of their opposite charge, the electron and the positron travel in opposite directions.

As the newly created e^-/e^+ pair propagates through the same local magnetic field as the primary photon, it may produce secondary bremsstrahlung

radiation under certain conditions. Analogously to the parameter χ of the magnetic pair production phenomenon, the emission probability as well as the spectral distribution of the radiation emitted per unit distance are governed by the parameter

$$\Upsilon \equiv \left(\frac{E_e}{m_e c^2}\right)\left(\frac{B_{\mathrm{tr}}}{B_q}\right), \tag{2.4}$$

where E_e is the energy of the electron. For primary photons in the ultra-high energy domain, the e^-/e^+ pair carries an energy such that $E_e \gg m_e c^2$. Under the assumption that the energy of the bremsstrahlung photons is significantly lower than the energy of the electron and the positron ($h\nu \ll E_e$), [144] defines the bremsstrahlung spectral distribution as

$$I(E_e, h\nu, B_{tr}) = 0.517\alpha_s \left(\frac{m_e c^2}{\lambda_e}\right)\left(\frac{\Upsilon^{2/3}}{E_e}\right)\left(\frac{h\nu}{E_e}\right)^{1/3}\left(1 - \frac{2}{3}\frac{h\nu}{E_e}\right). \tag{2.5}$$

For a given energy E_e and magnetic field strength B_{tr}, the bremsstrahlung emission peaks at $h\nu_{\mathrm{peak}} = E_e[3\Upsilon/(2+3\Upsilon)]$. As the e^-/e^+ pair loses energy via this emission process, the emission peak shifts towards lower values. The probability of an electron to emit a photon between energy $h\nu$ and $h\nu + d(h\nu)$ over a distance dx can be written as a function of the bremsstrahlung spectral distribution, such as

$$P_{\mathrm{brem}}(E_e, h\nu, B_{\mathrm{tr}}, dx) = dx \int_0^{E_e} I(E_e, h\nu, B_{\mathrm{tr}}) \frac{d(h\nu)}{h\nu}. \tag{2.6}$$

Equations 2.1 to 2.6 show a strong dependence of these magnetic processes to the strength of the local magnetic field. In the UHE domain, the relatively low intensity of the Sun's and the Earth's magnetic fields is compensated by the high energy of the primaries and therefore, probabilities for magnetic processes are high enough to generate electromagnetic cascading in their vicinity. In the following sections, the cases for which the local magnetic field corresponds to the one of the Sun and of the Earth, are discussed.

2.4.1 In the Solar Magnetic Field

As UHE photons travel near the Sun, they may initiate electromagnetic cascades if experiencing a strong enough magnetic field component transverse to their direction of propagation (see Figure 2.5 (left)). For a typical solar magnetic field intensity of 3 G, all primary photons with energy above 10^{19} eV convert to an e^-/e^+ pair if injected within a circle of radius $R_{\mathrm{inj}} = 1.5R_\odot$ centered on the Sun, with $R_\odot$ being the radius of the Sun [145]. This impact

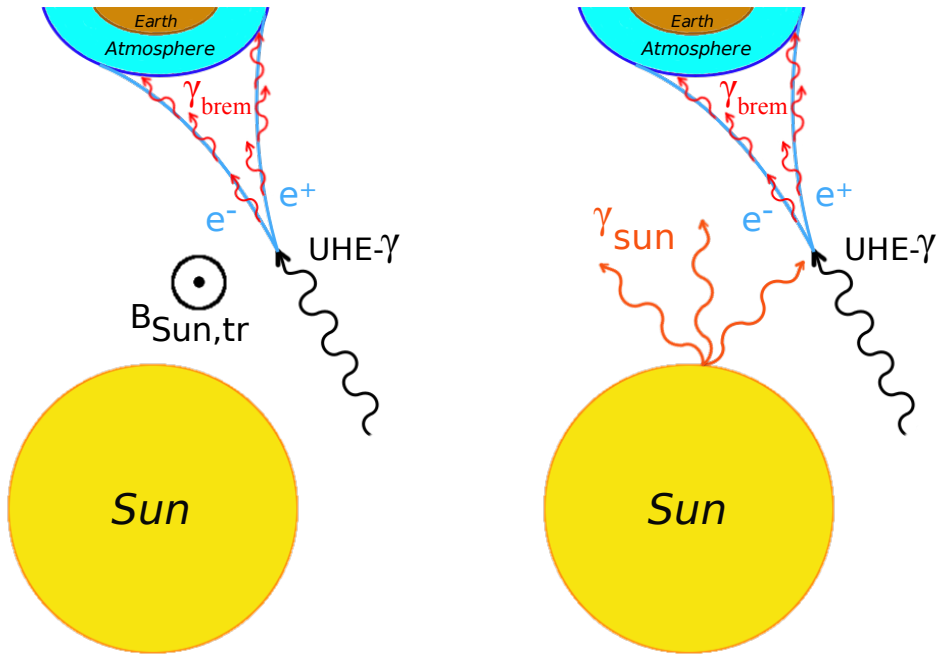

Figure 2.5: *Left*: Schematic view of an UHE photon interacting with the transverse component of the Sun's magnetic field to produce a pair of e^-/e^+ radiating bremsstrahlung photons. *Right*: Same as on the upper panel but in this scenario, the UHE photon is interacting with the solar photons.

parameter for 100% conversion can rise up to $R_{\rm inj} = 3R_\odot$ when considering photons with energies above 10^{20} eV. Although the rate of such events is expected to be rather small (only a few per decade), the deflection of the e^-/e^+ pair in the solar magnetic field, and the subsequent bremsstrahlung radiation produced may display a very peculiar spatial signature at the top of the Earth's atmosphere. In [145], Bednarek reports a collection of secondary photons in the shape of very prolate ellipse that can reach tens of kilometers in size, with the photons of highest energy concentrated in its core.

More recently, extensive simulations of UHE photons cascading in the Sun's vicinity were performed by considering two different modelizations of the solar magnetic field [146]: the simple dipole model and the dipole-quadrupole-current-sheet (DCQS) model [147]. Different impact parameters $R_{\rm inj}$, as well as several photon primary energies E_γ, were investigated. Probabilities for the primary photon to convert into an e^-/e^+ pair, and for the pair to emit bremsstrahlung radiation, are calculated using Equations 2.3 and 2.6, respectively. The top panel of Figure 2.6 shows the probability for an UHE photon of energy E_γ to convert into an e^-/e^+ pair as a function of $R_{\rm inj}$. While photons with energy $E_\gamma = 10$ EeV have 100% chance to convert if injected within $R_{\rm inj} = 2R_\odot$, photons with $E_\gamma = 100$ EeV have a conversion probability close

to unity if injected within $R_{\rm inj} = 4R_{\odot}$, therefore offering a search area for such phenomenon 16 times larger than the apparent size of the Sun viewed from Earth. Because the gyroradius of the electron and the positron is much larger than the distance along which they experience the solar magnetic field, the propagation of the electron and the positron can be assumed to occur in the same plane. The subsequent bremsstrahlung radiation emitted by the pair is produced in the direction of the e^-/e^+ propagation and in the vicinity of the Sun. The size of the footprint of the electromagnetic cascade when reaching the top of the Earth's atmosphere, as a function of the impact distance of the first conversion, and of the helicentric latitude of the UHE photon incident direction is shown on the bottom panel of Figure 2.6. As expected, the size of the footprint is a decreasing function of the impact distance: the further away from the Sun, the weaker the magnetic field experienced by the e^-/e^+ and therefore, the smaller the deviation of its trajectory, resulting in a smaller spatial distribution of the bremsstrahlung radiation.

Examples of footprint sizes for a 100 EeV photon primary are shown in Figure 2.7. For both solar magnetic field models, one can note the extended spatial distribution of the electromagnetic cascade that can reach up to several thousands of kilometers. As previously found in [145], the secondary photons with the highest energy are concentrated within the center of the distribution, i.e. the location the primary photon would have reached if it had not converted.

The energy range covered by the secondary photons spans over several orders of magnitude, from EeV down to MeV energies. Therefore, experiments observing at different wavelengths may be capable of observing the same electromagnetic cascades due to the extended nature of the footprint at the top of the Earth's atmosphere. Nevertheless, cosmic-ray detector arrays, such as Auger, should observe roughly 0.2 events per year from the direction of the Sun and with energy above 10 EeV. Therefore, taking into account the UHE photon production models discussed in the previous section, as well as the current limits put by Auger on the diffuse photon flux in the EeV domain, the number of expected events as described in this section remains very small.

In [148], photon cascades produced by photon-photon interactions are also presented in the context of UHE photons interacting with photons from the Sun (see right panel of Figure 2.5). By defining the probability of such process to occur as

$$P_{\gamma-\gamma} = n\,\sigma\,dx, \tag{2.7}$$

where n is the volume density of the solar photons, σ is the cross section for photon-photon interaction and dx is the path along which such interaction may occur. Using Planck's law of black bodies to determine the solar flux and assuming that every solar photon is emitted in the direction perpendicular to

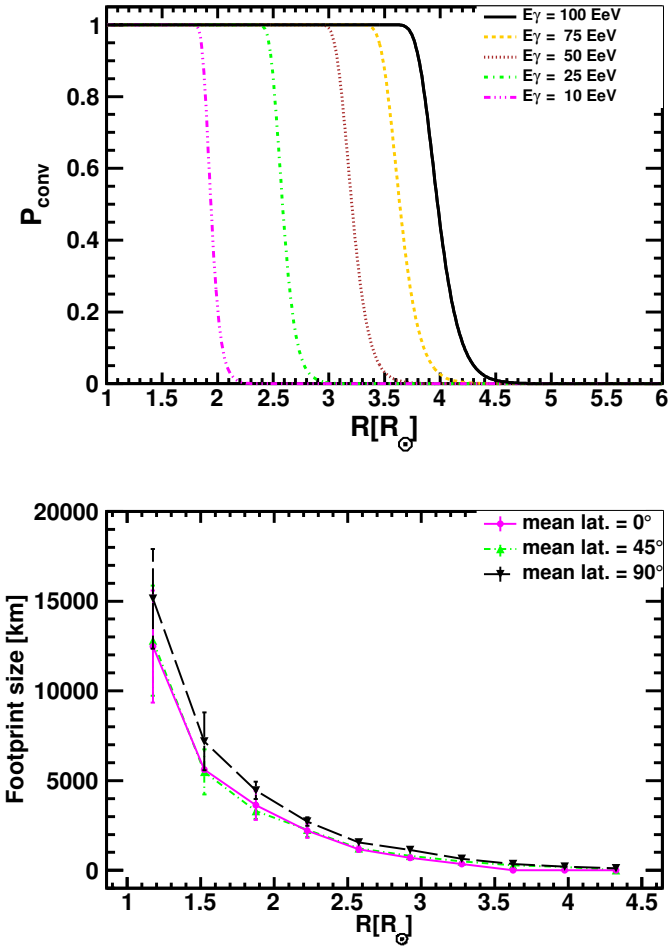

Figure 2.6: *Top*: Probability of an UHE photon with energy E_γ to convert into an e^-/e^+ pair in the solar magnetic field, as a function of the impact parameter. *Bottom*: Size of the electromagnetic shower at the top of the Earth's atmosphere generated by a primary photon of energy 100 EeV and taking into account secondary photons with energy higher than 1 TeV, as a function of the impact parameter and of the heliocentric latitude of the primary photon direction. Figure taken from [146].

the surface of the Sun, n is defined by the equation

$$n = \frac{1}{4\pi s^2}\frac{8\pi^2\nu_\odot^2}{c^3}[\exp(\frac{E_\odot}{k_B T_\odot} - 1)]^{-1}, \tag{2.8}$$

where s is the distance between the solar photon and the center of the Sun, $E_\odot = h\nu_\odot$ is the energy of the solar photons, k_B is the Boltzmann constant and $T_\odot = 5778$ K is the temperature at the surface of the Sun. The $1/(4\pi s^2)$ factor describes how the volume density decreases as the distance from the Sun

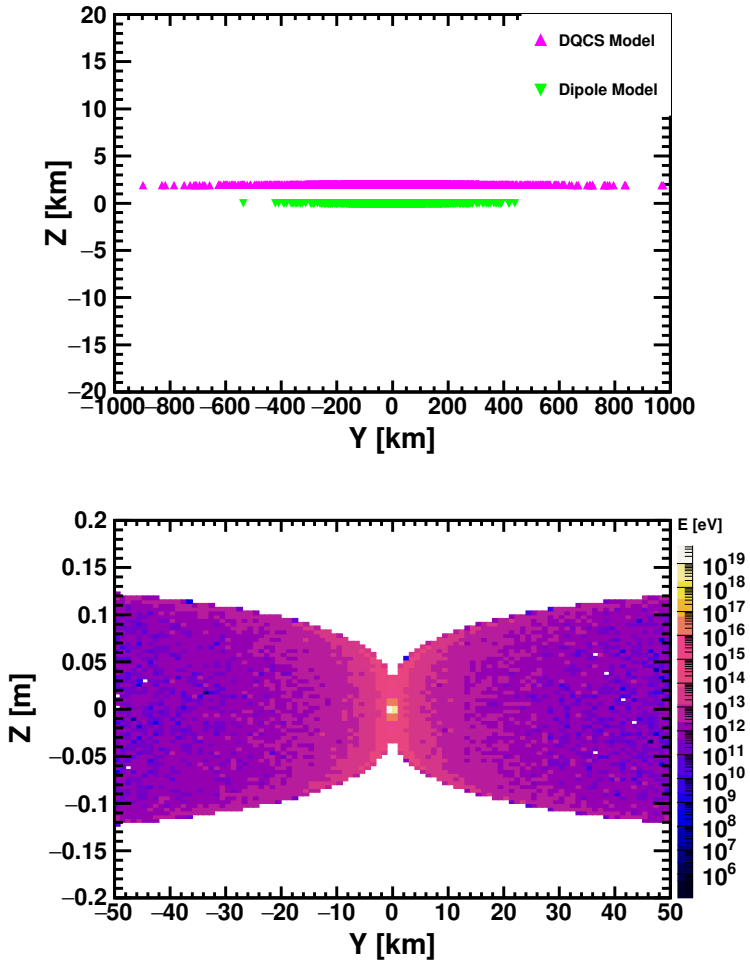

Figure 2.7: *Top*: Size of the footprint of an electromagnetic cascade on the top of the Earth's atmosphere produced by a 100 EeV primary photon with an heliocentric latitude of 0° for the two different solar magnetic field models and for $R_{\rm inj} = 3R_{\odot}$. Only photons with energy above 1 TeV are marked. *DQCS* footprint was shifted by 2 km in the positive z-direction for visual purposes. *Bottom*: Same plot as on the left but zoomed in on the core of the cascade and weighted by the energy of the secondary photons. For both plots, $x = 0$ and $y = 0$ correspond to the impact position of the primary photon if no magnetic conversion had occured. The positive z-direction points to the North while the positive y-direction points to the East. Figure taken from [146].

increases. The cross-section can be expressed using the equation from [149]:

$$\sigma = \frac{\pi}{2} r_e^2 (1 - v^2)[(3 - v^4) \log\left(\frac{1+v}{1-v}\right) - 2v(2 - v^2], \tag{2.9}$$

where r_e is the classical electron radius and $v = (\frac{E_\gamma E_\odot - m_e^2}{E_\gamma E_\odot})^{1/2}$, with E_γ the

energy of the UHE photon. By considering the UHE photon propagating along the direction defined by the Sun-Earth vector, one can write $dx = ds$. The photon-photon interaction can thus be written as:

$$P_{\gamma-\gamma} = \int_{s_0}^{s_1} ds \int_{\frac{m_e^2c^4}{E_\gamma}}^{\infty} n(s, E_\odot)\sigma(E_\odot)dE_\odot \tag{2.10}$$

$$= \frac{(\pi r_e R_\odot)^2}{(hc)^3}\left(\frac{1}{s_0} - \frac{1}{s_1}\right) \times \int_{\frac{m_e^2c^4}{E_\gamma}}^{\infty} (1-v^2)\left[(3-v^4)\log\left(\frac{1+v}{1-v}\right) - 2v(2-v^2)\right]\frac{E_\odot^2}{\exp(\frac{E_\odot}{k_B T_\odot}) - 1}dE_\odot, \tag{2.11}$$

for solar photons with energy such as $E_\odot \geq (m_e^2c^4)/E_\gamma$ and UHE photons propagating from s_0 to s_1. The calculation of the integral over $E_\odot$ has been performed numerically for solar photons with energies smaller than 10 eV, and for UHE photons between 10^{16} eV and 10^{20} eV propagating from an infinite distance ($s_0 = \infty$) to Earth $s_1 = -1$ AU , along the direction defined by the Sun-Earth vector [148]. Under these conditions, the probability $P_{\gamma-\gamma}$ for an UHE photon to produce an e^-/e^+ pair through its interaction with a solar photon does not go over 10^{-8}. Therefore, such a process can be excluded as a potential scenario for photon cascades.

2.4.2 In the Geomagnetic Field - The Preshower Effect

UHE photons propagating in the geomagnetic field can undergo similar magnetic processes (see Figure 2.8). For photons incident in the plane of the magnetic equator, magnetic pair production becomes significant for photons with energies above 5×10^{19} eV and occurs within 3 Earth's radii for photons with energies up to 10^{22} eV [134]. Moreover, larger values of the angle of incidence θ result in larger intensity of the transverse component of the geomagnetic field and such process becomes significant for large zenith angles [150]. Before reaching the top of the atmosphere, the newly created leptonic pair must travel through several radiation lengths, which leads to the emission of bremsstrahlung photons and the production of an electromagnetic cascade, constituted of the initial e^-/e^+ pair and of several lower energy photons. Such type of cascade is referred to as *preshower*, and has been studied early on in the context of various experiments [151, 152, 145]. By contrast with the fact that such cascade fully develops in the Sun's vicinity when the primary photon interacts with the solar magnetic field, the number of particles contained

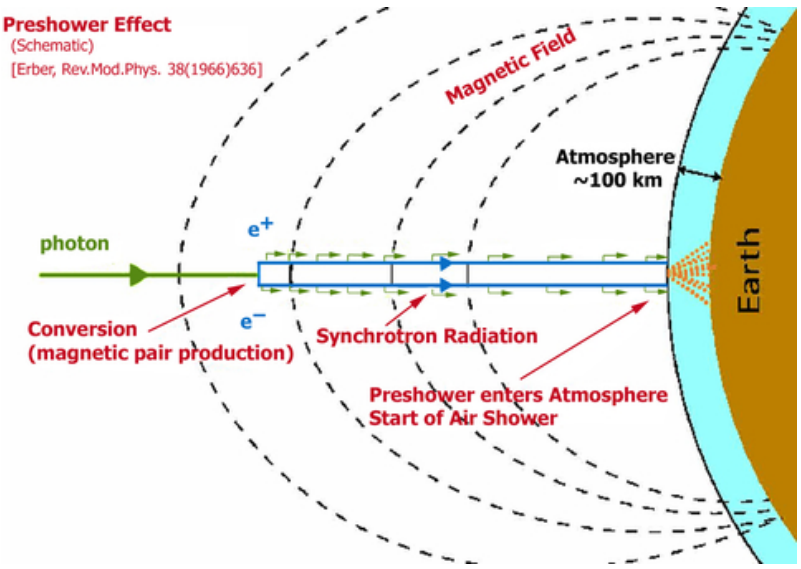

Figure 2.8: Schematic view of the preshower effect in the geomagnetic field. Credits: P. Homola.

in preshowers strongly depends on the distance between the top of the atmosphere and the location of the magnetic conversion point and consequently, on the angle of incidence θ of the primary photon. As this distance increases, the e^-/e^+ pair must travel a larger distance and therefore loses more energy via synchrotron radiation (i.e. more secondary photons are produced). Moreover, electrons with energies above 10^{15} eV are deflected in the geomagnetic field with an angle smaller than 10^{-5} degrees [150]. As a consequence, e^-/e^+ pair emits bremsstrahlung radiation in the form of a photon beam, and the spatial distribution of the secondary photons is constrained within a few centimeters at the top of the Earth's atmosphere.

In [135], a particular attention was given to the direction dependence of the preshower effect in the framework of the northern[1] and the southern sites of the Pierre Auger Observatory. Looking at the probability of UHE photons to cascade as a function of the azimuth angle, it was found that this probability raised as UHE photons were traveling closer to the magnetic poles, i.e. the North direction for the northern site and the South direction for the southern one, where the perpendicular component of the magnetic field is the strongest. Such property is important to note as it competes directly with the energy of the primary photon: photons of higher energy may not cascade if coming from a direction where this component is too weak, while photons of smaller energy may in fact produce preshowers if traveling in a region of the geomagnetic field

[1]Since the writing of this study, the northern site project for the Pierre Auger Observatory has been abandoned.

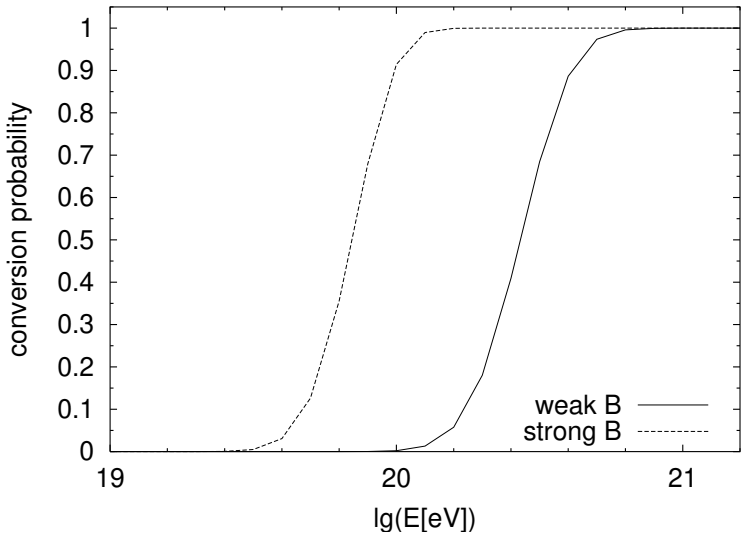

Figure 2.9: Probability of an UHE photon to convert into a e^-/e^+ pair as a function of its energy and for the strong and weak directions, at the Pierre Auger Observatory. Figure taken from [153].

where the same component is strong enough.

More recently, a new Monte-Carlo simulation algorithm named PRESHOWER was developed to simulate the cascading of UHE photons in the geomagnetic field [153]. This field is simulated with the International Geomagnetic Reference Field model (IGRF) [154]. To calculate the field strength along the propagation path of the UHE photon, the following parameters are needed: the geographical location of the observatory site (latitude and longitude), the direction of propagation of the primary photon in the local reference frame (zenith and azimuth angles) and the year of observation. The simulation begins with the propagation of the UHE photon within 5 Earth radii. As it travels, the transverse magnetic field strength, as well as the e^-/e^+ conversion probability, are calculated in steps of 10 kilometers using Equation 2.3. As an example, Figure 2.9 shows the probability of conversion of an UHE photon as a function of its energy and its direction of propagation at the Auger site in Malargue. Photons coming from the strong field direction (direction for which B_{tr} is the highest and corresponding to the zenith angle $\theta = 60°$ and to the azimuth angle $\phi = 177°$, with $\phi = 0°$ being the direction of the geographical North) are more likely to convert at lower energies than if coming from the weak field direction (zenith angle $\theta = 50°$ and azimuth angle $\phi = 357°$), especially for energies between 5×10^{19} eV and 5×10^{20} eV. Such directional dependence is consistent with the results obtained in [145] and discussed previously. The newly created e^-/e^+ pair emits secondary photons according to

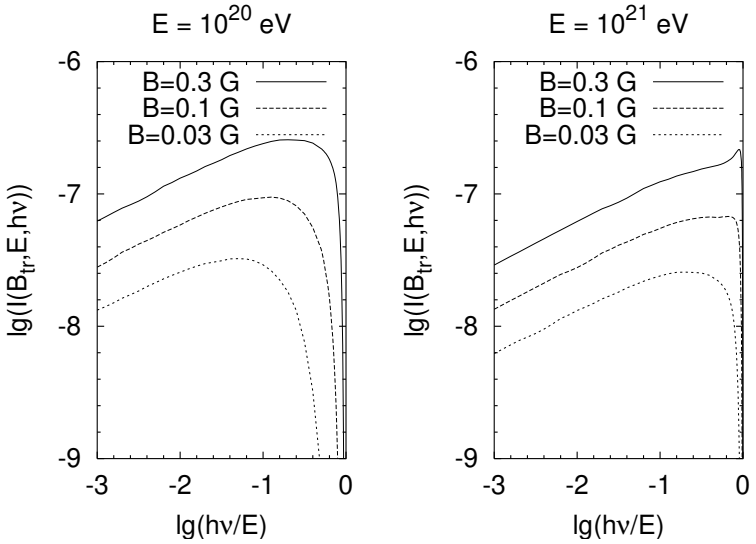

Figure 2.10: Spectral distributions of secondary photons using Equation 2.12, for primary photons of energy $E = 10^{20}$ eV (left) and $E = 10^{21}$ eV (right) and for various typical strengths of the transverse magnetic component. Figure Taken from [153].

the spectral distribution equation

$$I(E_e, h\nu, B_{\rm tr}) = \frac{2}{3} r_e^2 B_{\rm tr}^2 \left(\frac{E_e}{m_e c^2}\right)^2 f(h\nu) \frac{E_e}{\Upsilon (E_e - h\nu)^2}, \tag{2.12}$$

where $f(h\nu)$ corresponds to Equation 8 of [153]. This equation is a more general expression of Equation 2.5, for which the restriction $h\nu \ll E_e$ is removed. The probability of bremsstrahlung emission is calculated using Equation 2.6.

As secondary photons are emitted, they are checked for further magnetic conversion. All magnetic processes within the cascade development are calculated in steps of 1 kilometer, for all types of particles. Figure 2.10 shows the shape of the spectral distributions of the secondary photons for different primary energies and for typical values of the transverse magnetic component strength. As expected from the spectral analysis from [144] discussed above, these distributions peak at higher energies as the field strength increases. This algorithm ignores the influence of the solar winds as they affect the geomagnetic field at distances well beyond the region of conversion of UHE photons. Moreover, the time delay between electrons and photons being significantly smaller than the time resolution of cosmic-ray experiments, its effect is also neglected.

The final output of the algorithm consists in the altitude of the UHE photon conversion, the number of particles reaching the top of the atmosphere (photons and e^-/e^+), the maximum energy of each type of particle, the fraction

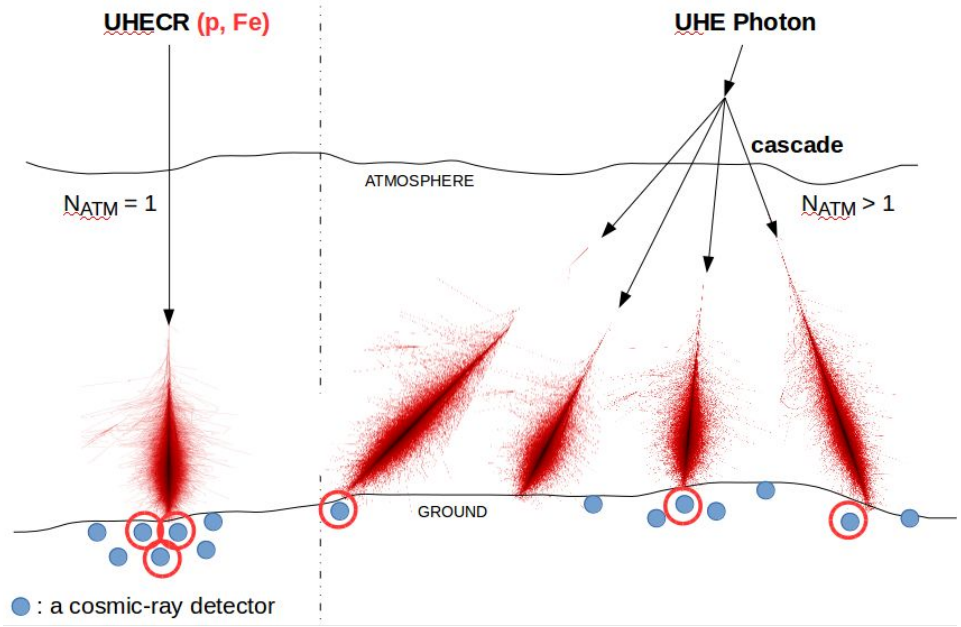

Figure 2.11: Schematic view of the different approaches to cosmic-ray detection. On the left, most cosmic-ray experiments are designed to look for single air showers produced by one primary particle. On the right, the approach undertaken by CREDO: a network of cosmic-ray detectors looking for multiple correlated air showers coming from the same UHE photon cascade occuring above the atmosphere. The distance between each air shower is variable and could be of several thousand kilometers, depending on the pre-cascading effect.

of the primary energy carried by the e^-/e^+ as well as the total energy each type carries.

2.5 Cosmic-Ray Ensembles: the CREDO Project

As described in Section 2.4.1, photons cascading in the Sun's magnetic field may produce an ensemble of secondary particles distributed at the top of the Earth's atmosphere over several thousands of kilometers, and spanning over several decades in energy. Similar processes may occur in the Universe on much larger scales when considering, for example, the interaction of an UHE photon with the magnetic field produced by neutrons stars. The collection of secondary particles poduced by such phenomena is henceforth referred to as cosmic-ray ensemble (CRE). As the spatial signature on the top of the atmosphere of these CREs may vary greatly with the distance at which the first interaction occurs and with the strength of the considered magnetic field(s) the UHE photon travels through, observing these correlated particles would provide precious information about the means by which UHE photons may be

produced and about their source of production. Whether these CREs contain only two particles, distanced by hundreds of kilometers, or are composed of thousands of them distributed along a thin line extending over thousands of kilometers, a network of detectors capable of registering EAS's produced by these particles and spread on a global scale may be able to observe and measure the correlation between these EAS's. Such endeavor has been undertaken by the Cosmic-Ray Extremely Distributed Observatory (CREDO) collaboration[1] [155, 156, 157, 158]. Inaugurated in August 2016, the main objective of CREDO is to connect together all kinds of detectors capable of observing particles from air showers, from the simple smartphone to the professional cosmic-ray experiments. By creating a global network and by developing new methods of particle detection, CREDO hopes to observe air showers produced at different locations on the surface of the Earth, but originating from the same physical phenomenon.

Figure 2.11 compares the approach used in major cosmic-ray experiments, such as Auger, where single air showers are recorded to the one initiated by the CREDO collaboration, where multiple cosmic-ray detectors spread on a global scale are part of one single network, searching for correlations between several air showers. As CREs may be spread on scales as large as the Earth's diameter, single localized experiments have practically no chance of observing them. However, if they are connected into one global network, CREs of various sizes are more likely to be observed. In addition to searching for spatial signature of CREs, the CREDO experiment also aims at investigating the time distribution of the CREs as they trigger ground detectors. Such endeavor is motivated by the non-replicated observations of cosmic-ray outbursts in the TeV-PeV regime, lasting from 20 seconds [159] up to 5 minutes [160].

As shown in the example of the UHE photon cascading in the Sun's magnetic field, the energy range of the secondary particles can span over several orders of magnitude. Therefore, all types of particle detectors may contribute to CREDO's search for CREs: gamma-ray telescopes, neutrino detectors, large cosmic-ray arrays, educational experiments, small scintillators, and smartphones.

The obvious necessity for a worldwide network has led the CREDO collaboration to develop its own smartphone application in order to record the radiation that constantly interacts with the photo-sensors of the camera. These particles can be of cosmic origin (secondary particles of air showers produced by cosmic rays) or from the natural background radiation. The advantage of such a tool is two-fold. First of all, smartphones are already available globally and used by billions of people, thus allowing a nearly costless deployment of particle detectors on a planetary scale. On the other hand, it promotes citizen

[1] website: credo.science

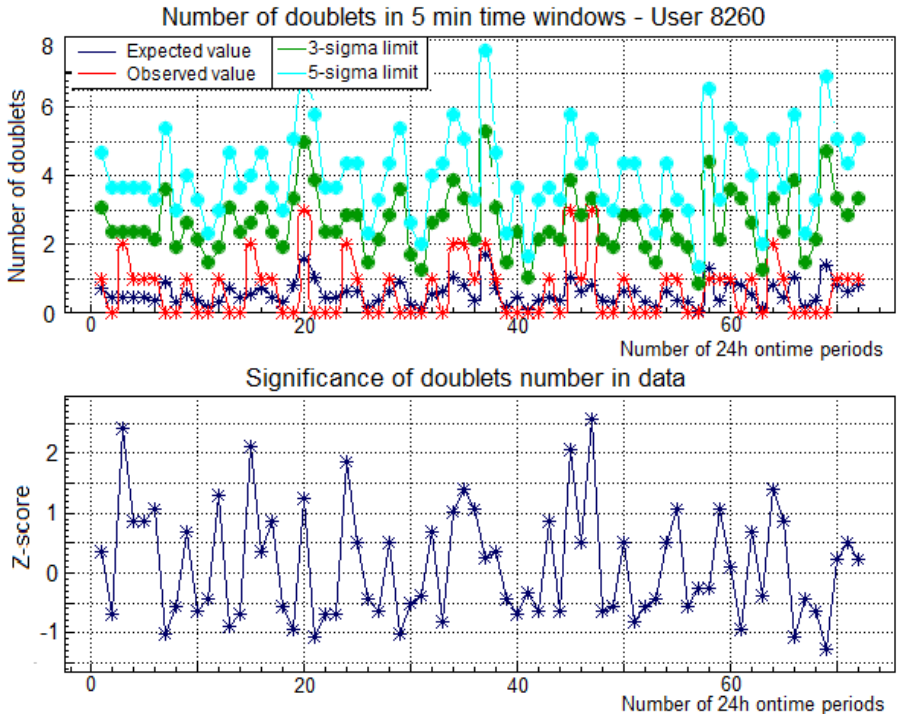

Figure 2.12: *Top*: Number of doublets (2 detections within 5 minutes) found in periods of 24 hours of app running, found in the data of one of CREDO's smartphone application user, in red. The expected value obtained from scrambled maps is shown in dark blue while the number of doublets needed to obtain a 3- or 5-sigma effect are shown in green and cyan, respectively. *Bottom*: Number of standard deviations of the observed value compared to the expected one.

science through the massive participation of non-scientists. In the context of CREDO, such public engagment goes beyond the simple data acquisition aspect. An active participation is indeed encouraged, through several mediums. First of all, data recorded by individual users is accessible via CREDO's API[2], where processing and data analysis tools are made available. On that platform, CREDO's application users can visualize how their detections look like (point-, worm- or line-like) and investigate the results from various analysis run on their data. One example of such analysis is presented in Figure 2.12. The basic principle is to look for excesses of number of doublets – defined as the number of occurences when 2 detections are obtained within 5 minutes – in 24 hours periods during which the application is running. This number is then compared to the expected value, obtained via the generation of scrambled maps which randomly redistribute the timestamps of the number of events obtained in the considered period. Z-score (sigma value) as well as 3- and 5-sigma

[2]website: api.credo.science/web/

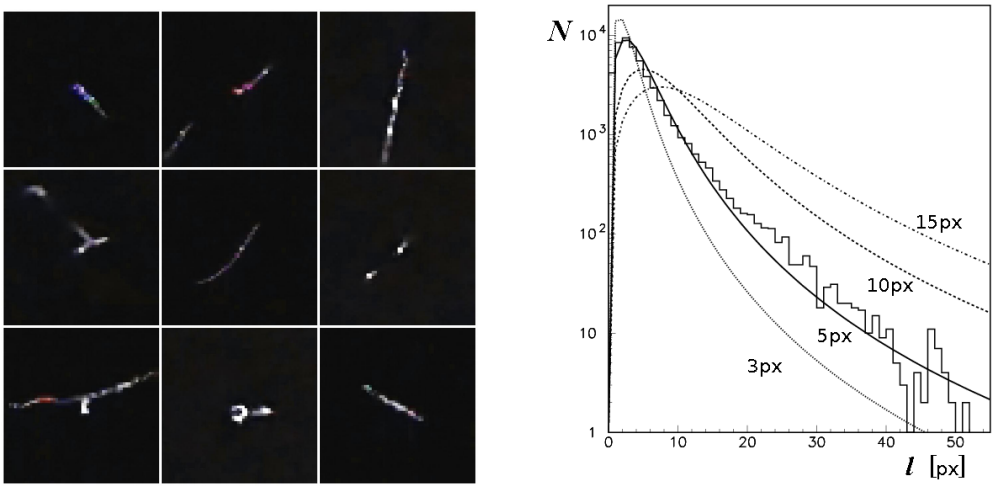

Figure 2.13: *Left*: Examples of tracks left by radiation on the smartphone cameras and recorded by the CREDO application. The frames have a dimension of 60×60 pixels. *Right*: Distribution of track lengths found in smartphone data obtained with the CREDO application, and related to the zenith angle of incoming particles by Equation 2.13. Various fits are shown for different values of the thickness h of the matrix layer. Figure taken from [158].

limits are calculated and displayed on the plot of Figure 2.12, which is available to each user on the API, via the Quantum Gravity Previewer tool. Such approach may spark a greater interest from non-scientists in participating on a higher level in science discovery. In fact, one of the key characteristic of the CREDO strategy is the open access of the algorithms developed for data acquisition and analysis. The algorithms are all available on GitHub[3], thus allowing any interested user to participate in their improvement.

Other analyses focusing on long traces found in the smartphone images (see Figure 2.13 (left)) can also be performed [158]. Such tracks are supposedly produced by muons produced in cosmic-ray showers entering the camera sensor's matrix at large zenith angle. The distribution of the angle θ can be expressed as a function of the length of the tracks l and the thickness of the smartphone camera's matrix h:

$$\frac{dN(\theta)}{d\theta} = \cos^{\gamma}(\theta), \tag{2.13}$$

where $\gamma \sim 2.0$ and $\theta = \arctan(l/h)$. As h is unknown, it can be consider as a free parameter that can be adjusted to fit the distribution. Such distribution is plotted in Figure 2.13 (right) for data obtained via the CREDO application, and several fits with different h are shown. According to this plot, the zenith angle distribution is best fitted for $h = 5$ pixels.

[3]website: github.com/credo-science/credo-api-tools

Another aspect of citizen science undertaken by the CREDO collaboration is the use of existing platforms such as *Zooniverse*[4], that provide online tools for data classification. As a matter of fact, CREDO has developed two data classification tools on this platform: Dark Universe Welcome and Private Particle Detective. The former requires the user to look for peculiar deviation in the average time of detection from detectors already connected to the CREDO network, while the latter asks to classify the images formed by particles on the smartphone camera and obtained via CREDO's smartphone application.

The very nature of particle cascades produced far away from the Earth's atmosphere requires a global network of detectors capable of observing correlations between air shower created in different parts of the world. The CREDO collaboration sees it as an opportunity to promote citizen science in order to effectively develop such network via the use of smartphones, which are already available worldwide, and the production of cheap pocket detectors that can be deployed in high schools to serve as educational tools for teachers and students. As of October 1st, 2020, the CREDO collaboration consists of 40 institutions spread over 18 countries, and more than 5,000,000 detections have been registered through the smartphone application.

[4]website: zooniverse.org

3. Ground-Based Imaging Gamma-Ray Astronomy

ENSUING the discovery of cosmic rays by V. Hess, and of the air showers resulting from their interaction with the atmosphere, several ground-based cosmic-ray experiments were developed to search for secondary particles. While the debate on the true nature of cosmic rays – whether they were mainly charged particles or gamma rays – was still raging, the discovery of the Cherenkov effect in the 1930s quickly offered a new channel of observation. In 1953, using a 25 cm mirror, a single PMT and a trash bin, W. Galbraith and J. V. Jelley became the first to detect the short light pulse arising from this effect [161]. Nevertheless, any conclusive observation of gamma-ray initiated air shower was still out of reach due to the dominating hadronic cosmic-ray background. The idea of combining multiple PMTs in order to obtain images of the Cherenkov pulses came almost 25 years later, after two decades of struggle to reduce the background contamination via various, but often unfruitful, techniques [162]. The *Imaging Atmospheric Cherenkov Telescope* (IACT) technique uses multi-pixel cameras to make images, which are analyzed and described using a set of discriminating parameters introduced by A. M. Hillas in 1985. The Whipple Observatory, a gamma-ray experiment located on the Mount Hopkins in Arizona, USA, was the first to measure the gamma-ray flux above 0.7 TeV from the Crab Nebula at 9σ after 82 hours of observation [163]. This observation was later confirmed at 45σ after significant upgrade of the telescope [164].

The early 2000s saw the birth of a third generation of imaging gamma-ray telescopes spread out across the globe, offering a full-sky view at very-high energy for the first time. In the northern hemisphere, the *Major Atmospheric Gamma-ray Imaging Cherenkov Telescope* (MAGIC) has been operating since 2005 and is today composed of two 17 m-diameter telescopes located in La Palma, Spain[1]. Noteworthy observations are the detection of one of the most distant gamma-ray source, 3C279, at $z = 0.536$ [165] as well as the detection of the gamma-ray burst GRB 190114C in the TeV energies [120]. In the same hemisphere, the *Very Energetic Radiation Imaging Telescope Array System*[2] (VERITAS) is an array of four imaging telescopes of 12 m diameter installed at the same location as the Whipple Observatory. Since the beginning of its operation in 2007, VERITAS has detected more than 60 gamma-ray sources, including the first starburst galaxy M82 [166] and the TeV gamma-ray emission of Tycho's supernova remnant [167]. In the southern hemisphere, the High Energy Stereoscopic System[3] (H.E.S.S.) is the only stereoscopic array to be composed of telescopes of different sizes (four 12 m- and one 28 m-diameter

[1]website: magic.mpp.mpg.de
[2]website: veritas.sao.arizona.edu
[3]website: mpi-hd.mpg.de/hfm/HESS

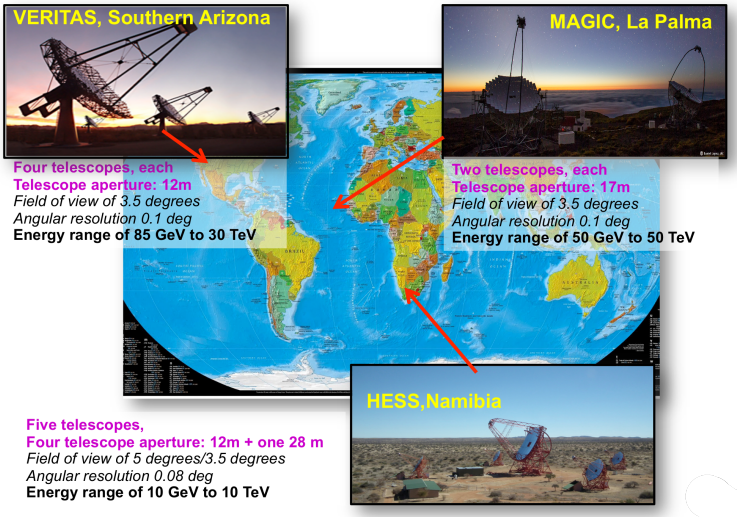

Figure 3.1: Overview of the operating ground-based imaging gamma-ray telescopes and their associated performances.

telescopes), allowing the observation of air showers at few GeV. Its location allows for the observation of sources not accessible by the first ground-based gamma-ray telescope, including the radio-galaxy Centaurus A, which was recently found to generate a gamma-ray flux at TeV energies in a region of several thousands of light-years [168]. The excellent angular resolution offered by these telescopes ($\sim 0.1°$) has allowed the observation of fine structures in gamma-ray sources and to distinguish various components within. A summary of the discussed gamma-ray telescopes is shown in Figure 3.1.

In this chapter, the properties of the Cherenkov light emitted by air showers are reviewed. Then, the underlying principles of the IACT technique are discussed, from light collection to image parametrization. In the second part, a closer look is given to how air showers coming at high zenith angles may be detected and discriminated against the cosmic-ray background by gamma-ray telescopes. To close this chapter, the Cherenkov Telescope Array (CTA), the next-generation IACT array currently under construction, is introduced, including its expected performance.

3.1 Imaging Atmospheric Cherenkov Telescopes

3.1.1 Cherenkov Emission in Air Showers

Charged particles passing through a dielectric medium with a refractive index n, at a velocity βc greater than the phase velocity of light c/n in the con-

sidered medium, may temporarily disrupt the polarization of the constituent molecules. As these molecules return to their original state, they emit wavelets which interfere constructively to form a forward-oriented cone of radiation called Cherenkov light, in honor of the physicist Pavel A. Cherenkov [169]. The minimum energy required for a charged particle of rest mass m_0 to trigger such effect can be expressed as:

$$E_{\text{thr}} = m_0 c^2 \sqrt{\frac{1}{1 - \frac{1}{n^2}}}. \tag{3.1}$$

In the air ($n = 1.0003$), Equation 3.1 gives a threshold energy of ~ 21 MeV for electrons, ~ 39 GeV for protons and ~ 4.3 GeV for muons. The opening angle of the cone formed by the emitted Cherenkov light depends on the refractive index of the medium and the velocity of the charged particle:

$$\cos\theta_c = \frac{1}{\beta n}, \tag{3.2}$$

resulting in a maximum opening angle of $\sim 1.4°$ in the air. From Equation 3.2 arises the condition that for the Cherenkov effect to take place, the refractive index at any wavelength $n(\lambda)$ must be greater than 1. Consequently, Cherenkov radiation is predominantly emitted in the visible spectrum and is maximized in transparent dielectric media. Finally, the number of Cherenkov photons emitted per unit path dl can be expressed by the Frank-Tamm formula [170]:

$$\frac{dN_{\text{Ch}}}{dl} = 2\pi\alpha_s(1 - \cos^2\theta_c)\left(\frac{1}{\lambda_{\text{min}}} - \frac{1}{\lambda_{\text{max}}}\right), \tag{3.3}$$

where $\lambda_{\text{min}} = 300$ nm $\leq \lambda \leq \lambda_{\text{min}} = 600$ nm is the typical sensitivity range of light sensors, and α_s is the fine structure constant. At sea level, this corresponds to ~ 0.5 photons/cm (or $\sim 10^4$ photons/radiation length) for a relativistic electron. The energy losses per unit path lenght due to Cherenkov emission are significantly lower than ionization or excitation losses and are proportional to λ^{-2}, resulting in a peak at short wavelengths, and giving a blue color to the phenomenon.

When focusing on air showers, it is important to keep in mind that the refractive index varies with the altitude, mostly due to the change of atmospheric pressure. In [20], this dependence is expressed by the function:

$$n(z) = 1 + 0.000283\frac{\rho_{\text{atm}}(z)}{\rho_{\text{atm}}(0)}, \tag{3.4}$$

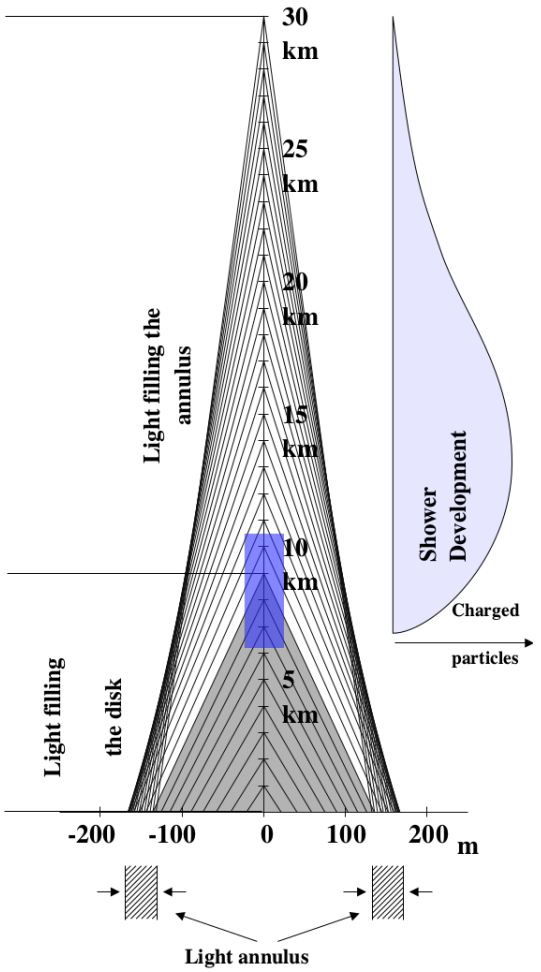

Figure 3.2: Schematic view of a vertical air shower Cherenkov emission. The blue rectangle represents the area where $\sim 50\%$ of the Cherenkov light is emitted. Above that area, the Cherenkov light produces a ring on the ground, with a radius of ~ 150 m from the shower core while below, a dimmer light pool is formed. The longitudinal profile of charged particles along the shower axis is also shown. Figure adapted from [35].

where $\rho_{\mathrm{atm}}(z)$ is the density of the air as a function of the altitude z, previously introduced in Section 1.1.1. Such a dependence directly affects the opening angle, varying from $\sim 0.2^\circ$ at an altitude of 30 km, where the refractive index is close to 1, to $\sim 1.4^\circ$ at the sea level. Such a variation, as well as the Coulomb scattering of electrons within the shower, contribute to the conic shape of the Cherenkov light profile shown in Figure 3.2. The light pool of Cherenkov radiation formed on the ground is constituted of two parts: a ring with radius ~ 150 m and thickness of several meters, stemming from the Cherenkov light emitted in the early stages of the shower development (above ~ 10 km in Figure 3.2), and a disk within the annulus which is filled

by Cherenkov light emitted by charged particles close to the ground. The scattering of electrons within the shower results in a smooth tail of Cherenkov light beyond the annulus that fades as the distance to the shower axis increases. One interesting consequence of Cherenkov radiation traveling slower than the charged particle is that near the shower axis, photons emitted at a later stage of the cascade development (closer to the ground) reach the surface before the photons emitted at its very beginning. Nevertheless, for vertical showers, the typical duration of a Cherenkov light pulse of an air shower remains in the order of a few nanoseconds. As highlighted in [68], most of the Cherenkov radiation is emitted near the shower maximum. For air showers initiated by gamma primaries of a few TeV, 50% of the Cherenkov light is produced within a cylinder centered around the maximum ($\sim$ 8 km), with height and diameter of approximately 4 km and 40 m, respectively. This cylinder is represented by the blue rectangle in Figure 3.2. In comparison, protons of similar energies produce a similar percentage of Cherenkov light in a cylinder of larger lateral extent ($\sim$ 150 m wide) centered at slightly lower altitudes. 25% of the total emitted Cherenkov light, responsible for the formation of the Cherenkov ring, is emitted above this cylinder while the remaining 25% is produced below, and creates local peaks of emission filling the Cherenkov pool. However, the highlighted features are consistent when considering air showers initiated by gamma primaries of a few TeV. In the case of proton showers, and of primaries of higher energy, the lateral profile of Cherenkov light at the ground is more similar to a featureless exponential decrease with respect to the distance to the shower axis.

As described in Section 1.1.2, the Heitler's model determines a linear relationship between the total number of electrons and the energy of the shower primary. If the total flux of Cherenkov photons is assumed to be proportional to the number of electrons in the shower, then the detection of the Cherenkov light can provide a calorimetric measurement of the shower, and a robust estimation of the primary energy. The relationship between the number of electrons N_e and the total number of Cherenkov photons emitted Q is expressed by the function [171]:

$$Q \simeq 3500 \int_0^{X_0} N_e(X) dX, \tag{3.5}$$

where X_0 is the atmospheric vertical depth at the ground level. It should however be noted that not all electrons have the energy required to trigger the Cherenkov effect. An estimation in [19] gives an average of $\sim$ 40% of the total number of electrons which is responsible for Cherenkov emission. In practice, the Cherenkov photon density $Q(r)$ as a function of the distance to the core

of the shower r, i.e. the lateral distribution, provides an effective mean to determine the primary energy, given the knowledge of the optimal distance r_{opt} at which the zenith angle of the shower does not significantly affect the value of $Q(r_{\text{opt}})$. Additionally, for a fixed primary energy, the photon density at any given distance to the core is on average smaller for heavier primaries, in the case of showers initiated close to the zenith.

3.1.2 Cherenkov Imaging Technic

Since the first ground-based Cherenkov telescope developed by W. Galbraith and J. V. Jelley in 1953, the technology behind IACTs has considerably improved, offering a greater sensitivity to the short Cherenkov pulses from air showers, as well as a better photon/hadron separation. Nevertheless, the basic principles at the core of this technology has varied very little over the years, and are represented in Figure 3.3. The Cherenkov light is reflected by a collection of segmented mirrors, arranged in a parabolic shape, onto a camera composed of one or more PMTs (representing pixels), located at the focal point of the mirrors (these PMTs are pictured by the individual polygons of the camera of Figure 3.3). The FOV of these PMTs, often found around $\sim 0.1°$, is crucial to the angular and energy resolutions of the camera. In order to reduce the noise from the night sky background, modern IACT cameras have fast triggering scheme, allowing low energy thresholds. In modern IACTs, the different trigger levels are often defined as such:

- **TL1**: At the PMT level, a minimal signal as well as a minimal number of photo-electrons, are required.

- **TL2**: At the camera level, **TL1** must be fulfilled by a minimal number of PMTs, usually neighbors to one another.

- **TL3**: In stereoscopic mode of observation (described later on in this section), a minimal number of telescopes must satisfy **TL2**.

As displayed in Figure 3.3, the shape of the image formed by the triggered PMTs directly depends on the characteristics of the air shower and therefore, on the nature of the primary. For a telescope pointing at a source of gamma rays, the Cherenkov photons emitted in the early stages of the shower development are reflected by the mirrors with a smaller angle than the one of photons emitted closer to the ground, and trigger PMTs closer to the center of the camera. Moreover, the time resolution of modern cameras also opens the possibility to analyze the rise time of each PMT, thus offering another discriminating factor used to improve the background rejection [173].

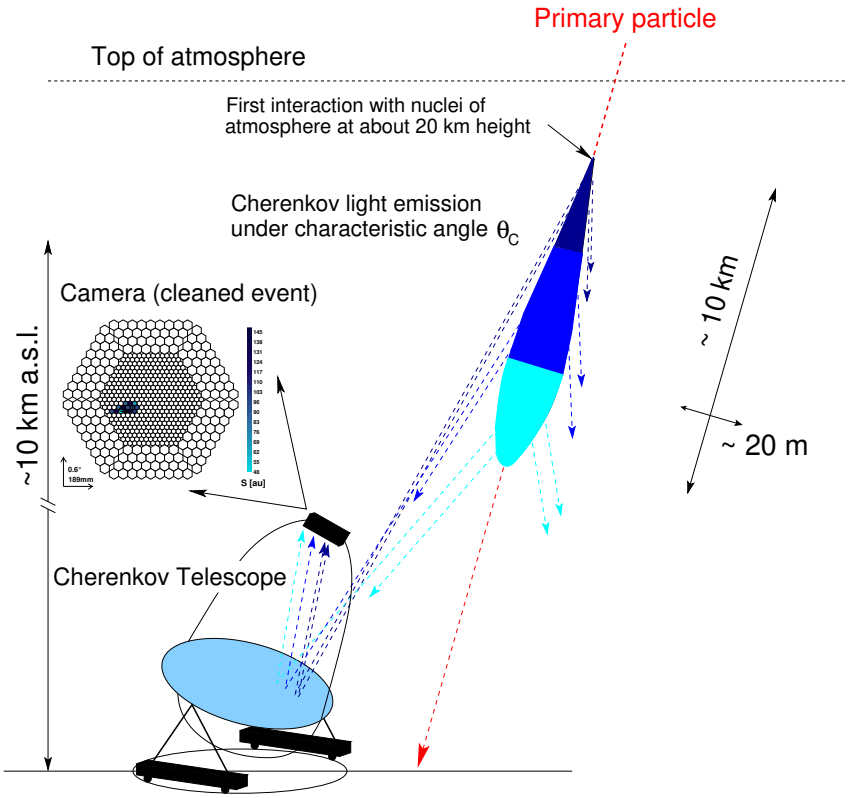

Figure 3.3: *The IACT technique*: the Cherenkov light emitted by an air shower is reflected by a large mirror at an angle depending on the altitude of emission, focusing it on a camera constituted of several PMTs. Figure taken from [172].

In the stereoscopic observation of air showers, several telescopes, spaced by $\sim$ 100 m, point in the same direction. Such a technique, first introduced in the early 1960s by A. E. Chudakov [174], does not only allow a better angular and energy resolution, but also a more accurate reconstruction of the impact location of the air shower, as well as of the direction of the primary. Another advantage of this mode of observation is that single muons may easily be rejected as they can only trigger one telescope. The concept is illustrated in Figure 3.4: multiple telescopes are viewing the same air shower from different perspectives and the intersection of the major axes of the cameras images reveals the primary direction. Similarly to the fluorescence technique described in the first chapter, the intersection of the planes formed by the shower axis and the telescopes unveils the impact location of the shower, as illustrated in the left panel of Figure 3.4.

Overall, the systematics due to the absence of calibration sources[4], and to

[4]However, IACTs may use the Cherenkov rings produced by atmospheric muons to calibrate the detectors [175].

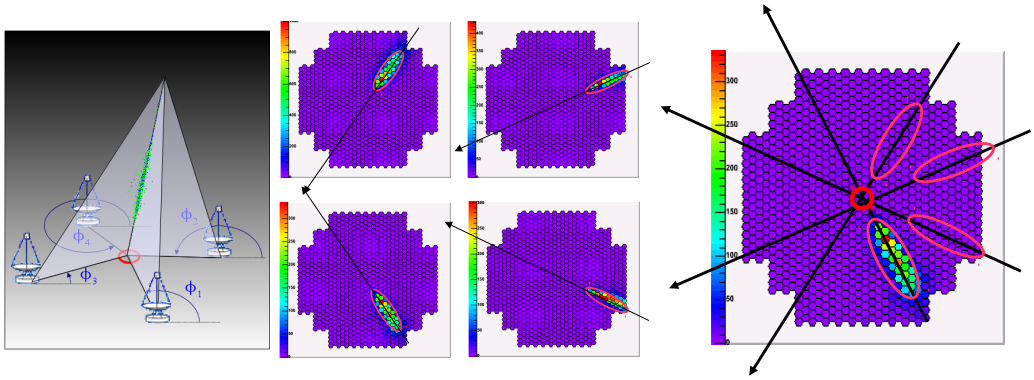

Figure 3.4: *Stereoscopic observation with IACTs*: several telescopes observing an air shower allow the reconstruction of its impact location, and of the direction of the primary that initiated it, via the orientation of the images formed on each camera. Figure taken from [35].

the changing nature of the atmosphere, result in an energy scale uncertainty of about $10 - 15\%$. High altitude observations may reduce the turbulences in the atmosphere, but high-energy showers, which penetrate deeper, may be harder to reconstruct, due to their potentially incomplete development. The duty cycle of IACTs, estimated around 10% is in fact also affected by the atmospheric conditions, limiting their use to clear and moonless nights. Nevertheless, despite their small FOV, IACTs have large collection area, thanks to the large area of the Cherenkov pool.

3.1.3 Image Parametrization and Background Rejection

In gamma-ray astronomy, the highest contribution to the background comes from the isotropic cosmic-ray flux. Consequently, any experiment dedicated to the observation of gamma rays must be capable of efficiently rejecting hadronic showers. In this endeavor, the images formed in the cameras of the IACTs consitute a powerful tool to identify the nature of the primaries initiating detected showers. While gamma rays tend to produce long, elliptically-shaped images, the hadronic showers generate wider and more irregular images, as illustrated in the top panel of Figure 3.5. Such a discrepancy can be explained by the properties of electromagnetic and hadronic showers: due to a larger lateral scattering of the pions in the latter, the electromagnetic sub-showers resulting from their decay, produce, on average, larger and more uneven images[5]. Moreover, while the images from gamma-ray showers tend to be aligned with the source position (the major axis of the elliptic image and the source position intersect), it is not the case for the isotropic cosmic-ray background. The shape

[5]Each sub-shower produces its own cluster of triggered PMTs.

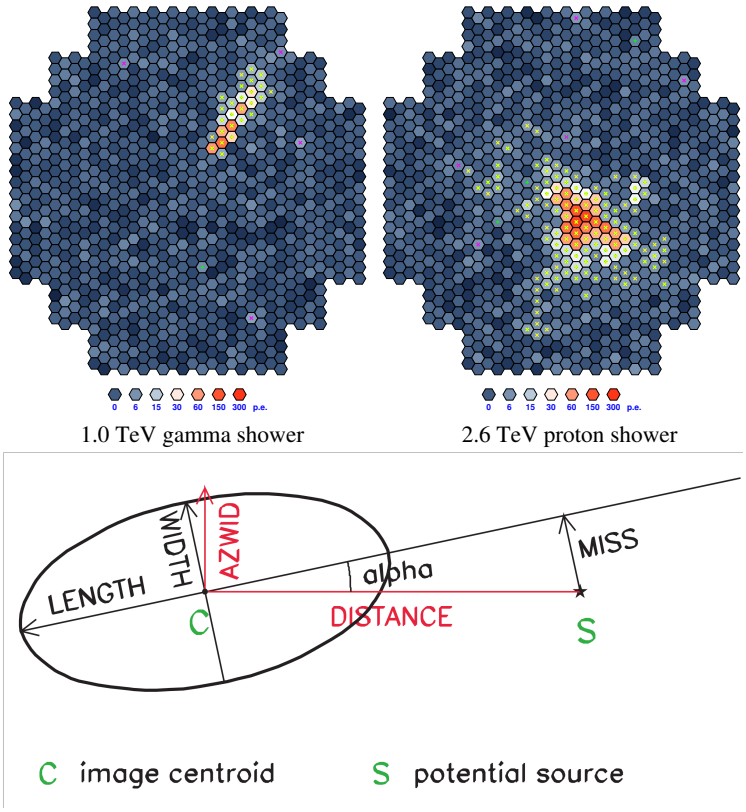

Figure 3.5: *Top*: Examples of images formed in IACT cameras by a TeV gamma shower (left) and a 2.6 TeV proton (right). Images taken from [176]. *Bottom*: Hillas parameters characterizing images formed on IACT cameras. The description of the parameters is given in the text. Figure taken from [162].

of the image is also tightly connected to the impact distance of the shower from the telescopes and different orientations affect the size of the image:

- ➢ If the shower core and the axis of the telescope are one and the same (null impact distance), a circular image will be formed at the center of the camera.
- ➢ For a null impact distance, the higher the angle of incidence of the shower, the further away from the center of the camera the image will be formed.
- ➢ If the shower core and the axis of the telescope are parallel, the greater the impact distance, the longer the image.

In order to quantify the characteristics of the images, A. M. Hillas introduced a set of parameters, called *Hillas paramaters*, which describes the geometry of the images [178]. These parameters are shown in the bottom panel of Figure 3.5 and are summarized hereafter:

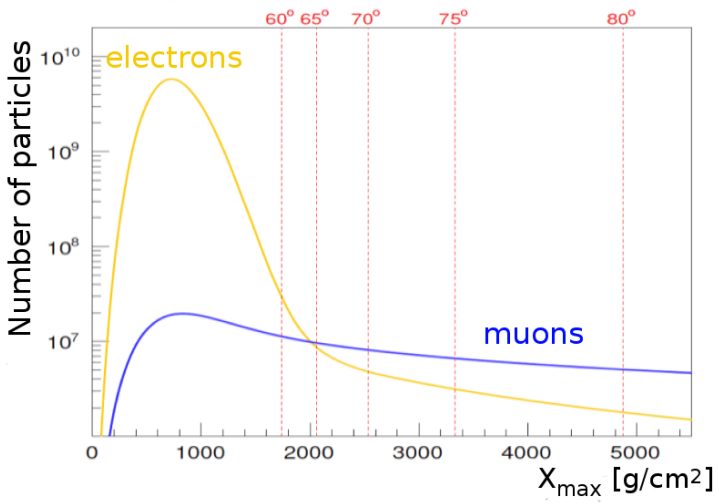

Figure 3.6: Longitudinal profiles of the muonic and electromagnetic components of a 10^{19} eV proton EAS observed at sea level as a function of the slant depth. The slant depth at sea level for a given zenith angle is given by the dashed red lines. Figure taken from [177].

- The *size* parameter, not shown in Figure 3.5, corresponds to the number of photo-electrons created by the Cherenkov light in the PMTs. It is strongly correlated with the energy of the primary which initiated the air shower, and depends on the distance between the detectors and the maximum of that shower.

- The *length* and the *width* correspond to the major and minor axes of the ellipse, respectively.

- The *distance* parameter characterizes the angular distance between the COG of the image and the position of the source.

- The *alpha* angle, describing the orientation of the image with respect to the source location.

- The *miss* paramater refers to the angular distance between the source location and the major axis.

- The *azimuthal width* corresponds to the r.m.s. spread of the image perpendicular to the distance parameter direction.

For point-sources of gamma rays, the *width* as well as the *miss* and *alpha* parameters are expected to be rather small in comparison to hadronic showers (source aligned with the telescopes axis). Moreover, small *azimuthal width*

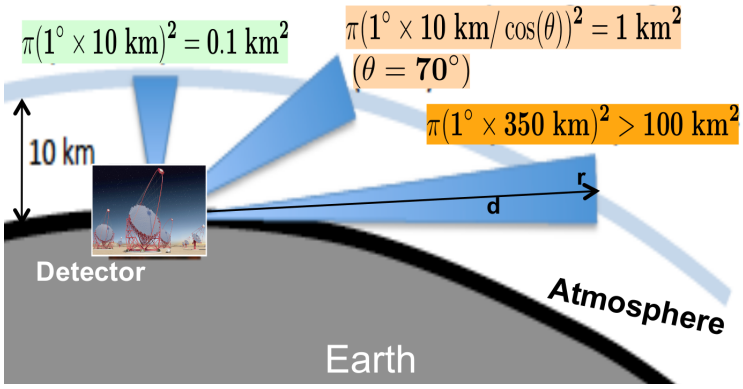

Figure 3.7: Collection area as a function of the zenith angle for an IACT with 1° FoV. Figure taken from [177].

resulting from narrow images with small *miss* constitute a powerful discriminating variable capable to veto most background images, as illustrated by the Whipple group's detection of the Crab Nebula and its 98% background rejection efficiency [163].

3.2 Nearly-horizontal Air Showers

As discussed in Chapter 1, the muon component of air showers can be used to identify the nature of the primary, as gamma showers tend to be more muon poor in comparison to hadronic ones. The standard mode of observation of air showers by IACTs, i.e. low zenith angle directions, does not offer the possibility to clearly distinguish the Cherenkov emission of muons from the emission of electrons. Energy losses of electrons due to ionization are approximately two orders of magnitude greater than the one suffered by muons. Air showers coming at large zenith angles ($\theta \geq 75^\circ$) may therefore see their electromagnetic component almost completely absorbed, resulting in muons dominating the cascade development (see Figure 3.6). In the TeV-PeV energy range, nearly-horizontal air showers produced by protons and heavy nuclei display a muon plateau past the shower maximum, starting at an altitude of $\sim$ 20 km, with a larger muon content for heavier nuclei. This plateau is however absent in gamma shower development.

In [179], a special attention is given to the Cherenkov light emitted by nearly-horizontal showers, and to the potential of IACTs to detect them. Although muons are much less efficient at emitting Cherenkov radiation than electrons, their preponderance in the late stage of the air shower development, as well as the fact that muons emit such radiation closer to the surface, make the muonic component potentially detectable by IACTs. While the Cherenkov

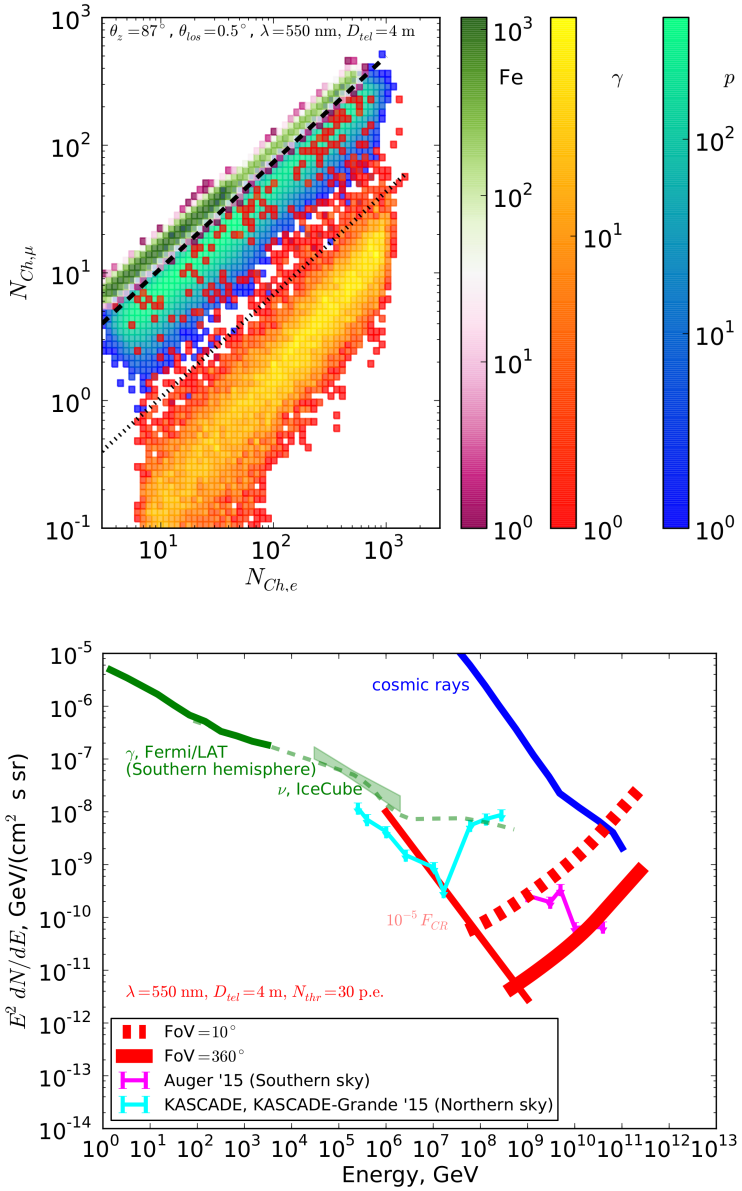

Figure 3.8: *Top*: Distribution of Cherenkov photon from the electromagnetic component vs. the muonic component for gamma (red-yellow), proton (blue-green) and iron (magenta-green) showers simulated in the energy range 1-100 PeV and for a zenith angle $\theta = 87°$. *Bottom*: Sensitivity of different Cherenkov telescopes set-up in the nearly-horizontal observation mode investigated in [179]. The sensitivity of various experiments and the cosmic-ray flux are also displayed for comparison. Figures taken from [179].

light pool can be up to a few hundreds of meters wide in the case of vertical showers, it may reach up to a few kilometers when the showers come at a very high zenith angle, considerably increasing the potential collection area,

as shown in Figure 3.7.

The Cherenkov emission of nearly-horizontal air showers detected by IACT cameras is therefore the result of both the narrow electromagnetic component and the wider muonic one. As a consequence, images formed by gamma showers are more compact and small, while the larger fraction of muons in the proton and iron showers results in images shaped in the form of longer tracks or halos. Moreover, the relative amount of Cherenkov photons from electrons and muons is particle type-dependent. Figure 3.8 (top) shows a scatter plot of the number of such photons in camera images for different primaries (gamma, proton and iron) simulated in the energy range 1-100 PeV. A correlation between the two sources of Cherenkov photons is noteworthy, especially for iron showers, and as expected, the number of Cherenkov photons stemming from the muonic component is significantly higher for iron and proton primaries than for gammas. A clear separation appears between all the primaries. Finally, in addition to a larger spatial extent, nearly-horizontal air showers also display a longer time scale (in the order of a few μs), which is independent of the primary type.

To summarize, looking for air showers at high zenith angle offers a greater collection area and an accessibility to the Cherenkov emission from muons. Nevertheless, due to the geometry of the cascade development, the Cherenkov light is emitted further away from the telescopes. In the TeV domain, such property leads to the formation of very small images, often within a single pixel and therefore, results in a poor photon/hadron separation. However, in the EeV regime, the dominating muonic component can produce brighter and larger images, so that such separation can be recovered. As shown in the bottom panel of Figure 3.8, the sensitivity of gamma-ray telescopes using the nearly-horizontal observation mode may be comparable to the sensitivities of UHECR experiments, making IACTs competitive for the detection of UHE particles.

3.3 The Cherenkov Telescope Array

The Cherenkov Telescope Array (CTA) is the next-generation of ground-based observatory dedicated to the detection of very high energy (VHE) gamma rays [180, 181]. With two sites located in the northern and the southern hemispheres (referred to as CTA-North and CTA-South, respectively), a full sky coverage by a same experiment is made possible for the first time. The energy range covered by the observatory, spanning over 4 orders of magnitude, from a few GeV up to several hundreds of TeV, will allow the observation of transient sources of gamma rays, as well as extreme accelerators, such as PeVatrons

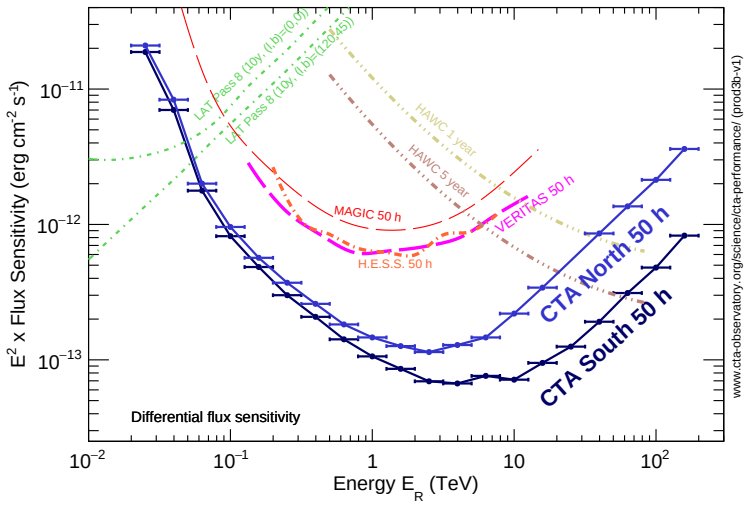

Figure 3.9: Differential energy flux sensitivities of CTA-North and CTA-South for 50h observation time necessary to obtain a 5-sigma detection of a point source of gamma rays. These sensitivities are compared to the ones from other experiments (see Reference [181]). Figure taken from [181].

[182]. Thanks to an unprecedented angular resolution of almost one arcminute and a FOV up to 8°, CTA will also constrain acceleration mechanisms in fine structures, and will offer the possibility to survey the sky at a faster rate and to observe extended sources of gamma-ray emission. The search for dark matter annihilation in spectral features will be significantly improved thanks to a better energy resolution of $\sim 10\%$. The fast positioning of the telescopes, and the temporal resolution of both sites, will also provide fast follow-up on short transient sources, such as GRBs, and a better understanding of AGN flares. Overall, the improved background rejection, combined with a larger collection area, and with a higher angular resolution, will offer a sensitivity about one order of magnitude better than existing IACT experiments (see Figure 3.9), opening the door for potential undiscovered gamma-ray emitters.

As mentioned previously, CTA will be composed of one site in each hemisphere. The southern one, located in Chile, will be mostly dedicated to the study of gamma-ray emission in the inner part of Galaxy and from the Galactic center. On the other hand, the northern site covering $\sim 0.6\,\mathrm{km}^2$, based in La Palma, Spain (see Figure 3.10), where the MAGIC telescopes are operating, will be dedicated to bright extra-galactic sources. In order to achieve their goals, different telescopes and lay-outs have been studied to optimize both arrays and three types of telescopes have been developed:

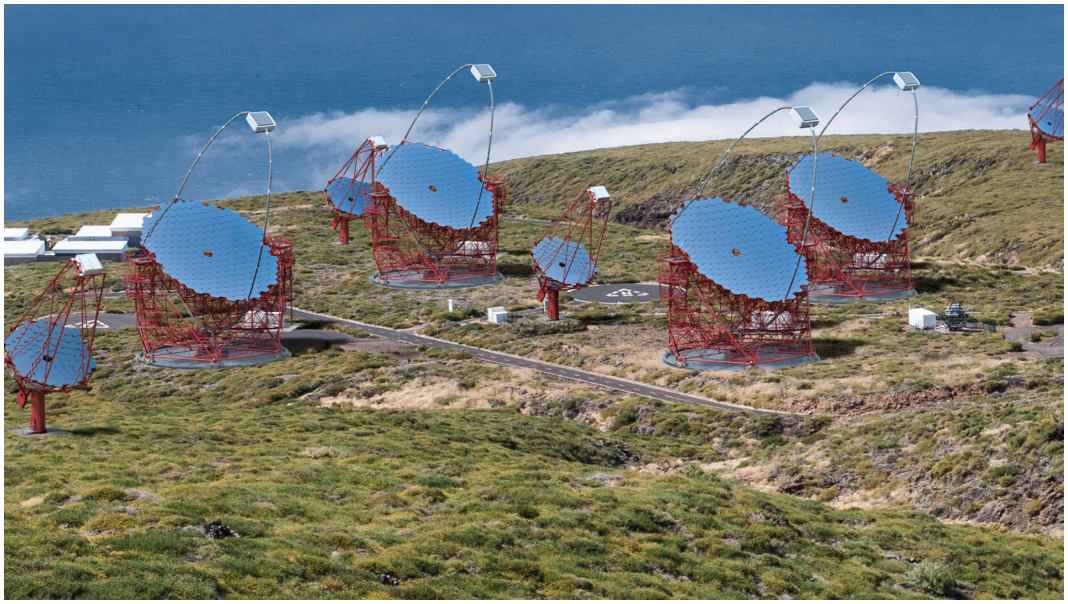

Figure 3.10: Artistic view of a portion of the northern site of CTA located in La Palma. The four LSTs are visible, as well as a few MSTs. Credits: Gabriel Pérez Diaz, IAC, SMM.

- *Large-Sized Telescope* (LST): equipped with a parabolic mirror of 23 m diameter and a camera of 2500 PMTs with a 0.1° FOV (for a total 4.5° FOV); four of these telescopes will be installed on each site. The size of the mirror will allow them to collect Cherenkov light from low-energy showers (down to $\sim$ 30 GeV), and their short repositioning time will offer the opportunity to follow up on GRB alerts within 20 seconds.

- *Medium-Sized Telescope* (MST): the design of this 12 m telescope is still ongoing and prototypes for two types of MSTs have been developed. The first one, based on H.E.S.S. and VERITAS telescopes, consists of a 8° FOV Davies-Cotton reflector redirecting the Cherenkov light onto a camera made of 1500 pixels of 0.18° FOV (for a total 7.6° FOV). The second, more innovative prototype, is a Schwarzschild–Couder dual-mirror of similar diameter and FOV, equipped with a camera of 11,000 pixels (PMTs or SiPMs) of 0.067° FOV. 15 and 25 of these MSTs will be installed at the northern and sourthern sites, respectively. The higher number of telescopes compared to previous experiments, as well as the higher reconstruction quality, will offer greater sensitivity to showers in the energy range 0.1-10 TeV.

- *Small-Sized Telescope* (SST): sensitive to the highest end of the energy range covered by CTA, the 4 m-diameter SST will only be deployed at the southern site. Due to the lower flux of TeV gamma rays, a large number

of SSTs ($\sim$ 70), as well as a greater spacing to account for the bigger Cherenkov light pool, are being considered. Three different designs have been proposed to reduce the total costs (see discussion in [181]), with a FOV between 8° and 10°, and 1300 to 2000 pixels of $0.2° - 0.3°$.

To summarize, 19 telescopes (15 MSTs + 4 LSTs) will be built at the northern site, covering an area of 0.6 km^2, and an energy range between 20 GeV and 20 TeV, while 99 telescopes (70 SSTs + 25 MSTs + 4 LSTs) will be installed at the southern location over an area of 4 km^2, with a sensitivity to energies up to 300 TeV. Unlike previous gamma-ray experiments, CTA will be an open observatory, allowing observation proposals from scientists outside the collaboration, and making the data publicly available.

4. The Preshower Effect at CTA-North

REPRODUCING the characteristics of EAS's, as well as the electronic response of detectors, with Monte-Carlo simulation softwares is an inevitable step in setting up the expectations of any type of measurement performed by these detectors. In this chapter, the properties of EAS's produced by UHE photons that have undergone the preshower effect are investigated, by simulating their propagation, magnetic conversion and cascade development, all the way down to the images that they form in the cameras of IACTs, taking the example of CTA-North (see Figure 4.1). The results are compared with other types of UHE primaries in order to highlight the major differences between the air showers they produce.

4.1 Preshower Effect above the Atmosphere

The preshower effect, introduced in Section 2.4.2, is simulated by the PRESHOWER algorithm [153], and results in a collection of low energy photons and e^+/e^- pairs reaching the top of the atmosphere. The first step in the simulation chain is the propagation of UHE photons in the geomagnetic field and the calculation of the e^+/e^- pair conversion probability. For a photon propagating over a distance R, the probability of converting to an e^+/e^- pair is described by Equation 2.3. The top panel of Figure 4.2 shows the conversion probabilities obtained for different primary energies, and as a function of the azimuth angle. For a given azimuth angle, the probability increases with the energy and is null for photons with energy of a few EeV. The azimuth angle for

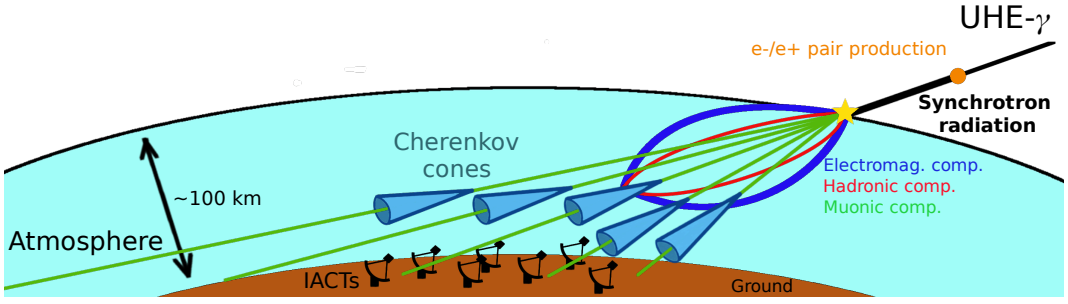

Figure 4.1: An UHE photon interacting with the transverse component of the geomagnetic field produces an e^+/e^- pair ~1000 km above sea level which emits bremsstrahlung photons. As such a process can repeat itself for some of these photons, a collection of particles (mainly photons and a few e^+ and e^-) reaches the top of the atmosphere. Consequently, atmospheric air showers are produced, and in the case of nearly-horizontal showers, mainly the muonic component reaches the IACTs on the ground, which detect the Cherenkov emission of this component.

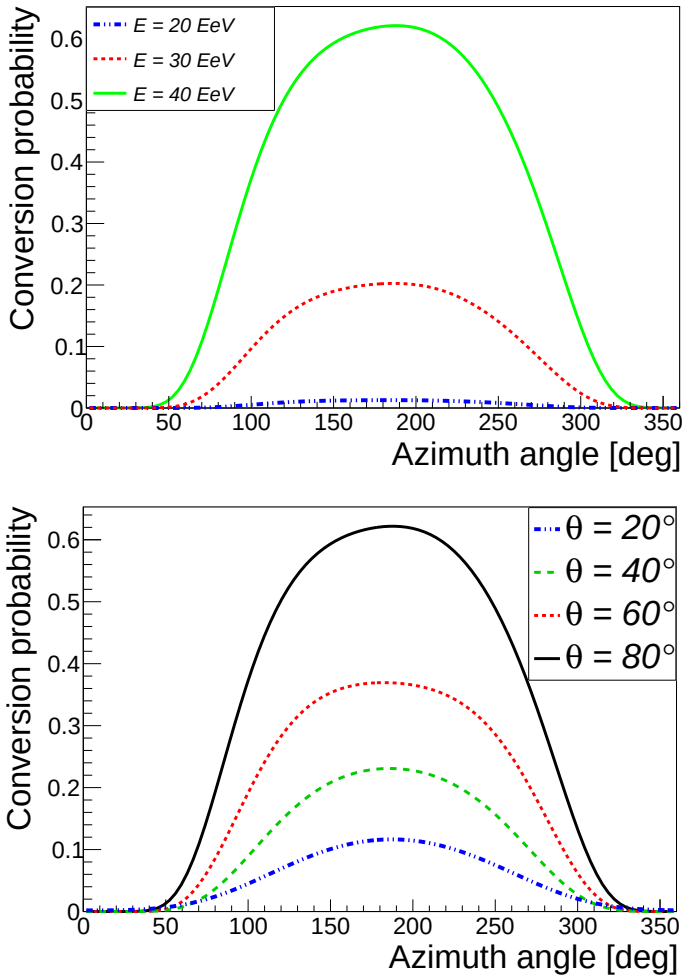

Figure 4.2: Probabilities of an UHE photon to convert into an e^+/e^- pair in the geomagnetic field. *Top*: Conversion probabilities at zenith angle $\theta = 80°$ for different primary energies. *Bottom*: Conversion probabilities for a 40 EeV primary photon at different zenith angles. Both plots are obtained for La Palma ($28°45'43.2''N, 17°53'31.2''W$) coordinates (azimuth angle, $\phi = 0°$ means that the particle comes from the geomagnetic South).

which the maximum conversion probability is reached, depends on the location of the observation site. For La Palma, which is on the northern hemisphere, the peak is observed in the direction of the geomagnetic North. This characteristic arises from the fact, that the geomagnetic field gets stronger as the geomagnetic axis is approached. For the case of La Palma site, photons coming from a more northern direction tend to travel nearer this axis compared to the ones having a more southern trajectory. Consequently, they experience a stronger magnetic field, and are more likely to create an e^+/e^- pair. The bottom panel of Figure 4.2 shows that the conversion probability also increases with the zenith angle.

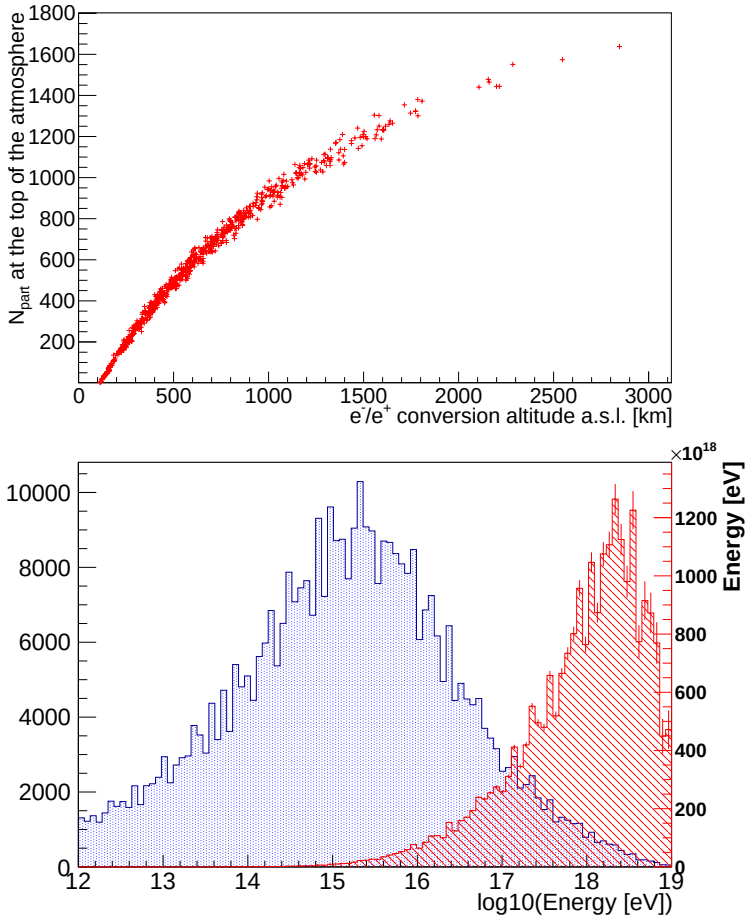

Figure 4.3: *Top*: Number of particles reaching the top of the atmosphere (at ∼100 km) as a function of the altitude at which a 40 EeV primary photon creates an e^+/e^- pair. *Bottom*: (Blue dotted histogram) Energy distribution of bremsstrahlung photons reaching the top of the atmosphere for 1000 simulations of UHE photon primary of 40 EeV, coming from direction defined by zenith and azimuth angles of $\theta = 80°$ and $\phi = 180°$, respectively. (Red hatched histogram) The same histogram weighted by energy (right Y-axis).

Such behavior can be explained by the fact that the geomagnetic field increases as the altitude decreases. Therefore, for nearly-horizontal arrival direction, the photon travels across a larger region of space where the geomagnetic field is the strongest.

If such conversion occurs, the e^+/e^- pair travels along the direction of the primary photon and its trajectory is slightly deflected due to the geomagnetic field. The main energy loss process being bremsstrahlung radiation, the probability of an electron with energy E to emit a photon between energy $h\nu$ and $h\nu + d(h\nu)$ over a distance dx can be described by Equation

2.6. For bremsstrahlung photons of the highest energy, pair production can occur again and the whole process previously described may repeat itself. In the case of a cascading 40 EeV primary photon, secondary photons do not create e^+/e^- pairs. The actual number of bremsstrahlung photons produced strongly depends on the altitude at which the primary photon creates the first pair, as shown on the top panel of Figure 4.3. Consequently, only the original e^+/e^- pair and an ensemble of photons reach the top of the atmosphere. The bottom panel of Figure 4.3 shows the energy distribution of the secondary photons of the preshower down to 10^{12} eV obtained from the simulation of 1000 preshowers, with secondary photons covering more than 7 orders of magnitude in energy.

In order to get an idea of the spatial distribution of particles at the top of the atmosphere, one can calculate the linear displacement Δx of the e^+/e^- pair due to its deflection from the primary photon trajectory caused by the geomagnetic field. It can be approximated by:

$$\Delta x \simeq \frac{L^2}{2R}, \tag{4.1}$$

where R is the radius of curvature of the e^+/e^- trajectory, and is approximately equal to 10^{13} km for a 20 EeV electron (the same for the positron which is deflected in the opposite direction than the electron due to its opposite charge) and for a typical transverse magnetic field of 0.1 G. With $L \simeq 1000$ km as the electron path length, $\Delta x \ll 1$ mm is obtained. Such a small spatial distribution is well below the resolution of UHECR and gamma-ray experiments, and the subsequent EAS produced by the collection of particles is seen as one single air shower.

In this dissertation, UHE photons coming at high zenith angles are the main focus. The reasons are two-fold: as discussed in the previous chapter, the photon/hadron separation is recovered at ultra-high energies when looking at nearly-horizontal EAS's, and the preshower effect occurs at high zenith angles. For the CTA-North site, the simulations are performed at zenith angle $\theta = 80°$ and azimuth angle $\phi = 180°$ (geomagnetic North direction). 40 EeV primaries are also considered, as they constitute a good compromise between conversion probability and simulations run time.

4.2 Extensive Air Showers with CORSIKA

The next link in the simulation chain is the simulation of atmospheric air showers. In this section, the program used in this endeavor is briefly introduced, along with the several options that have been chosen to run these simulations. Then, the results obtained for the longitudinal profiles and the

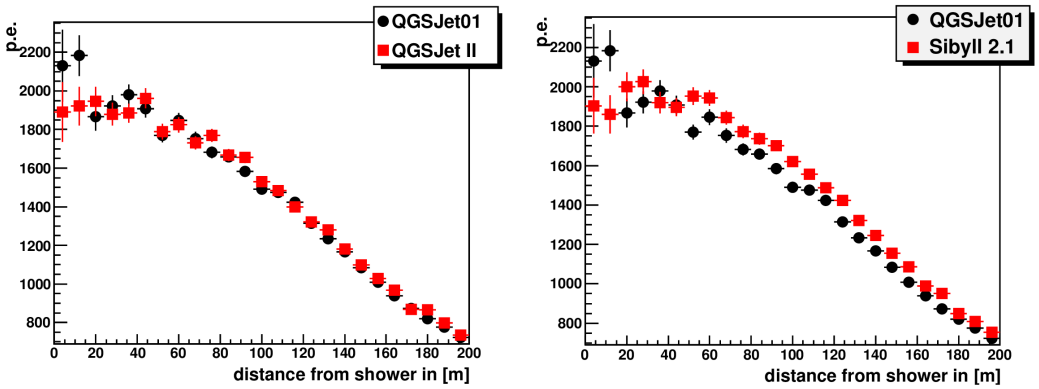

Figure 4.4: Cherenkov lateral profile of 1 TeV proton showers for different hadronic models: QGSJet01 [183], QGSJETII [184, 185] and Sibyll 2.1 [186].

ground distributions of particle in the case of a preshowering UHE photon, are presented. These results are also be compared to the ones from EAS's initiated by other primaries.

4.2.1 CORSIKA Simulation Software

EAS produced by high-energy particles can be simulated with the *Cosmic Ray Simulations for KAscade* (CORSIKA) [187] software, a Monte-Carlo simulation program that tracks the propagation of cascade particles in the atmosphere and implements particle interactions. It was originally developed for the KASCADE-Grande experiment[1] [188], but its constant improvement has made it into a powerful tool used in multiple experiments. UHECR observatories take advantage of the available ground distribution of particles, and gamma-ray telescopes obtain predictions of the shape of the images formed by the simulated Cherenkov light. As discussed in Section 1.1.3, particle interactions are described by models that may give different predictions for the average values of observables and for shower-to-shower fluctuations. In the TeV energy range, uncertainties between hadronic models are estimated around 5% for the lateral distribution of Cherenkov light [189]. Figure 4.4 shows the differences in these distributions between different hadronic models. In the UHE domain, the Cherenkov light is so abundant that variations from one model to another are expected to have little effect on the images formed on IACT cameras.

The CORSIKA program offers the possibility to investigate various features of EAS's, including their longitudinal profile and their lateral distribution on the ground. Unless specified otherwise, the CORSIKA version used in this work is 6.990 [190], with the QGSJETII-03 [184, 185] and the UrQMD

[1] website: web.ikp.kit.edu/KASCADE

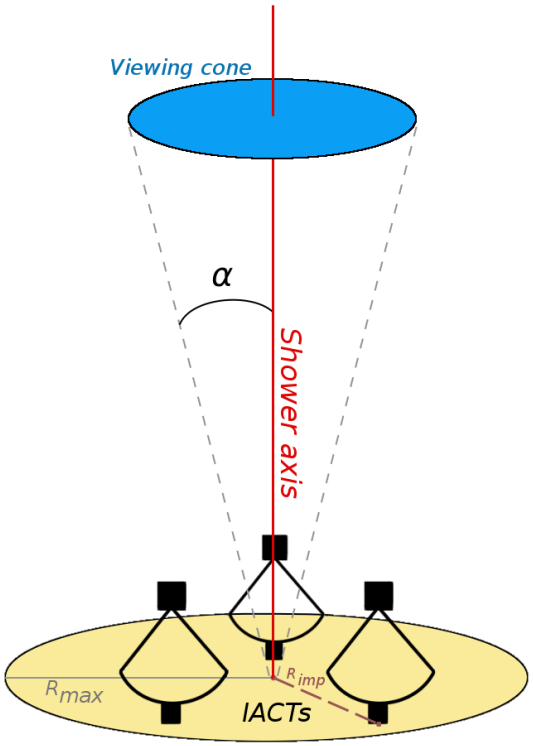

Figure 4.5: Geometry and parameters of the CORSIKA simulations: the maximum impact distance $R_{\max}$ of the shower axis and the viewing cone angle α within which a shower axis direction is randomly chosen.

[191, 192] hadronic models to simulate high and low energy interactions, respectively. The options that have been selected during the compilation of the program are described below.

List of Selected Options

- **PRESHOWER**: The preshower effect can be directly implemented within the CORSIKA simulations. It is the same as the stand-alone version discussed above, although the collection of particles at the top of the atmopshere is used as an input to the air shower simulation. The location of the observation site, as well as the time of observation, must be specified as the Earth's magnetic field is time-dependent. UHE photons that do not convert are discarded.

- **SLANT**: This option allows the description of longitudinal profiles as a function of the slant depth along the EAS axis, which is more appropriate for the study of nearly-horizontal air showers.

➢ **CURVED**: At high zenith angles, the curvature of the Earth must be accounted for. This curvature is described by a 5-layer model which evaluates the air density ρ_{air} for each layer, as a function of the altitude:

$$\rho_{\text{air}}(h) = a_i + b_i \exp\left(\frac{-h}{c_i}\right), \tag{4.2}$$

where a_i, b_i and c_i are free parameters for layers $i = 1, .., 4$ (layer 1 starting at sea level). The fifth and last layer is simply described by the relation $\rho_{\text{air}}(h) = a_5 - b_5 h/c_5$.

➢ **THIN**: As the number of secondary particles in an air shower roughly scales with the energy of the primary, it may become rapidly inefficient and time-consuming to track the propagation and the interactions of each one of these particles for EAS's produced by UHE primaries. To overcome this issue, the *thin sampling* method has been introduced [193]. The principle of such method is to define an energy threshold E_{thin} below which particles are no longer described invidually. Instead, if all particles within a group, produced via any interaction, has an energy E_i below E_{thin}, one particle is randomly chosen with a probability $p_i = E_i / \sum_j E_j$. For energy conservation purposes, a weight $w_i = w_p/p_i$ is attributed to the tracked particle, where w_p is the weight of the parent particle[2]. To limit artifical fluctuations due to the thin sampling method, especially far from the shower core, a weight limit w_{lim} beyond which the sampling is not performed anymore has been introduced. Any particle with a weight above that limit is individually tracked. In order to limit the increase in CPU usage due to this particular condition, an optimal weight limit can be found such that $w_{\text{lim}} = \epsilon E_0$, where $\epsilon = E_{\text{thin}}/E_0$. In this dissertation, the thinning is kept as low as possible such that CPU usage time does not exceed 3 days. For low energy primaries, the thinning is deactivated while for UHE particles, ϵ does not take values above 10^{-5}.

➢ **CERENKOV**: As the name suggests, this option activates the production of Cherenkov light by the charged particles in the air showers [194, 195]. The Cherenkov emission band is chosen between 250 and 700 nm and the angle of emission is considered independent of the wavelength. This option also allows the definition of a telescope array which center location can be randomized with respect to the location of the simulated shower core. Such feature enables the randomization of the shower core on a disk (of radius R_{max}) perpendicular to the shower axis, i.e. to the arrival direction defined by the zenith and azimuth angles

[2] $w_p = 1$ if the parent particle had an energy above E_{thin}, or >1 if below.

of the primary particle, as ilustrated in Figure 4.5. Single showers can therefore be used multiple times as the array center is shifted within the disk defined by $R_{\max}$.

➢ **VIEWCONE**: This option enables the definition of a cone of apex angle 2α, centered around the predefined shower direction, with its apex pointing towards the detectors. Showers are generated within this cone, which allows simulations of both point ($\alpha = 0°$) and diffuse ($\alpha > 0°$) sources (see Figure 4.5).

Unless specified otherwise, energy thresholds, below which particles are not longer tracked, have been kept to their default values: 0.3, 0.3, 0.003 and 0.003 GeV for hadrons, muons, electrons and gammas, respectively.

4.2.2 Longitudinal Profile and Ground Distribution

As stated in Section 3.2, looking at nearly-horizontal EAS's allows the observation of the muonic component, which can be used to discriminate EAS's induced by cosmic rays from the ones produced by gamma rays. In order to investigate how the longitudinal profiles of nearly-horizontal air showers produced by 40 EeV primaries differ from other primaries, EAS's generated by iron nuclei, protons and photons, with and without the preshower effect, were simulated for the direction defined by the zenith and azimuth angles $\theta = 80°$ and $\phi = 180°$, respectively. While the longitudinal profiles of all considered primaries follow the same pattern, i.e. a peak due to the electromagnetic component followed by a slowly decreasing plateau emerging from muons, the absolute number of muons produced by these primaries varies, as illustrated on the top panel of Figure 4.6. As discussed in Chapter 1, the hadronic component being weaker in showers initiated by photons, EAS's produced by protons and iron nuclei are more muon-rich. Moreover, as predicted by Equation 1.36, air showers produced by iron nuclei have a larger muon content than the ones initiated by protons. On the other hand, the muon content of EAS's induced by photons that have first converted in the geomagnetic field is fairly similar to the one of those induced by unconverted photons. The small discrepancy can be explained by the fact that photons that have "preshowered" generate photons of lower energies that reach the atmosphere, resulting in a smaller cross section of photo-pion production, which is responsible for the muonic component in electromagnetic showers (see Section 1.1.2). The bottom panel of Figure 4.6 shows the different components of photon-induced EAS's with preshower effect. In the early stages of air shower development, the electromagnetic component dominates and reaches a maximum. However, due to

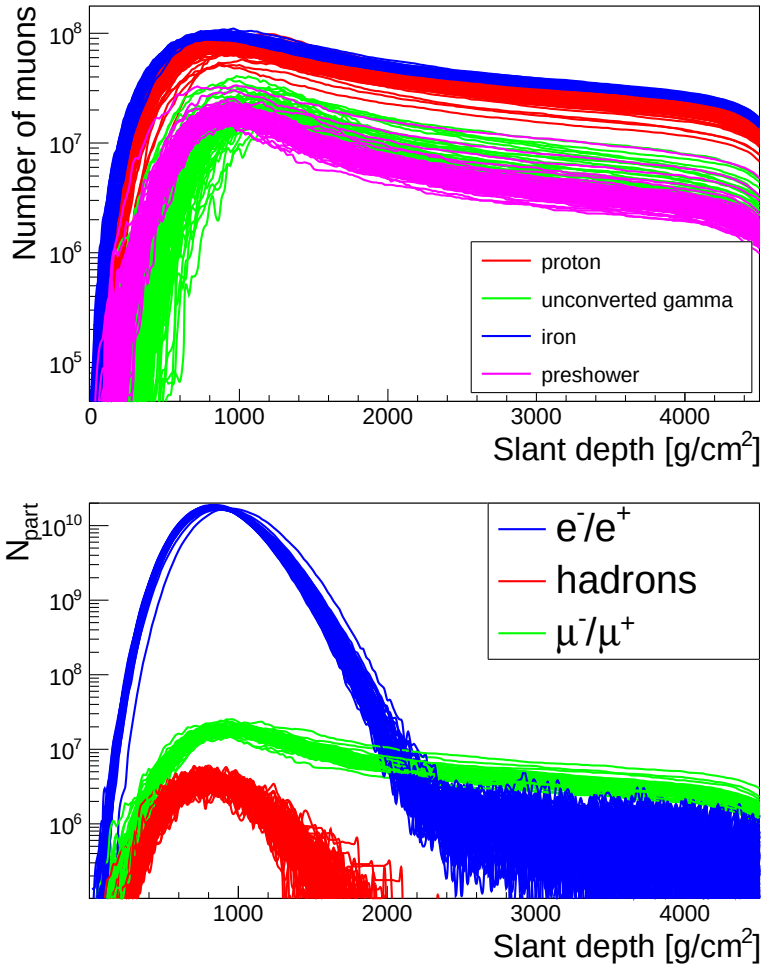

Figure 4.6: *Top*: Longitudinal development of the muonic component of nearly-horizontal EAS's produced by 40 EeV primaries. *Bottom*: Longitudinal profiles of electrons, hadrons and muons of 10 nearly-horizontal EAS's produced by 40 EeV photons affected by the preshower effect. NOTE: the location of the CTA-North site at 2200 m is equivalent to a slant depth of 4550 g/cm^2 at 80° zenith angle.

ionization and bremsstrahlung emission, electrons and positrons suffer significant energy losses and as a consequence, their number in the later stage of the shower drops drastically once the EAS maximum is reached. On the other hand, muons tend to lose energy through the same processes on much larger distances, resulting in an accumulation of these particles as the EAS development progresses and in the existence of a muon plateau.

The top panel of Figure 4.7 shows the $X_{\max}$ distributions for all the primaries considered. As seen in this plot, EAS's initiated by preshowers tend to reach their maximum higher in the atmosphere than the ones produced by

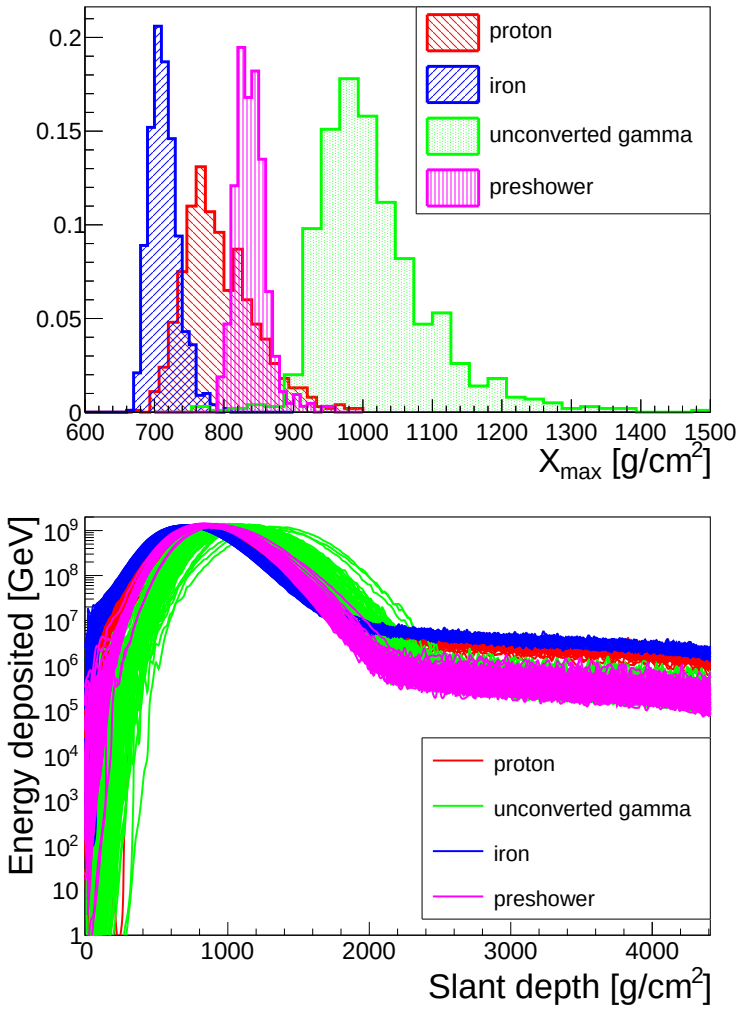

Figure 4.7: *Top*: $X_{\max}$ distribution of the nearly-horizontal EAS's initiated by 40 EeV primaries. *Bottom*: Energy deposited in the atmosphere by the Cherenkov light emitted by the same EAS's. NOTE: the location of the CTA-North site at 2200 m is equivalent to a slant depth of 4550 g/cm^2 at 80° zenith angle.

unconverted UHE photons. This is largely due to the fact that the first interaction point (where the $\gamma \to e^- e^+$ conversion occurs) is located up to several thousands of kilometers above the atmosphere. Such property makes EAS's from "preshowered" photons more similar to hadronic ones, such that experiments relying solely on $X_{\max}$ measurements may misinterprete the primary identification if such an effect is not taken into account. The evolution of the energy deposited in the atmosphere by the Cherenkov radiation is shown on the bottom panel of Figure 4.7. This evolution closely follows the longitudinal profiles of charged particles, with the electromagnetic "bump" and the muon

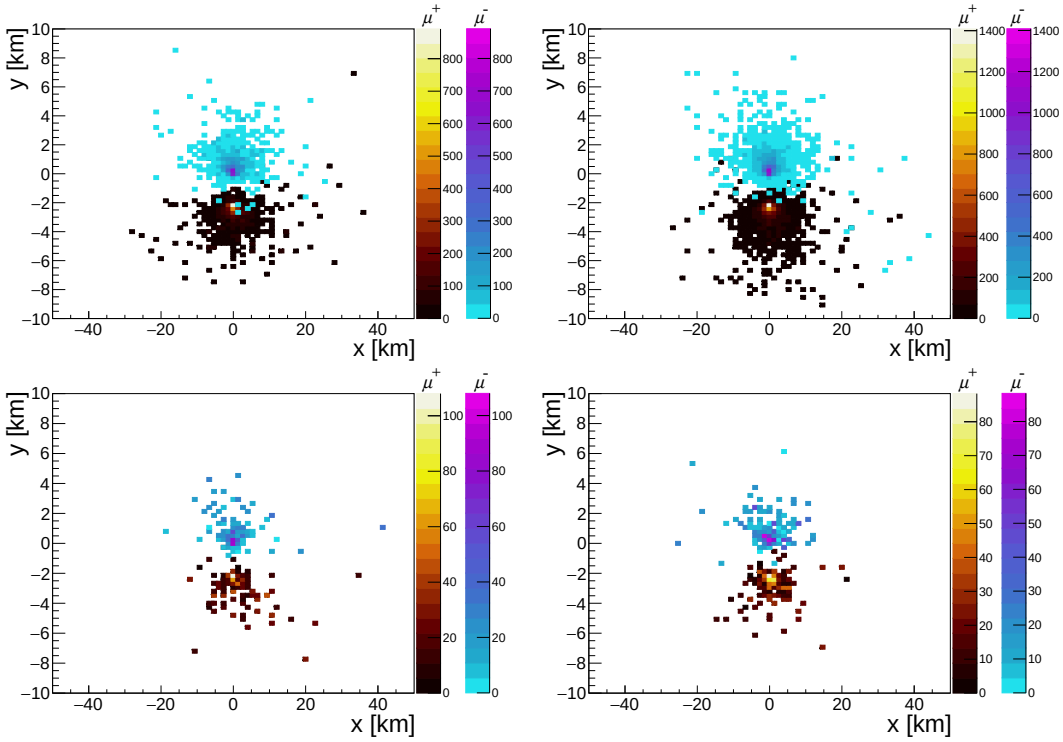

Figure 4.8: Distribution of negative and positive muons at ground level (2200 m a.s.l.) for nearly-horizontal EAS's initiated by 40 EeV protons (top left), iron nuclei (top right), unconverted gammas (bottom left) and UHE photons with preshower effect (bottom right). Showers are coming from the positive x direction. For visualization purposes, the distribution of positive muons is shifted by 2 km in the negative y direction.

plateau clearly visible. One striking feature is the fact that, while the bump is only slightly shifted due to the different average $X_{\max}$ for different primaries, the peak value of Cherenkov emission remains the same for all of them, meaning that, at $X_{\max}$, the amount of Cherenkov light produced depends very little on the type of primary. However, differences start to appear when the muon plateau emerges and their relative Cherenkov light abundance is similar to the longitudinal profile of muons shown in Figure 4.6. The study of the longitudinal profiles with IACTs may in fact provide additional information on the energy and on the type of the particles and reduce the uncertainties on both parameters. A method to measure the $X_{\max}$ of EAS's with IACTs is presented in [196], achieving resolutions $< 15\,\mathrm{g/cm^2}$ in the best cases for gamma rays, protons and iron nuclei. Such study is however limited to the energy range between 10 TeV and 300 TeV as well as to 20° zenith angle, and additional research in the case of UHE nearly-horizontal showers would be necessary for preshower observations.

Due to the different abundances of muons in EAS's produced by photons

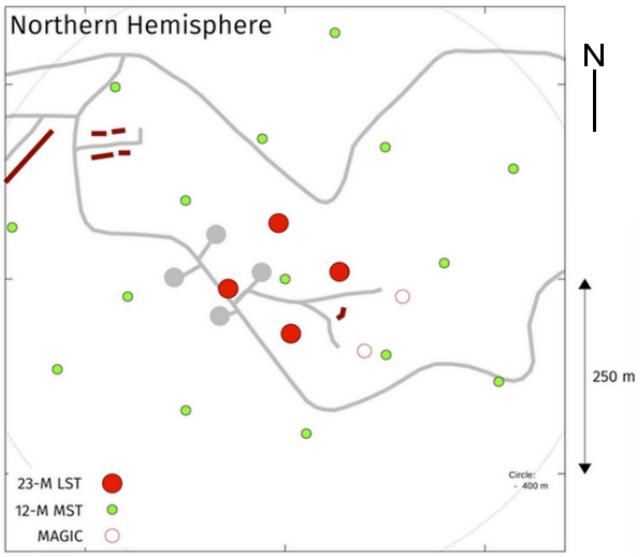

Figure 4.9: Lay-out of CTA-North, taken from *https://www.cta-observatory.org/about/array-locations/la-palma/*. Since the time the simulations were performed, the planned layout for CTA-North was slightly modified and is different from the one presented in this plot.

and by hadrons, and to the more narrow lateral spread of the former ones, the ground distribution of muons also constitutes a powerful discriminator to identify the nature of primaries. Such a distribution is plotted in Figure 4.8 for all previously considered primaries, with the negative and positive muon components separated. The abundance of muons follows the longitudinal profiles order discussed in the previous section, with iron-induced EAS's being the most muon-rich and converted UHE photons air showers being the least. Although a shift of 2 km in the negative y direction was applied to the distribution of positive muons for better visualization, the separation between μ^- and μ^+, due to the influence of the geomagnetic field, is clearly visible. The size of the footprint is characteristic of nearly-horizontal air showers, i.e. extended in the direction of the shower, with muons being spread over more than 60 km (30km) in the x direction for iron nuclei (converted UHE photons) events.

Although muons are much less efficient at emitting Cherenkov radiation than electrons, their preponderance in the late stage of the EAS development, as well as the fact that muons emits such radiation closer to the surface, make the muonic component detectable by telescopes looking over the horizon.

4.3 CTA-North Detectors Response

The detection of the Cherenkov light is performed by the cameras of IACTs. CORSIKA's outputs are piped into *sim_ telarray* [194, 195], a software that simulates the detectors response of the telescopes array, including the camera electronics, the optical-ray tracing and the recording of photons in the photo-multiplier tubes. The *production-I* settings allow us to define the properties of each type of the telescopes planned to be part of the array in La Palma (4 LSTs and 15 MSTs, in the configuration shown in Figure 4.9). The number of pixels needed for each telescope to be triggered is set to 3, and the number of telescopes needed to trigger the system is left to the default value of 2. A background of photo-electrons (p.e.) is simulated at 122 MHz (0.122 p.e./ns) for each telescope, in order to account for the night-sky background (NSB). The telescopes pointing direction is set to the $\theta = 80°$, $\phi = 180°$ direction with an offset of 0.5° in zenith angle for the preshower simulations. Such offset is introduced to simulate a wobble mode of observation, as documented and used in the case of the MAGIC telescope. Such observation mode consists in pointing the telescopes slightly off the source. By doing so, both background and signal can be measured with the same systematics, as the background is measured with the same zenith angle and the same weather conditions [197].

The energy cuts given in Section 4.2.1 lead to a large amount of emitted Cherenkov light, that saturates the PMTs of the cameras. For this reason, these cuts were increased up to 6000, 4000, 500 and 500 GeV for hadrons, muons, electrons and gammas, respectively. The impact of energy cuts on the shower development and on the characteristics of the camera images is studied in the last chapter. The maximal impact distance $R_{\max}$ is set to 1300 m in order to insure that a large fraction of the simulated events triggers the array. Figure 4.10 shows the location of the impact point of EAS's initiated by UHE photons with preshower effect and that have triggered the array. The array is located at the (0,0) coordinates and the telescopes are pointed parallel to the x axis, in the positive x direction, which corresponds to the arrival direction of the showers. While the area of the array is about 0.6 km^2, the ellipse forms a collection area of approximately 15 km^2, which can be increased if larger $R_{\max}$ values are used (see Section 6.3.1). Considering an efficiency of 1, such area provides a rough estimation of 2.6 km^2 for the aperture of CTA-North at 80° zenith angle. Compared to the typical aperture of ~ 0.1 km^2 for IACT experiments in the standard vertical mode of observation, a considerable gain is obtained in the nearly-horizontal direction, as previously illustrated in Figure 3.7.

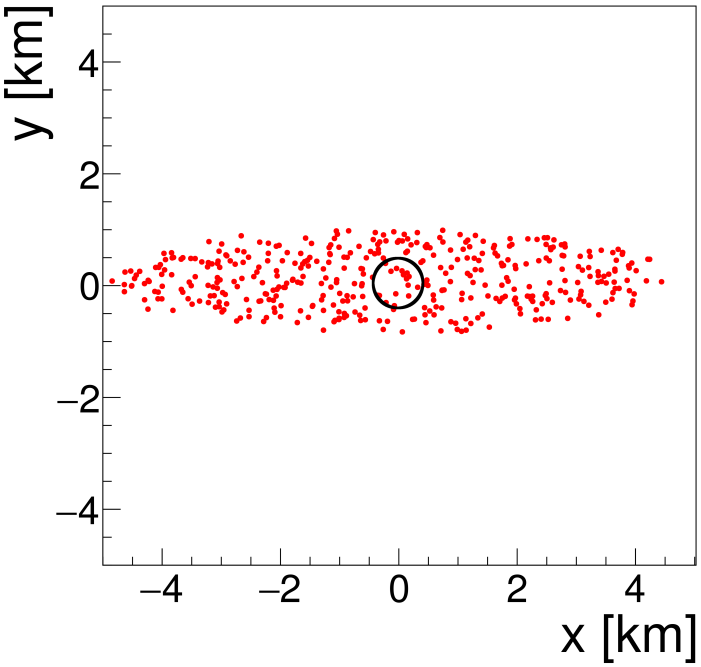

Figure 4.10: Location of impact points (red dots) of EAS's produced by preshowering UHE photons that have triggered the array located at (0,0), which is represented by a black circle of area 0.6 km^2. Showers are coming from the positive x direction, parallel to the x axis.

4.3.1 Hillas Parameters Distributions

As previously discussed, the nearly-horizontal mode of observation with IACTs is effective at very and ultra-high energies. For primaries with energy between a few GeV and a few TeV, the images formed in the cameras consist of 1 or 2 pixels, leading to a photon/hadron separation of poor quality. In order to recover a good separation, higher energies must be observed, as illustrated by the recent observation of the Crab nebula by the MAGIC collaboration in the zenith angle range $70° - 80°$ [198]. In the EeV regime, the size and the features of the images enable their description via the Hillas parameters, which are used to retrieve this photon/hadron separation. The distributions of the Hillas parameters discussed in Chapter 3 are shown in Figure 4.11 for 40 EeV protons, converted and unconverted photons. The *size*, *witdh*, *length* and *distance* distributions all display several peaks, which are characteristic of the existence of images with significantly different geometrical features, and of the fact that the CTA-North array is composed of telescopes with different properties. Nevertheless, these distributions clearly show that images formed by EAS's produced by converted UHE photons are both dimmer and smaller than the ones from protons, as illustrated in Figure 4.12. The conversion of

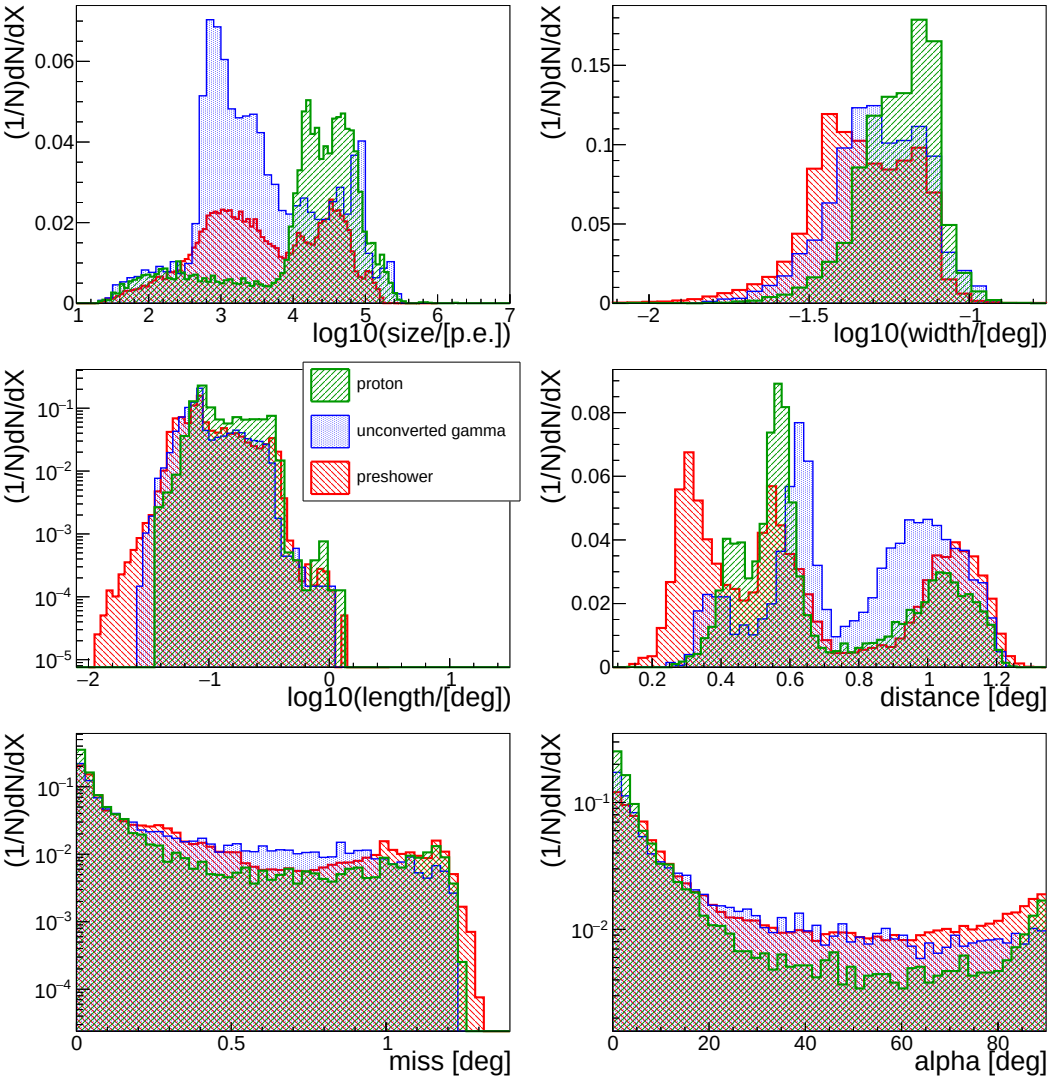

Figure 4.11: Distributions of the Hillas parameters for nearly-horizontal EAS's produced by 40 EeV protons, converted and unconverted photons, using the *sim_telarray* configuration described in the text.

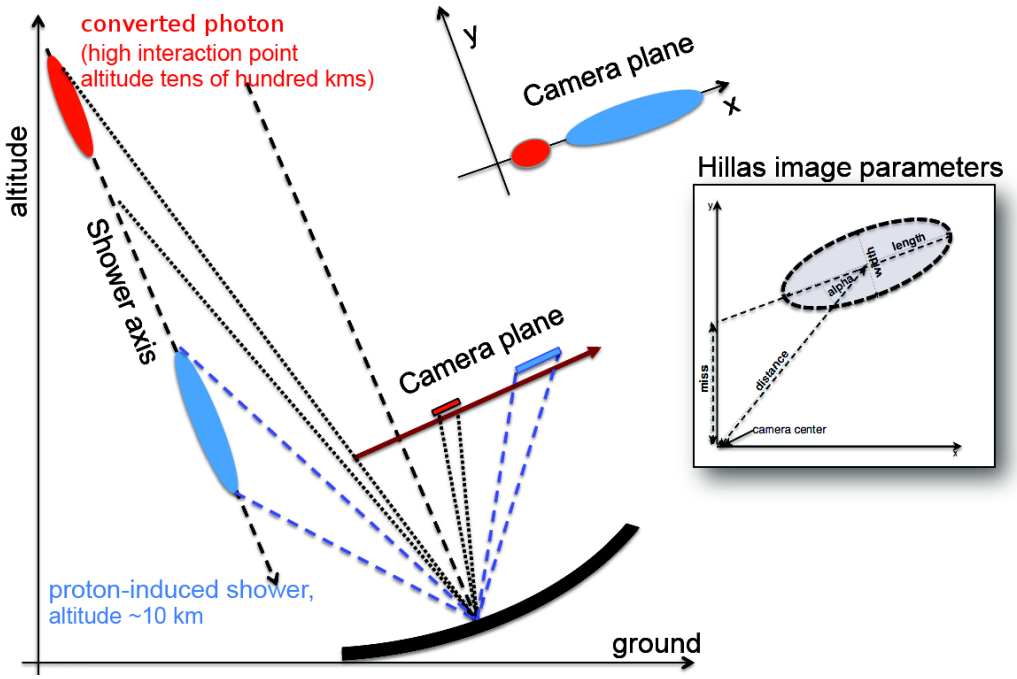

Figure 4.12: Schematic view of how the primary interation point location affects the Hillas parameters of the images formed on the cameras of IACTs.

an UHE photon produces multiple photons in the EeV regime, which initiate EAS's. These EAS's reach their maximum development at a much closer distance to the IACTs than the ones produced by the UHE protons. However, proton-induced EAS's contain far more muons and may generate brighter images, as illustrated by the *size* distributions. One common feature is the existence of ring-shaped images which are characteristic of the muonic component. Nonetheless, as previously highlighted, images formed by hadronic EAS's tend to be more irregular and larger compared to the one of EAS's produced by photons. Consequently, the *length* and *width* distributions show a greater proportion of large events in the case of proton-induced showers. On the other hand, one should note that images formed by converted-photon showers are smaller than the ones from unconverted photons, due to the fact that the maximum of Cherenkov emission is reached further away from the telescopes (see right panel of Figure 4.7) in the first case. Secondly, the higher altitude of the first interaction point of converted photons, due to the preshower effect, leads to smaller angles between the incident angle of the Cherenkov light onto the IACT mirrors, and the reflected angle onto the cameras (see Figure 4.12). Therefore, in the case of preshowers, the distance between the center of the images and the simulated source is lower, and events with smaller *distance* parameter values are expected. Finally, the *miss* and *alpha* distributions are

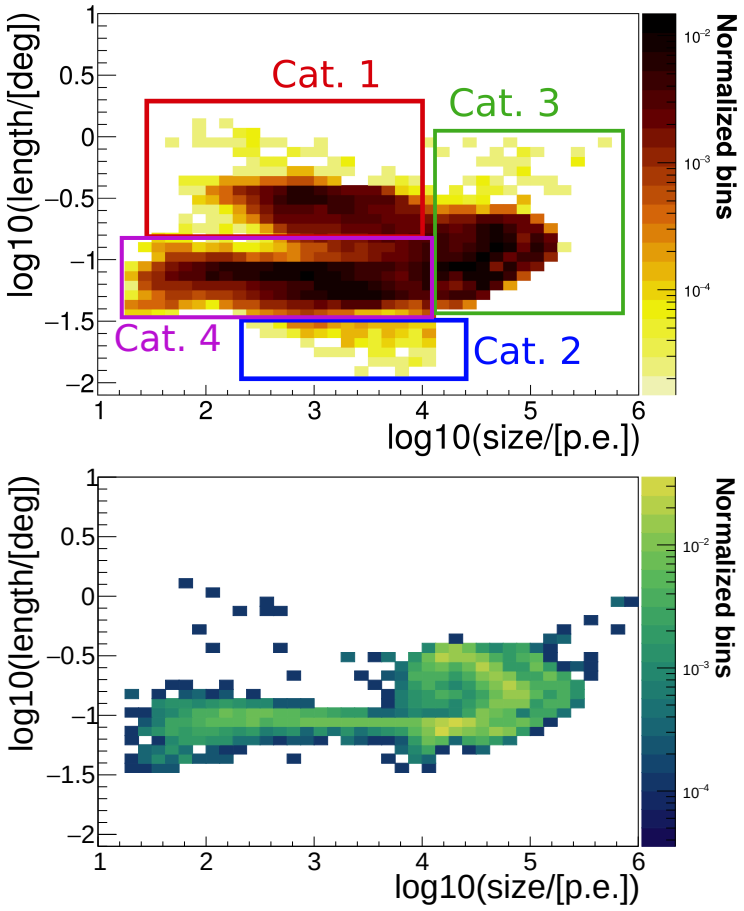

Figure 4.13: Scatter plot of *size* vs. *length* parameters for converted UHE photons (top) and for protons (bottom). Categories of phase spaces are highlighted in rectangles. **Category 1**: $\log_{10}(size) < 4$ and $\log_{10}(length) > -0.8$. **Category 2**: $\log_{10}(length) < -1.5$. **Category 3**: $\log_{10}(size) > 4$. **Category 4**: $\log_{10}(size) < 4$ and $-1.5 < \log_{10}(length) < -0.8$.

characteristic of images formed mostly by the muon component, with an angular distance between the simulated source and the major axis of the image reaching values up to a few degrees and their relative orientation spanning the full range of possible angular values ($[0°; 90°]$).

Figure 4.13 shows the scatter plot of the *size* and *length* parameters for both proton and converted photon primaries. In the latter case, several clusters are clearly distinguishable and consequently, they have been assigned to different categories for further analysis. When compared to the proton scatter plot, one can observe that categories 1 and 2 are exclusive to converted photons. They correspond to large dim images and small images, respectively. Such difference between the two plots could be used to provide a rough classification of observed events. Within categories 1, 3 and 4, distinct bands are also

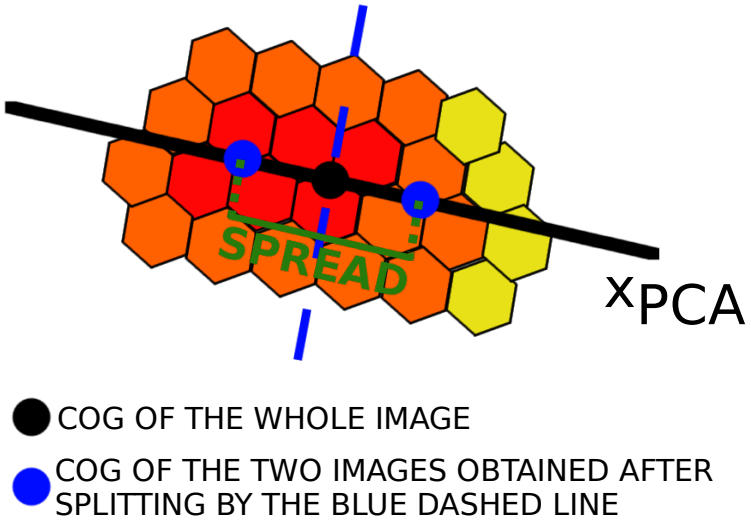

Figure 4.14: Schematic view of the PCA. The principal axis x_{PCA} minimizes the variance of the pixels coordinates. The blue dashed line split the image in two, perpendicularly to x_{PCA} and through the COG of the image. The *spread* parameter characterizes the distance between the COG of the two images newly defined on each side of the blue dashed line. The intersection between x_{PCA} and the blue dashed line, which defines $x_{\mathrm{PCA}} = 0$.

noticeable due to the two different telescope types that compose CTA-North.

4.3.2 Camera Images

The images formed in the cameras of the telescopes are constituted of pixels representing each of the PMTs. The Cherenkov light produces photo-electrons which are registered if the resulting signal is above a given threshold. The images have therefore a geometry that is defined by the distribution of triggered pixels in the camera. This distribution can be analyzed via a principal component analysis (PCA) [199] which general purpose is to find the axis that minimizes the variance of any dataset. In the general case, IACT images are elliptical and such axis often corresponds to the major axis. The principle of the PCA applied in this context is illustrated in Figure 4.14. Once the principal axis (x_{PCA}) is found, the image is splitted in two through its center-of-gravity (COG), perpendicularly to x_{PCA}. Such operation allows to define two new COG and a *spread* parameter that represents the distance between them. In this analysis, the coordinates of the pixels are previously normalized such that comparison between different categories of images or between images stemming from different types of telescopes, can be performed. The intersection between x_{PCA} and the blue dashed line defines $x_{\mathrm{PCA}} = 0$. Next,

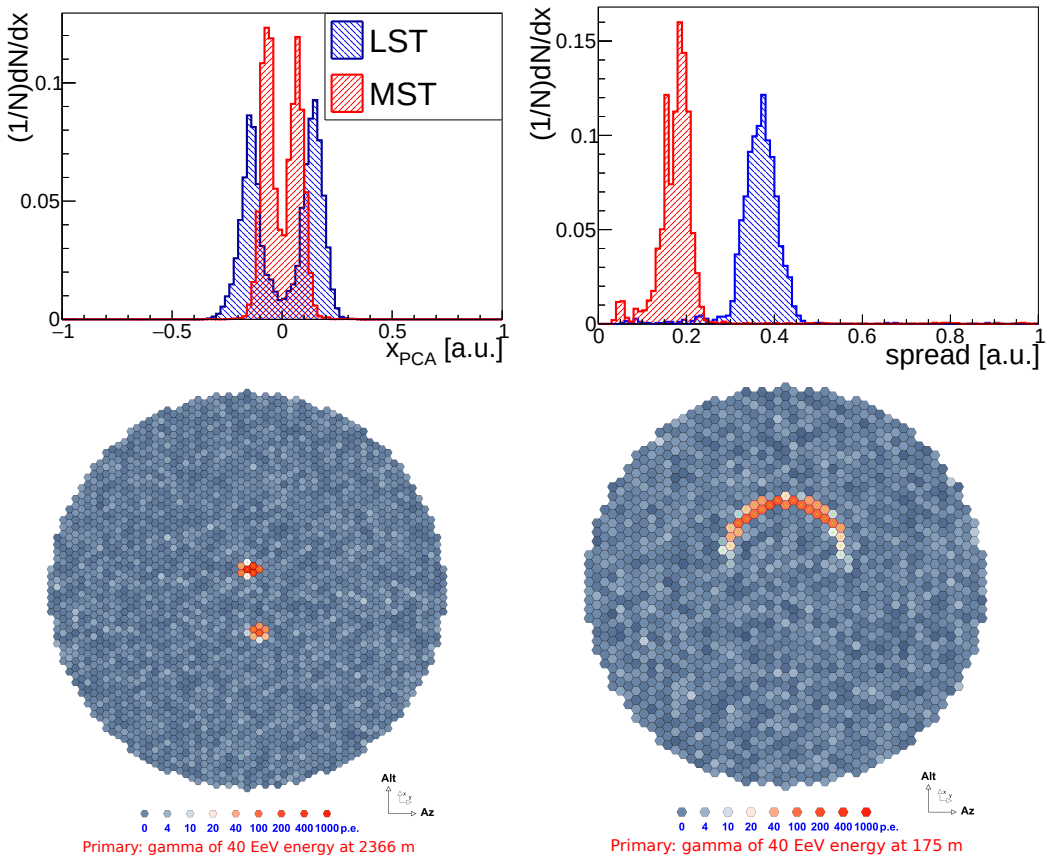

Figure 4.15: PCA analysis of converted UHE photons events falling into the **Category 1** of *size* vs. *length* scatter plot. *Top panel*: Distributions of the projection of the triggered pixels coordinates onto the PCA axis, weighted by the signal in the pixel (left) and of the distance between the center of gravity of the two images formed after splitting of the initial image at $x_{\mathrm{PCA}} = 0$ (right). LST and MST results are shown separately. *Bottom panel*: Examples of images from LSTs (left) add MSTs (right).

the pixels coordinates and intensity are projected onto x_{PCA} to quantify the images features. In this section, the PCA is applied to the categories of Figure 4.13 previously defined, in order to identify the features that may be expected in the observation of air showers initiated by converted UHE photons.

➢ **Category 1**: This category contains the largest images and can be used to reject UHE protons. The top-left panel of Figure 4.15 shows the presence of two distinct peaks in the projection of the pixels intensity onto the principal axis, for both LSTs and MSTs. These peaks are especially apparent for the former type of telescopes and are characterized by a larger distance between them. Such a feature is well exhibited by the *spread* distributions in the top-right panel of Figure 4.15, showing a larger mean

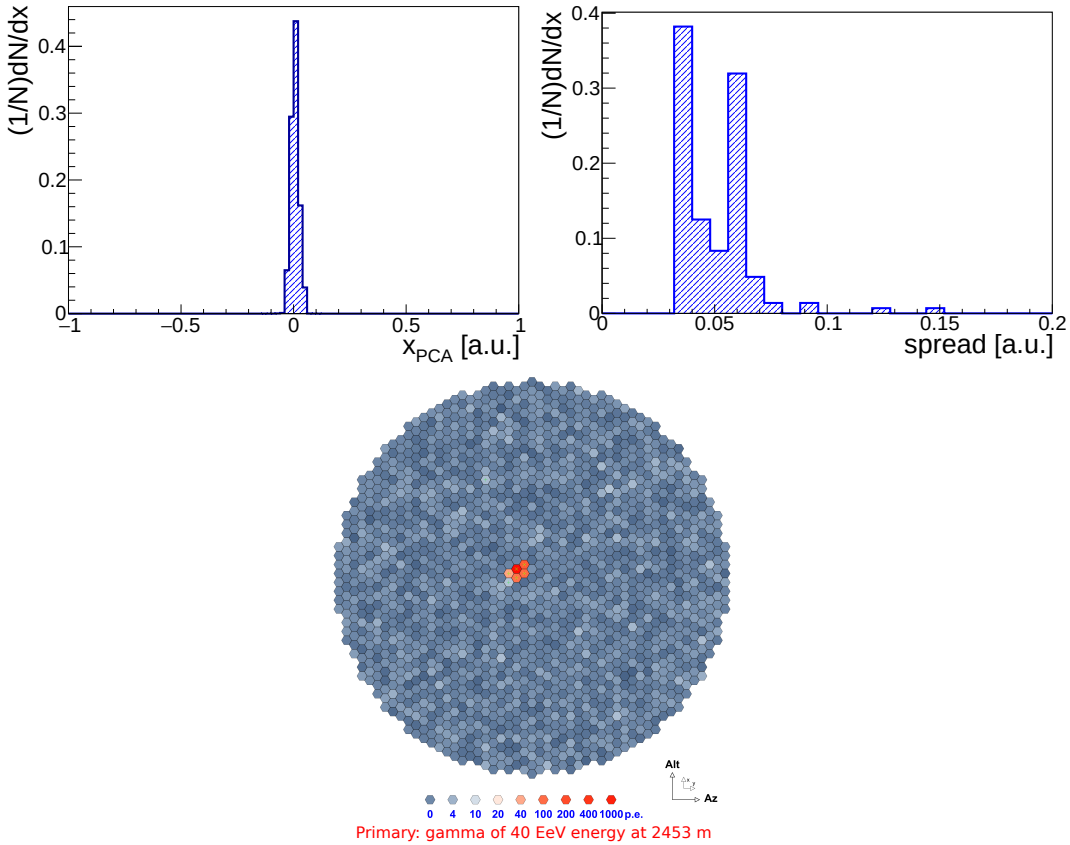

Figure 4.16: Same as in Figure 4.15 but for **Category 2**. Note that only MSTs are considered in this catagory as no image from LSTs meets the criteria of **Category 2**.

value. Filters, such as setting a minimum distance of empty pixels between the COG of the two images obtained after splitting, can be applied to identify whether these peaks are due to continuous images or whether they are due to several individual images that are in fact formed in the camera. Because LSTs display more prounounced peaks, finding cameras recording two individual images is expected, as seen in the bottom-left panel of Figure 4.15. Such expectation has been influenced by the study found in [200], where the possibility to find two individual images in IACT cameras formed by sub-showers, one led by a positron and the other by an electron, is discussed. Due to their opposite charge, the geomagnetic field may move these sub-showers apart and two images may be formed in the cameras. In the nearly-horizontal scenario, the same phenomenon may be happening for positive and negative muons, as the ground distributions of Figure 4.8 show. On the other hand, MSTs seem to show a larger fraction of partial muon rings, and a stronger intensity

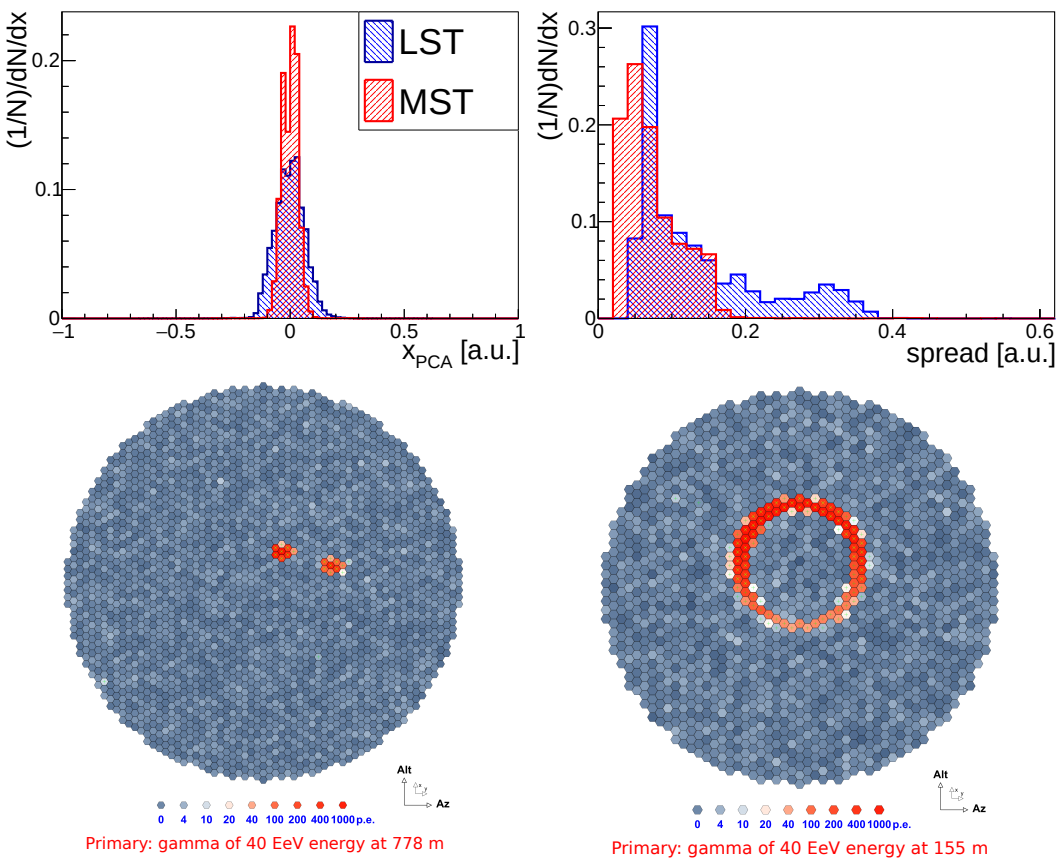

Figure 4.17: Same plots as in Figure 4.15 but for **Category 3**.

of pixels at $x_{\mathrm{PCA}} < 0$ or $x_{\mathrm{PCA}} > 0$ could explain the fact that the two peaks are less marked.

➢ **Category 2**: Also exclusive to converted photon primaries, this category includes small images composed of 3 to 5 adjacent triggered pixels which are only found in MSTs. The projection on the principal axis results in a very narrow peak shown in the top-left panel of Figure 4.16 and the splitting of the image in two naturally leads to very small distances between the two subsequent COG (top-right panel of Figure 4.16). An example of such image is shown in the bottom panel of Figure 4.16.

➢ **Category 3**: This category, common to proton and converted photon primaries, contains the brightest images. However, because the *length* parameter covers a large range of values, images of all sizes and geometrical shapes can be found, explaining the absence of multiple peaks and the size of the distribution width situated between the ones of categories 1 and 2 (see top-left panel of Figure 4.17). The *spread* distributions in

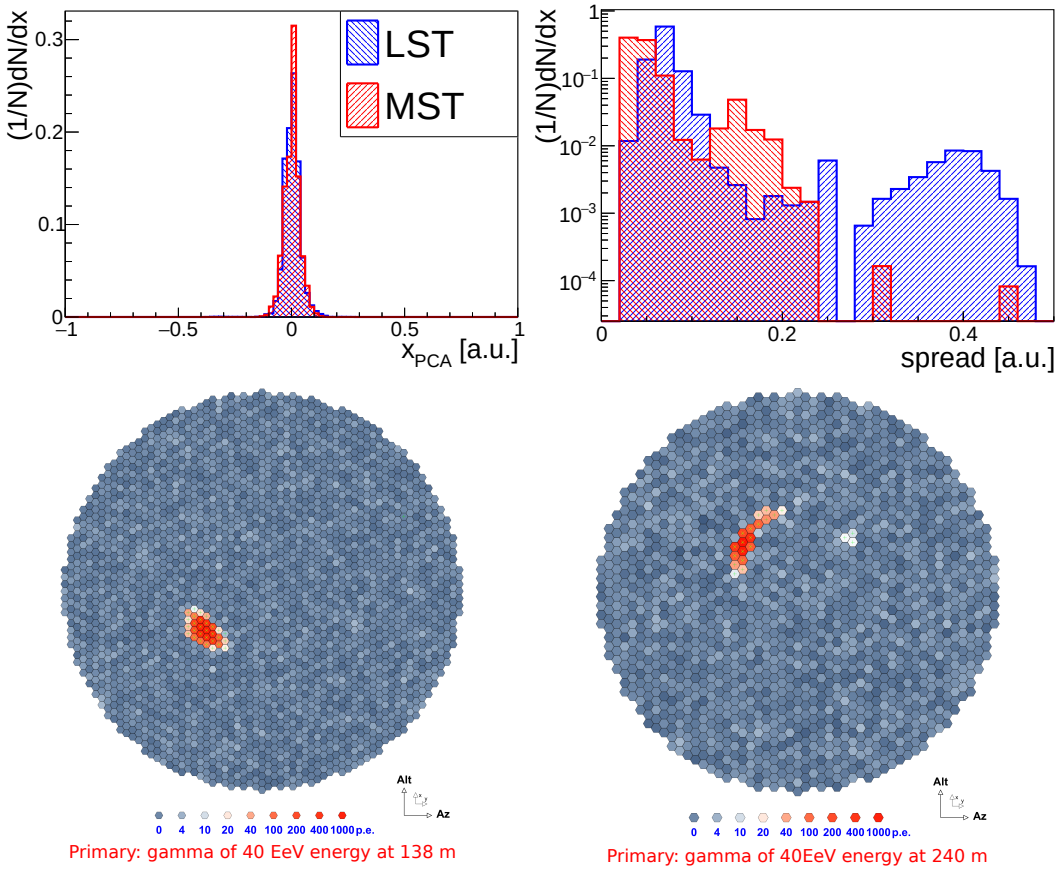

Figure 4.18: Same plots as in Figure 4.15 but for **Category 4**.

the top-right panel of Figure 4.17 also show a wider range of distance between the COG of the two images obtained after splitting. Typical images are shown in the bottom panel of Figure 4.17: couple of images (as in Category 1 but brighter) and full muon rings.

➢ **Category 4**: In this category, also found for both primaries, the *size* parameter spans over a large range of value while the *length* parameter covers a domain large enough to include different types of images, with narrow peaks of the pixel projection onto the principal axis for both types of telescopes (see top-left panel of Figure 4.18). On the other hand, the *spread* distributions shown in top-right panel of Figure 4.18 exhibits larger distances between the COG of the images obtained after splitting in the case of MSTs. Similarly to category 1, partial muon rings can be found in MSTs (see bottom panel of Figure 4.18). However, their fraction is lower and MSTs of category 4 mostly contain images like the one shown in the bottom-left panel of Figure 4.18 but smaller.

5. Evaluation of the Photon/Hadron Separation

In observational astronomy and for any channel of observation, the sensitivity of a telescope is directly related to the efficiency with which one can extract signal from background. In the case of gamma-ray astronomy, the background is composed of EAS's generated by an isotropic flux of cosmic rays. In order to correctly discriminate these EAS's against the ones produced by preshowers, a multivariate analysis based on the characteristics of the camera images has to be performed. Although several methods exist (as discussed in [201]), the use of *Boosted Decision Trees* (BDT) has proven to be the most efficient at improving the background rejection in the leading gamma-ray experiments, such as H.E.S.S. [202] and MAGIC [203]. In this chapter, we briefly review the basic elements of the BDT analysis developed in the TMVA package [204], and we evaluate the preshower/cosmic-ray background separation for different preshower scenarios. The sets of parameters used for different preshower scenarios are specified in the *PRESHW-1300Y* format, where Y refers to the nature of the source (P if it is a point source with $\alpha = 0°$ or D if it is a diffuse source with $\alpha = 5°$), and where $R_{\rm max} = 1300$ m. In these scenarios, the same parameters are used as for the previous chapter: the zenith and azimuth angles are set to $\theta = 80°$ and $\phi = 180°$, respectively; the primary energy $E = 40$ EeV; and the energy cuts are 6000, 4000, 500 and 500 GeV for hadrons, muons, electrons and gammas, respectively.

5.1 Background Simulation

The cosmic-ray background was simulated for a pure composition of protons, for the maximum impact distance $R_{\rm max} = 1300$ m, a viewing cone angle $\alpha = 5°$, and for an energy range extending from 10 TeV to 10 EeV (13 energies simulated as shown in the first row of Table 5.1). Due to the lower energies involved than in the case of preshowers, the energy cuts were set to the default values of 0.3, 0.3, 0.003 and 0.003 GeV for hadrons, muons, electrons and gammas, respectively. The simulated differential spectrum of cosmic rays takes into account the steepening in the knee region (~ 3 PeV) and the hardening around the ankle (~ 3 EeV), and is described as follow:

$$\frac{dN_{\rm CR}(E)}{dE} = N_0 \left(\frac{E}{E_0}\right)^{-\Gamma}, \tag{5.1}$$

expressed in $\mathrm{m^{-2}s^{-1}sr^{-1}TeV^{-1}}$(see footnote[1] for the set of parameters used at different energy ranges). Figure 5.1 and the third row of Table 5.1 show the

[1] $\{N_0, E_0, \Gamma\}$ is $\{10.9 \times 10^{-2}, 1\,\mathrm{TeV}, 2.75\}$ for $E < 3$ PeV [205]; $\{2.98 \times 10^{-11}, 3\,\mathrm{PeV}, 3\}$ for $3\,\mathrm{PeV} \leq E < 3\,\mathrm{EeV}$; and $\{2.98 \times 10^{-20}, 3\,\mathrm{EeV}, 2.75\}$ for $E \geq 3$ EeV.

differential spectrum of expected cosmic rays for an observation time Δt of 30 hours:

$$\frac{dN_{\mathrm{CR,exp}}}{dE} = A \times \Delta t \times \Omega \times \frac{N_{\mathrm{trig}}(E)}{N_{\mathrm{sim}}(E)} \frac{dN_{CR}(E)}{dE}, \tag{5.2}$$

where $A = \pi R^2_{\mathrm{max}}$ is the simulated area in the plane perpendicular to the shower direction, $\Omega = 2\pi(1 - \cos(\alpha))$ is the solid angle and $N_{\mathrm{trig}}(E)/N_{\mathrm{sim}}(E)$ is the fraction of cosmic-ray events of energy E triggering the array. For each energy, we simulated $N_{\mathrm{sim}}(E) = 1500$ showers and the number $N_{\mathrm{trig}}(E)$ which triggered the array is given in the second row of Table 5.1. The number of expected cosmic-ray events above an energy E is simply obtained by integrating Equation 5.2 over the appropriate energy range and considering the differential cosmic-ray spectra previously described. The results are shown in the last row of Table 5.1.

Figure 5.2 (top) shows the number of telescopes triggered by the simulated cosmic-ray background as well as by point (*PRESHW-1300P*) and diffuse (*PRESHW-1300D*) sources of preshower. As can be seen, the cosmic-ray background tends to trigger fewer telescopes than preshowers. This difference can be explained by the fact that the cosmic-ray background observed by the array is dominated by air showers generated by low-energy particles ($\sim$TeV) which contain muons of lower energy than in the case of preshower-induced air showers. Hence, the amount of Cherenkov light produced by these muons is not sufficient to irradiate and trigger a large number of telescopes. It should be noted that the few cosmic-ray events that trigger a large number of telescopes (15 and above) correspond to the upper end of the simulated energy range (10 EeV). The bottom panel of Figure 5.2 shows the discrepancy between the simulated $\vec{V}_{\mathrm{sim}}$ and reconstructed $\vec{V}_{\mathrm{rec}}$ directions via the ψ

E [TeV]	10	30	100	300	10^3	3×10^3	10^4
N_{trig}	121	446	865	1100	1219	1321	1382
$dN_{\mathrm{CR,exp}}/dE$ [TeV^{-1}]	214238	38509	2725	169	7	0.36	0.01
$N_{\mathrm{CR,exp}}(> E)$	1224780	660132	155649	28888	3829	540	51

E [TeV]	3×10^4	10^5	3×10^5	10^6	3×10^6	10^7
N_{trig}	1426	1437	1435	1435	1432	1436
$dN_{\mathrm{CR,exp}}/dE$ [TeV^{-1}]	3×10^{-4}	10^{-5}	4×10^{-7}	10^{-8}	4×10^{-10}	10^{-11}
$N_{\mathrm{CR,exp}}(> E)$	6	0.5	0.06	0.005	7×10^4	8×10^{-5}

Table 5.1: *Cosmic-ray background simulations* – Number of cosmic-ray events triggering the array (out of 1500 showers simulated for each energy E), differential spectrum of expected cosmic-ray events and number of events expected above E, as a function of the simulated energy and for an observation time of 30 hours.

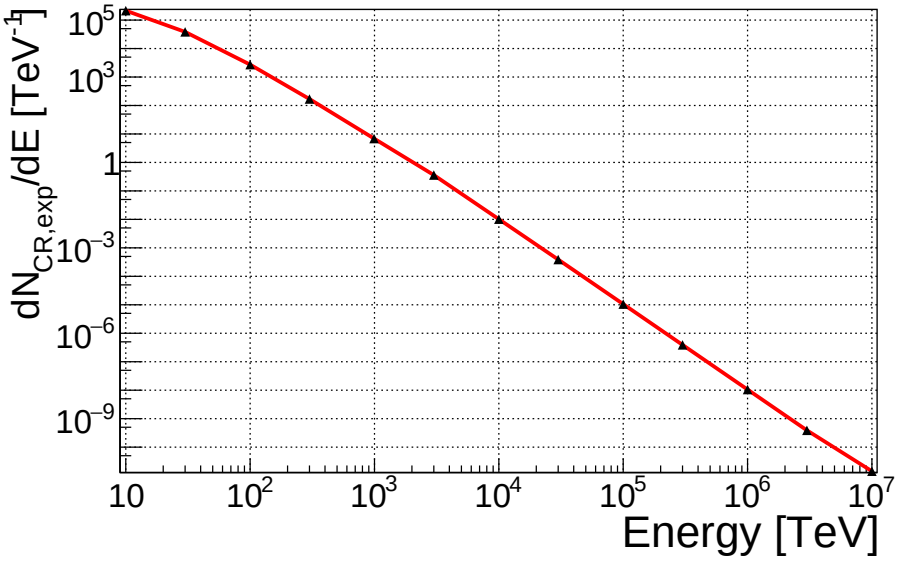

Figure 5.1: Number of expected cosmic-ray background events for 30 hours of observation time with maximum impact distance $R_{\mathrm{max}} = 1300$ m obtained by convoluting the differential cosmic-ray flux with the fraction of simulated air showers that triggers the array, the solid angle Ω, the observation time Δt and the simulated area πR^2_{max}.

angle[2]. The reconstruction yields better results in the case of point sources ($\psi^{\mathrm{PRESHW-1300P}}_{\mathrm{median}} = 0.28°$), as the difference between the air shower axis and the pointing directions of the telescopes is less significant than in the case of diffuse sources ($\psi^{\mathrm{PRESHW-1300D}}_{\mathrm{median}} = 0.59°$ and $\psi^{\mathrm{CR}}_{\mathrm{median}} = 0.72°$).

5.2 Hillas Parameters used in Multivariate Analysis

As discussed in Chapter 3, the Hillas parameters, that characterize the images formed on the telescopes cameras by the Cherenkov light, strongly depend on the nature and the energy of the primary particle that generated the EAS, and can therefore be used to discriminate signal and background events. The parameters selected for this analysis are chosen based on their importance (also called ranking) when running the BDT analysis: the more a given variable is used to build decision trees, the higher its ranking. Figure 5.3 shows the distributions of four Hillas parameters deemed the most important to the clas-

[2]

$$\psi = \arccos\left(\vec{V}_{\mathrm{sim}}.\vec{V}_{\mathrm{rec}}\right) \tag{5.3}$$

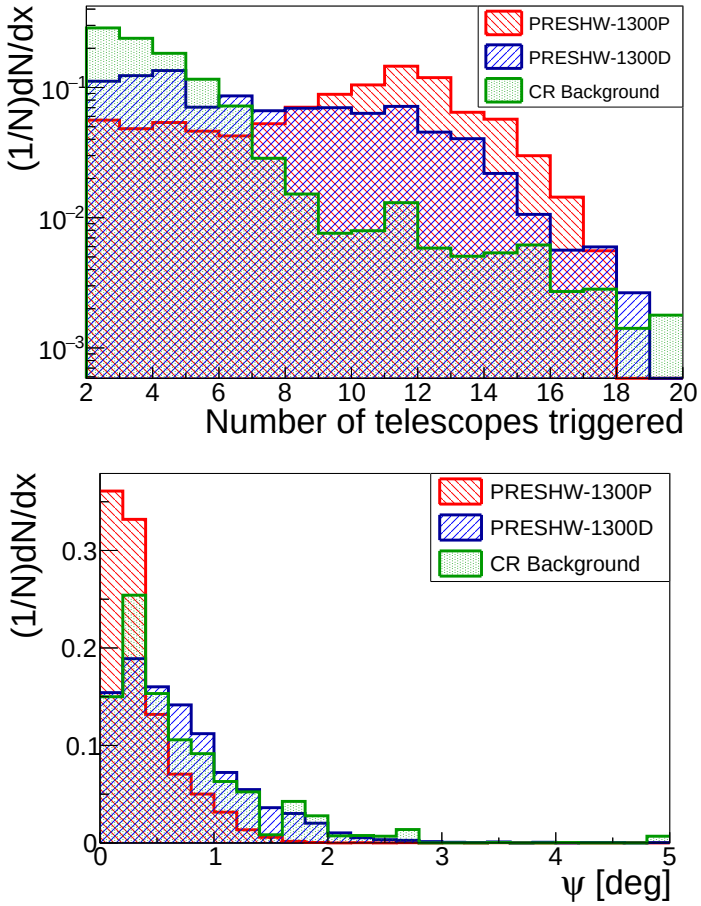

Figure 5.2: *Top*: Normalized distributions of the number of telescopes triggered by air showers generated by the cosmic-ray background (with $R_{\max} = 1300$ m) and by the preshower effect of different parameters. *Bottom*: Normalized distributions of the difference between reconstructed and simulated directions for the same air showers.

sification process of cosmic-ray background and preshowers created in different scenarios, i.e. the *size*, *width*, *length* and *distance* parameters.

The differences observed in the *size*, *length* and *width* can be explained with the same arguments given in Section 4.3.1: UHE proton showers are both richer in muons and spatially larger, therefore producing brighter and bigger images. On the other hand, since the cosmic-ray background extends down to a few TeVs, smaller images are also generated, as the peaks at low *length* and *width* values for the proton cosmic-ray distributions show. The bottom-right panel of Figure 5.3 shows a clear difference in the distribution of the distance parameter between point sources, and diffuse sources and cosmic-ray background, with diffuse sources – and especially of preshowers – showing a more extended distribution of this parameter. This is due to the fact that by

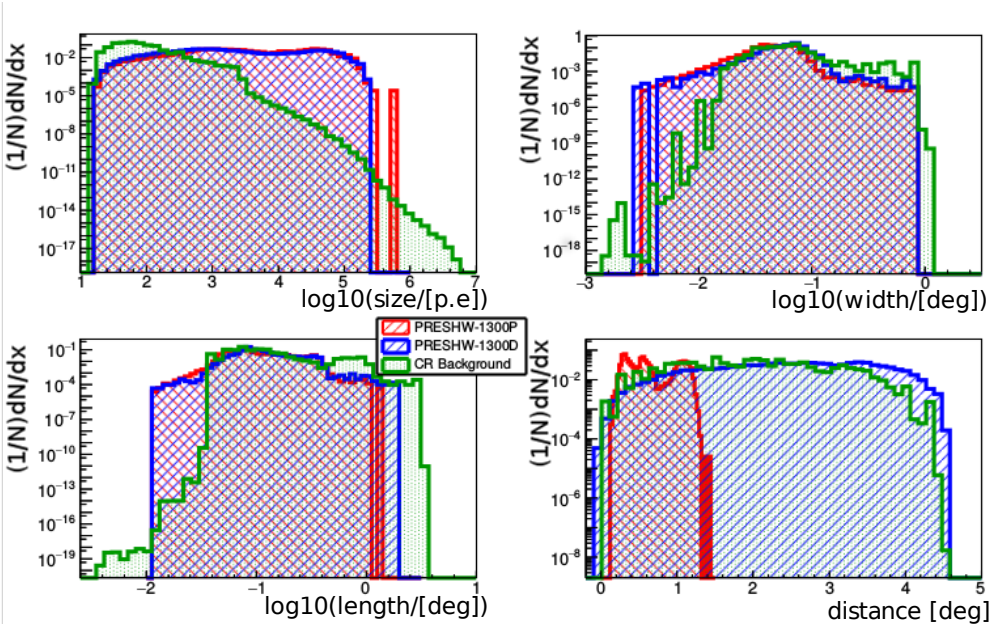

Figure 5.3: Normalized distributions of the four Hillas parameters used in the multivariate analysis for both preshower and cosmic-ray background simulations.

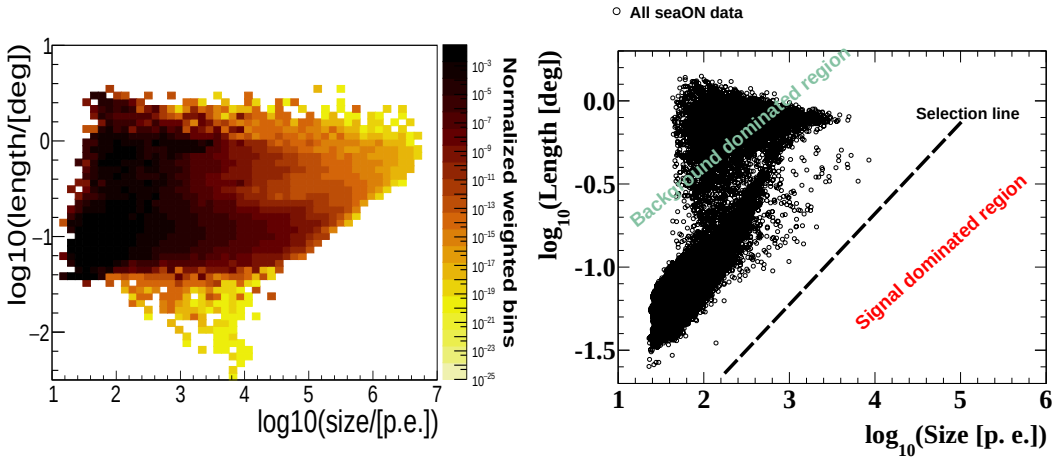

Figure 5.4: *Left panel*: Scatter plot of *size* and *length* parameters for the cosmic-ray background, weighted by the cosmic-ray spectrum index. *Right panel*: Same scatter plot as measured by the MAGIC telescopes in [206].

nature, diffuse sources have a larger spread of angle distribution between the axis of the EAS and the one of the telescopes.

The *size* vs. *length* scatter plot obtained for the cosmic-ray background and shown in the left panel of Figure 5.4 is consistent with observations from MAGIC (see right panel of Figure 5.4) [206] in a 30 hours time period in the

darkest region, where events of energies in the $\sim$ TeV-PeV range are observed. The muon rings of different intensities are also noticeable but the vast majority of the images are dim and small.

5.3 Multivariate Analysis

5.3.1 Building a Decision Tree

The basic principle of a decision tree is to classify events by applying successive cuts on the variables that characterize them. In order to grow such a tree, one needs to define a training sample composed of events of known nature (signal or background). Each of these events is characterized by a set of n variables $\{x_1, x_2, .., x_n\}$. The growing of the tree starts at the *root node*, where all the events of the training sample are contained. A first binary split is applied to the dataset based on the variable and its corresponding cut value that produce the best signal/background separation. The same operation is then repeated for each of the two resulting subsets, until one of the criteria set to stop the building of the tree is met (maximum depth of the tree, minimum number of events in a node, etc...). Each of the last nodes, also called *leaf nodes*, is then labeled *signal* or *background* depending on the class of the majority of events contained in it (see Figure 5.5). Individual trees are very sensitive to fluctuations in the training sample and therefore constitute weak classifiers. To overcome this problem, multiple trees are trained into a *forest* and misclassified events gain a *boost weight* that increase their importance when the next tree is grown: this is the *boosting* procedure and it is performed by the *AdaBoost* method found in the TMVA package.

5.3.2 Hyperparameters

One of the advantages of the BDT method lies in the fact that very little tuning of the method's parameters (also called *hyperparameters*) is required. In this section, the hyperparameters that characterize the BDT method and the values they were given, are discussed.

The number of trees (NT) to be grown can be determined by looking at the fraction of misclassified events for each newly constructed tree. As more trees are grown, this fraction should converge towards 0.5, the threshold value for which no more additional separation power can be obtained from the data. $NT = 800$ provides both a good separation power, and also a value above which trees do not significantly improve it. Another parameter that has an impact on the separation power is the maximum depth ($MaxD$) of the trees. A good compromise is found with $MaxD = 3$, preventing overtraining (an issue

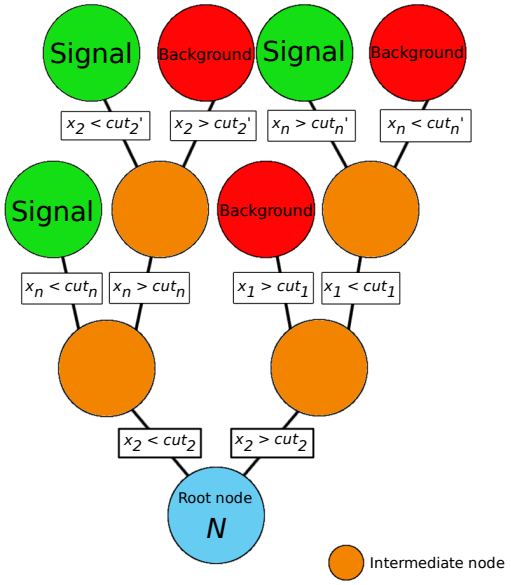

Figure 5.5: Schematic view of a decision tree.

that arises when a classifier becomes too sensitive to statistical fluctuations and therefore, does not perform well on independent samples) but also providing an efficient signal/background separation. The minimum fraction of training events contained in a node (*MinNodeSize*) must also be carefully set. A high value would leave leaf nodes with a too high percentage of misclassified events while a low value would lead to overtraining. An acceptable balance is achieved by using the value of 2.5%. The number of cuts *nCuts* used to find the optimal node splitting for each variable was set to 500 in the case of point sources of UHE photons and to 300 in the case of diffuse sources. Finally, the *Gini coefficient* [207] was selected as a separation criterion to find the optimal cut value at each node by comparing the background and signal distributions of the training variables.

5.3.3 Boosted Decision Trees Scores and Efficiencies

The ultimate goal of the BDT method is to assign a score to the training samples, such that the separation between signal and background score distributions is maximum. Such BDT score distributions are shown in the top panel of Figure 5.6. By applying successive cuts on these distributions, one can calculate the evolution of the signal and background efficiencies (as shown in the bottom panel of Figure 5.6) and obtain the best *Matthews correlation coefficient* [208] in order to evaluate the quality of the classification of the

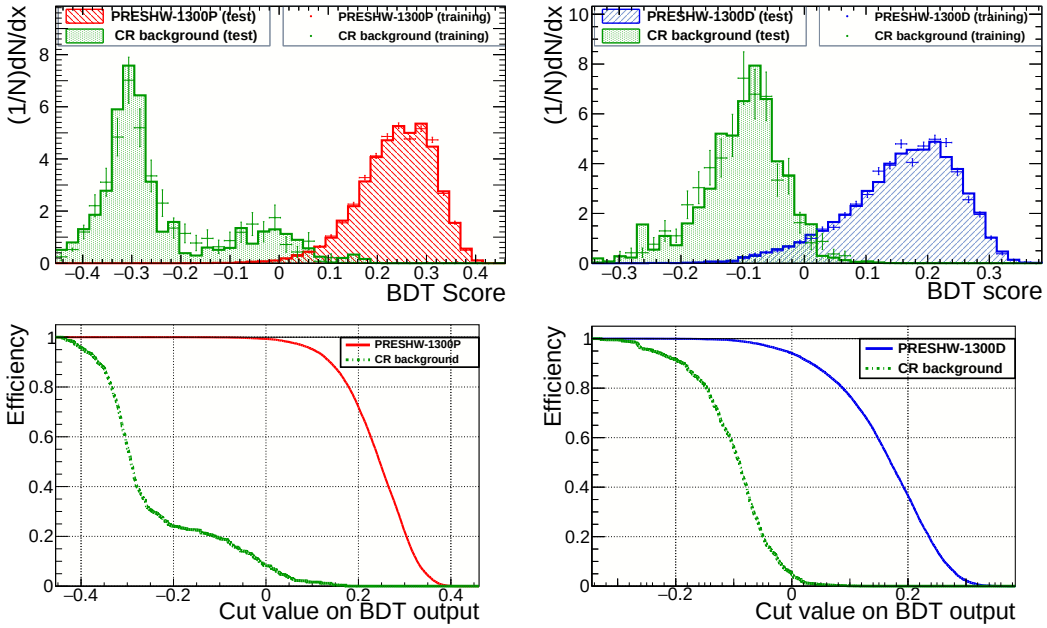

Figure 5.6: *Top*: BDT score distributions of the testing and training samples of cosmic-ray background and preshower events. *Bottom*: Efficiencies obtained for cosmic-ray background and preshower events using test samples as a function of cut value applied to BDT distributions above. Point and diffuse source of UHE photons are on the left and right panel, respectively.

training sample. It varies from -1 (total contradiction between prediction and observation) to 1 (perfect prediction) and is given by the formula:

$$MCC = \frac{TP \times TN - FP \times FN}{\sqrt{(TP + FP)(TP + FN)(TN + FP)(TN + FN)}}, \tag{5.4}$$

where TP is the number of signal events classified as signal (true positive), TN the number of background events classified as background (true negative), FP the number of background events classified as signal (false positive), and FN the number of signal events classified as background (false negative). Figure 5.7 shows the evolution of this parameter for different cut values performed on the training sample BDT distributions.

In order to evaluate the quality of the trained classifier, it is then used to classify an independent test sample of preshower and cosmic-ray background events. The optimal cut value previously obtained from the training sample is then applied to the BDT score distribution of the test sample, and the final efficiencies are calculated. The same procedure is then applied to all simulation parameter sets and a summary of the results[3] is given in Table 5.2.

[3]The background contamination characterizes the percentage of background events that

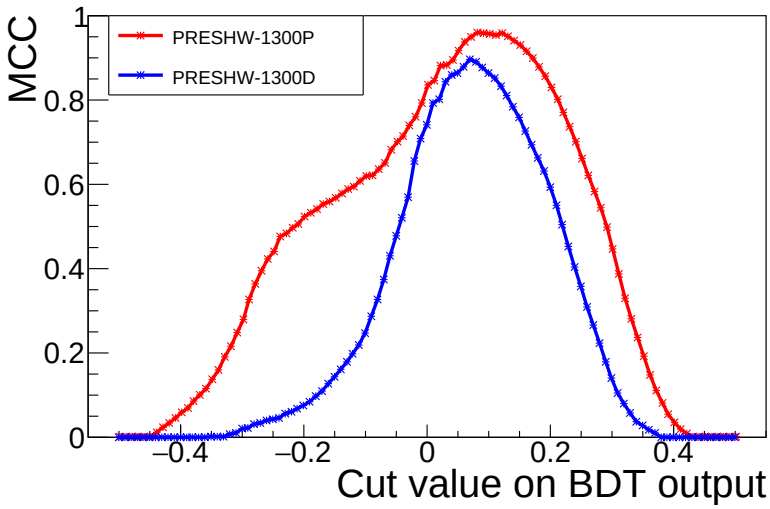

Figure 5.7: MCC values obtained as a function of the cut applied on the BDT distributions of training samples for different preshower scenarios.

These results show that the preshowers can be efficiently discriminated from the dominating cosmic-ray background. In fact, increasing the cut on the BDT distributions to 0.18 (0.12) for point (diffuse) sources of UHE photons leads to the possibility of having background-free observations with a signal efficiency of 80% (70%). Another noticeable feature is the fact that diffuse sources of preshowers are not as well discriminated from cosmic-ray background as preshowers initiated by a point source of UHE photons. Such a discrepancy can be explained by the very similar distributions of the *distance* parameters between the diffuse cosmic-ray background and the diffuse source of UHE photons.

	Best MCC	BDT cut value	Sig. Eff. (ϵ_{BDT})	Back. Con.	Sig. Pur.
PRESHW-1300P	0.96	0.08	96.6%	2.1%	97.9%
PRESHW-1300D	0.89	0.07	83.8%	0.4%	99.6%

Table 5.2: Summmary of the BDT classification results obtained for different parameter sets of preshower simulations. The signal efficiency (Sig. Eff. = ϵ_{BDT}), the background contamination (Back. Con.) as well as the signal purity (Sig. Pur.) for the best MCC value obtained are shown.

have been identified as signal, i.e. the background rejection efficiency is simply (1- Back. Cont.), while the signal purity characterizes the percentage of true signal events in the sample labeled as signal.

6. Discussion and Outlook

New results on the efficiency of the photon/hadron separation obtained in Chapter 5 can be used to investigate the effective area of CTA-North, as well as the number of events expected from UHE photon production models or from limits set by UHECR experiments introduced in Chapter 2. In this chapter, the aperture of the array for the preshower scenarios previously studied is calculated, and the results are used as an input to the calculation of the upper limits on the rate of such a phenomenon for diffuse flux of UHE photons given by production models and by limits prodived by Auger, and for point-source searches performed by TA and Auger. The effect of some of the simulation parameters on the EAS and on the images formed in the IACT cameras, such as the maximum impact distance and the energy cuts, are also briefly discussed. Finally, other scenarios involving conversion of UHE photons in electromagnetic fields, as well as possible observation proposals, are presented.

6.1 Effective Area

The effective area corresponds to the area within which the shower core must lie in order for the telescopes to detect the shower. It is a function of the energy E of the primary and of the zenith and azimuth angles, θ and ϕ, respectively, and can be expressed as:

$$A_{\text{eff}}(E,\theta,\phi,\epsilon_{\text{BDT}}) = \pi R_{\text{max}}^2 \Omega \frac{N_{\text{trig}}(E,\theta,\phi,\epsilon_{\text{BDT}})}{N_{\text{conv}}}, \tag{6.1}$$

where R_{max} is the maximum impact distance defined previously, $N_{\text{trig}}(E,\theta,\phi,\epsilon_{\text{BDT}})$ is the number of events that have triggered the telescope array and that have been correctly identified as preshowers (that is the signal efficiency ϵ_{BDT} must be taken into account when calculating this term), N_{conv} is the number of UHE photons that converted (taking into account the conversion factor ϵ_{conv} of UHE photons at the given direction of observation, it is simply $N_{\text{sim}} \times \epsilon_{\text{conv}}$ with $N_{\text{sim}} = 10000$), and Ω is the solid angle in steradian ($\Omega = 2\pi(1 - cos(\alpha))$ for diffuse sources, where α is the viewcone angle previously defined and $\Omega = 1$ for point sources as there are no dependence on the solid angle in this case). The effective area and its relation to the described variables are illustrated in Figure 6.1. The results obtained for the effective area in the case of preshowers are shown in the second row of Table 6.1.

Because of limitations on the simulated energies of electromagnetic particles within the EAS, these values are conservative. Lower limits would increase the number of Cherenkov photons emitted, and therefore increase the number

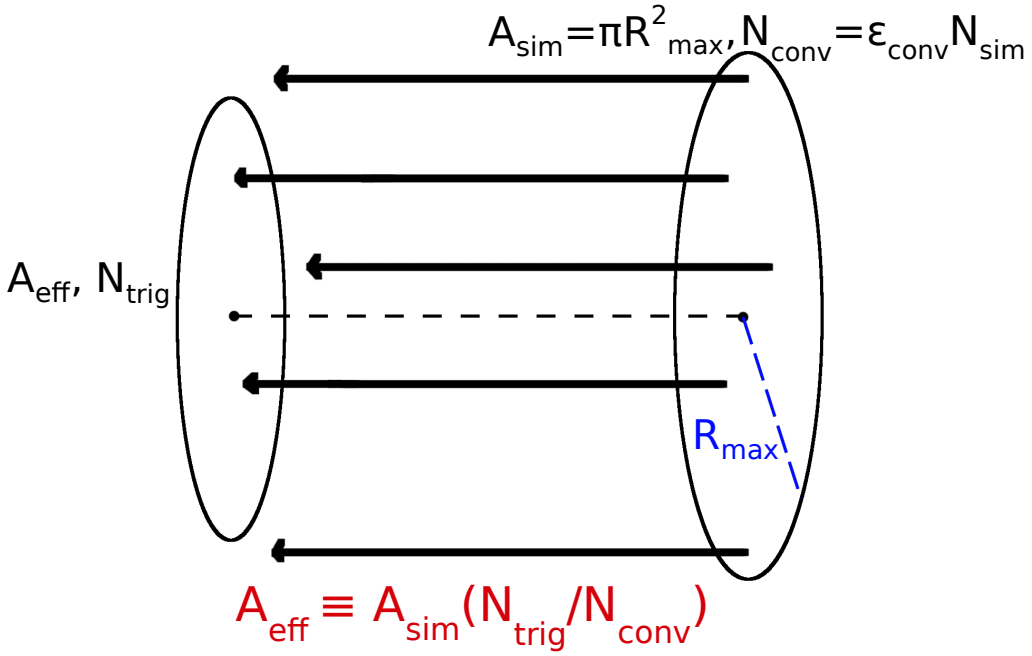

Figure 6.1: Definition of the effective area – relation between the number of preshower events simulated N_{conv} in a generation plane A_{sim} within which events are simulated homogeneously, and the effective area A_{eff} with N_{trig} events triggering the array.

of events triggering the telescope arrays. Nevertheless, such increase could be compensated by a smaller ϵ_{BDT} value when considering completely background free observations. Moreover, the actual field of view of CTA-North telescopes is larger than the viewing cone angle α used to simulate diffuse sources. Consequently, the Ω factor is expected to be slightly larger than what was computed here in the case of diffuse sources. Finally, the effective area is expected to significantly increase with the energy of the UHE photons, as EAS's would be initiated by higher energy bremsstrahlung photons.

	PRESHW-1300P	PRESHW-1300D
Aperture [km^2]	3.42	0.05
SHDM	2.7×10^{-3}	3.1×10^{-6}
GZK	4.0×10^{-5}	4.7×10^{-8}
AUGER$_{\text{diff.}}$	3.3×10^{-5}	3.9×10^{-8}

Table 6.1: *Diffuse source of UHE photons* – Summary of the results obtained for a given aperture and associated number of expected preshowers for 30 hours observation time. Different preshower simulation sets are shown. SHDM and GZK rows correspond to the UHE photons production models referred to in the text while the AUGER$_{\text{diff.}}$ correspond to the limits put by Auger on the integral diffuse photon flux [138].

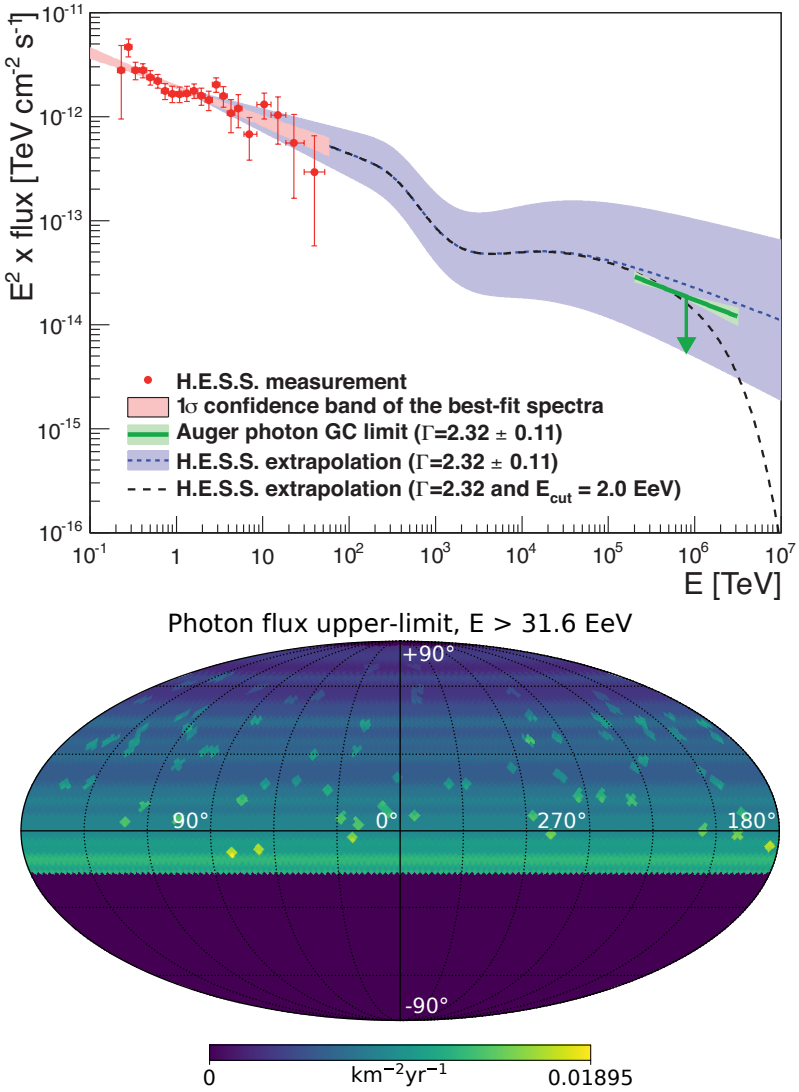

Figure 6.2: *Top*: Photon flux of the Galactic Center as measured by H.E.S.S. [182] (red dots) and extrapolated by Auger to obtain limits in the UHE regime (green line) [142]. Figure taken from [142]. *Bottom*: Upper limits (95% C.L.) on the point-source photon flux above 31.6 EeV set by TA. Figure taken from [143].

6.2 Event Rates

In order to calculate the number of preshower events that can be expected in the observation configuration presented in this work, an estimation of the UHE photon flux $\phi_\gamma(E)$ from various production models is needed. First of all, the diffuse UHE photon production models, such as SHDM decay [111] and GZK photon emission [106], introduced in Section 1.5.2, as well as the limits put by

Auger on the the integral diffuse UHE photon flux [138], are considered. The number of expected preshowers is defined as:

$$N_{\text{preshw}}(E) = \phi_{\gamma-\text{diff}}(40 \text{ EeV})\epsilon_{\text{conv}}\Delta t A_{\text{eff}}, \tag{6.2}$$

where ϵ_{conv} is the probability for an UHE photon to produce a preshower in the previously given direction and is equal to 0.67, Δt is the observation time and A_{eff} is the effective area previously calculated. The values taken for the SHDM model, the GZK emission and Auger limits at 40 EeV, expressed in $\text{km}^{-2}\text{yr}^{-1}\text{sr}^{-1}$, are 2.7×10^{-2}, 4.1×10^{-4} and 3.4×10^{-4}, respectively (see Figure 2.4). Such diffuse flux must be multiplied by 4π when considering point sources of UHE photons. The numbers of preshowers that can be expected from these scenarios and for a typical observation time of 30 hours are shown in Table 6.1.

Focusing on targeted searches for point sources of UHE photons by different experiments, an estimation of the number of expected preshowers from upper limits put on the UHE photon flux emerging from such sources, as well as from possible flares that could potentially "boost" UHE photon emission, can be provided. While searches for UHE photon point sources were performed by Auger [142] (see discussion in Section 2.3.2), they were limited to the energy range $10^{17.3} < E < 10^{18.5}$ eV. However, the extrapolation of the TeV gamma-ray flux of the Galactic Center measured by H.E.S.S. [182] to the EeV domain and performed by Auger in [142] (see top panel of Figure 6.2) puts an upper limit to 0.034 $\text{km}^{-2}\text{yr}^{-1}$ in this energy range. Upper limits reported by the TA collaboration above 31.6 EeV give an average of 0.0071 $\text{km}^{-2}\text{yr}^{-1}$ for the point-source UHE photon flux (see Table 2 of [143]). Sky maps of upper limits at 95% C.L. are also displayed in Figure 3 of [143] and give upper limits up of 0.019 $\text{km}^{-2}\text{yr}^{-1}$ near the equator for energies above 31.6 EeV, in the most optimistic case (see bottom panel of Figure 6.2). These values are reported in the second row of Table 6.2. Using Equation 6.2, the number of preshowers expected from these point-source photon flux upper limits in non-transient mode, can be estimated. Results are reported in the third row of Table 6.2.

In 2018, the H.E.S.S. telescope array observed the very-high energy emission of the afterglow of gamma-ray burst (GRB) GRB 180720B, several hours after the prompt emission phase [209]. The energy spectrum of the source, obtained after correction due to the Extragalactic Background Light (EBL) absorption, in the energy range 100 – 440 GeV is characterized by a flux normalization of $\sim 7.52 \times 10^{-10}$ $\text{TeV}^{-1}\text{cm}^{-2}\text{s}^{-1}$ at 0.154 TeV (see top panel of Figure 6.3). The next year, the MAGIC observatory observed the flaring of GRB 190114C for several hours, one minute after its first detection by other experiments [120]. In this observation, the fitting of the spectrum, after EBL correction, puts a flux of 9.59×10^{-8} $\text{TeV}^{-1}\text{cm}^{-2}\text{s}^{-1}$ at 0.154 TeV (see bottom

panel of Figure 6.3). From these values, a *boosting* factor R can be derived. It is defined as the ratio of the emission flux in the afterglow or flaring phase to the one of the Galactic Center in non-transient emission mode, at 0.154 TeV, estimated by the H.E.S.S. observatory [182] $(1.47 \times 10^{-10}\,\mathrm{TeV^{-1}cm^{-2}s^{-1}})$[1]. In the case of H.E.S.S. afterglow observation, this ratio is approximately equal to 5 while in the case of MAGIC flare detection, $R = 652$. Such ratio provides an order of magnitude of the amount by which photon emission can be boosted when a GRB is occuring. Assuming that this boost can be extended to the EeV range, the number of expected preshower events for both values of R is calculated by simply multiplying the second row of Table 6.2 with R. Results are shown in the 4^{th} and 5^{th} row of Table 6.2. In these scenarios, the expected number of preshowers is significantly higher than in the case of diffuse emission of UHE photons, reaching up to 0.17 preshower events in 30 hours observation time. Considering that a $R = 652$ boost could be observed in other sources, the required source intrinsic flux to obtain one preshower event ($N_{\mathrm{preshw}} = 1$) at 40 EeV and for 30 hours of observation is equivalent to $(0.034/0.17) \simeq 0.2\,\mathrm{km^{-2}yr^{-1}}$, which is about one order of magnitude above the upper limits set by Auger and TA.

Larger maximum impact distances R_{max} as well as different observation mode (such as one described in [179], where telescopes are pointing in different directions just above the horizon) could increase the aperture and therefore, the number of expected preshowers. In fact, a compromise could be found if the pointing direction of each telescope was slightly shifted relative to one another, in order to cover a larger strip of the atmosphere above the horizon to look for a diffuse flux. Letting their field of view overlap would also allow stereoscopic observations.

	$\mathrm{AUGER_{point}}$	$\langle \mathrm{TA}_{E>31.6\,\mathrm{EeV}} \rangle$	$\max(\mathrm{TA}_{E>31.6\,\mathrm{EeV}})$
$\phi_{\gamma-\mathrm{p.}}(40\ \mathrm{EeV})\ [\mathrm{km^{-2}yr^{-1}}]$	0.034	0.0073	0.019
N_{preshw} – non-transient ($R = 1$)	2.7×10^{-4}	5.7×10^{-5}	1.5×10^{-4}
– $R = 5$	1.4×10^{-3}	2.9×10^{-4}	7.6×10^{-4}
– $R = 652$	0.17	0.037	0.09

Table 6.2: *Point sources of UHE photons* – Summary of the number of preshowers expected in the case of point sources of UHE photons for 30 hours observation time.. The UHE photon flux in the second row is obtained from the upper limits put by Auger on the extrapolation of the H.E.S.S. measurements of the Galactic Center in the energy range $10^{17.3}$ eV - $10^{18.5}$ eV, and from upper limits derived by TA, as described in the text. The number of expected preshowers are obtained using Equation 6.2 for these upper limits and for UHE photons emission boosted by a factor R in the case of GRBs observed by MAGIC and H.E.S.S..

[1] This value is calculated from a power-law, $dN/dE = \psi(E/\mathrm{TeV})^{-\alpha}$, where $\psi = 1.92 \times 10^{-12}\,\mathrm{TeV^{-1}cm^{-2}s^{-1}}$ is the flux normalization and $\alpha = 2.32$ is the spectral index.

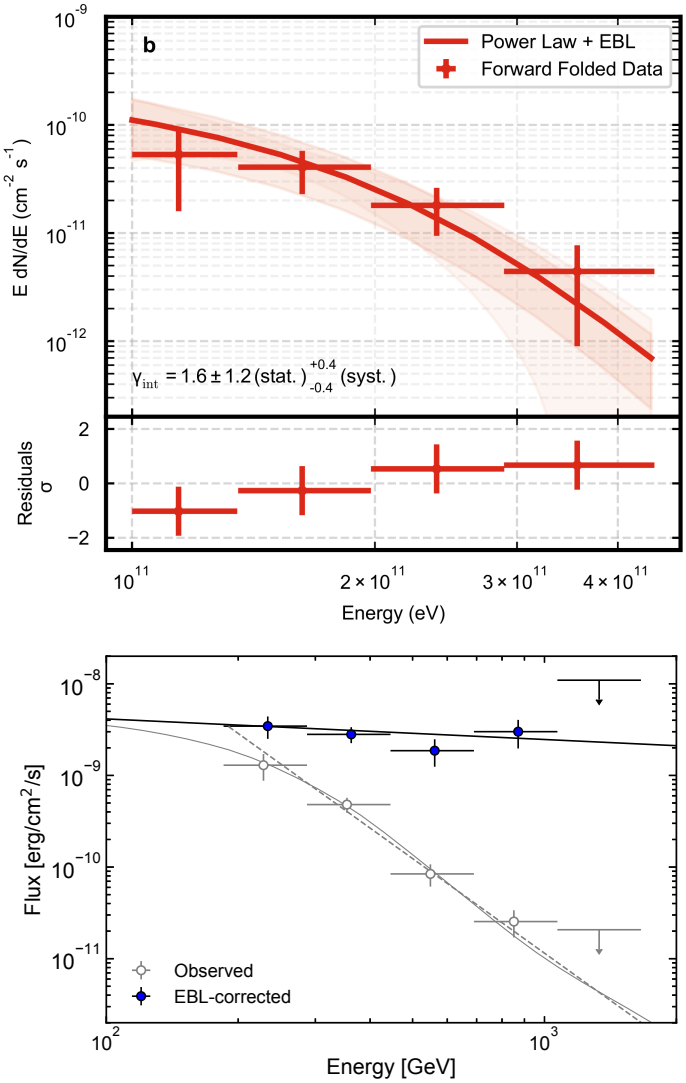

Figure 6.3: *Top*: Energy spectrum of GRB 180720B measured by H.E.S.S., 10 hours after triggering FERMI Gamma-ray Burst Monitor ($T_0 \equiv$ July 20^{th} 2018, 14:21:39 UT). The data is fitted with by the function $F_{\rm obs}(E) = F_{\rm int}(E) \times e^{-\tau(E,z)}$ where the exponential accounts for the EBL absorption at $z = 0.653$ and $F_{\rm int}(E) = F_{0,\rm int}(E/E_{0,\rm int})^{-\gamma_{\rm int}}$ describes the intrinsic spectrum of the sources, with $\gamma_{\rm int} = 1.6 \pm 1.2(\text{stat.}) \pm 0.4(\text{syst.})$ and $F_{0,\rm int} = [7.52 \pm 2.03(\text{stat.}) ^{+4.53}_{-3.84}(\text{syst.})] \times 10^{-10}$ TeV^{-1} cm^{-2} s^{-1} at $E_{0,\rm int} = 0.154$ TeV. Figure taken from [209]. *Bottom*: Observed and EBL-corrected energy spectra of MAGIC observation of GRB 190114C over the period between $T_0 + 62$ s and $T_0 + 2454$ s ($T_0 \equiv$ January 14^{th} 2018, 20:57:03 UT). The EBL-corrected spectrum is fitted with a power-law function $dF/dE = f_0 \times (E/E_0)^{-\gamma}$, with $\gamma = -2.22 ^{+0.23}_{-0.25}(\text{stat.}) ^{+0.21}_{-0.26}(\text{syst.})$ and $f_0 = [8.45 ^{+0.68}_{-0.65}(\text{stat.}) ^{+4.42}_{-3.97}(\text{syst.})] \times 10^{-9}$ TeV^{-1}cm^{-2}s^{-1} at $E_0 = 0.46$ TeV. Figure taken from [120].

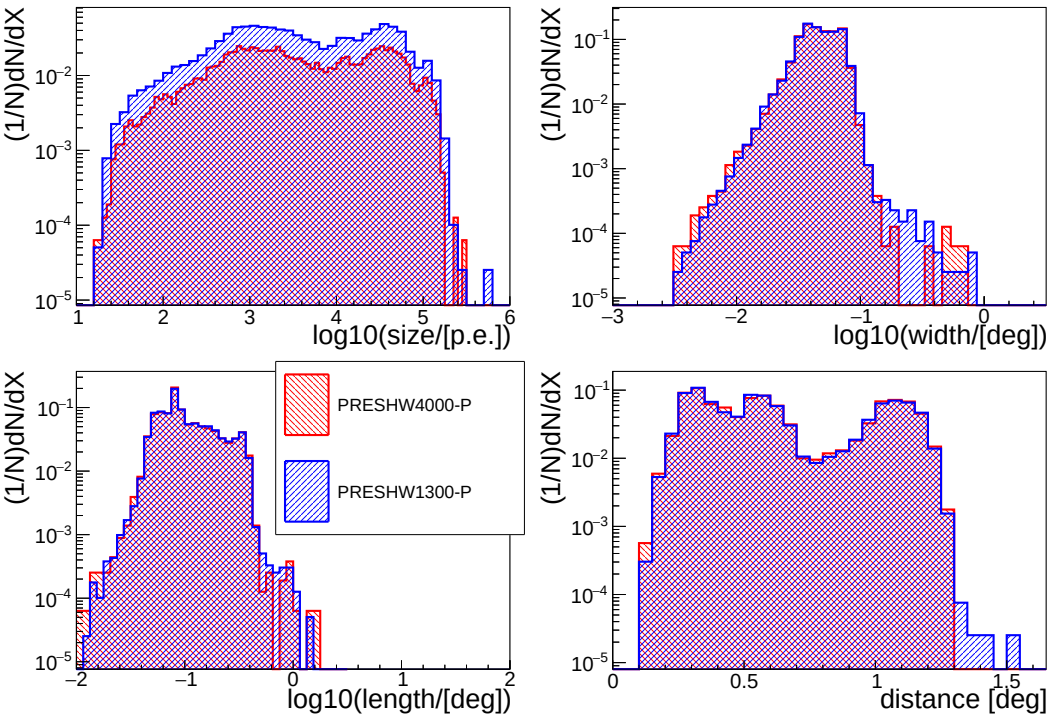

Figure 6.4: Normalized Hillas distributions for point sources of preshower with maximal impact distance $R_{\max} = 1300$ m (blue) and $R_{\max} = 4000$ m (red).

6.3 Influence of Simulation Parameters

The results presented in this dissertation were obtained for a particular set of simulation parameters. In this section, the effects due to the modification of the maximal impact distance $R_{\max}$ and the energy cuts on the results of these simulations are discussed.

6.3.1 Impact Distance

In order to investigate the influence of the $R_{\max}$ parameter, the preshower effect and the cosmic-ray background were also simulated for $R_{\max} = 4000$ m. Figure 6.4 shows the Hillas distributions obtained for preshower point source simulations with $R_{\max} = 4000$ m. Comparison with the Hillas distributions, from the point source scenario with $R_{\max} = 1300$ m shown in Figure 5.3, is also provided. Having a larger impact distance does not change the Hillas parameter distributions (similar distributions for cosmic-ray background and diffuse source of preshower are also found) and therefore, the BDT distributions and the efficiencies obtained are similar as in the case of $R_{\max} = 1300$ m. However, the fraction of events triggering the array to the number of events

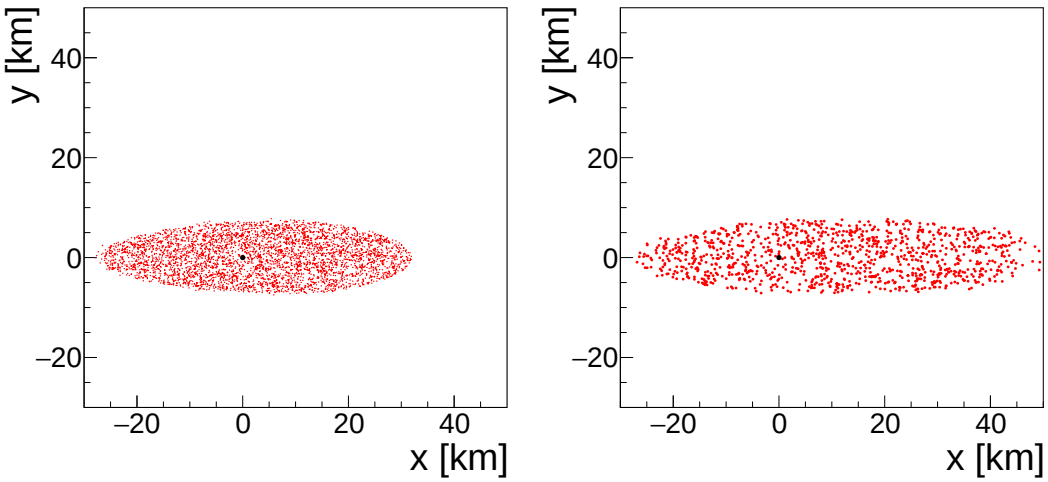

Figure 6.5: Location of impact points (red dots) of EAS's produced by converted UHE photons that have triggered the array located at (0,0) which is represented by a black disk, for different maximal impact distances $R_{\rm max} = 8$ km (left) and 20 km (right).

simulated drastically drops (EAS's reaching the ground at larger distances from the center of the array). The resulting decrease in $N_{\rm trig}/N_{\rm sim}$ is compensated by the larger $\pi R^2_{\rm max}$ and similar effective areas are obtained as for $R_{\rm max} = 1300$ m.

Nevertheless, the size of the collection area on the ground for 40 EeV converted photons in the nearly-horizontal direction is significantly larger than in the standard mode of observation. Figure 6.5 shows the size of the area for which preshower events, represented by red dots, have triggered the telescopes of CTA-North, for $R_{\rm max} = 8$ and 20 km. For $R_{\rm max} = 20$ km, the size of the area is $\sim 1450\,{\rm km}^2$, and does not increase significantly for larger $R_{\rm max}$ values. If an efficiency of 1 is considered, such collection area results in an optimal aperture of $\sim 250\,{\rm km}^2$ at zenith angle $\theta = 80°$. One can note the growing asymmetry of the collection area when compared to the location of CTA-North (black dot), as more events with the shower core hitting in front of the telecopes, trigger the array.

6.3.2 Energy Cuts

The influence of the energy cuts on the Hillas distributions is illustrated in Figure 6.6. While the red histograms are the distributions from the standard cuts used, so far, in this analysis, the blue ones are obtained for lower energy cuts $E^{\rm low}_{\rm cut}$, i.e. 300, 300, 3 and 3 GeV, for hadrons, muons, electrons and gammas, respectively. The Hillas distributions of the cosmic-ray background used in the multivariate analysis of Chapter 5 are also shown for comparison. The

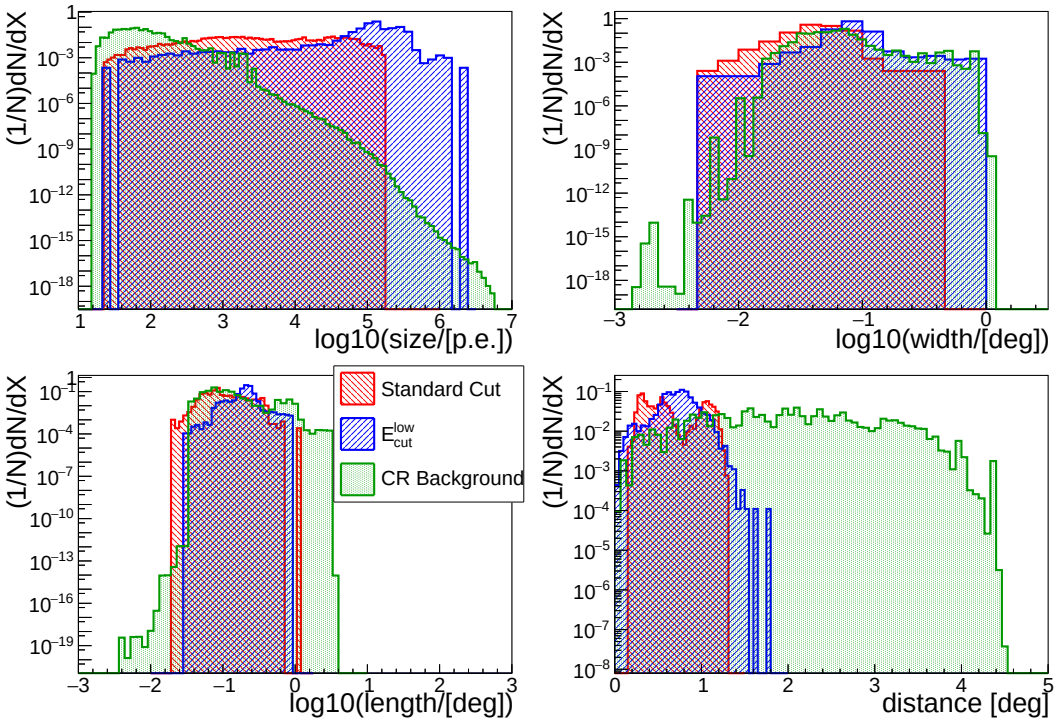

Figure 6.6: Normalized Hillas distributions for point sources of preshower with standard energy cuts used in the BDT analysis (red) and with lower energy cuts described in the text (blue). Cosmic-ray background distributions are also shown in green.

lower energy cuts are essentially characterized by brighter and larger images. These two features are easily explained by the fact that charged particles of lower energies also emit Cherenkov radiation (as long as their energy remains above the energy required for such emission to occur, as discussed in Chapter 3). Moreover, the larger lateral spread of these particles leads to images formed further away from the source location, resulting in higher values of the *distance* parameter. While a new BDT analysis would provide a better understanding of the impact of the lower energy cuts on the photon/hadron separation, one may assume, from the little variations observed in the Hillas distributions when compared to the ones of the cosmic-ray background, that the signal efficiency would not decrease significantly.

In that regard, Figure 6.7 shows the BDT score distributions and the efficiencies obtained for energy cuts set to $E_{\mathrm{cut}}^{\mathrm{low}}$ when simulating point sources of converted UHE photons with $R_{\mathrm{max}} = 1300$ m. This preliminary results shows that even in this case, the photon/hadron separation remains very good and observation of preshower events in the nearly-horizontal direction could still be performed at high signal efficiencies and low background contamination.

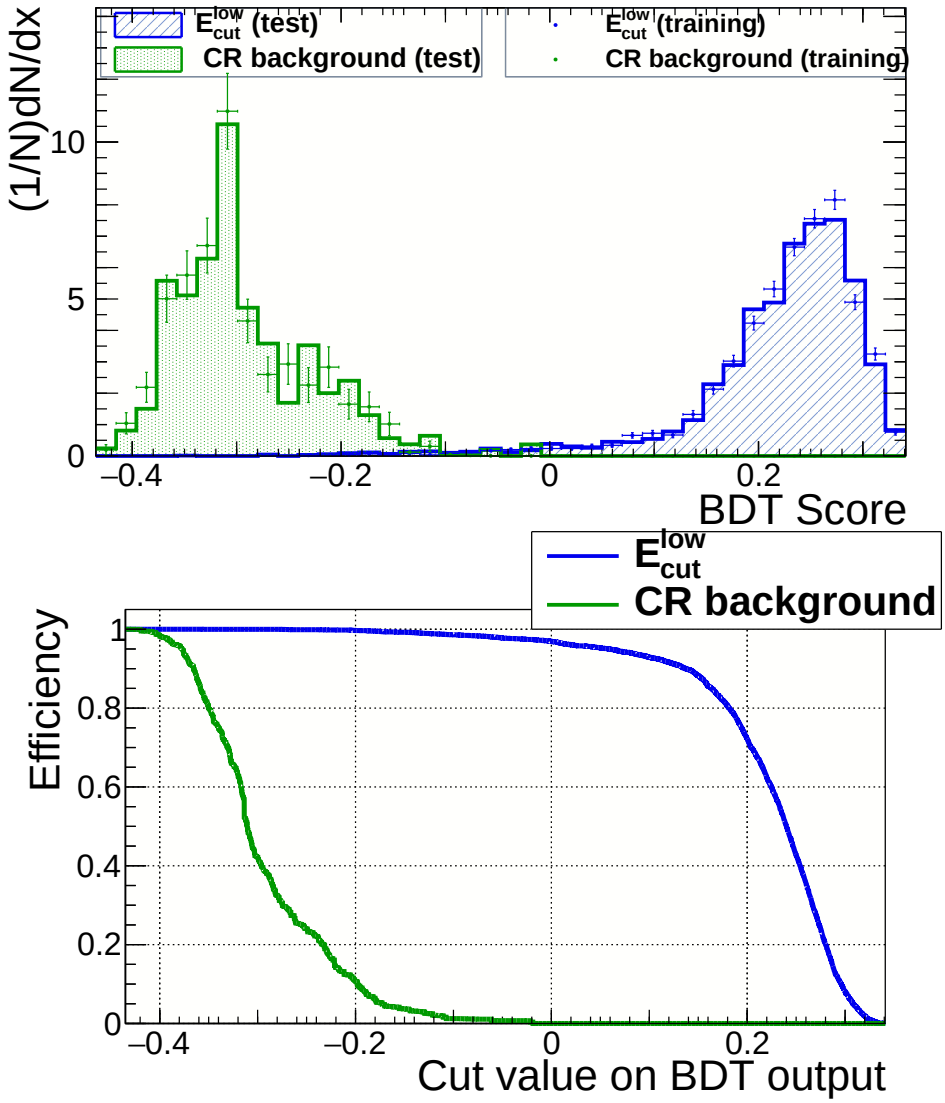

Figure 6.7: BDT score distributions of the testing and training samples (top) and efficiencies (bottom) of cosmic-ray background and point source of converted UHE photons with $R_{\max} = 1300$ m and with the energy cuts $E_{\text{cut}}^{\text{low}}$ described in the text.

6.4 Outlook

In addition to searching for preshower events in historical data obtained by existing gamma-ray telescopes in optimal pointing directions (high zenith angles, northern (southern) directions in the Northern (Southern) hemisphere), new observation campaign could be carried out with a single telescope, such as the First G-APD Cherenkov Telescope (FACT), also located in La Palma, al-

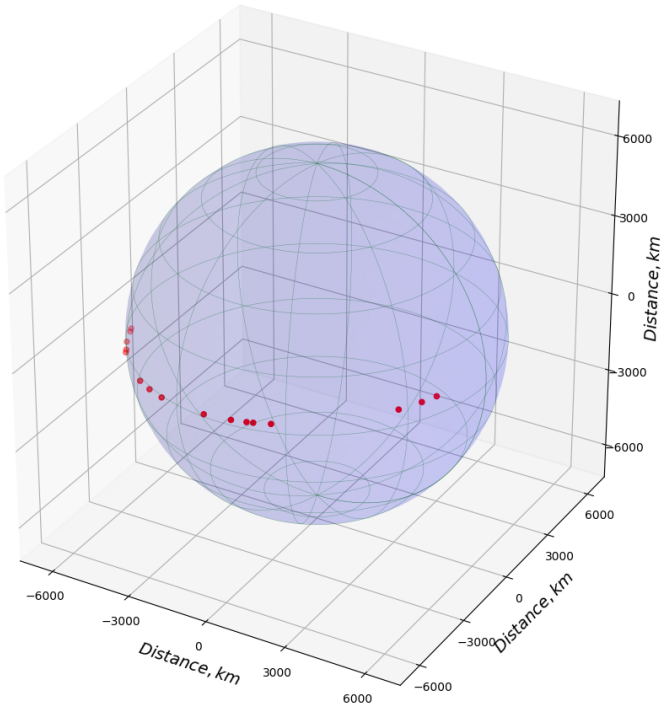

Figure 6.8: Positions of CRE photons (red dots) with energy > 1 TeV, arriving on a plane with the size of the Earth, and produced by a 1 EeV electron entering the Galaxy and propagating over 8.5 kpc.

lowing to reach larger sensitivities with larger observation time. In the nearly-horizontal direction, the size of the Cherenkov pool is sufficiently large to keep the chances of observing preshowers just as high as if multiple telescopes were used. In this endeavor and for further research, a contact has been made with the FACT collaboration and simulations are currently ongoing to determine whether FACT could actually correctly identify preshower events. If so, a proposal in order to obtain time of observation with FACT will be submitted.

As discussed in Chapter 2, the CREDO collaboration is dedicated to the search of CREs, groups of a minimum of two cosmic rays with a common primary interaction vertex or the same parent particle, formed in different scenarios. One example of such scenario is illustrated in Figure 6.8, where the spatial distribution of photons with energy over 1 TeV are shown on a sphere with the size of the Earth. This distribution is the result of the synchrotron emission of a 1 EeV electron propagating through the Galaxy, over 8.5 kpc. Investing the distance between each of the photons is essential to determine whether or not spatially and time correlated air showers could in fact be observed by gamma-ray telescopes.

In Figure 6.9, images formed in the cameras of CTA-North by air-showers

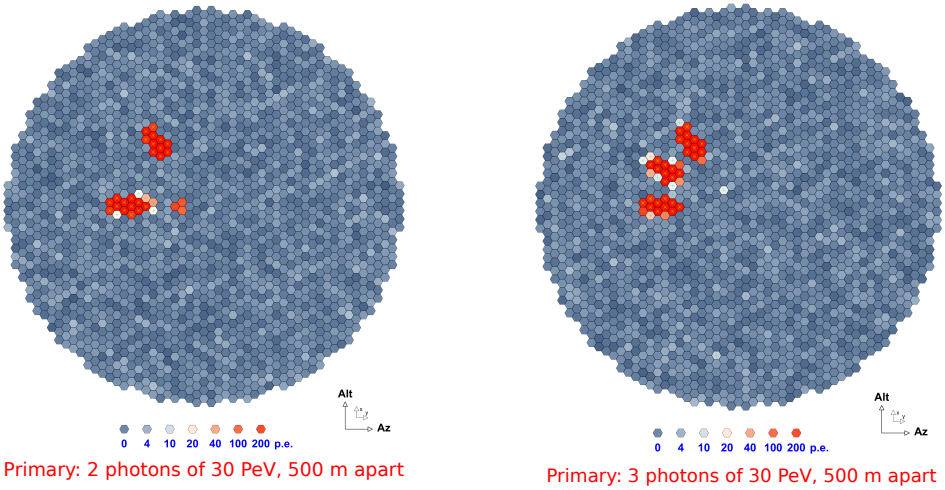

Figure 6.9: Example of images formed in CTA-North cameras by multiple air-showers produced by 30 PeV photons located 500 m apart. The image on the left is for 2 of such photons while the one on the right is for 3 photons.

generated 500 m apart by 2 or 3 30 PeV photons coming at a 20° zenith angle, are shown. The resolution of the cameras allow to distinguish each of these air showers, as one cluster of triggered pixels correspond to one EAS, and the peculiarity of the images formed would enable efficient discrimination against any other type of observed event.

CONCLUSION

The observation of UHE photons constitutes an essential piece of the UHECR puzzle. Their detection would provide more insights on the nature and the source of UHECRs. However, UHE photons propagating through strong magnetic fields have a non-zero probability of converting into a pair of e^-/e^+, which would subsequently emit bremsstrahlung radiation. When such a conversion occurs in the Earth's magnetic field, this phenomenon is referred to as *preshower* effect. In this dissertation, the feasibility of observing very inclined air showers produced by this effect was investigated, taking the example of the next generation of gamma-ray telescopes developed by the CTA collaboration, with a special attention given to CTA-North, which is planned to be located in La Palma, Canary Islands. Using the PRESHOWER algorithm, the properties of the electromagnetic cascade generated above the atmosphere through the preshower effect were studied, examining the influence of the energy of the primary photon, as well as of its arrival direction. The results have shown that the conversion probability was higher for larger zenith angles and in the direction of the geomagnetic North. In this analysis, it was found that the optimal configuration providing a good balance between computing time and trigger efficiency was for 40 EeV photons coming at a 80° zenith from the geomagnetic North direction. It was also demonstrated that the number of particles contained in the preshower cascade increases with the altitude of the first conversion, and that the energy spectrum of these particles covers a large energy range (more than 6 orders of magnitude), making this effect observable by experiments operating at different wavelengths.

As the preshower cascade reaches the atmosphere, an EAS is generated. Using the CORSIKA simulation software, the properties of EAS's produced by a cascade induced by converted UHE photons and by other primaries (protons, iron nuclei and unconverted photons) were studied in the configuration previously described. It was established that due to a higher first interaction point, the mean $X_{\max}$ of EAS's generated by UHE photons, which had previously undergone the preshower effect, was close to the one of hadronic primaries, potentially making them more difficult to identify by experiments relying on

$X_{\max}$ measurements. Aside from the higher conversion probability, the choice for very inclined direction of observation is justified by the fact that nearly-horizontal air showers have their hadronic and electromagnetic components almost completely absorbed, leading to muons dominating the later stages of cascade development. Similarly to $X_{\max}$, the muonic component varies from one primary to another and can be used to identify the nature of observed EAS's. It was shown that, in the case of preshower cascades, the amount of produced muons, as well as the spatial signature on the ground, are significanly smaller than for protons and iron nuclei, while the Cherenkov emission at $X_{\max}$ remains similar.

The Cherenkov emission of EAS's can be detected with the cameras of CTA telescopes as it forms images of shapes and intensities that depend on the properties of the EAS's. Using the sim_telarray package to simulate the cameras response, the differences between the images formed by EAS's produced by the primaries previously listed, were analyzed, using the Hillas parameters, such as the *size* (intensity), *width*, *length* and *distance*, to characterize them. Overall, it was found that images produced by converted UHE phtotons were dimmer and smaller, as well as closer to the simulated direction, than in the case of other considered primaries. Compared to images from hadronic showers, the poorer muon content and the smaller lateral distribution of EAS's produced by preshower cascades are responsible for the lower intensity, for the smaller geometrical sizes, as well as for the shorter distances between the simulated direction and the center of the images. On the other hand, the only apparent difference between converted and unconverted photons was found in the *distance* parameter distributions, showing smaller values in the former scenario. Such a discrepancy could be explained by the higher first interaction point of preshower cascades (up to several thousands of kilometers above the atmosphere), leading to smaller angles between the Cherenkov radiation and the telescopes axis. More thorough investigation of the differences between images formed by proton-induced EAS's and converted UHE photons EAS's was performed with a Principle Component Analysis. It was shown shown that dim double images were almost exclusive to the latter primary.

The potential of Hillas parameters also allowed us to assess the separation power one could hope to obtain between converted UHE photons and the dominating cosmic-ray background during a 30-hour observation campaign with CTA-North. To determine this separation, a cosmic-ray background was simulated between 10 TeV and 10 EeV, and composed exclusively of protons. The *size* vs. *length* scatter plot of the simulated background showed good agreement with the results from high zenith angle observations performed by MAGIC in the context of tau-neutrino searches [206]. A maximum impact distance of 1300 m and a viewing angle of 5° were set, and point and diffuse

sources of UHE photons were considered. For both scenarios, the separation power was calculated using boosted decision trees on the Hillas distributions, and the Matthews correlation coefficient was used to evaluate the best efficiency cut on unbalanced datasets. Such separation was proven to be very good for both point and diffuse sources of UHE photons: 96.6% efficiency and 2.1% background contamination in the former scenario and 83.8% efficiency and 0.4% background contamination for the latter. Thefore, background-free observations could be expected at efficiencies higher than 80%.

Using these results, the aperture and the number of expected preshowers were calculated for different UHE photon production models, as well as for upper limits set by Auger and TA for point and diffuse sources. Although these numbers were found to be low, the potential of Cherenkov detectors in adopting different observation modes (nearly-horizontal direction and/or extended mode) in order to discriminate UHE photon primaries from cosmic-ray background was highlighted. Moreover, at 40 EeV, the required integral diffuse photon flux to obtain $N_{\mathrm{preshw}} = 1$ for a 30-hour observation time and for an aperture of 3.42 km^2 was calculated to be around 10.1 km^{-2}year^{-1}sr^{-1}. This value is significantly above the prediction given by the UHE photons production models and the upper limits on the integral diffuse UHE photon flux put by Auger and TA. However, in the case of point sources and GRB flares, the UHE photon flux could be boosted by a factor as large as 652. Such value was obtained by comparing the photon flux of the Galactic Center in the non-transient emission mode to the measured flux of GRB 190114C's flare by the MAGIC telescopes. In this scenario, the minimum required flux to obtain $N_{\mathrm{preshw}} = 1$ was estimated to be around 0.2 km^{-2}year^{-1}, which is approximately one order of magnitude higher than upper limits put by Auger and TA at 40 EeV.

In this work, it was demonstrated that the IACT technique could be used to probe physical phenomena not only in the TeV domain, but also in the EeV regime. Although the rate of expected preshower events was found to be quite low, the photon/hadron separation, obtained by adopting the nearly-horizontal observation mode, allows for strong filters to be applied in order to identify such events with high degree of confidence. A new method for observation of UHE photons in the EeV domain, consisting in searching for preshower cascades in the nearly-horizontal direction, was proposed. Such a strategy could already be applied to other experiments, such as MAGIC, which already contains data in the observation mode discussed in this work, in the Crab Nebula vicinity.

Searches for particles with low expected flux using IACTs have been previously performed, as it is the case for the tau neutrino or UHE cosmic rays. Moreover, multimessenger alerts obtained from other operating observatories

may allow a fast pointing of the telescopes towards cosmic events suspected to be capable of producing UHE photons, such as interactions between UHE cosmic rays possibly produced by AGNs and the CMB, or gamma-ray bursts. An alert system would significantly increase the chance probability to observe UHE photons. Such a potential is well illustrated by the detection of a 290 TeV neutrino by IceCube, the direction of which is highly correlated with blazar TXS 0506+056 observed by MAGIC, FERMI-LAT and many other experiments [210]. Moreover, a program of observation could be run on catalogs of high energy sources, with observation time significantly higher than the 30h presented in this dissertation.

The work presented in this dissertation falls within the strategy adopted by the CREDO collaboration [155, 156, 157, 158], namely the introduction of a multi-channel approach to the search of cosmic-ray ensembles [211]. This reasearch was published in the proceedings of the 35^{th} and 36^{th} International Cosmic Ray Conferences [212, 213], and more recently in Astroparticle Physics journal [214]. As a member of this collaboration, my work has also involved the analysis of detections obtained with smartphones using the CREDO application [158] to look for clusters of events, and the simulation of magnetic cascades occuring in the Sun's magnetic field [146].

Bibliography

[1] V. F. Hess. Über Beobachtungen der durchdringenden Strahlung bei sieben Freiballonfahrten. *Phys. Z.*, 13:1084, 1912.

[2] J. Linsley. Evidence for a primary cosmic-ray particle with energy 10^{20} eV. *Phys. Rev. Lett.*, 10:146, 1963. doi: 10.1103/PhysRevLett.10.146.

[3] F. G. Schröder. News from cosmic ray air showers. *Proc. of 36th ICRC*, 030, 2019. doi: pos.sissa.it/358/030/.

[4] S. Chapman. The absorption and dissociative or ionizing effect of monochromatic radiation in an atmosphere on a rotating Earth, part II - Grazing incidence. *Proc. Phys. Soc.*, 43:483, 1931. doi: 10.1088/0959-5309/43/5/302.

[5] W. Swider and M. E. Gardner. On the accuracy of certain approximations for the Chapman function. *Environmental Research Papers*, 272, 1967.

[6] W. Swider. The determination of the optical depth at large solar zenith distances. *Planet. Space Sci.*, 12:761, 1964. doi: 10.1016/0032-0633(64)90056-X.

[7] D. Heck. The CURVED version of the air shower simulation program CORSIKA. *Report FZKA 6954*, Forschungszentrum Karlsruhe, 2004. INIS: 35047001.

[8] W. Heitler. *The Quantum Theory of Radiation.* Oxford University Press, London, third edition, 1954. Section 38 - p. 386.

[9] B. Rossi and K. Greisen. Cosmic-Ray Theory. *Rev. Mod. Phys.*, 13:240, 1941. doi: 10.1103/RevModPhys.13.240.

[10] T. Stanev. *High-Energy Cosmic Rays and Particle Physics.* Spinger-Praxis, second edition, 2010.

[11] J. A. Seibert. X-ray imaging physics for nuclear medicine technologists. Part 1: Basic principles of X-ray production. *J. Nucl. Med. Technol.*, 32:139, 2004.

[12] H. Bethe and W. Heitler. On the stopping of fast particles and on the creation of positive electrons. *Proc. Roy. Soc. A: Mathematical, Physical and Engineering Sciences*, 146(856):83, 1934. doi: 10.1098/rspa.1934.0140.

[13] K. Greisen. *Progress in cosmic ray physics*, volume 3. North Holland Pub. Co., Amsterdam, 1956.

[14] J. Matthews. A Heitler model of extensive air showers. *Astropart. Phys.*, 22:387, 2005. doi: 10.1016/j.astropartphys.2004.09.003.

[15] T. Stanev and H. P. Vankov. Simple Monte-Carlo simulation for solving methodological problems of detecting the extensive air showers electron component. *Comp. Phys. Comm.*, 4:47, 1972. doi: 10.1016/0010-4655(72)90030-6.

[16] J. Linsley. Structure of large air showers at depth 834 g/sq cm^{-2}. *Proc. of 15th ICRC*, 12:89, 1977.

[17] D. Newton, J. Knapp, and A. A. Watson. The optimum distance at which to determine the size of a giant air shower. *Astropart. Phys.*, 26:414, 2007. doi: 10.1016/j.astropartphys.2006.08.003.

[18] J. Nishimura and K. Kamata. The lateral and the angular structure functions of electron showers. *Progr. Theor. Phys.*, 6:93, 1958. doi: 10.1143/PTPS.6.93.

[19] K. Greisen. Cosmic ray showers. *Ann. Rev. Nucl. Part. Sci.*, 10:63, 1960. doi: 10.1146/annurev.ns.10.120160.000431.

[20] T. K. Gaisser, R. Engel, and E. Rescani. *Cosmic Rays and Particle Physics*. Cambridge University Press, Second edition, 2016. doi: 10.1017/CBO9781139192194.

[21] T. K. Gaisser and A. M. Hillas. Reliability of the method of Constant Intensity Cuts for reconstructing the average development of vertical showers. *Proc. of 15th ICRC*, 8:353, 1977. Bibcode: 1977ICRC....8..353G.

[22] R. Ulrich, R. Engel, and M. Unger. Hadronic multiparticle production at ultra-high energies and extensive air showers. *Phys. Rev. D*, 83:054026, 2011. doi: 10.1103/PhysRevD.83.054026.

[23] D. Heck et al. CORSIKA: a Monte-Carlo code to simulate extensive air showers. *Report FZKA 6019*, Forschungszentrum Karlsruhe, 1998. Bibcode: 1998cmcc.book.....H.

[24] T. Pierog. Hadronic interactions and air showers: Where do we stand? *EPJ Web Conf.*, 208:02002, 2019. doi: 10.1051/epjconf/201920802002.

[25] S. S. Ostapchenko. Monte-Carlo treatment of hadronic interactions in enhanced Pomeron scheme: QGSJET-II model. *Phys. Rev. D*, 83:014018, 2011. doi: 10.1103/PhysRevD.83.014018.

[26] S. S. Ostapchenko. QGSJET-II: physics, recent improvements, and results for air showers. *EPJ Web Conf.*, 52:02001, 2013. doi: 10.1051/epjconf/20125202001.

[27] T. Pierog et al. EPOS LHC: Test of collective hadronization with data measured at the CERN Large Hadron Collider. *Phys. Rev. C*, 92:034906, 2014. doi: 10.1103/PhysRevC.92.034906.

[28] F. Riehn et al. The hadronic interaction model Sibyll 2.3c and Feynman scaling. *Proc. of 35th ICRC*, 301, 2017. doi: 10.22323/1.301.0301 .

[29] A. Fedynitch and R. Engel. Revision of the high energy hadronic interaction models PHOJET/DPMJET-III. *Proc. of 14th Int. Conf. Nucl. R. Mech.*, 291, 2015.

[30] S. S. Ostapchenko and M. Bleicher. Constraining pion interactions at very high energies by cosmic ray data. *Phys. Rev. D*, 93:051501, 2016. doi: 10.1103/PhysRevD.93.051501.

[31] Pierre Auger Collaboration. Muons in air showers at the Pierre Auger Observatory: Mean number in highly inclined events. *Phys. Rev. D*, 91:032003, 2015. doi: 10.1103/PhysRevD.91.032003.

[32] Telescope Array Collaboration. Mass composition of ultra-high energy cosmic rays with the Telescope Array surface detector data. *Phys. Rev. D*, 98:02202, 2018. doi: 10.1103/PhysRevD.99.022002.

[33] Pierre Auger Collaboration. Testing hadronic interactions at ultra-high energies with air showers measured by the Pierre Auger Observatory. *Phys. Rev. Lett.*, 117:192001, 2015. doi: 10.1103/PhysRevLett.117.192001.

[34] H. Dembinski et al. Report on tests and measurements of hadronic interaction properties with air showers. *EPJ Web Conf*, 210:02004, 2018. doi: 10.1051/epjconf/201921002004.

[35] M. de Naurois and D. Mazin. Ground-based detectors in very-high-energy gamma-ray astronomy. *Comptes rendus physiques*, 16:610, 2015. doi: 10.1016/j.crhy.2015.08.011.

[36] A. M. Hillas. Differences between gamma-ray and hadronic showers. *Space Science Reviews*, 75:17, 1996. doi: 10.1007/BF00195021.

[37] F. D. Kahn and I. Lerche. Radiation from cosmic ray air showers. *Proc. Roy. Soc.*, 289(1417), 1966. doi: 10.1098/rspa.1966.0007.

[38] G. A. Askaryan. Excess negative charge of an electron-photon shower and its coherent radio emission. *Sov. Phys. JETP*, 14(2):441, 1962.

[39] F. G. Schröder. Radio detection of cosmic-ray air showers and high-energy neutrinos. *Prog. Part. Nucl. Phys.*, 93:1, 2017. doi: 10.1016/j.ppnp.2016.12.002.

[40] A. M. Hillas et al. Calculations on the particle and energy-loss densities in extensive air showers at large axial distances. *Conf. Proc. C*, 690825:533, 1969.

[41] J. Hersil et al. Observations of extensive air showers near the maximum of their longitudinal development. *Phys. Rev. Lett.*, 6:22, 1961. doi: 10.1103/PhysRevLett.6.22.

[42] J. Hersil et al. A measurement of the air fluorescence yield. *Nucl. Instrum. Meth. A*, 372(3):527, 1996. doi: 10.1016/0168-9002(95)01423-3.

[43] R. M. Baltrusaitis et al. The Utah Fly's Eye detector. *Nucl. Instrum. Meth. A*, 240(2):410, 1985. doi: 10.1016/0168-9002(85)90658-8.

[44] Pierre Auger Collaboration. Data-driven estimation of the invisible energy of cosmic ray showers with the Pierre Auger Observatory. *Phys. Rev. D*, 100:082003, 2019. doi: 10.1103/PhysRevD.100.082003.

[45] S. Ogio for the Telescope Array Collaboration. Telescope Array experiment. *EPJ Web Conf*, 208:08002, 2019. doi: 10.1051/epjconf/201920808002.

[46] D. Ivanov for the Telescope Array Collaboration. Energy spectrum measured by the Telescope Array experiment. *Proc. of 36th ICRC*, 298, 2019. doi: pos.sissa.it/358/298/.

[47] C. Song et al. Energy estimation of UHE cosmic rays using the atmospheric fluorescence technique. *Astropart. Phys.*, 14:7, 2000. doi: 10.1016/S0927-6505(00)00101-8.

[48] J. Linsley. Spectra, anisotropies and composition of cosmic rays above 1000 gev. *Proc. of 18th ICRC*, 12:144, 1983. Bibcode: 1983ICRC...12..135L.

[49] Telescope Array Collaboration. The cosmic-ray energy spectrum observed with the surface detector of the Telescope Array experiment. *Astrophys. J.*, 768(1):1, 2013. doi: 10.1088/2041-8205/768/1/l1.

[50] Telescope Array Collaboration. The cosmic ray energy spectrum between 2 PeV and 2 EeV observed with the TALE detector in monocular mode. *Astrophys. J.*, 865(L1):74, 2018. doi: 10.3847/1538-4357/aada05.

[51] A. Castellina for the Pierre Auger Collaboration. Highlights from the Pierre Auger Observatory. *Proc. of 36th ICRC*, 004, 2019. doi: pos.sissa.it/358/004/.

[52] Pierre Auger Collaboration. The Pierre Auger cosmic ray observatory. *Nucl. Instrum. Meth. A*, 798:172, 2015. doi: 10.1016/j.nima.2015.06.058.

[53] V. Novotny for the Pierre Auger Collaboration. Radio detection of high-energy cosmic rays with the Auger Engineering Radio Array. *Proc. of 36th ICRC*, 374, 2019. doi: pos.sissa.it/358/374/.

[54] F. Schröder for the Pierre Auger Collaboration. Radio detection of high-energy cosmic rays with the Auger Engineering Radio Array. *Nucl. Instrum. Meth. A*, 824:648, 2016. doi: 10.1016/j.nima.2015.08.047.

[55] A. Castellina for the Pierre Auger Collaboration. AugerPrime: the Pierre Auger Observatory upgrade. *EPJ Web Conf.*, 210:06002, 2019. doi: 10.1051/epjconf/201921006002.

[56] O. Deligny for the Pierre Auger and the Telescope Array Collaborations. The energy spectrum of ultra-high energy cosmic rays measured at the Pierre Auger Observatory and at the Telescope Array. *Proc. of 36th ICRC*, 234, 2019. doi: pos.sissa.it/358/234/.

[57] V. Verzi for the Pierre Auger Collaboration. Measurement of the energy spectrum of ultra-high energy cosmic rays using the Pierre Auger Observatory. *Proc. of 36th ICRC*, 450, 2019. doi: pos.sissa.it/358/450/.

[58] K. Greisen. End to the cosmic-ray spectrum? *Phys. Rev. Lett.*, 16:748, 1966. doi: 10.1103/PhysRevLett.16.748.

[59] G. T. Zatsepin and V. A. Kuzmin. Upper limit of the spectrum of cosmic rays. *JETP Lett.*, 4:78, 1966. Bibcode: 1966JETPL...4...78Z.

[60] N. Sakaki for the AGASA Collaboration. Cosmic ray energy spectrum above $3 \times 10^1 8$ ev observed with AGASA. *Proc. of 27th ICRC*, 333, 2001.

[61] M. Takeda for the AGASA Collaboration. Energy determination in the Akeno Giant Air Shower Array experiment. *Astropart. Phys.*, 19:447, 2003. doi: 10.1016/S0927-6505(02)00243-8.

[62] High Resolution Fly's Eye Collaboration. Measurement of the flux of ultra-high energy cosmic rays from monocular observations by the High Resolution Fly's Eye experiment. *Phys. Rev. Lett.*, 92:151101, 2004. doi: 10.1103/PhysRevLett.92.151101.

[63] High Resolution Fly's Eye Collaboration. Monocular measurement of the spectrum of UHE cosmic rays by the FADC detector of the hires experiment. *Astropart. Phys.*, 26:157, 2005. doi: 10.1016/j.astropartphys.2004.12.006.

[64] A. Coleman for the Pierre Auger Collaboration. Measurement of the cosmic ray flux near the second knee with the Pierre Auger Observatory. *Proc. of 36th ICRC*, 225, 2019. doi: pos.sissa.it/358/225/.

[65] E. Kido for the Telescope Array Collaboration. Implications of the cosmic ray spectrum from the second knee to the ankle region observed by the ta and tale experiment for the cosmic ray proton sources. *Proc. of 36th ICRC*, 313, 2019. doi: pos.sissa.it/358/313/.

[66] T. Abu-Zayyad et al. The knee and the second knee of the cosmic-ray energy spectrum. 2018. arXiv: 1803.07052.

[67] Pierre Auger Collaboration. Combined fit of spectrum and composition data as measured by the Pierre Auger Observatory. *J. Cosm. Astropart. Phys.*, 04:038, 2017. doi: 10.1088/1475-7516/2017/04/038.

[68] A. M. Hillas. The origin of ultra-high energy cosmic rays. *Ann. Rev. Astron. Astrophys.*, 22:425, 1984. doi: 10.1146/annurev.aa.22.090184.002233.

[69] A. Yushkov for the Pierre Auger Collaboration. Mass composition of cosmic rays with energies above $10^{17.2}$ eV from the hybrid data of the Pierre Auger Observatory. *Proc. of 36th ICRC*, 482, 2019. doi: pos.sissa.it/358/482/.

[70] W. Hanlon for the Telescope Array Collaboration. Telescope Array 10 year composition. *Proc. of 36th ICRC*, 280, 2019. doi: pos.sissa.it/358/280/.

[71] V. de Souza for the Pierre Auger Collaboration. Measurements of the depth of maximum of air-shower profiles at the Pierre Auger Observatory and their composition implications. *XXV European Cosmic Ray Symposium*, 2016.

[72] W. Hanlon, J. Bellido, J. Belz, S. Blaess, V. de Souza, D. Ikeda, P. Sokolsky, Y. Tsunesada, M. Unger, A. Yushkov, for the Pierre Auger Collaboration, and the Telescope Array Collaboration. Report of the working group on the mass composition of ultra-high energy cosmic rays. *JPS Conf. Proc.*, 19:011013, 2018. doi: 10.7566/JPSCP.19.011013.

[73] J. Bellido for the Pierre Auger Collaboration. Depth of maximum of air-shower profiles at the Pierre Auger Observatory: Measurements above $10^{17.2}$ eV and composition implications. *Proc. of 35th ICRC*, 506, 2017. doi: pos.sissa.it/301/506/.

[74] Pierre Auger Collaboration. Large scale distribution of ultra-high energy cosmic rays detected at the Pierre Auger Observatory with zenith angles up to 80°. *Astropart. Phys.*, 802:111, 2015. doi: 10.1088/0004-637x/802/2/111.

[75] Telescope Array Collaboration. Search for anisotropy of ultra-high energy cosmic rays with the Telescope Array experiment. *Astropart. Phys.*, 757:26, 2012. doi: 10.1088/0004-637X/757/1/26.

[76] E. Roulet for the Pierre Auger Collaboration. Large-scale anisotropies above 0.03 EeV measured by the Pierre Auger Observatory. *Proc. of 36th ICRC*, 408, 2019. doi: pos.sissa.it/358/408/.

[77] Pierre Auger Collaboration. Cosmic-ray anisotropies in right ascension measured by the Pierre Auger Observatory. *Astropart. Phys.*, 891:142, 2020. doi: 10.3847/1538-4357/ab7236.

[78] A. di Matteo for the Pierre Auger and the Telescope Array Collaborations. Full-sky searches for anisotropies in UHECR arrival directions with the Pierre Auger Observatory and the Telescope Array. *Proc. of 36th ICRC*, 439, 2019. doi: pos.sissa.it/358/439/.

[79] S. Troitsky for Telescope Array Collaboration. Telescope Array anisotropy summary. *Proc. of 35th ICRC*, 548, 2017. doi: pos.sissa.it/301/548/.

[80] L. Caccianiga for the Pierre Auger Collaboration. Anisotropies of the highest energy cosmic-ray events recorded by the Pierre Auger Observatory in 15 years of operation. *Proc. of 36th ICRC*, 206, 2019. doi: pos.sissa.it/358/206/.

[81] J. P. Huchra, L. M. Macri, K. L. Masters, et al. The 2MASS Redshift Survey: description and data release. *Astrophys. J. Supp.*, 199:26, 2012. doi: 10.1088/0067-0049/199/2/26.

[82] W. H. Baumgartner et al. The 70 month Swift-BAT all-sky hard x-ray survey. *Astrophys. J. Supp.*, 207:19, 2013. doi: 10.1088/0067-0049/207/2/19.

[83] M. Ajello et al. 3FHL: the third catalog of hard Fermi-LAT sources. *Astrophys. J. Supp.*, 232:18, 2017. doi: 10.3847/1538-4365/aa8221.

[84] Pierre Auger Collaboration. An indication of anisotropy in arrival directions of ultra-high energy cosmic rays through comparison to the flux pattern of extragalactic gamma-ray sources. *Astrophys. J.*, 853:L29, 2018. doi: 10.3847/2041-8213/aaa66d.

[85] K. Kawata for the Telescope Array Collaboration. Updated results on the UHECR hotspot observed by the Telescope Array experiment. *Proc. of 36th ICRC*, 310, 2019. doi: pos.sissa.it/358/310/.

[86] H. Takami and K. Sato. Does galactic magnetic field disturb the correlation of the highest energy cosmic rays with their sources? *Astrophys. J.*, 681:1279, 2008. doi: 10.1088/0004-637x/724/2/1456.

[87] T. Stanev. Ultra-high energy cosmic rays and the large-scale structure of the galactic magnetic field. *Astrophys. J.*, 479:290, 1997. doi: 10.1086/303866.

[88] T. Stanev, R. Engle, J. Alvarez-Muñiz, and D. Seckel. Ultra-high energy cosmic rays and magnetic fields. *Nucl. Phys. B - Proc. Supp.*, 110:491, 2002. doi: 10.1016/S0920-5632(02)01544-X.

[89] K. Kotera and A. V. Olinto. The astrophysics of ultra-high energy cosmic rays. *Ann. Rev. Astron. Astrophys.*, 49:119, 2010. doi: 10.1146/annurev-astro-081710-102620.

[90] L. M. Widrow. Origin of galactic and extragalactic magnetic fields. *Rev. Mod. Phys.*, 74:775, 2002. doi: 10.1103/RevModPhys.74.775.

[91] F. Vazza et al. Probing the origin of extragalactic magnetic fields with fast radio bursts. *Month. Not. Roy. Astr. Soc.*, 480(3):3907, 2018. doi: 10.1093/mnras/sty1968.

[92] T. E. Clarke et al. A new radio-x-ray probe of galaxy cluster magnetic fields. *Astrophys. J.*, 547(2):11, 2001. doi: 10.1086/318896.

[93] A. Neronov and I. Vovk. Evidence for strong extragalactic magnetic fields from Fermi observations of TeV blazars. *Science*, 328:73, 2010. doi: 10.1126/science.1184192.

[94] F. A. Aharonian, S. R. Kelner, and A. Y. Prosekin. Angular, spectral, and time distributions of highest energy protons and associated secondary gamma-rays and neutrinos propagating through extragalactic magnetic and radiation fields. *Phys. Rev. D*, 82:043002, 2010. doi: 10.1103/PhysRevD.82.043002.

[95] E. Waxman and J. Miralda-Escude. Images of bursting sources of high-energy cosmic rays. I: Effects of magnetic fields. *Astrophys. J.*, 472:L89, 1996. doi: 10.1086/310367.

[96] G. R. Farrar, R. Jansson, I. J. Feain, and B. M. Gaensler. Galactic magnetic deflections and Centaurus A as a UHECR source. *J. Cosm. Astropart. Phys.*, 01:023, 2013. doi: 10.1088/1475-7516/2013/01/023.

[97] J. L. Puget, F. W. Stecker, and J. H. Bredekamp. Photonuclear interactions of ultra-high energy cosmic rays and their astrophysical consequences. *Astrophys. J.*, 205:638, 1976. Bibcode: 1976ApJ...205..638P.

[98] F. W. Stecker and M. H. Salamon. Photodisintegration of ultra-high-energy cosmic rays: A new determination. *Astrophys. J.*, 512:521, 1999. doi: 10.1086/306816.

[99] M. Lemoine and E. Waxman. Anisotropy vs chemical composition at ultra-high energies. *J. Cosm. Astropart. Phys.*, 2009(11):009, 2009. doi: 10.1088/1475-7516/2009/11/009.

[100] A. Celotti and G. Ghisellini. The power of blazar jets. *Month. Not. Roy. Astr. Soc.*, 385(1):283, 2008. doi: 10.1111/j.1365-2966.2007.12758.x.

[101] B. Zhang et al. Low-luminosity gamma-ray bursts as the sources of ultra-high energy cosmic ray nuclei. *Phys. Rev. D*, 97:083010, 2018. doi: 10.1103/PhysRevD.97.083010.

[102] A. Gruzinov G. R. Farrar. Giant AGN flares and cosmic ray bursts. *Astrophys. J.*, 693:329, 2009. doi: 10.1088/0004-637X/693/1/329.

[103] B. A. Nizamov and M. S. Pshirkov. Constraints on the AGN flares as sources of ultra-high energy cosmic rays from the Fermi-LAT observations. *J. Cosm. Astropart. Phys.*, 03:060, 2020. doi: 10.1088/1475-7516/2020/03/060.

[104] P. Bhattacharjee and G. Sigl. Origin and propagation of extremely high-energy cosmic rays. *Phys. Rep.*, 327(3-4):109, 2000. doi: 10.1016/S0370-1573(99)00101-5.

[105] V. Berezinsky. Ultra-high energy cosmic rays. *Nucl. Phys. B (Proc. SUppl.)*, 81:311, 2000. doi: 10.1016/S0920-5632(99)00891-9.

[106] G. Gelmini, O. Kalashev, and D. Semikoz. GZK photons as ultra-high energy cosmic rays. *J. Exp. Theo. Phys. Lett.*, 106:1061, 2008. doi: 10.1134/S106377610806006X.

[107] V. A. Kuzmin and V. A. Rubakov. Ultra-high energy cosmic rays: a window to post-inflationary reheating epoch of the Universe? *Phys. Atom. Nucl.*, 61:1028, 1998. arXiv: astro-ph/9709187.

[108] V. Berezinsky, M. Kachelrieß, and A. Vilenkin. Ultra-high energy cosmic rays without Greisen-Zatsepin-Kuzmin cut-off. *Phys. Rev. Lett.*, 79:4302, 1997. doi: 10.1103/PhysRevLett.79.4302.

[109] M. Birkel and S. Sarkar. Extremely high-energy cosmic rays from relic particle decays. *Astropart. Phys.*, 9(4):297, 1998. doi: 10.1016/S0927-6505(98)00028-0.

[110] V. A. Kuzmin and I. I. Tkachev. Ultra-high energy cosmic rays, superheavy long-lived particles, and matter creation after inflation. *J. Exp. Theo. Phys. Lett.*, 68:271, 1998. doi: 10.1134/1.567858.

[111] J. Ellis et al. Ultra-high energy cosmic rays particle spectra from crypton decays. *Phys. Rev. D*, 74:115003, 2006. doi: 10.1103/PhysRevD.74.115003.

[112] W. Kolb and M. S. Turner. *The Early Universe*. Frontiers in Physics, 1990.

[113] P. Bhattacharjee and N. C. Rana. Ultra-high energy particle flux from cosmic strings. *Phys. Rev. B*, 246:365, 1990. doi: 10.1016/0370-2693(90)90615-D.

[114] C. T. Hill. Monopolonium. *Nucl. Phys. B*, 224:469, 1983. doi: 10.1016/0550-3213(83)90386-3.

[115] P. Bhattacharjee, C. T. Hill, and D. N. Schramm. Grand unified theories, topological defects, and ultra-high energy cosmic rays. *Phys. Rev. Lett.*, 69:567, 1992. doi: 10.1103/PhysRevLett.69.567.

[116] D. Fargion, B. Mele, and A. Salis. Ultra-high energy neutrino scattering onto relic light neutrinos in galactic halo as a possible source of highest energy extragalactic cosmic rays. *Astrophys. J.*, 517:725, 1999. doi: 10.1086/307203.

[117] T. J. Weiler. Cosmic-ray neutrino annihilation on relic neutrinos revisited: a mechanism for generating air showers above the Greisen-Zatsepin-Kuzmin cutoff. *Astropart. Phys.*, 11:303, 1999. doi: 10.1016/S0927-6505(98)00068-1.

[118] L. Maccione, S. Liberati, and G. Sigl. Ultra-high energy photons as probes of Lorentz symmetry violations in stringy space-time foam models. *Phys. Rev. Lett.*, 105:021101, 2010. doi: 10.1103/PhysRevLett.105.021101.

[119] S. Liberati and L. Maccione. Lorentz violation: Motivation and new constraints. *Ann. Rev. Nucl. Part. Sci.*, 59:245, 2009. doi: 10.1146/annurev.nucl.010909.083640.

[120] MAGIC Collaboration. Teraelectronvolt emission from the -ray burst GRB 190114C. *Nature*, 575:455, 2019. doi: 10.1038/s41586-019-1750-x.

[121] MAGIC Collaboration. Bounds on Lorentz invariance violation from MAGIC observation of GRB 190114C. *Phys. Rev. Lett.*, 125:021301, 2020. doi: 10.1103/PhysRevLett.125.021301.

[122] M. Risse for the Pierre Auger Collaboration. An upper limit to photons from first data taken by the Pierre Auger Observatory. *6th Rencontre du Vietnam*, 2007. arXiv: astro-ph/0701065.

[123] G. I. Rubtsov et al. Upper limit on the ultra-high energy photon flux from AGASA and Yakutsk data. *Phys. Rev. D*, 73:063009, 2020. doi: 10.1103/PhysRevD.73.063009.

[124] D. R. Bergman for the HiRes Collaboration. Fitting the HiRes spectra and monocular composition. *Nucl. Phys. Proc. Suppl.*, 136:40, 2005. doi: 10.1016/j.nuclphysbps.2004.10.042.

[125] D. Hooper, A. M. Taylor, and S. Sarkar. Cosmogenic photons as a test of ultra-high energy cosmic ray composition. *Astropart. Phys.*, 34:340, 2011. doi: 10.1016/j.astropartphys.2010.09.002.

[126] K-H. Kampert and B. Sarkar. Ultra-high energy photon and neutrino fluxes in realistic astrophysical scenarios. *Proc. of 32th ICRC*, 2:198, 2011. doi: 10.7529/ICRC2011/V02/1087.

[127] Pierre Auger Collaboration. Upper limit on the cosmic-ray photon fraction at eev energies from the pierreauger observatory. *Astropart. Phys.*, 31:399, 2009. doi: 10.1016/j.astropartphys.2009.04.003.

[128] C. Heiter et al. Production and propagation of ultra-high energy photons using CRPropa 3. *Astropart. Phys.*, 102:39, 2018. doi: 10.1016/j.astropartphys.2018.05.003.

[129] H. P. Vankov, N. Inoue, and K. Shinozaki. Ultra-high energy gamma rays in the geomagnetic field and atmosphere. *Phys. Rev. D*, 67:043002, 2003. doi: 10.1103/physrevd.67.043002.

[130] L. D. Landau and I. Ya. Pomeranchuk. Limits of applicability of the theory of bremsstrahlung electrons and pair production at high-energies. *Dokl. Akad. Nauk SSSR*, 92:535, 1953.

[131] L. D. Landau and I. Ya. Pomeranchuk. Electron-cascade processes at ultra-high energies. *Dokl. Akad. Nauk SSSR*, 92:735, 1953.

[132] A. B. Migdal. Bremsstrahlung and pair production in condensed media at high energies. *Phys. Rev.*, 103:1811, 1956. doi: 10.1103/PhysRev.103.1811.

[133] Pierre Auger Collaboration. An upper limit to the photon fraction in cosmic rays above 10^{19} eV from the Pierre Auger Observatory. *Astropart. Phys.*, 27:155, 2007. doi: 10.1016/j.astropartphys.2006.10.004.

[134] B. McBreen and C. Lambert. Interactions of high-energy ($e > 5 \times 10^{19}$ eV) photons in the Earth's magnetic field. *Phys. Rev. D*, 24(9):2536, 1981. doi: 10.1103/PhysRevD.24.2536.

[135] P. Homola et al. Characteristics of geomagnetic cascading of ultra-high energy photons at the southern and northern sites of the Pierre Auger Observatory. *Astropart. Phys.*, 27:174, 2007. doi: 10.1016/j.astropartphys.2006.10.005.

[136] D. J. Bird et al. Detection of a cosmic ray with measured energy well beyond the expected spectral cutoff due to cosmic microwave radiation. *Astrophys. J.*, 441:144, 1995. doi: 10.1086/175344.

[137] M. Risse and P. Homola. Search for ultra-high energy photons using air showers. *Mod. Phys. Lett. A*, 22:749, 2007. doi: 10.1142/S0217732307022864.

[138] J. Rautenberg for the Pierre Auger and the Telescope Array Collaborations. Limits on ultra-high energy photons with the Pierre Auger Observatory. *Proc. of 36th ICRC*, 398, 2019. doi: pos.sissa.it/358/398/.

[139] Telescope Array Collaboration. Constraints on the diffuse photon flux with energies above 10^{18} eV using the surface detector of the Telescope Array experiment. *Astropart. Phys.*, 110:8, 2019. doi: 10.1016/j.astropartphys.2019.03.003.

[140] Y. Fomin et al. Constraints on the flux of $\sim (10^{16} - 10^{17.5})$eV cosmic photons from the EAS–MSU muon data. *Phys. Rev. D*, 95:123011, 2017. doi: 10.1103/PhysRevD.95.123011.

[141] KASCADE-Grande Collaboration. KASCADE-Grande limits on the isotropic diffuse gamma-ray flux between 100 TeV and 1 EeV. *Astrophys. J.*, 848:1, 2017. doi: 10.3847/1538-4357/aa8bb7.

[142] Pierre Auger Collaboration. A targeted search for point sources of EeV photons with the Pierre Auger Observatory. *Astrophys. J.*, 837:L25, 2017. doi: 10.3847/2041-8213/aa61a5.

[143] Telescope Array Collaboration. Search for point sources of ultra-high-energy photons with the Telescope Array surface detector. *Month. Not. Roy. Astr. Soc.*, 492:3984, 2020. doi: 10.1093/mnras/stz3618.

[144] T. Erber. High-energy electromagnetic conversion processes in intense magnetic fields. *Rev. Mod. Phys.*, 38:626, 1966. doi: 10.1103/RevModPhys.38.626.

[145] W. Bednarek. Cascades initiated by EHE photons in the magnetic field of the Earth and the Sun. 1999. arXiv: astro-ph/9911266.

[146] D. Niraj for the CREDO Collaboration. Cosmic-ray ensembles as signatures of ultra-high energy photons interacting with the solar magnetic field. 2018. arXiv: 1811.10334.

[147] M. Banaszkiewicz, W. I. Axford, and J. F. McKenzie. High-energy electromagnetic conversion processes in intense magnetic fields. *Astron. Astrophys.*, 337:940, 1998. Bibcode: 1998A&A...337..940B.

[148] Alex Kääpä. Analysis of super-preshowers at the Pierre Auger Observatory. Master's thesis, University of Wuppertal, 2016.

[149] W. Greiner and J. Reinhardt. *Quantum Electrodynamics*, volume 1. Springer, fourth edition, 2010.

[150] F. A. Aharonian, B. L. Kanevsky, and V. A. Sahakian. On some peculiarities of EAS initiated by gamma rays of extremely high energies. *J. Phys. G*, 17:1909, 1991. doi: 10.1088/0954-3899/17/12/012.

[151] S. Karakuła and W. Tubek. The influence of EHE photon interaction with Earth's magnetic field and LPM effect on the cascade development in the atmosphere. *Memorie della Società Astronomia Italiana*, 67:65, 1996. Bibcode: 1996MmSAI..67...65K.

[152] S. Karakuła. Can EHE photons be responsible for the highest energy cosmic ray showers? *Front. Obj. Astrophys. Part. Phys.*, 57:355, 1997. Bibcode: 1997foap.conf..355K.

[153] P. Homola et al. Simulation of ultra-high energy photon propagation in the geomagnetic field. *Comput. Phys. Commun.*, 173:71, 2005. doi: 10.1016/j.cpc.2005.07.001.

[154] E. Thébault et al. International Geomagnetic Reference Field: the 12th generation. *Earth, Planets and Space*, 67:79, 2015. doi: 10.1186/s40623-015-0228-9.

[155] D. Góra for the CREDO Collaboration. Cosmic-Ray Extremely Distributed Observatory: status and perspectives. *Universe*, 4(11):111, 2018. doi: 10.3390/universe4110111.

[156] K. Almeida Cheminant for the CREDO Collaboration. Cosmic Ray Extremely Distributed Observatory: a global network of detectors to probe contemporary physics mysteries. *Acta Phys. Pol. B Proc. Supp.*, 11(3):489, 2018. doi: 10.5506/APhysPolBSupp.11.489.

[157] D. Góra for the CREDO Collaboration. Cosmic Ray Extremely Distributed Observatory: Status and perspectives of a global cosmic ray detection framework. *Proc. of 36th ICRC*, 272, 2019. doi: pos.sissa.it/358/272/.

[158] R. Kamiński and T. Wibig for the CREDO Collaboration. CREDO project. *Acta Phys. Pol. B*, 50:2001, 2019. doi: 10.5506/AphysPolB.50.2001s.

[159] D. J. Fegan, B. McBreen, and C. O'Sullivan. Observation of a burst of cosmic rays at energies above 7×10^{13} eV. *Phys. Rev. Lett.*, 51:2341, 1983. doi: 10.1103/PhysRevLett.51.2341.

[160] G. R. Smith, M. Ogmen, E. Buller, and S. Standil. Possible observation of a burst of cosmic-ray events in the form of extensive air showers. *Phys. Rev. Lett.*, 50:2110, 1983. doi: 10.1103/PhysRevLett.50.2110.

[161] W. Galbraith and J. V. Jelley. Light pulses from the night sky associated with cosmic rays. *Nature*, 171:349, 1953. doi: 10.1038/171349a0.

[162] A. M. Hillas. Evolution of ground-based gamma-ray astronomy from the early days to the Cherenkov Telescope Array. *Astropart. Phys.*, 43:19, 2013. doi: 10.1016/j.astropartphys.2012.06.002.

[163] T. C. Weekes et al. Observation of TeV gamma rays from the Crab nebula using the Atmospheric Cherenkov Imaging Technique. *Astrophys. J.*, 342:379, 1989. doi: 10.1086/167599.

[164] M. J. Lang et al. TeV observations of the Crab nebula and other plerions in the epoch 1988-91. *Proc. of 22nd ICRC*, page 204, 1991. Bibcode: 1991ICRC....1..204L.

[165] M. Errando for the MAGIC Collaboration. Discovery of very-high energy gamma rays from the flat spectrum radio quasar 3C 279 with the MAGIC telescope. *AIP Conf. Proc.*, 1085:423, 2008. doi: 10.1063/1.3076698.

[166] VERITAS Collaboration. A connection between star formation activity and cosmic rays in the starburst galaxy M82. *Nature*, 462:770, 2009. doi: 10.1038/nature08557.

[167] VERITAS Collaboration. Discovery of TeV gamma-ray emission from Tycho's supernova remnant. *Astrophys. J.*, 730(2):L20, 2011. doi: 10.1088/2041-8205/730/2/l20.

[168] H.E.S.S. Collaboration. Resolving acceleration to very-high energies along the jet of Centaurus A. *Nature*, 582:356, 2020. doi: 10.1038/s41586-020-2354-1.

[169] P. A. Cherenkov. Visible radiation produced by electrons moving in a medium with velocities exceeding that of light. *Phys. Rev.*, 52(4):378, 1937. doi: 10.1103/PhysRev.52.378.

[170] F. Katz. Cherenkov light imaging in astroparticle physics. *Nucl. Inst. Meth. A*, 952:161654, 2020. doi: 10.1016/j.nima.2018.11.113.

[171] P. K. F. Grieder. *Extensive Air Showers.* Springer, 2010. doi: 10.1007/978-3-540-76941-5.

[172] H. Bartko, F. Goebel, R. Mirzoyan, W. Pimpl, and M. Teshima. Tests of a prototype multiplexed fiber-optic ultra-fast FADC data acquisition system for the MAGIC telescope. *Nucl. Inst. Meth. A*, 548:464, 2005. doi: 10.1016/j.nima.2005.05.029.

[173] E. Aliu et al. Improving the performance of the single-dish cherenkov telescope MAGIC through the use of signal timing. *Astropart. Phys.*, 30:293, 2009. doi: 10.1016/j.astropartphys.2008.10.003.

[174] A. E. Chudakov, V. L. Dadykin, V. I. Zatsepin, and N. M. Nesterova. On the high-energy photons from local sources. *Proc. of 6th ICRC*, 4:199, 1963. Bibcode: 1963ICRC....4..199C.

[175] A. C. Rovero, K. Harris, Y. Jiang, and M. A. Lawrence. Calibration of an atmospheric Cherenkov telescope using muon ring images. *AIP Conf. Proc.*, 280:1176, 1993. doi: 10.1063/1.44151.

[176] H. J. Volk and K. Bernlohr. Imaging very-high energy gamma-ray telescopes. *Exp. Astr.*, 25:173, 2009. doi: 10.1007/s10686-009-9151-z.

[177] A. Neronov. Cosmic-ray composition measurements in the knee energy range with MAGIC. *MAGIC meeting*, 26/05/17, 2017.

[178] A. M. Hillas. Cherenkov light images of EAS produced by primary gamma rays and by nuclei. *Proc. of 19th ICRC*, 3:445, 1985. Bibcode: 1985ICRC....3..445H.

[179] A. Neronov, D. V. Semikoz, I. Vovk, and R. Mirzoyan. Cosmic-ray composition measurements and cosmic ray background-free gamma-ray observations with Cherenkov telescopes. *Phys. Rev. D*, 94:123018, 2016. doi: 10.1103/PhysRevD.94.123018.

[180] CTA Collaboration. Introducing the CTA concept. *Astropart. Phys.*, 43:3, 2013. doi: 10.1016/j.astropartphys.2013.01.007.

[181] CTA Consortium. *Science with the Cherenkov Telescope Array.* World Scientific, 2019. doi: 10.1142/10986.

[182] H.E.S.S. Collaboration. Acceleration of petaelectronvolt protons in the Galactic Centre. *Nature*, 531:476, 2016. doi: 10.1038/nature17147.

[183] N. N. Kalmykov, S. S. Ostapchenko, and A. I. Pavlov. Quark-gluon-string model and EAS simulation problems at ultra-high energies. *Nucl. Phys. B Proc. Suppl.*, 52:17, 1997. doi: 10.1016/S0920-5632(96)00846-8.

[184] S. S. Ostapchenko. On the re-summation of enhanced Pomeron diagrams. *Phys. Lett. B*, 636:40, 2006. doi: 10.1016/j.physletb.2006.03.026.

[185] S. S. Ostapchenko. Nonlinear screening effects in high energy hadronic interactions. *Phys. Rev. D*, 74:014026, 2006. doi: 10.1103/PhysRevD.74.014026.

[186] R. Engel et al. Air shower calculations with the new version of SIBYLL. *Proc. of 26th ICRC*, 1:415, 1999. Bibcode: 1999ICRC....1..415E.

[187] D. Heck, J. Knapp, J.N. Capdevielle, G. Schatz, and T. Thouw. CORSIKA: A Monte-Carlo code to simulate extensive air showers. *Report FZKA 6019*, Forschungszentrum Karlsruhe, 1998.

[188] J. Engler et al. The kascade project. *Nucl. Phys. B Proc. Suppl.*, 14:336, 1990. doi: 10.1016/0920-5632(90)90441-V.

[189] CTA Consortium. Design concepts for the Cherenkov Telescope Array CTA: an advanced facility for ground-based high-energy gamma-ray astronomy. *Exp. Astr.*, 32:193, 2011. doi: 10.1007/s10686-011-9247-0.

[190] D. Heck and T. Pierog. Extensive Air Shower Simulation with CORSIKA: A user's guide (version6.99x). 2011.

[191] S.A. Bass et al. Microscopic models for ultra-relativistic heavy ion collisions. *Prog. Part. Nucl. Phys.*, 41:255, 1998. doi: 10.1016/S0146-6410(98)00058-1.

[192] M. Bleicher et al. Relativistic hadron-hadron collisions in the ultra-relativistic quantum molecular dynamics model. *J. Phys. G*, 25:1859, 1999. doi: 10.1088/0954-3899/25/9/308.

[193] A. M. Hillas. Shower simulation: lessons from MOCCA. *Nucl. Phys. B Proc. Suppl.*, 52:2942, 1997. doi: 10.1016/S0920-5632(96)00847-X.

[194] K. Bernlohr. Impact of atmospheric parameters on the atmospheric Cherenkov technique. *Astropart. Phys.*, 12:255, 2000. doi: 10.1016/S0927-6505(99)00093-6.

[195] K. Bernlohr. Simulation of imaging atmospheric Cherenkov telescopes with CORSIKA and sim_telarray. *Astropart. Phys.*, 30:149, 2008. doi: 10.1016/j.astropartphys.2008.07.009.

[196] A. G. Delgado Giler et al. Measuring the depth of shower maximum of extensive air showers using Cherenkov light. *Astropart. Phys.*, 124:102508, 2020. doi: 10.1016/j.astropartphys.2020.102508.

[197] T. Bretz, D. Dorner, B. Riegel, D. Höhne, and K. Berger for the MAGIC Collaboration. Comparison of On-Off and Wobble mode observations for MAGIC. *Proc. of 29th ICRC*, 4:311, 2005.

[198] MAGIC Collaboration. MAGIC very large zenith angle observations of the Crab nebula up to 100 TeV. *Astron. Astrophys.*, 635:A158, 2020. doi: 10.1051/0004-6361/201936899 .

[199] K. Pearson. LIII. on lines and planes of closest fit to systems of points in space. *The London, Edinburgh, and Dublin Philosophical Magazine and Journal of Science*, 2(11):559, 1901. doi: 10.1080/14786440109462720.

[200] J. Sitarek, D. Sobczynska, K. Adamczyk, and M. Szanecki. V-shaped Cherenkov images of magnetically-separated gamma rays. *Proc. of 36th ICRC*, 795, 2019. doi: pos.sissa.it/358/795/.

[201] R. Bock et al. Methods for multidimensional event classification: a case study using images from a Cherenkov gamma-ray telescope. *Nucl. Inst. Meth. A*, 516:511, 2004. doi: 10.1016/j.nima.2003.08.157.

[202] S. Ohm, C. van Eldik, and K. Egberts. Gamma-hadron separation in very-high energy gamma-ray astronomy using a multivariate analysis method. *Astropart. Phys.*, 31:383, 2009. doi: 10.1016/j.astropartphys.2009.04.001.

[203] J. Albert et al. Implementation of the Random Forest Method for the Imaging Atmospheric Cherenkov Telescope MAGIC. *Nucl. Inst. Meth. A*, 588:424, 2007. doi: 10.1016/j.nima.2007.11.068.

[204] A. Hoecker, P. Speckmayer, J. Stelzer, J. Therhaag, E. von Toerne, and H. Voss. TMVA: Toolkit for Multivariate Data Analysis. *PoS ACAT*, page 040, 2007. arXiv: physics/0703039.

[205] B. Wiebel. Chemical composition in high energy cosmic rays. *Wuppertal Univ. - WU B*, 94-08, 1994.

[206] MAGIC Collaboration. Limits on the flux of tau neutrinos from 1 PeV to 3 EeV with the MAGIC telescopes. *Astropart. Phys.*, 102:77, 2018. doi: 10.1016/j.astropartphys.2018.05.002.

[207] C. Gini. Variability and mutability. *Reprinted in Pizetti*, 1912.

[208] B. Matthews. Comparison of the predicted and observed secondary structure of T4 phage lysozyme. *Biochim. Biophys.*, 405:442, 1975. doi: 10.1016/0005-2795(75)90109-9.

[209] H.E.S.S. Collaboration. A very-high energy component deep in the gamma-ray burst afterglow. *Nature*, 575:464, 2019. doi: 10.1038/s41586-019-1743-9.

[210] IceCube, Fermi-LAT, MAGIC, AGILE, ASAS-SN, HAWC, H.E.S.S., INTEGRAL, Kanata, Kiso, Kapteyn, Liverpool Telescope, Subaru, Swift/NuSTAR, VERITAS, and VLA/17B-403 Collaborations. Multimessenger observations of a flaring blazar coincident with high-energy neutrino IceCube-170922A. *Science*, 361:eaat1378, 2018. doi: 10.1126/science.aat1378.

[211] P. Homola for the CREDO Collaboration. Public engagement as a scientific tool to implement multi-messenger strategies with the Cosmic-Ray Extremely Distributed Observatory. *Proc. of ASTERICS conf.*, 034, 2019. doi: pos.sissa.it/357/034/.

[212] K. Almeida Cheminant and D. Góra for the CREDO Collaboration. Search for electromagnetic super-preshowers using gamma-ray telescopes. *Proc. of 35th ICRC*, 860, 2017. doi: pos.sissa.it/301/860/.

[213] K. Almeida Cheminant and D. Góra for the CREDO Collaboration. Search for ultra-high energy photons: observing the preshower effect with gamma-ray telescopes. *Proc. of 36th ICRC*, 688, 2019. doi: pos.sissa.it/358/688/.

[214] K. Almeida Cheminant and D. Góra for the CREDO Collaboration. Search for ultra-high energy photons through preshower effect with gamma-ray telescopes: Study of CTA-North efficiency. *Astropart. Phys.*, 123:102489, 2020. doi: 10.1016/j.astropartphys.2020.102489.

List of Figures

List of Tables

Acronyms

AGASA: Akeno Giant Air Shower Array

AGN: Active Galactic Nucleus

Auger: Pierre Auger Observatory

BDT: Boosted Decision Trees

CMB: Cosmic Microwave Background

COG: Center-Of-Gravity

CORSIKA: COsmic Ray SImulations for KAscade

CR: Cosmic Ray

CREDO: Cosmic Ray Extremely Distributed Observatory

CTA: Cherenkov Telescope Array

DQCS: Dipole Quadrupole Current Sheet

EAS: Extensive Air Showers

EBL: Extragalactic Background Light

EeV: Exa-ElectronVolt (10^{18} eV)

EGMF: ExtraGalactic Magnetic Field

FD: Fluorescence Detector

Fermi-LAT: Fermi-Large Area Telescope

FOV: Field Of View

GeV: Giga-ElectronVolt (10^9 eV)

GRB: Gamma-Ray Burst

IACT: Imaging Atmospheric Cherenkov Telescope

H.E.S.S.: High Energy Stereoscopic System

KASCADE: KArlsruhe Shower Core and Array DEtector

LDF: Lateral Distribution Function

LIV: Lorentz Invariance Violation

LST: Large Size Telescope

MAGIC: Major Atmospheric Gamma Imaging Cherenkov Telescopes

MCC: Matthews Correlation Coefficient

MST: Medium Size Telescope

NSB: Night-Sky Background

PCA: Principal Component Analysis

p.e.: photo-electron

PeV: Peta-ElectronVolt (10^{15} eV)

PMT: PhotoMultiplier Tube

QGSJET: Quark-Gluon String JET

SD: Surface Detector

SHDM: Super-Heavy Dark Matter

TA: Telescope Array

TeV: Tera-ElectronVolt (10^{12} eV)

TMVA: Toolkit for Multivariate Data Analysis

UHE: Ultra-High Energy

UHECR: Ultra-High Energy Cosmic Rays

UrQMD: Ultra relativistic Quantum Molecular Dynamics

UV: UltraViolet

VERITAS: Very Energetic Radiation Imaging Telescope Array System